Jan Sigurd Beddari Blackstad

Observations on the Hippocampal Formation

A study on the anatomy of the dentate-ammonic region in mink, sheep, and domestic pig, and spatial representations in the CA1 and subiculum of rats.

Doctoral thesis

NTNU
Norwegian University of
Science and Technology

Jan Sigurd Beddari Blackstad

Observations on the Hippocampal Formation

A study on the anatomy of the dentate-ammonic region in mink, sheep, and domestic pig, and spatial representations in the CA1 and subiculum of rats.

Thesis for the Degree of Philosophiae Doctor

Trondheim, April 2022

Norwegian University of Science and Technology
Faculty of Medicine and Health Sciences
Kavli Institute for Systems Neuroscience

NTNU
Norwegian University of
Science and Technology

"Lust and learning," Katherine once said. "That's really all there is, isn't it?"

— John Williams, Stoner

Sammendrag

Hippocampusformasjonen omfatter et område i hjernen hos pattedyr som er essensielt for romlig navigasjon og episodiske minner. Overordnet inndeles området i tre subregioner: Gyrus dentatus, cornu ammonis (CA1, CA2 og CA3), og subiculum. Størsteparten av fibre fra hjernebarken kommer fra lag II og III i entorhinal cortex (EC) og terminerer i ulike deler av hjerneområdet. Kort fortalt strekker fibrene seg fra EC lag II til gyrus dentatus og CA3, mens fibrene fra EC lag III ender i CA1 og subiculum.

I DG danner de kortikale fibrene synapser med kornceller som, i stedet for å projisere tilbake til EC, sender sine aksoner (såkalte *mosefibre*) til CA3-feltet og samt kollateraler til det dype polymorflaget i gyrus dentatus. CA3 på sin side sender sine akson-kollateraler til CA1 som projiserer tilbake til EC og til subiculum. Til sist projiserer subiculum, tilsvarende CA1, også tilbake til EC og andre kortikale og subkortikale regioner.

I denne avhandlingen presenteres to anatomiske beskrivelser av dentate gyrus og cornu ammonis 3, samt to elektrofysiologiske studier av celler i CA1 og subiculum.

I den første artikkelen presenteres en kvalitativ og kvantitativ beskrivelse av den mest tallrike glutamaterge nervecellen i det dype polymorflaget av gyrus dentatus hos mink, *mosecellen*. Denne celletypen er en del av en tilbakemeldingssløyfe med de overliggende korncellene. Studien bruker Golgi-fargede histologiske snitt som muliggjorde datamaskinbaserte tredimensjonale rekonstruksjoner av cellenes dendrittiske tre. Hos mink er mosecellenes soma og proksimale dendritter lokalisert i polymorflaget, mens distale dendritter strekker seg inn i nabofeltene, inkludert CA3. Studien legger spesielt vekt på mosecelledendritter som strekker seg opp i det granulære og molekylære laget av gyrus dentatus (gm-dendritter), i endesonen til fibre fra EC. Disse gm-dendrittene opptrådte oftere hos mink sammenlignet med rotter.

I den andre artikkelen observerte og rapporterte vi cytologiske og fiberarkitektoniske trekk ved gyrus dentatus og den tilstøtende CA3-enden hos sau og gris.

Fokus var på aksonkollateralene til korncellene i gyrus dentatus som lager et tett fibernettverk i det underliggende polymorflaget. Studien brukte blokker av samme hippocampus farget med enten Golgi eller Timm-thionin, noe som muliggjorde en direkte sammenligning av cytologiske detaljer og lokalisasjonen til mosefiberfiberterminalene, visualisert i Timm-farging av sink. Vi konkluderte med at våre observasjoner av kollateralpleksus muliggjorde en mer presis lokalisasjon av grensen mellom gyrus dentatus og CA3 enden enn tilsvarende grense om den var basert på cytoarkitektonikk alene.

I den tredje artikkelen spurte vi om nevronene i subiculum representerte flere trekk ved en navigasjonsopplevelse og sammenliknet observasjonene med representasjonene til nerveceller i CA1-regionen. Datainnsamling til både artikkel III og IV ble gjennomført i et såkalt «åpent rom»-eksperiment (en kvadratisk boks uten andre objekter) og mens dyrene utførte en oppgave som krevde minner om et belønningssted.

Analysene viste at mens CA1-celler stort sett representerte kun posisjon, var nevroner i subiculum modulert av posisjon, hoderetning og løpehastighet i kombinasjon. Den blandede representasjonen var også sterkere under oppgaven som krevde romlig hukommelse.

I den fjerde og siste artikkelen reproduserte vi tidligere funn som viser at pyramideceller i CA1 representerer et dyrs egosentriske posisjon i et gitt miljø. Rådataene var imidlertid ikke overbevisende og virket å bestå av flere ulike funksjonelle celletyper, hvilket ledet til at vi testet validiteten av den statistiske modellen ved hjelp av et simulert datasett bestående av celler med forhåndsdefinerte romlige representasjoner. Analysen viste at modellen, når den ble brukt på celler med blandede representasjoner av romlige egenskaper, produserte et høyt antall falske positive egosentriske celler. Dette understreker viktigheten av å bruke statistiske modeller som kvantifiserer det relative bidraget til hver kovariant når man analyserer nerveceller med blandede representasjoner.

Navn kandidat: Jan Sigurd Beddari Blackstad

Institutt: Kavli Institute for Systems Neuroscience / Centre for Neural

Computation

Veileder(e): May-Britt Moser & Edvard I. Moser

Finansieringskilde:

Abstract

The hippocampal formation is a brain region essential for spatial navigation and episodic memories. It is composed of three main subregions: The dentate gyrus, cornu ammonis (subdivided into CA1, CA2, and CA3), and the subiculum. The main cortical input to the region arises from layer II and III of the entorhinal cortex (EC) and terminates in a precise spatial order. In short, EC fibers from layer II project to the DG and CA3, while layer III fibers project to the CA1 and subiculum.

In the DG, the cortical fibers terminate onto granule cells which, instead of projecting back to the EC, send their axons (so-called mossy fibers) to the CA3 field and give off collaterals to the deep polymorphic layer of the DG. The CA3 in turn, by axon collaterals of pyramidal cells, projects to the CA1 which project back to the EC and to the subiculum. Finally, the subiculum, like CA1, also reciprocally projects back to the EC and other cortical and subcortical regions.

In this thesis, two anatomical descriptions of the dentate gyrus and cornu ammonis 3, and two electrophysiological studies of cells in the CA1 and the subiculum, are presented.

The first article presents a qualitative and quantitative description of the main glutamatergic neuron in the deep polymorphic layer of the DG in mink, the dentate mossy cell. These cells are part of a modulatory feedback-loop with the superficial granule cells. The study uses Golgi-stained histological sections that enabled computer based three-dimensional reconstructions of dendritic arbors. In mink, the soma and proximal dendrites of mossy cells are located in the DG polymorphic layer, while distal dendrites extend into the neighboring fields, including CA3. Special emphasis was on dendrites ascending into the granular and molecular layer of the DG (gm-dendrites), the terminal zone of fibers from the EC. These gm-dendrites were more numerous in mink compared to rats.

In the second article we observed and reported cytological and fibroarchitectonic features of the DG and adjacent CA3 end in sheep and domestic pig. The focus was on the axon collaterals of granule cells that make a dense fiber network in the DG polymorphic layer before the main unbranched fibers leave the DG and ascend to the CA3. The study used blocks of the same hippocampus stained with either Golgi or Timm-thionin which allowed for a direct comparison of cytological details and location of mossy fiber terminals, visualized by Timm-staining of the zinc contained in the latter. We found that the border between the DG and adjacent CA3 was better defined using the mossy fiber system as a guide compared to definitions using only cytoarchitecture.

In the third and fourth paper, properties of the spatial representations of neurons in the subiculum and CA1 of rats is presented. Data for both studies were recorded during open field experiments and a spatial task that required memory of a reward location.

In the third paper we asked if the neurons in subiculum represented multiple features of a navigational experience and contrasted the observed modulation of subicular neurons with the representations of CA1 principal neurons. The analysis showed that while CA1 cells were mostly modulated by position, subicular neurons were modulated by position, head direction, and running speed in combination. The mixed representation was also stronger during the spatial task.

Finally, in the fourth paper we replicated previous findings that CA1 pyramidal neurons were modulated by an animal's egocentric relationship to its environment. The raw data was, however, not convincing and very heterogenous, which led us to test the validity of the model using a simulated dataset of spatially selective units with predefined representations. The analysis showed that the model, when applied to cells with conjunctive representations, produced a high number of false positive egocentric cells. This underlines the importance of using statistical models that quantify the relative contribution of each covariate when analyzing units with mixed representations.

Acknowledgments

"Sometimes, immersed in his books, there would come to him the awareness of all that he did not know, of all that he had not read; and the serenity for which he labored was shattered as he realized the little time he had in life to read so much, to learn what he had to know."

— John Williams, Stoner

Publication list

Blackstad, J. S., Osen, K. K., Scharfman, H. E., Storm-Mathisen, J., Blackstad, T. W., & Leergaard, T. B. (2016). Observations on hippocampal mossy cells in mink (Neovison vison) with special reference to dendrites ascending to the granular and molecular layers. Hippocampus, 26(2), 229-245. doi:10.1002/hipo.22518

Blackstad, J. S., Osen, K. K., & Leergaard, T. B. (in preparation for Hippocampus). The fibro- and cytoarchitecture demarcating the boundary between the dentate gyrus and CA3 end in sheep (Ovis aries) and domestic pig (Sus scrofa domesticus).

Ledergerber, D., Battistin, C., Blackstad, J. S., Gardner, R. J., Witter, M. P., Moser, M. B., Roudi, Y. & Moser, E. I. (2021). Task-dependent mixed selectivity in the subiculum. Cell Rep, 35(8), 109175. doi:10.1016/j.celrep.2021.109175

Carpenter, J., Blackstad, J. S., Dunn, B., Moser, E. I., & Moser, M. B. (in preparation). Egocentric tuning in hippocampal neurons: Using simulations to estimate misclassification rates.

x

Table of Contents

Introduction

The hippocampal formation is an evolutionary old part of the mammalian brain essential for spatial navigation and episodic memory (Scoville & Milner, 1957; Penfield & Milner, 1958; O'Keefe & Nadel, 1978; Maguire et al., 1997; Moser et al., 2017; Witter et al., 2017). It is composed of three cortical areas: the dentate gyrus (DG), the cornu ammonis subfields CA1, CA2, and CA3 (the hippocampus proper), and the subiculum (Andersen et al., 2006; van Strien et al., 2009; Cappaert et al., 2015), Fig.1, 2).

The hippocampus proper and subiculum are both three-layered with a middle pyramidal layer where the somata of mostly pyramidal cells are located, a deep oriens layer populated by the basal dendrites of the pyramidal cells and several classes of interneurons, and a superficial molecular layer containing the apical dendrites of the pyramidal cells (Cajal, 1911; Lorente De Nó, 1934). The molecular layer in CA3 is subdivided into three zones: the most basal stratum lucidum, the middle stratum radiatum, and the superficial stratum lacunar-molecular layer (Fig.2B). The latter two are continuous with the layers of CA1 and subiculum, while the stratum lucidum is discontinued in CA1 (Amaral & Witter, 1989; O'Mara et al., 2001; Andersen et al., 2006; van Strien et al., 2009; Cappaert et al., 2015).

The DG is also a three-layered cortex which folded concavity, in sections cut perpendicular to the long axis of the hippocampus, embraces the end of the hippocampus proper (CA3) (Cajal, 1911; Amaral, 1978; Amaral et al., 2007). Instead of a prominent pyramidal layer, the DG feature a middle granular layer populated by densely packed, cone-like, minute granule cell somata that extend dendrites into the superficial molecular layer. Basal to the granular layer is a polymorphic layer which is populated by GABAergic interneurons and a population of glutamatergic neurons named mossy cells (Amaral, 1978).
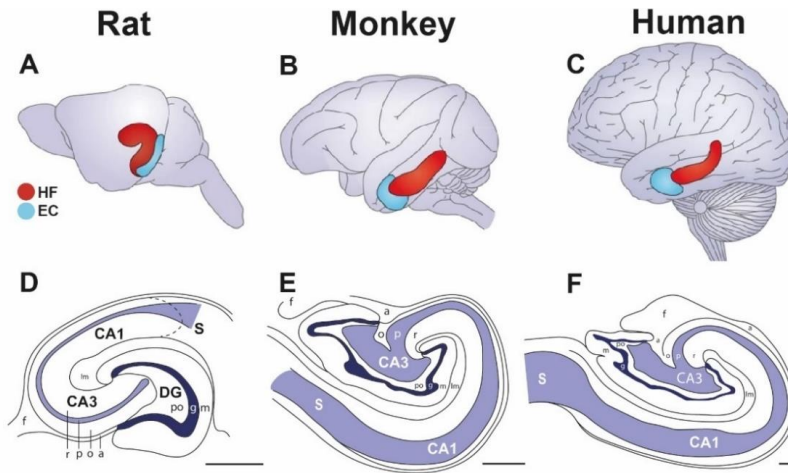
Fig.1. Cross-species comparison of the hippocampal formation (HF) and entorhinal cortex (EC). (A-C) Structures superimposed on the brain modified from Strange et al., 2014, (D-F) Schematic drawing of cross-sections of the dentate gyrus (DG), cornu ammonis (CA3, CA1), and subiculum (S) with the middle DG granular (g, deep blue) and CA pyramidal layer (p, light blue) colored. Drawings are based on histological Timm and thionin stained sections from (D) Haug 1974 (material provided by Finn-Mogens Haug, Division of Anatomy, Department of Molecular Medicine, Institute of Basic Medical Sciences, University of Oslo, Norway), (E) Kondo et al., 2009 and Amaral and Lavenex (2006), and (F) Stephan (1983). Abbreviations: a, alveus; f, fimbria; lm, lacunar-molecular layer; m, molecular layer; o, stratum oriens; po, polymorphic layer; r, stratum radiatum. Scale bar (D-F) = 1 mm.

On its most lateral side, the DG molecular layer is fused with the lacunar-molecular layer of the hippocampus proper and subiculum, making out the hippocampal fissure (Cajal, 1911; Lorente De Nó, 1934; Humphrey, 1967) Fig. 1D-F, 2). Although considerable species differences exist, the area fused with the hippocampus proper and subiculum is often referred to as the hidden blade, while the opposite end facing the subarachnoidal space on the medial side of the hemisphere, is called the exposed blade (Fig. 2B).

The basic circuitry of the hippocampal formation is remarkably well conserved across mammals (Seress, 2007; Witter et al., 2017).
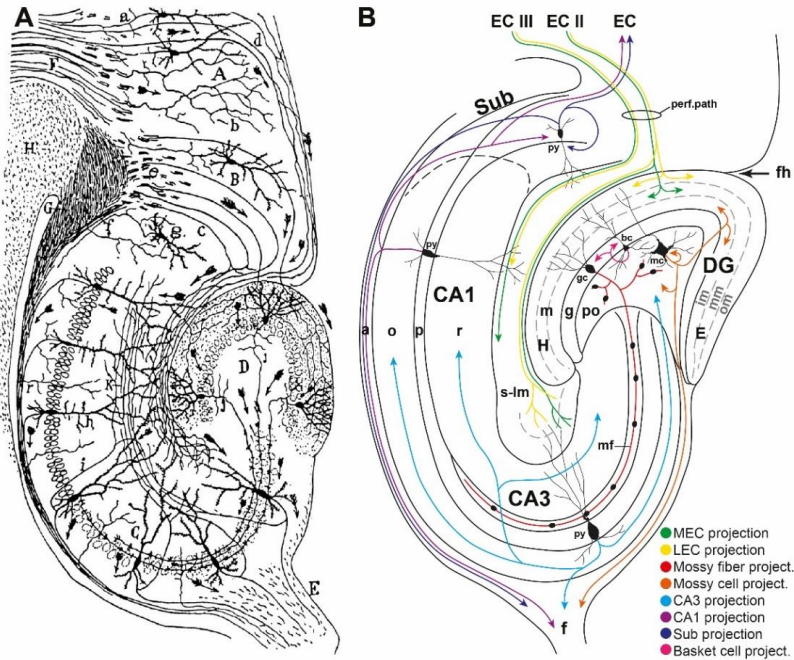
Fig.2. Overview of the anatomy and main excitatory fibre pathways in the hippocampal region (in rats).

(A) Reproduction of part of Ramón y Cajal's (1911) figure 479 based on observations from rabbit. (B) Colored representation of the hippocampus and main excitatory cells and their projections. modified from from Taxt T, Storm-Mathisen J 1984 Neuroscience and Cajal 1911 (his Fig.274). Abbreviations: a, alveus; CA1, cornu ammonis 1; CA3, cornu Ammonis 3; E, exposed blade; EC, entorhinal cortex; fh, fissura hippocampi; g., granular layer; gc, granule cell; H, hidden blade, im, inner molecular layer; m, molecular layer; mc, mossy cell; mf, mossy fiber; mm, middle molecular layer; o, stratum oriens; om, outer molecular layer; p, pyramidal layer; perf.path, perforant path; po, polymorphic layer; py, pyramidal cell; r, stratum radiatum; s-lm, lacunar-molecular layer; Sub, subiculum.

Cortical fibers targeting the region largely originate in the entorhinal cortex (EC) and terminate, via the *perforant path*, in the molecular layer of the DG and the lacunar-molecular layer of the CA-fields and subiculum, innervating the apical dendrites of granule -and pyramidal cells respectively (Blackstad, 1956, 1958; Witter et al., 1989; van Strien et al., 2009; Cappaert et al., 2015). The projection from the EC is divided into two distinct partitions, with fibers from layer II terminating in the DG and CA3, and fibers from cells in EC layer III exclusively targeting the CA1 and subiculum (Steward, 1976; van Groen et al., 1986; Witter et al., 1988; Witter et al., 1989; Yeckel & Berger, 1990; Tamamaki & Nojyo, 1993;

Witter et al., 2017). While the pyramidal cells in CA1 and subiculum, similar to most regions in the neocortex, reciprocally innervate the deep layers of the EC (van Groen et al., 1986; Felleman & Van Essen, 1991), the DG and CA3 uniquely do not project fibers back to the EC (Ramón y Cajal, 1893; Cajal, 1911; Andersen et al., 1969; Amaral & Lavenex, 2006). The DG granule cells instead project to the CA3 via long unbranched parallel fibers with regularly spaced giant terminals (*mossy fibers*) that assemble a large bundle in the stratum lucidum just apical to the pyramidal layer (*the mossy fiber bundle*, Fig. 2) (Ramón y Cajal, 1911; Lorente de Nó, 1934; Blackstad et al., 1970; Gaarskjaer, 1978; Swanson et al., 1978; Gaarskjaer et al., 1982).

The mossy fibers also give off collaterals forming a dense plexus within the polymorphic layer (Claiborne et al., 1986; Acsády et al., 1998). These fibers innervate the dentate mossy cells via similar, but smaller, giant terminals as in the CA3. In addition, several classes of interneurons are targeted by small *en passage* terminals of the mossy fiber collaterals in the polymorphic layer (Acsády et al., 1998). The mossy cells and GABAergic interneurons in turn provide feedback to granule cells by projecting axons to the inner molecular layer and the granular layer respectively, both at a different septotemporal level than the cell of origin (Blackstad, 1956; Zimmer, 1971; Swanson et al., 1978; Laurberg, 1979; Laurberg & Sorensen, 1981; Swanson et al., 1981; Blackstad, 1985; Soriano & Frotscher, 1994).

The main intrinsic excitatory projections of the CA3 are the so-called Schaffer-collaterals that mainly terminate on the dendrites of pyramidal cells in CA1, although some collaterals are also part of a back-projections to the DG. In the CA1 fibers from both CA3 and the EC layer III converge onto pyramidal cells, which project to the subiculum, and as already mentioned, to the EC. Finally, in the subiculum the input signal from CA1 pyramidal cells and EC layer III is relayed back to the EC and several other cortical and subcortical regions, of which many of the target areas are shared with those of CA1.

Functional properties of the hippocampal formation and para-hippocampal region

While historically considered to be mainly involved in olfaction (fourth-order olfactory centers of Ramón y Cajal (1911)), it is now well established that the hippocampal formation and surrounding brain regions (*the parahippocampal region* (Cappaert et al., 2015)) are essential for spatial navigation and episodic memory (Moser et al., 2017). Humans and other mammals with hippocampal lesions suffer acute anterograde amnesia (the loss of the ability to form new memories, see Scoville & Milner (1957) and Penfield & Milner (1958)) and perform badly on tasks that require spatial memories (Morris et al., 1982). In addition, the hippocampal region is amongst the first to show signs of pathology in early onset of Alzheimer's disease which is accompanied by impaired spatial and episodic memory (Apostolova et al., 2006; Albert et al., 2011).

The behavioral and clinical observations are supported by a large amount of electrophysiological evidence of single cells and populations of cells in the hippocampal region that represents different modalities of space (Moser et al., 2017). A large proportion of pyramidal and mossy cells in the CA-fields and the DG are place-modulated and active only at specific locations in an environment, *i.e.*, place cells (O'Keefe & Dostrovsky, 1971; O'Keefe, 1976), while so-called grid cells in the closely connected entorhinal cortex have spiking activity at multiple locations that, when superimposed on a 2D projection of the recording environment, make out a continuous tessellating grid of equilateral triangles (Fyhn et al., 2004; Hafting et al., 2005; Stensola et al., 2012). In addition, head direction tuned cells have been reported in the dorsal presubiculum, parasubiculum, and entorhinal cortex (Ranck, 1984; Taube et al., 1990; Sargolini et al., 2006), border and boundary respondent cells in the entorhinal cortex and subiculum (Solstad et al., 2008; Lever et al., 2009; Stewart et al., 2014; Poulter et al., 2021), and speed-modulated and object-respondent cells in the entorhinal cortex (Kropff et al., 2015; Hoydal et al., 2018). The behavioral and physiological data in combination imply that the sense of space and episodic memories are anatomically closely connected in the brain (van Strien et al., 2009). It has been

proposed by several authors that the hippocampus may have evolved as a structure specialized for spatial navigation and that a memory system was built on top of this structure as animals developed more sophisticated brains (O'Keefe & Nadel, 1978; Treves et al., 2008; Buzsáki & Moser, 2013).

The hippocampus, being a simple three-layered allocortex, offers a unique opportunity to understand both basic information processing in neural systems and complex functions such as memory and navigation, and is thus a gateway to the more complex human brain and the very things that make us human: our ability to learn, remember, and share our knowledge.

Objectives

In biology, the structure of an organ or system is thought to determine its function. The same is true for the brain in general, and the specific brain regions supporting different functions. The hippocampal formation offers a unique opportunity to correlate anatomical observations with functional properties since so much is known about its functional properties in both man and smaller mammals (Andersen et al., 2006; Strange et al., 2014; Moser et al., 2017). To further advance the field, detailed descriptions of both the neural architecture and functional properties of the cells in the region is essential.

In this thesis I aim to describe anatomical and physiologic features of all major subregions of the hippocampal formation, namely the dentate gyrus, cornu ammonis, and subiculum. The main focus of the anatomical studies is on the dentate-ammonic region, while the physiological studies focus on CA1 and subiculum.

The main objectives of this thesis are as follows:

I)   Describe the dentate gyrus and dentate mossy cells in mink

II)   Describe the DG and CA3 end in sheep and domestic pig with focus on the DG/CA3 border.

III)   Compare the physiological properties of cells in the CA1 and subiculum in rat.

IV)   Test the validity of methods used for reporting egocentric bearing cells in the CA1.

Article I | The dentate mossy cell in mink

Understanding how the hippocampus supports complex functions such as episodic memories and spatial navigation, requires detailed knowledge of the anatomy and connections of single cells and cell systems in the region. While several anatomical and physiological descriptions of the pyramidal cells in the CA-fields and granule cells in the DG are available (Spruston & McBain, 2006), the main excitatory neuron in the DG polymorphic layer, the dentate mossy cell, has attracted less attention historically (Scharfman & Myers, 2012). Although first described and named so by Amaral (1978), the mossy cell has only in recent years been identified as an important modulatory element in the hippocampal circuitry (Scharfman, 2016, 2018). A single mossy cell receives disynaptic input from the perforant path via giant terminals of mossy fiber collaterals (Claiborne et al., 1986; Acsády et al., 1998), and in turn send axons to the inner third of the DG molecular layer, of both hemispheres in rat, synapsing onto dendrites of granule cells and inhibitory basket cells at different septotemporal levels from the cell of origin (Zimmer, 1971; Swanson et al., 1978; Laurberg & Sorensen, 1981; Ribak et al., 1985; Botterill et al., 2021; but see Ma et al., 2021). The mossy cells in this way distribute the activity of granule cells at one septotemporal level to granule cells located at multiple other locations in the hippocampus, potentially acting both excitatory, and indirectly inhibitory (Sloviter, 1991; Sloviter et al., 2003; Ratzliff et al., 2004; Jinde et al., 2013; Scharfman & Bernstein, 2015).

A less emphasized feature of mossy cells is that they also may receive monosynaptic input from the entorhinal cortex by means of special so-called gm-dendrites extending into the granular and the molecular layer of the DG. These dendrites are briefly described by some authors and seem to be common in primates (Buckmaster & Amaral, 2001), but less so in rodents (Amaral, 1978; Scharfman, 1991; Buckmaster, 2012). A detailed description of their appearance and possible importance for the hippocampal circuitry was until recently not available.

The first article in this thesis presents a detailed qualitative and quantitative anatomical description of dentate mossy cells in mink with special emphasis on the gm-dendrites and their relation to the granular and molecular layers, as well

as the relation of the entire mossy cell dendritic arbor to the mossy fiber collateral plexus, i.e., the z-zone of Blackstad et al. (1963), and the DG/CA3 border. The study builds on the previous description of the mink hippocampus by Gościcka et al. (1993).

Article II | The dentate-ammonic boundary in sheep and pig

Understanding the human brain and ultimately advance medical care are the main reasons for using animal models in biological research. To achieve these goals, and avoid misinterpretation of research data, it is pivotal to identify correct homologies between brain regions in different mammals.

Although the hippocampus is remarkably similar across species, there are substantial variations in the DG and the adjacent CA3 end (named proximal CA3 or CA3c by others, Seress, 2007; Amaral et al. 2007; Cappaert et al., 2015). In rat, the polymorphic layer has a triangular cross section abutting on the end of the CA3 pyramidal layer (Šmejda Haug, 1974; Kjonigsen et al., 2015), while in species closer to humans, the polymorphic layer is stretched out to a thin band capping the expanded CA3 end (Buckmaster & Amaral, 2001; Kondo et al., 2008, 2009). In primates, in addition, the CA3 end becomes destratified without a distinct pyramidal layer, while the granular and molecular layers increase in length, forming several folds or "dents" that justify the term "dentate gyrus" (and "fascia dentata" for the granule and molecular layers together, Kondo et al., 2009). In sum, these alterations make it difficult to draw a definitive border between the DG and the CA3 end and to identify homologies in different species based on cytoarchitecture alone, as reflected in a variety of border definitions and nomenclature.

A prominent example of troubling nomenclature and border definitions includes the classical comparative study of mouse, rabbit, monkey and human hippocampus by Lorente de Nó (1934) in which he misinterpreted the polymorphic layer in mouse as an extension of the cornu ammonis named CA4, while the polymorphic layer in rabbit, monkey, and man was defined as a second blade of CA4. Although the term CA4 is often regarded as a misnomer (Amaral, 1978), it still occurs in many publications on the hippocampus of both the rodent and primate hippocampus (Strange et al., 2014).

Another misnomer is the term «area dentata» which defines the CA3 end as part of the DG as done in a series of histochemical studies of the pig hippocampus (Holm & Geneser, 1989, 1991b, 1991a). In more recent publications, the DG polymorphic layer is often referred to as the hilus or hilar area (Amaral et al., 2007; Scharfman & Myers, 2012; Cappaert et al., 2015; Scharfman, 2016),

which is reasonable in rodents where the polymorphic layer fills in most of the concavity formed by the granular and molecular layers, but is very confusing when used in species with a band-shaped polymorphic layer where most of the concavity is made up of the expanded CA3 end.

In the first article we delineate the DG/CA3 border in mink using Timm-thionin- and Golgi-stained sections. The former method visualizes the zinc-containing synaptic terminals of the hippocampal mossy fibers and their collaterals together with thionin-staining of cells, while the Golgi-method stains a random sample of neurons with dendrites and unmyelinated axons such as the mossy fibers. Used together, the two histological techniques allowed a precise definition of the DG/CA3 border based on three main criteria: (I) The high contrast between the Timm-positive, dense plexus of mossy fiber collaterals in the polymorphic layer and the Timm-negative, cell poor oriens and radiate layers of the CA3 end; (II) The location of the soma and excrescence-studded proximal dendrites of mossy cells within the collateral plexus while gm-dendrites extend into the granular and molecular layers and distal portion of main dendrites sometimes reach into the CA3 end; and (III) The dendritic arbors of CA3 pyramidal cells that avoid the polymorphic layer, in part by bending around the tip of the hidden blade of the DG to reach the lacunar-molecular layer. Accordingly, we hypothesize that these same criteria may be applied to delineate the DG/CA3 border also in species closer to primates and in effect be a guide to more reliable subdivision homologies between mammalian species in the hippocampal formation.

The second manuscript therefore presents a detailed description of the dentate gyrus and CA3 end in sheep and domestic pig with focus on the DG/CA3 border using Timm-thionin- and Golgi-stained sections.

Article III | Task-dependent mixed selectivity in the subiculum

The subiculum is the major long-range output region of the hippocampal formation (O'Mara et al., 2001; van Strien et al., 2009; Cappaert et al., 2015). In sections cut across the septotemporal long axis of the hippocampus, the subiculum is located in-between the CA1 and the presubiculum (Fig.2). The layering of the subiculum is less distinct than in the CA1, but Ramón y Cajal (1911) described three main layers: a superficial plexiform layer, a wide layer of dispersed medium and large pyramidal cells, and a deep layer of polymorphic cells. The pyramidal cells in the subiculum are mainly innervated by axons from the CA1 and perforant path fibers from the entorhinal cortex to the lacunar-molecular layer (Cappaert et al., 2015). Based on the efferent projections, the subiculum can be divided into three subregions in the transverse plane (Cappaert et al., 2015). The axon projections from the region closest to CA1 is remarkably similar to the projections from the latter, targeting areas such as infra -and prelimbic cortices, prefrontal and orbitofrontal cortex, the medial and lateral entorhinal cortex, the septal complex, hypothalamus, thalamus, and the amygdala. The middle part of the subiculum projects to the midline-thalamic nuclei, and the outermost part projects *mainly* to the presubiculum and the retrosplenial cortex (Witter & Groenewegen, 1990; Witter et al., 1990; Naber & Witter, 1998). In contrast to CA1, axons originating in the subiculum usually do not branch into collaterals that target multiple regions (Naber & Witter, 1998; Bienkowski et al., 2018; Cembrowski et al., 2018).

Less is known about the functional properties of subicular neurons compared to cells in the neighboring CA-fields and the entorhinal cortex. Subpopulations of cells in subiculum have broad place fields that are often anchored to environmental boarders or objects (Lever et al., 2009; Stewart et al., 2014; Poulter et al., 2021) or heading direction representations on multidirectional tracks (Olson et al., 2017). Since the pyramidal cells in the subiculum receives input from modalities such as hippocampal place cells and entorhinal grid-, head direction-, object vector-, and speed-cells, similar to the input to CA1 pyramidal cells, it is striking that the representations in the two areas are so dissimilar.

Thus, in the third paper we aim to compare how spatial modalities such as position, head direction and speed are represented in the subiculum and CA1 of rats. A comparison between random foraging and a spatial task is also presented.

Paper IV | Egocentric tuning in hippocampal neurons: Using simulations to estimate misclassification rates

The spatial representations observed in principal neurons in the hippocampal formation, such as those of place- and grid-cells, have for the most part, been interpreted as point coordinates in a Cartesian system, *i.e.*, in an allocentric frame of reference (O'Keefe & Nadel, 1978; Moser et al., 2008; Moser et al., 2017; Wang et al., 2020). The spatial representation of these cells does not seem to be dependent on the body orientation, running speed or moving direction of the animal (O'Keefe, 1976).

Recent reports have, however, claimed that some hippocampal cells in CA1 are modulated by the animal's head direction relative to goals or arbitrary positions in an environment (Sarel et al., 2017; Jercog et al., 2019). For the purpose of this thesis, these cells will be referred to as *egocentric bearing cells*. These representations were first reported in bats performing a goal-directed task (Sarel et al., 2017), and then later in mice during open field experiments (Jercog et al., 2019). In both instances, a large proportion of these cells also conjunctively represented allocentric place and head direction.

Egocentric bearing cells are usually presented using a polar plot depicting firing rate and angular tuning towards a goal and rarely the potential influence of inter-dependent covariates and behavioral biases are communicated, if ever considered. Since egocentric bearing cells in the hippocampus often have conjunctive spatial representations, it is imperative to use statistical methods that enable a quantification of each covariate.

In the fourth manuscript, we first aim to replicate the findings of egocentric bearing cells in the hippocampus of rats during open field recordings using similar statistical methods as Jercog et al., (2019). Secondly, using the sampled behavior as basis, we simulate five populations of cells with representations similar to those reported in the main cell layers of the hippocampal formation. These cell populations are analyzed using the same statistical framework as for the real neural data. This enables a quantification of false positive and false negative rats which are used to evaluate the validity of dataset.

Synopsis of methods

Article I | Observations on Hippocampal Mossy Cells in Mink (Neovision vison) with Special Reference to Dendrites Ascending to the Granular and Molecular Layers

This study was initiated by the late professor Theodor W. Blackstad (1925-2003) who collected the dataset and made the initial and most pivotal observations during the middle to late eighties. The dataset and early manuscript notes were then after his passing saved by his near college K.K. Osen. The project was reinitiated in 2011 by J.S. Blackstad and K.K. Osen, and with the collective effort of colleagues at the Institute of Basic Medical Sciences in Oslo, completed and published during the fall of 2015.

The data were obtained from nine healthy adult mink (Neovison vison) bred and euthanized by at the Norwegian Veterinary College (details of each animal are provided in table 1 of the publication). The animals were selected for euthanasia for other purposes and terminated using the standard methods in the fur industry at that time. The brains were removed within 0.5 - 2 hours after death and some tissue around the hippocampus was removed before immersion fixation. Brains were either destined for Golgi-impregnation (four animals, fixed in a solution with 3% paraformaldehyde and 1.25% glutaraldehyde) or Timm-thionin-staining (five animals, fixed in a solution with 3% glutaraldehyde and 0.3-0.4% sodium sulphide). For more specific details of staining protocols see Blackstad et al., 1984 and Blackstad et al.,2016 for Golgi-staining, and Haug (1973), Zimmer & Haug (1978), and Holm & Geneser (1989) for Timm-thionin staining.

      The brains destined for Timm-staining were cut on a cryostat in 40 μm sections and counterstained with thionin, while the hippocampi destined for Golgi-staining were cut in blocks at various planes either from the whole brain or from the isolated hippocampus, subjected to chromation (2.4% potassium dichromate with 0.2% osmium tetroxide for two days and 3% potassium dichromate for a few days) and to 0.75% silver nitrate for two days before being submerged in ascending ethanol concentrations and treated with a propylene

oxide-epoxy resin (Araldite) mixture and pure Araldite on the next day. Dehydration liquids were saturated with silver chromate to avoid the impregnation of fine structures to be washed out.

Stained blocks were cut in 100-190 µm thick sections with a hot steel knife (70°C) on a sledge microtome, to cut effortlessly through the hard epoxy resin blocks, and mounted on slides under a coverslip in unpolymerized resin that was cured at approximately 60°C under heavy weights to secure flattened sections, procedures important for correct 3D-reconstructions.

Golgi-stained sections were inspected in a light microscope with dry-, water-, and oil-immersion objectives. Camera lucida drawings of cytoarhictectural details were made using a Leitz drawing tube and moisture resistant paper, at a magnification of 580 in most cases or 1,524 in rare instances. Drawings of consecutive sections were manually aligned using histological details at the lower and upper surface of the sections as a guide. For measuring the x, y-coordinates, a digitizing table and custom software tool (MicroTrace, Leergaard and Bjaalie, 1995) were used. The z-coordinates were collected using an enlarged dial with measures attached to the fine focus knob on the microscope and corrected for the different refractive indexes of embedding and immersion media (for details and empirically determined refractive index see Blackstad et al., 1984).

Several unpublished custom software tools developed by T.W. Blackstad, running on Silicon Graphics Indigo, were used for quantification, 3D-reconstructions, and calculations of dendritic segment lengths. Measures of gm-dendrites were made from two-dimensional camera lucida drawings and confirmed in high-resolution digital images. No corrections were made for possible shrinkage of tissue.

Article II | The fibro -and cytoarchitecture demarcating the boundary between the dentate gyrus and CA3 end in sheep (Ovis aries) and domestic pig (Sus scrofa domestics)

The histological sections used in this study were obtained from the histological archive at the department of molecular medicine, Institute of Basic Medical Sciences at the University of Oslo and were initially collected and prepared by the late professor Theodor W. Blackstad (1925-2003) in collaboration with the late professor Finn Geneser (1938-2018).

The material comprises Golgi- and Timm-thionin-stained sections of the hippocampi of two sheep (8 weeks old) and Golgi-sections of one domestic pig (age unknown) cut perpendicular to the curved septotemporal long axis of the isolated hippocampi. The sheep brains were immersion-fixed for 10 hours in a solution with 3% glutaraldehyde and 0.4% sodium sulfide and were used for both Golgi-staining and Timm-staining of sections from alternating tissue blocks. The pig brain, which was most probably perfusion-fixed with glutaraldehyde, was used only for Golgi-staining which followed the same protocol as described in article I (Blackstad et al., 2016) after an additional immersion of the tissue blocks in 1% paraformaldehyde for 10 days.

Tissue blocks for Timm-staining, after the sulfide-containing fixative, were immersed in a 30% sucrose solution for 13-15 hours, and then cut in 40 µm thick sections on a cryostat. Sections were mounted on slides and counterstained with thionin (for detailed description of staining see article I and Holm & Geneser, 1989). In addition, the material includes three Timm-thionin-stained and three thionin-stained horizontal sections of pig brain prepared at the University of Aarhus.

The study is based on light-microscopy and high-resolution images acquired with an automated slide scanner system (Axio Scan Z1, Carl Zeiss MicroImaging, Jena Germany). The material is limited, but the combination of the two staining methods applied to sections of adjacent blocks cut perpendicular to the long axis

of the same hippocampus enables unique observations of the cyto -and fibroarchitecture in an optimal plane of sectioning in the two artiodactylae.

Article III | Task-dependent mixed selectivity in the Subiculum

Rats were chronically implanted with drives guiding tetrodes into either the dorsal one-third of the CA1 or the subiculum. Tetrodes for recordings in the subiculum were evenly distributed along the transverse axis of the cell layer, while there was a tendency for CA1 tetrodes to be placed closer to the subiculum than to CA2. In total cell counts from each region, there was, however, no bias, meaning that single tetrodes closer to CA2 had a larger cell yield and thus contributed more to the dataset than single tetrodes closer to subiculum. Rats were trained to forage for chocolate treats in a classical open field experiment (OF) (1.5 x 1.5 meter) and in a spatial task (ST) adapted from Pfeiffer and Foster (2013) in the same environment. In short, in the ST the floor mat of the arena had an even grid of 1-cm-diameter holes that by plastic tubing hidden underneath the apparatus could be filled with chocolate oat milk by the experimenter. Rats learned to alternate between receiving reward in a stable home well location and a randomly selected well location. The sudo-random sequence of reward locations was made using the rand-function in MATLAB and manually editing instances when well location closely together occurred sequentially to avoid clustering of reward locations.

Article IV | Egocentric tuning in hippocampal neurons: Using simulations to estimate misclassification rates

Electrode recordings in rats were obtained using chronically implanted drives carrying tetrodes into the dorsal CA1. Histological sections were stained for Nissl to identify tetrode locations. On the transverse axis the tetrode locations were somewhat biased towards locations close to the CA2 border (5 tetrodes) and the mid portion of CA1 (7 tetrodes). No tetrodes were placed immediately close to the subiculum.

Animals were trained for the same tasks that were used in the third article (Ledergerber et al., 2021), i.e. open field recordings and a spatial task (Pfeiffer & Foster, 2013), but for the purpose of the fourth manuscript, only data from open field recordings were included in the analysis.

To test the performance of the criteria used for defining egocentric bearing cells we simulated five populations of differently spatially tuned cells which were superimposed over the experimentally collected running path of the animals. These functional cell types included egocentric bearing cells, place cells, head direction cells, conjunctive head direction and place cells, and conjunctive place and egocentric bearing cells. 1000 simulated cells per population were tested in 86 behavioral sessions.

Synopsis of results

Article I | Observations on Hippocampal Mossy Cells in Mink (Neovision vison) with Special Reference to Dendrites Ascending to the Granular and Molecular Layers

The DG in mink appears relatively broader than in rat. In cross sections, the expanding CA3 end seems to excavate the superjacent polymorphic layer, which remains thicker in the corners underneath the two crests, hidden and exposed, of the granular and molecular layers. Similar to rodents (Šmejda Haug, 1974; Kjonigsen et al., 2015), the pyramidal layer is distinct to the end of the CA3, here curving towards the hidden (suprapyramidal) blade. In thionin-stained sections, thus, there is a distinct border between the cell-rich polymorphic layer and the cell-poor radiate and oriens layers of the CA3 end, a distinction that is confirmed and enhanced by the dense Timm-staining of the mossy fiber collateral plexus which fills in the polymorphic layer except for traces of a Timm-negative subgranular zone. In Golgi sections, the dendrites of CA3 pyramidal cells appear confined to the CA3, with apical dendrites bending around the hidden end of the DG to reach into the lacunar-molecular layer.

Like the situation in rodents, mossy cells in mink have large thorny excrescences on their proximal dendrites, located less closely to the soma than in rat, but still restricted to the polymorphic layer (Amaral, 1978; Frotscher et al., 1991; Buckmaster et al., 1996; Buckmaster, 2012). The distal dendrites, which are covered by small spines, branch in both the transverse and septotemporal plane, some reaching into the adjacent CA3. The thinner and straighter gm-dendrites ascending to the granular and molecular layers seem more numerous in mink than in rat, but fewer than in monkey (rat: on average 1 per cell, Scharfman, 1991; mink: approx. 2.8 per cell, range 0-8; monkey: approximately 5 per cell, Buckmaster & Amaral, 2001). In mink, they constitute on average 12% (maximum 29%) of the total dendritic length and typically branch once or twice as they reach all the way across the molecular layer of the DG (covering the terminal area of both the lateral and medial perforant path). The data suggest that mossy cells in species closer to primates and humans might have a larger amount of

monosynaptic input from the entorhinal cortex via the perforant path, in addition to the disynaptic input via the collateral plexus.

Article II | The fibro -and cytoarchitecture demarcating the boundary between the dentate gyrus and CA3 end in sheep (Ovis aries) and domestic pig (Sus scrofa domestics)

This publication to our knowledge features the first detailed description of the dentate gyrus in adult sheep (see however an overview in Rose, 1942), while it adds to previous descriptions of the so-called "*dentate area*" in domestic pig (Holm & Geneser, 1989, 1991b, 1991a; Holm & West, 1994). The mossy fiber system with its collateral plexus is regarded by us as the main organizing element for the DG and the CA3 including their mutual border.

The shape of the dentate gyrus and CA3 end of ungulates is intermediate to that of mink (Blackstad et al., 2016) and primates (Buckmaster & Amaral, 2001; Kondo et al., 2008, 2009) with a more rounded surface and a thinner polymorphic layer than in mink, capping the more expanded CA3 end which in contrast to mink is destratified with an even distribution of pyramidal cells serving to blur the DG/CA3 border in thionin-sections. As documented in pairs of Timm-thionin- and Golgi-stained sections of the same hippocampus, the mossy fiber collateral plexus coincides with the polymorphic layer apart from its Timm-negative subgranular zone, thus serving as a reliable guide to the localization of the DG/CA3 borderline. The Golgi-sections, besides validating the borderline based on Timm-thionin-staining, also serve to approve the scattered transition of the main mossy fibers from the collateral plexus to the CA3 end as described in rabbit and guinea pig by Ramón y Cajal 110 years ago. The material indicates a so-called lamellar orientation of the scattered mossy fibers within the CA3 end analogous to the previously documented orientation of fibers in the rat mossy fiber bundle (Andersen et al., 1969; Blackstad et al., 1970; Andersen et al., 1971).

The scattering of mossy fibers is clearly related to the scattering of neurons within the expanded CA3 end, where we identified three subtypes of pyramidal cells (apical, non-apical, and dentate pyramids) similar to those described in monkey (Buckmaster & Amaral, 2001; Kondo et al., 2008). Of the three subtypes, only the least numerous dentate subtype has dendrites penetrating the DG. Dendrites of the apical subtype, which dominate in the

hidden part of the CA3 end, bend around the hidden blade of the DG to reach the lacunar-molecular layer. Mossy cells in sheep and pig, feature large spiny excrescences on proximal dendrites, but closer to the soma than in mink (Blackstad et al., 2016), while distal main dendrites tend to reach deeper into the CA3. With reservation for the lack of reliable quantitative data in sheep and pig, mossy cells in said species feature fewer gm-dendrites to the granular and molecular layers than in mink (Blackstad et al., 2016) and monkey (Buckmaster & Amaral, 2001), but more than in rat (Scharfman, 1991).

In view of the observations in Article I and II in the carnivore mink and the artiodactylae sheep and pig, it is tempting to speculate that the mossy fiber system with its collateral plexus may serve as a useful defining feature of the DG/CA3 border also in other mammals, including primates, and thus enabling a more reliable translation of research in rodents and other model animals of these functionally distinct areas so critical for both memory and spatial navigation, as well as being affected in many different human brain pathologies.

Article III | Task-dependent mixed selectivity in the Subiculum

Principal cells in the subiculum, in contrast to CA1 place cells, are most often active across the whole recorded arena, though some seems to be modulated by environmental borders in agreement with previous reports (Lever et al., 2009; Stewart et al., 2014; Poulter et al., 2021). A substantial number of both CA1 and subicular neurons represent conjunctive information about position, head direction and running speed.

To better understand the influence of each covariate (position (P), head direction (H), and running speed (S)) on the observed information content, a Poisson generalized linear model (GLM) that considers multiple covariates simultaneously was applied. Subicular neurons were most strongly modulated for a combination of all three components combined (PHS), while CA1 neurons were more influenced by the combination of position and running speed. Quantification of the contributions of each covariate revealed that CA1 is mainly modulated by position, while subicular neurons are more strongly influenced by all three covariates.

In contrast to CA1, the proportion of subicular cells that were significantly modulated by alle three covariates increased during the spatial task. When decoding for P, H, and S simultaneously the error was also significantly lower in subiculum during the spatial task compared to open field experiments. This error was also lower for CA1 neurons during the spatial task, but less so compared to subicular neurons.

Article IV | Egocentric tuning in hippocampal neurons: Using simulations to estimate misclassification rates

Using the same statistical model as Jercog et al. (2019) we were able to replicate the findings of egocentric bearing cells in mice in our CA1 dataset from rats (57% of recorded units in CA1 were significantly tuned to egocentric bearing compared to a shuffled distribution). Only 36 out of 569 identified egocentric bearing cells were not place modulated. A number of cells also looked like they were tuned to head-direction while many of the place cells had place fields at the border or corners of the environment. In general, the population of cells defined as egocentric bearing cells were very heterogenous and seemed to represent multiple covariates. These observations demonstrated the need for a critical evaluation of the statistical model. This was achieved using a dataset of simulated neurons with predefined spatial representations.

The simulations showed that the statistical model correctly classified egocentric bearing cells in 85.2% of instances but misclassified 25% of place cells and 53% of conjunctive head direction and place cells as egocentric bearing cells. Conjunctive place and egocentric bearing cells were only significant in 51% of the instances, while head-direction cells were correctly classified in all instances. For place cells a strong relationship was observed between false positives and both increased noise level and field size. We also computed false negative and false positives rates per session and found a large variability indicating a potentially strong influence of behavior on the model.

In conclusion, we hypothesize that the observed egocentric tuning in the hippocampal formation is largely confounded by combination of conjunctive spatial representations and possible behavioral biases. The model performs well on purely egocentric bearing cells, but the majority of egocentric bearing cells observed in the hippocampus are conjunctive place cells. The influence of each covariate needs to be quantified before definite conclusions about egocentric representations in the hippocampus can be made.

Discussion

Comparative perspectives and border definitions

The structural variation in the overall appearance of the DG and the subjacent CA3 end in the species investigated in this thesis, is in line with previous reports including other mammals (Ramón y Cajal, 1893; Cajal, 1911; Lorente De Nó, 1934; Amaral et al., 2007; Seress, 2007; Hevner, 2016). In rat, the granular and molecular layers of the DG at most levels form a deep U or V-shaped concavity which is largely filled by the polymorphic layer (Šmejda Haug, 1974), while in sheep, pig and primates the DG is relatively larger with the polymorphic layer forming a thin band capping the expanded unstratified CA3 end. The mink in this respect represents an intermediate stage of development between the rodent and the two artiodactylae with preservation of a distinct pyramidal layer in the CA3 end, while the ungulate hippocampus seems to be intermediate to mink and primates. A comparison of the DG of rat, mink, ungulates (pig), and monkey is shown in figure 3.

In the first two manuscripts, we identified the borderline between the DG polymorphic layer and the CA3 using the mossy fibers with their collateral plexus as the organizing principle. This approach was possible because both studies use a combination of Timm-thionin- and Golgi-stained histological sections, the former which stains heavy metals, and particularly the zinc containing mossy fiber terminals (Smejda Haug, 1973), and the latter which stains cellular details including unmyelinated axons such as the thin mossy fibers. Our definition is a continuation of Ramón y Cajal´s emphasis on the fiber systems in the hippocampus as a defining feature of subdivisions, and an alternative to previous border definitions in the same area based on cytoarchitecture (Lorente De Nó, 1934; Holm & Geneser, 1991b; Cappaert et al., 2015). It is also a continuation of an existing defining feature of CA3 pyramidal cells which, in contrast to other pyramidal cells of the hippocampus, are characterized by thorny excrescences postsynaptic to the mossy fiber giant terminals (Amaral & Lavenex, 2006; Spruston & McBain, 2006). In a more recent publication, Witter et al. (2017) defined two hippocampal circuits based on the two parts of the perforant path

projection from layer II and III of the entorhinal cortex. Building further on this rationale we base the border definition between the DG and the CA3 end on the distribution and mode of termination of the mossy fibers in CA3 and their collaterals in the polymorphic layer, one synapse downstream of the layer II perforant path projection to the DG. The strikingly different fibre organization and mode of termination of the mossy fibers in the DG polymorphic layer and the CA3 end support such a two-part division.
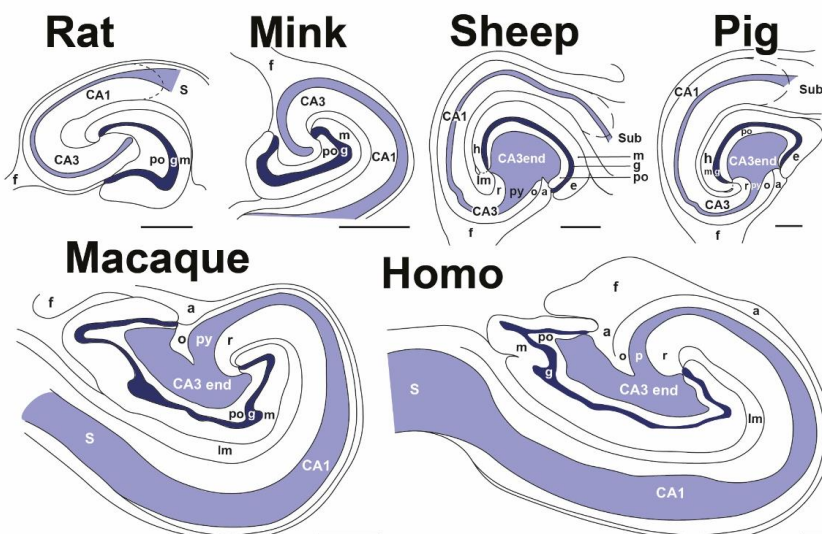
Fig.3. Cross-species comparison of the dentate gyrus (DG) and cornu ammonis (CA3, CA1) of the four species investigated (rat, mink, sheep, and pig) and comparable sections from macaque monkey and human (homo). The DG granular (g) and pyramidal layer (py) of the cornu ammonis is colored. Schematics are based on Nissl and Timm-stained sections from Finn-Mogens Smedja Haug (rat), Blackstad at al. 2016 (mink), Blackstad et al. (in press, sheep and pig), Kondo et al., 2009 (macaque monkey), and Andersen et al., 2006 and Stephan 1983 (human). Abbreviations: a, alveus; e, DG exposed blade; f, fimbria; h, DG hidden blade; lm, lacunar-molecular layer; m, molecular layer; o, stratum oriens; po, polymorphic layer; r, stratum radiatum; S/Sub, subiculum. Scale bars = 1 mm.

In the CA3 in rat, the main mossy fibers, after initially being positioned both apical and basal to the pyramidal layer (in the proximal or so-called CA3c), assemble just apical to the pyramidal cell somata in a dense mossy fiber bundle that ends abruptly at the CA2 border (Blackstad et al., 1970; Gaarskjaer, 1978; Claiborne et

34

al., 1986). Within the mossy fiber bundle, the fibers are unbranched and oriented in parallel within the same septotemporal level as their granular cells of origin, and perpendicular to their target pyramidal cells which are also organized in parallel to each other, the whole pattern resembling the strict geometrical organization of the granule cell parallel fibers and Purkinje-cells in the cerebellar cortex (Voogd & Glickstein, 1998; D'Angelo et al., 2011). In rat, each mossy fiber synapse on approximately 15 CA3 pyramidal cells via moss-like en passant presynaptic giant terminals that are distributed relative evenly along the length of the axon (Blackstad et al., 1970; Gaarskjaer, 1978; Claiborne et al., 1986), each pyramidal cell being potentially contacted by approximately 72 granule cells (Amaral & Lavenex, 2006).

In sheep and pig, in contrast to rat, but consistent with Ramon y Cajal's observations in rabbit and guinea pig, the main mossy fibers within the expanded CA3 end occur scattered in the lamellar plane, converging towards a mossy fiber bundle at the beginning of the main CA3, with a transitional region resembling the beginning of the mossy fiber bundle in the rat CA3 (Cajal, 1911; Blackstad et al., 1970). The scattering of fibers is clearly related to the scattering of pyramidal cells in the CA3 end which is typical also in primates including humans (Sutula et al., 1989; Buckmaster & Amaral, 2001; Kondo et al., 2008, 2009), thus indicating preservation of the mossy fiber system across mammals, although with systematic modifications throughout the phylogenesis.

Before entering the CA3, each mossy fiber gives off approximately 7 thin, branching collaterals to the polymorphic layer of the DG that branch extensively and together make about 7-12 large terminals similar to, but smaller than the giant terminals of the main fibers, 160 to 200 smaller varicosities, and some intermediate forms (Claiborne et al., 1986; Acsády et al., 1998). The giant terminals make contact with the thorny excrescences of the mossy cells, the smaller terminals are thought to terminate on GABAergic interneurons, while the intermediate forms terminate on both mossy cells and GABAergic interneurons (Acsády et al., 1998). In sum, the potential number of GABAergic neurons innervated by dentate granule cells largely outnumber the excitatory mossy and pyramidal cells. In contrast to the main mossy fibers, the collaterals in the

polymorphic layer extend in both the transverse and septotemporal direction (Claiborne et al., 1986; Acsády et al., 1998). This seems likely to be the case also in sheep and pig, but due to their curved course and branching, we were not able to trace or reconstruct the collaterals to any extent in our material.

Our observations support the notion that the mossy fiber system, and thus the intrinsic connectivity of the hippocampus, is similarly organized in the carnivore and the ungulates, and in agreement with previous reports in rodents and primates (Andersen et al., 1969; Blackstad et al., 1970; Andersen et al., 1971; Kondo et al., 2008). In our opinion, a DG/CA3 border founded on the mossy fiber system is thus more precise and serves as a more reliable basis for definition of homologies between species than a border based on cytoarchitecture alone.

To the same end, the candidate also proposes to abandon the terms *hilus* and *hilar area*, which are often used as synonyms for the DG polymorphic layer, but in many instances also includes the CA3 end (Amaral et al., 2007; Scharfman & Myers, 2012), thus disregarding the different functions and ontogenetic origin of the two adjoined cortices.

Mossy cells

Another marked change from rodents to primates is the number of the special gm-dendrites ascending from the mossy cells to the granular and molecular layer of the DG, which increases from 1 per cell in rat (Amaral, 1978; Scharfman, 1991; Buckmaster, 2012) to about 2.8 in mink (Blackstad et al., 2016), and about 5 in monkey (Buckmaster & Amaral, 2001). The number in sheep and pig might be in-between rat and mink, although the number in ungulates might be an underestimate since no detailed description of the dendritic arbor of mossy cells in these species exists. The high number in monkey, suggests that also in humans the mossy cells may get significantly more monosynaptic input from the perforant path than in rodents.

The significance of this difference is not known, but recent studies have shown that mossy cells in rodents often have spatial representations with multiple firing fields and that an estimated 88% of the population is active across

multiple environments (Danielson et al., 2017; GoodSmith et al., 2017; Senzai & Buzsaki, 2017). In comparison only 9% of granule cells and 29% of CA3 pyramidal cells are active in any given environment (GoodSmith et al., 2017). Mossy cell representations also remap comparable to CA3 pyramidal cells when the animal is moved to a new environment, or the researcher manipulates features of the same room (Senzai & Buzsaki, 2017). In contrast, granule cells rarely have place fields, and seldom more than one, and remap less robustly (GoodSmith et al., 2017; Senzai & Buzsaki, 2017).

If the mossy cell activity is mainly driven by granule cell input through the mossy fiber collaterals, it might seem strange that mossy cells do not adapt to the sparse firing activity of their neighboring granule cells, and that they also rarely inherit the spatial fields of these monosynapticly connected cells (Senzai & Buzsaki, 2017). The mossy fiber terminals are, however, strongly potentiating (Henze et al., 2002; Lysetskiy et al., 2005; Vyleta et al., 2016; Senzai & Buzsaki, 2017) and each granule cell, by the collaterals in the polymorphic layer, in a conservative estimate, synapse with seven to twelve mossy cells each (Claiborne et al., 1986; Acsády et al., 1998). In rats, there are approximately 1.2 million granule cells while there is in total approximately 50 000 neurons in the polymorphic layer, including interneurons. If only 9% of granule cells are active at each moment in time, this population still outnumbers the mossy cells manyfold. The skewed ratio and super potent synapses imply a high degree of convergence from multiple granule cells onto each single mossy cell which would make inheritance of single place fields unlikely and increase the probability of sufficient synaptic transmission even in the case when most of the granule cell population was silent. The degree of convergence of granule cells may be less in species with a long and slim polymorphic layer than in rat, a notion supported by the spatially limited labeling of mossy fiber collaterals in macaque monkey (Kondo et al., 2008, their figure 6 and 9). The situation might be similar in ungulates (article II, figure 10).

This effect could, however, be compensated by an increased number of granule cells and as well as a possible increased size of the dendritic arbor of mossy cells in species closer to humans. In article I, table 3 (Blackstad et al., 2016), we compared the reported total dendritic length of mossy cells in mouse, rat,

mink, and monkey. The results indicated that the dendritic arbors of mossy cells increase in species closer to primates compared to the rodents. Although we have no comparable measure for the ungulates, it seems rational to assume that mossy cells in these species follow the same trend which would position them intermediate to mink and primates.

Nakazawa (2017) in a preview article speculated that mossy cell activity might be driven by indirect input from the entorhinal cortex by means of the CA3 back-projection to the polymorphic layer or via semilunar granule cells that reside in the molecular layer and provenly synapse onto mossy cells (Williams et al., 2007; Larimer & Strowbridge, 2010). Said author and many others, however, seem to overlook the possibility that mossy cells are receivers of monosynaptic input from the entorhinal cortex through the gm-dendrites that extend across the terminal zone of axonal projections from both the lateral and medial entorhinal cortex in the DG molecular layer, or by perforant path projections from the deep layers of the entorhinal cortex that terminate in the polymorphic layer (Deller et al., 1996). No matter which input carries the strongest weight, mossy cells likely receive a proportion of inputs from the entorhinal cortex that bypasses the granule cells, as also emphasized by Nakazawa (2017).

It should be noted that mossy cells, in addition to the collateral input from granule cells (Claiborne et al., 1986; Acsády et al., 1998), the backprojection from CA3 (Zimmer, 1971; Schwerdtfeger & Sarvey, 1983; Ishizuka et al., 1990; Li et al., 1994; Scharfman, 2007), and the potential monosynaptic input from the entorhinal cortex, also receive inputs from local inhibitory neurons (Buckmaster et al., 1993), are monosynapticly interconnected with other mossy cells (Ma et al., 2021), and are targeted by cholinergic fibers (Deller et al., 1999; Sun et al., 2017) from the brain stem that cause a long-lasting excitatory potentiation. Mossy cells are thus far more than just receivers of mossy fibers and likely harbor very complex representations.

The physiological and anatomical observations raise the possibility that mossy cell potentially could influence spiking activity and place field representations in

granule cells more strongly than granule cells influence mossy cells. Mossy cells project both ipsi -and contralaterally (in rodents) to the inner third of molecular layer of the DG (Blackstad, 1956; Laurberg, 1979; Laurberg & Sorensen, 1981; Swanson et al., 1981) (but see (Houser et al., 2021)) and reach far in the septotemporal plane targeting the dendrites of thousands of granule cells and inhibitory basket cells. These basket cells again may target as many as ten thousand granule cells each through their axonal projections (Andersen et al., 2006). This mixed excitatory and inhibitory influence could predetermine the excitability of granule cells to the input from the entorhinal cortex and contribute to the sparse firing activity of granule cells. This would also be in line with ontogenetic studies indicating that the polymorphic layer (and probably the mossy cells) is present when the late-born granule cells arrive from a separate germinal center (Altman & Bayer, 1990a, 1990b, 1990c), studies in the adult mice which show that the first glutamatergic input to newborn granule cells is from mossy cells and that this contact is essential for granule cell maturation (Marqués-Marí et al., 2007; Vivar et al., 2012), and the intriguing line of research that implicate mossy cells as key regulators of neurogenesis in the adult hippocampus, both through synaptic innervation of neuronal stem cell in the subgranular zone and by secretion of trophic factors such as sonic hedgehog (Yeh et al., 2018; Gonzalez-Reyes et al., 2019). Recent evidence also shows that the synapses between the presynaptic mossy cells and postsynaptic granule cells undergo LTP which could strengthen the influence of these connections (Hashimotodani et al., 2017).

The encoding of memories is thought to partly rely on the ability of the dentate granule cells to generate unique combinations of activity which is relayed to the CA3 (Treves et al., 2008). The sparse firing activity of granule cells is thought to generate this code, a phenomenon referred to as *pattern separation* (Leutgeb et al., 2007; Myers & Scharfman, 2009; Nakazawa, 2017). It is tempting to speculate that the increased need for encoding more complex memories in animals closer to humans, and thus an increased need for pattern separation, is facilitated by increased monosynaptic input from the entorhinal cortex onto mossy cells by their gm-dendrites.

Conjunctive coding in CA1/sub

The third and fourth manuscript presents physiological data confirming that CA1 - and subicular neurons are modulated by multiple variables including position, head direction, and running speed, but that the degree of how much these variables account for the firing of the cells in the two areas is different. While CA1 neurons are more modulated by position and running speed, neurons in the subiculum were modulated by all three covariates, and this modulation was stronger during a spatial task. This is in line with previous reports that subicular neurons often represent borders and/or heading direction (Lever et al., 2009; Stewart et al., 2014; Poulter et al., 2021), while evidence of head directional tuning in CA1 during open field experiments historically has been sparse apart from a recent report of CA1 place cells representing head direction towards visual cues (Acharya et al., 2016).

When comparing the much-described representations in CA1 place cells with the less spatially selective firing of subicular neurons it is perhaps not surprising that cells in the subiculum represents a more complex mix of variables than cells in their neighboring region. The major cortical input to the subiculum is, however, similar to CA1, originating in the EC layer III (van Groen et al., 1986; Witter et al., 1988; Witter & Amaral, 1991; Cappaert et al., 2015). This and the projection from the CA1 make out the largest proportion of fibers terminating in the subiculum (Cappaert et al., 2015). In contrast, the DG and CA3 is mainly targeted by perforant path fibers originating in layer II of the EC (Steward, 1976; Witter et al., 1989; Tamamaki & Nojyo, 1993). Given these anatomical considerations, the fact that CA1 and CA3 pyramidal cells spatial representations are so similar and contrasting to the representations in subiculum is a conundrum.

The CA1, which project densely to the subiculum, do receive a major projection from CA3 which in turn is monosynaptically and disynaptically connected to the layer II projection from the EC (Amaral & Witter, 1989; van Strien et al., 2009; Cappaert et al., 2015). This input likely influences the spatial tuning of CA1 cells.

The subiculum in turn therefore receives both direct EC layer III input from as well as the mixed and processed input from EC layer II and layer III that have been forwarded by the DG, CA3, and CA1 respectively.

The CA1 projection to subiculum is strictly organized along the transverse axis in such a way that CA1 projections originating close to the CA2 border terminate in the subicular area closest to presubiculum, while CA1 projections originating close to the subiculum target areas just across the border of the two regions (Tamamaki et al., 1987; Amaral et al., 1991; Cappaert et al., 2015). Axons from the middle portion of CA1 target the middle portion of the subiculum. It would be rational to assume that the well-connected areas in CA1 and subiculum should have correlated spatial representations, but evidence of this has so far not been presented.

The intrinsic connectivity of the subiculum might explain why the CA1 and subiculum have such contrasting spatial representations. The main cell layer of the subiculum is much less densely packed than the CA1 pyramidal layer, and inhabited by two types of pyramidal cells, bursting and regular spiking, the former being more locally connected, and the latter connected to neurons along the whole transverse axis of the subiculum (Cajal, 1911; Witter & Groenewegen, 1990; Ishizuka, 2001; O'Mara et al., 2001; Witter, 2006; Cappaert et al., 2015; Cembrowski et al., 2018). Thus, although the input from CA1 to subiculum is distributed in a strict columnar fashion (Tamamaki et al., 1987; Amaral et al., 1991), the intrinsic connectivity of part of the principal cell population in subiculum likely distributes the CA1 signals along the whole transverse axis of the region. This contrasts with CA1 that has a weak intrinsic connectivity (Tamamaki et al., 1987; Amaral et al., 1991; Harris et al., 2001; Cappaert et al., 2015) which might lead to less mixed representations in this region.

In future attempts at dissecting the functionality of the subiculum, it might also be fruitful to separately analyze areas of the subiculum based on both input and output targets. In addition to the segregated input from CA1 in three transverse regions, the subiculum also, as previously mentioned, segregates its output in three related partitions along the same axis (Cappaert et al., 2015). In addition,

the projections from entorhinal cortex are also organized along the transverse axis with fibers from the lateral entorhinal cortex targeting the area closest to CA1 and fibers from the medial entorhinal cortex terminating closer to presubiculum (Tamamaki & Nojyo, 1995; Witter et al., 2000; Naber et al., 2001; Kim & Spruston, 2012). Since axons from subicular neurons do not collateralize and thus target only one selected region (Naber & Witter, 1998; Bienkowski et al., 2018; Cembrowski et al., 2018), the functional information relayed from subiculum to downstream targets could vary along the transverse axis.

Egocentric bearing cells

In the fourth manuscript, we report that principal cells in the CA1 have similar egocentric properties as previously reported in mice (Jercog et al., 2019) and bats (Sarel et al., 2017) when analyzed using the same statistical model of Jercog et al. (2019). The validity of this statistical model is tested using a population of spatially tuned simulated cells and the real behavior of animals recorded in 86 behavioral sessions. We found that when the cells have conjunctive representations, such as place and head direction modulation, the model produced a large amount of false positive data, meaning that a large proportion of the simulated non-egocentric cells were falsely classified as egocentric bearing cells. In fact, even for purely allocentric place cells a large proportion (25%) of the cells were misclassified as egocentric bearing cells using this statistical framework. The model also seemed to be influenced to a large extent by behavior as false negative and positive rates varied to a large extent between different sessions. The findings imply that allocentric representations and behavioral biases are confounding egocentric representations and need to be accounted for when analyzing data recorded from the hippocampus and other brain areas that are known to represent spatial navigation.

In the third manuscript, a Poisson generalized linear model was applied to assess the influence of each covariate in the recorded population of subicular and CA1 principal cells. This type of statistical framework was chosen as it considers multiple covariates simultaneously and allow the researcher to calculate the

strength of each covariates' influence on the observed tuning of the cell. A similar statistical model was used by Acharya and colleges (2016) to avoid behavioral biases within the place field to influence the observed angular tuning of hippocampal place cells. Further revisions of the fourth manuscript will include a generalized linear model similar to that used in the third paper (Lederberger et al., 2021).

The analysis in the fourth manuscript underlines the importance of choosing a model that considers the potential influence of different covariates and how polar plots of egocentric or allocentric directional modulation might tell only part of the story, and potentially lead to misinterpretations of the reported data.

Concluding remarks

In the first article we present a detailed description of the dentate mossy cells and the dentate gyrus in mink. The study is based on histological material stained with the Timm-thionin- and Golgi-methods which enable a description of both the cyto -and fibroarchitecture. The combination of methods enabled us to define the DG/CA3 border based on the mossy fiber collateral plexus, revealed in Timm-staining, and the CA3 pyramidal cell dendrites observed in Golgi sections. In the second article, we apply the same delineation criteria to the CA3 and DG in the artiodactylae sheep and pig, the former which has rarely been studied before, while the latter has been subject of several histochemical studies in which the CA3 end is incorrectly regarded as part of the DG. Our findings offer a solution to the delineation of the DG/CA3 border which may apply to all mammals.

In the third paper, we investigate the representations of neurons in the subiculum, the main output region of the hippocampus, using electrophysiological data acquired during open field experiments and a spatial task. The findings are compared to CA1 data and show that both CA1 and subicular neurons conjunctively represent position, head direction and running speed, but that this mixed selectivity is stronger in the subiculum and augmented during a spatial task.

Finally, in the fourth paper we test the currently used methods for reporting egocentric bearing cells in the hippocampus on a simulated dataset and show that the statistical model produces a high degree of false positive results when applied to cells with conjunctive representations, which in light of the mixed selectivity of cells in CA1 reported in the third manuscript and the apparent conjunctive allocentric place representations in the populations of egocentric bearing cells, imply that a proper investigation of the influence of confounding variables is needed before concluding that egocentric coding as a hippocampal formation is a real phenomenon.

In conclusion, this thesis work presents two anatomical descriptions of the main input region of the hippocampal circuitry, the DG and CA3, in mink, sheep, and pig, as well as two electrophysiological studies of cells in the main output regions

CA1 and the subiculum in rats. Data from all major subregions of the hippocampal formation is presented from different vantage points providing both anatomical and functional descriptions of these areas and the single cells that inhabits them. Of special mention is the comparative aspect which highlight the similarities and differences between the hippocampus of our most used animal model, the rodents, and species sequentially closer to humans.

References

Acharya, L., Aghajan, Z. M., Vuong, C., Moore, J. J., & Mehta, M. R. (2016). Causal Influence of Visual Cues on Hippocampal Directional Selectivity. *Cell, 164*(1-2), 197-207. doi:10.1016/j.cell.2015.12.015

Acsády, L., Kamondi, A., Sík, A., Freund, T., & Buzsáki, G. (1998). GABAergic cells are the major postsynaptic targets of mossy fibers in the rat hippocampus. *J Neurosci, 18*(9), 3386-3403. doi:10.1523/jneurosci.18-09-03386.1998

Albert, M. S., DeKosky, S. T., Dickson, D., Dubois, B., Feldman, H. H., Fox, N. C., . . . Phelps, C. H. (2011). The diagnosis of mild cognitive impairment due to Alzheimer's disease: Recommendations from the National Institute on Aging-Alzheimer's Association workgroups on diagnostic guidelines for Alzheimer's disease. *Alzheimer's & Dementia, 7*(3), 270-279. doi:https://doi.org/10.1016/j.jalz.2011.03.008

Altman, J., & Bayer, S. A. (1990a). Migration and distribution of two populations of hippocampal granule cell precursors during the perinatal and postnatal periods. *J Comp Neurol, 301*(3), 365-381. doi:10.1002/cne.903010304

Altman, J., & Bayer, S. A. (1990b). Mosaic organization of the hippocampal neuroepithelium and the multiple germinal sources of dentate granule cells. *J Comp Neurol, 301*(3), 325-342. doi:10.1002/cne.903010302

Altman, J., & Bayer, S. A. (1990c). Prolonged sojourn of developing pyramidal cells in the intermediate zone of the hippocampus and their settling in the stratum pyramidale. *J Comp Neurol, 301*(3), 343-364. doi:10.1002/cne.903010303

Amaral, D. G. (1978). A Golgi study of cell types in the hilar region of the hippocampus in the rat. *J Comp Neurol, 182*(4 Pt 2), 851-914.

Amaral, D. G., Dolorfo, C., & Alvarez-Royo, P. (1991). Organization of CA1 projections to the subiculum: A PHA-L analysis in the rat. *Hippocampus, 1*(4), 415-435. doi:https://doi.org/10.1002/hipo.450010410

Amaral, D. G., & Lavenex, P. (2006). Hippocampal Neuroanatomy. In P. Andersen, R. Morris, D. G. Amaral, T. Bliss, & J. O'Keefe (Eds.), *The Hippocampus Book* (pp. 37-115). Oxford: Oxford University Press.

Amaral, D. G., Scharfman, H. E., & Lavenex, P. (2007). The dentate gyrus: fundamental neuroanatomical organization (dentate gyrus for dummies). *Prog Brain Res, 163*, 3-22. doi:10.1016/s0079-6123(07)63001-5

Amaral, D. G., & Witter, M. P. (1989). The three-dimensional organization of the hippocampal formation: a review of anatomical data. *Neuroscience, 31*(3), 571-591. doi:10.1016/0306-4522(89)90424-7

Andersen, P., Bliss, T. V., Lomo, T., Olsen, L. I., & Skrede, K. K. (1969). Lamellar organization of hippocampal excitatory pathways. *Acta Physiol Scand, 76*(1), 4a-5a. doi:10.1111/j.1748-1716.1969.tb04499.x

Andersen, P., Bliss, T. V., & Skrede, K. K. (1971). Lamellar organization of hippocampal pathways. *Exp Brain Res, 13*(2), 222-238. doi:10.1007/bf00234087

Andersen, P., Morris, R., Amaral, D. G., O'Keefe, J., & Bliss, T. (2006). *The hippocampus book*. New York, NY, US: Oxford University Press.

Apostolova, L. G., Dinov, I. D., Dutton, R. A., Hayashi, K. M., Toga, A. W., Cummings, J. L., & Thompson, P. M. (2006). 3D comparison of hippocampal atrophy in amnestic mild cognitive impairment and Alzheimer's disease. *Brain, 129*(11), 2867-2873. doi:10.1093/brain/awl274

Bienkowski, M. S., Bowman, I., Song, M. Y., Gou, L., Ard, T., Cotter, K., . . . Dong, H. W. (2018). Integration of gene expression and brain-wide connectivity reveals the multiscale organization of mouse hippocampal networks. *Nat Neurosci, 21*(11), 1628-1643. doi:10.1038/s41593-018-0241-y

Blackstad, J. S., Osen, K. K., Scharfman, H. E., Storm-Mathisen, J., Blackstad, T. W., & Leergaard, T. B. (2016). Observations on hippocampal mossy cells in mink (Neovison vison) with special reference to dendrites ascending to the granular and molecular layers. *Hippocampus, 26*(2), 229-245. doi:10.1002/hipo.22518

Blackstad, T. W. (1956). Commissural connections of the hippocampal region in the rat, with special reference to their mode of termination. *J Comp Neurol, 105*(3), 417-537. doi:10.1002/cne.901050305

Blackstad, T. W. (1958). On the termination of some afferents to the hippocampus and fascia dentata. *Cells Tissues Organs, 35*(3), 202-214. doi:10.1159/000141409

Blackstad, T. W. (1963). Ultrastructural Studies on the Hippocampal Region. In W. Bargmann & J. P. Schadé (Eds.), *Prog Brain Res* (Vol. 3, pp. 122-148): Elsevier.

Blackstad, T. W. (1985). Laminar specificity of dendritic morphology: Examples from the guinea pig hippocampal region. In F. K. Agnati L (Ed.), *Quantitative Neuroanatomy in Transmitter Research* (pp. 55–69.). New York and London: Plenum Press.

Blackstad, T. W., Brink, K., Hem, J., & Jeune, B. (1970). Distribution of hippocampal mossy fibers in the rat. An experimental study with silver impregnation methods. *J Comp Neurol, 138*(4), 433-449. doi:10.1002/cne.901380404

Blackstad, T. W., Osen, K. K., & Mugnaini, E. (1984). Pyramidal neurones of the dorsal cochlear nucleus: a Golgi and computer reconstruction study in cat. *Neuroscience, 13*(3), 827-854. doi:10.1016/0306-4522(84)90099-x

Botterill, J. J., Gerencer, K. J., Vinod, K. Y., Alcantara-Gonzalez, D., & Scharfman, H. E. (2021). Dorsal and ventral mossy cells differ in their axonal projections throughout the dentate gyrus of the mouse hippocampus. *Hippocampus, 31*(5), 522-539. doi:10.1002/hipo.23314

Buckmaster, P. S. (2012). Mossy cell dendritic structure quantified and compared with other hippocampal neurons labeled in rats in vivo. *Epilepsia, 53 Suppl 1*(Suppl 1), 9-17. doi:10.1111/j.1528-1167.2012.03470.x

Buckmaster, P. S., & Amaral, D. G. (2001). Intracellular recording and labeling of mossy cells and proximal CA3 pyramidal cells in macaque monkeys. *J Comp Neurol, 430*(2), 264-281. doi:10.1002/1096-9861(20010205)430:2<264::aid-cne1030>3.0.co;2-3

Buckmaster, P. S., Strowbridge, B. W., & Schwartzkroin, P. A. (1993). A comparison of rat hippocampal mossy cells and CA3c pyramidal cells. *J Neurophysiol, 70*(4), 1281-1299. doi:10.1152/jn.1993.70.4.1281

Buckmaster, P. S., Wenzel, H. J., Kunkel, D. D., & Schwartzkroin, P. A. (1996). Axon arbors and synaptic connections of hippocampal mossy cells in the rat in vivo. *J Comp Neurol, 366*(2), 271-292. doi:10.1002/(sici)1096-9861(19960304)366:2<270::aid-cne7>3.0.co;2-2

Buzsáki, G., & Moser, E. I. (2013). Memory, navigation and theta rhythm in the hippocampal-entorhinal system. *Nat Neurosci, 16*(2), 130-138. doi:10.1038/nn.3304

Cajal, R. y. (1911). *Histologie du systéme nerveux de l'homme et des vertébrés. T.II*. Paris, Malonie.

Cappaert, N. L. M., van Strien, N., & Witter, M. (2015). Chapter 20. Hippocampal Formation (pp. 511-573).

Cembrowski, M. S., Wang, L., Lemire, A. L., Copeland, M., DiLisio, S. F., Clements, J., & Spruston, N. (2018). The subiculum is a patchwork of discrete subregions. *Elife, 7*. doi:10.7554/eLife.37701

Claiborne, B. J., Amaral, D. G., & Cowan, W. M. (1986). A light and electron microscopic analysis of the mossy fibers of the rat dentate gyrus. *J Comp Neurol, 246*(4), 435-458. doi:10.1002/cne.902460403

D'Angelo, E., Mazzarello, P., Prestori, F., Mapelli, J., Solinas, S., Lombardo, P., . . . Congi, L. (2011). The cerebellar network: From structure to function and dynamics. *Brain Research Reviews, 66*(1), 5-15. doi:https://doi.org/10.1016/j.brainresrev.2010.10.002

Danielson, N. B., Turi, G. F., Ladow, M., Chavlis, S., Petrantonakis, P. C., Poirazi, P., & Losonczy, A. (2017). In Vivo Imaging of Dentate Gyrus Mossy Cells in Behaving Mice. *Neuron, 93*(3), 552-559.e554. doi:10.1016/j.neuron.2016.12.019

Deller, T., Katona, I., Cozzari, C., Frotscher, M., & Freund, T. F. (1999). Cholinergic innervation of mossy cells in the rat fascia dentata. *Hippocampus, 9*(3), 314-320. doi:10.1002/(sici)1098-1063(1999)9:3<314::Aid-hipo10>3.0.Co;2-7

Deller, T., Martinez, A., Nitsch, R., & Frotscher, M. (1996). A Novel Entorhinal Projection to the Rat Dentate Gyrus: Direct Innervation of Proximal Dendrites and Cell Bodies of Granule Cells and GABAergic Neurons. *The Journal of Neuroscience, 16*(10), 3322-3333. doi:10.1523/jneurosci.16-10-03322.1996

Felleman, D. J., & Van Essen, D. C. (1991). Distributed hierarchical processing in the primate cerebral cortex. *Cereb Cortex, 1*(1), 1-47. doi:10.1093/cercor/1.1.1-a

Frotscher, M., Seress, L., Schwerdtfeger, W. K., & Buhl, E. (1991). The mossy cells of the fascia dentata: a comparative study of their fine structure and synaptic connections in rodents and primates. *J Comp Neurol, 312*(1), 145-163. doi:10.1002/cne.903120111

Fyhn, M., Molden, S., Witter, M. P., Moser, E. I., & Moser, M. B. (2004). Spatial representation in the entorhinal cortex. *Science, 305*(5688), 1258-1264. doi:10.1126/science.1099901

Gonzalez-Reyes, L. E., Chiang, C. C., Zhang, M., Johnson, J., Arrillaga-Tamez, M., Couturier, N. H., . . . Durand, D. M. (2019). Sonic Hedgehog is expressed by hilar mossy cells and regulates cellular survival and neurogenesis in the adult hippocampus. *Sci Rep, 9*(1), 17402. doi:10.1038/s41598-019-53192-4

GoodSmith, D., Chen, X., Wang, C., Kim, S. H., Song, H., Burgalossi, A., . . . Knierim, J. J. (2017). Spatial Representations of Granule Cells and Mossy Cells of the Dentate Gyrus. *Neuron, 93*(3), 677-690.e675. doi:10.1016/j.neuron.2016.12.026

Gościcka, D., Stankiewicz, W., & Szpinda, M. (1993). Hippocampus in the N. American mink (Mustela vison Brisson, 1756). *Arch Vet Pol, 33*(1-2), 129-134.

Gaarskjaer, F. B. (1978). Organization of the mossy fiber system of the rat studied in extended hippocampi. II. Experimental analysis of fiber distribution with silver impregnation methods. *J Comp Neurol, 178*(1), 73-88. doi:10.1002/cne.901780105

Gaarskjaer, F. B., Danscher, G., & West, M. J. (1982). Hippocampal mossy fibers in the regio superior of the European hedgehog. *Brain Res, 237*(1), 79-90. doi:10.1016/0006-8993(82)90558-3

Hafting, T., Fyhn, M., Molden, S., Moser, M. B., & Moser, E. I. (2005). Microstructure of a spatial map in the entorhinal cortex. *Nature, 436*(7052), 801-806. doi:10.1038/nature03721

Harris, E., Witter, M. P., Weinstein, G., & Stewart, M. (2001). Intrinsic connectivity of the rat subiculum: I. Dendritic morphology and patterns of axonal arborization by pyramidal neurons. *J Comp Neurol, 435*(4), 490-505. doi:10.1002/cne.1046

Hashimotodani, Y., Nasrallah, K., Jensen, K. R., Chávez, A. E., Carrera, D., & Castillo, P. E. (2017). LTP at Hilar Mossy Cell-Dentate Granule Cell Synapses Modulates Dentate Gyrus Output by Increasing Excitation/Inhibition Balance. *Neuron, 95*(4), 928-943.e923. doi:10.1016/j.neuron.2017.07.028

Henze, D. A., Wittner, L., & Buzsáki, G. (2002). Single granule cells reliably discharge targets in the hippocampal CA3 network in vivo. *Nat Neurosci, 5*(8), 790-795. doi:10.1038/nn887

Hevner, R. F. (2016). Evolution of the mammalian dentate gyrus. *J Comp Neurol, 524*(3), 578-594. doi:10.1002/cne.23851

Holm, I. E., & Geneser, F. A. (1989). Histochemical demonstration of zinc in the hippocampal region of the domestic pig: I. Entorhinal area, parasubiculum, and presubiculum. *J Comp Neurol, 287*(2), 145-163. doi:10.1002/cne.902870202

Holm, I. E., & Geneser, F. A. (1991a). Histochemical demonstration of zinc in the hippocampal region of the domestic pig: II. Subiculum and hippocampus. *J Comp Neurol, 305*(1), 71-82. doi:10.1002/cne.903050108

Holm, I. E., & Geneser, F. A. (1991b). Histochemical demonstration of zinc in the hippocampal region of the domestic pig: III. The dentate area. *J Comp Neurol, 308*(3), 409-417. doi:10.1002/cne.903080308

Holm, I. E., & West, M. J. (1994). Hippocampus of the domestic pig: a stereological study of subdivisional volumes and neuron numbers. *Hippocampus, 4*(1), 115-125. doi:10.1002/hipo.450040112

Houser, C. R., Peng, Z., Wei, X., Huang, C. S., & Mody, I. (2021). Mossy Cells in the Dorsal and Ventral Dentate Gyrus Differ in Their Patterns of Axonal Projections. *J Neurosci, 41*(5), 991-1004. doi:10.1523/jneurosci.2455-20.2020

Hoydal, O. A., Skytoen, E. R., Moser, M.-B., & Moser, E. I. (2018). Object-vector coding in the medial entorhinal cortex. 286286. doi:10.1101/286286 %J bioRxiv

Humphrey, T. (1967). The development of the human hippocampal fissure. *Journal of anatomy, 101*(Pt 4), 655-676.

Ishizuka, N. (2001). Laminar organization of the pyramidal cell layer of the subiculum in the rat. *J Comp Neurol, 435*(1), 89-110. doi:10.1002/cne.1195

Ishizuka, N., Weber, J., & Amaral, D. G. (1990). Organization of intrahippocampal projections originating from CA3 pyramidal cells in the rat. *J Comp Neurol, 295*(4), 580-623. doi:10.1002/cne.902950407

Jercog, P. E., Ahmadian, Y., Woodruff, C., Deb-Sen, R., Abbott, L. F., & Kandel, E. R. (2019). Heading direction with respect to a reference point modulates place-cell activity. *Nature Communications, 10*(1), 2333. doi:10.1038/s41467-019-10139-7

Jinde, S., Zsiros, V., & Nakazawa, K. (2013). Hilar mossy cell circuitry controlling dentate granule cell excitability. *Front Neural Circuits, 7*, 14. doi:10.3389/fncir.2013.00014

Kim, Y., & Spruston, N. (2012). Target-specific output patterns are predicted by the distribution of regular-spiking and bursting pyramidal neurons in the subiculum. *Hippocampus, 22*(4), 693-706. doi:10.1002/hipo.20931

Kjonigsen, L. J., Lillehaug, S., Bjaalie, J. G., Witter, M. P., & Leergaard, T. B. (2015). Waxholm Space atlas of the rat brain hippocampal region: three-dimensional delineations based on magnetic resonance and diffusion tensor imaging. *Neuroimage, 108*, 441-449. doi:10.1016/j.neuroimage.2014.12.080

Kondo, H., Lavenex, P., & Amaral, D. G. (2008). Intrinsic connections of the macaque monkey hippocampal formation: I. Dentate gyrus. *J Comp Neurol, 511*(4), 497-520. doi:10.1002/cne.21825

Kondo, H., Lavenex, P., & Amaral, D. G. (2009). Intrinsic connections of the macaque monkey hippocampal formation: II. CA3 connections. *J Comp Neurol, 515*(3), 349-377. doi:10.1002/cne.22056

Kropff, E., Carmichael, J. E., Moser, M. B., & Moser, E. I. (2015). Speed cells in the medial entorhinal cortex. *Nature, 523*(7561), 419-424. doi:10.1038/nature14622

Larimer, P., & Strowbridge, B. W. (2010). Representing information in cell assemblies: persistent activity mediated by semilunar granule cells. *Nat Neurosci, 13*(2), 213-222. doi:10.1038/nn.2458

Laurberg, S. (1979). Commissural and intrinsic connections of the rat hippocampus. *Journal of Comparative Neurology, 184*(4), 685-708. doi:https://doi.org/10.1002/cne.901840405

Laurberg, S., & Sorensen, K. E. (1981). Associational and commissural collaterals of neurons in the hippocampal formation (hilus fasciae dentatae and subfield CA3). *Brain Res, 212*(2), 287-300.

Ledergerber, D., Battistin, C., Blackstad, J. S., Gardner, R. J., Witter, M. P., Moser, M. B., . . . Moser, E. I. (2021). Task-dependent mixed selectivity in the subiculum. *Cell Rep, 35*(8), 109175. doi:10.1016/j.celrep.2021.109175

Leergaard, T. B., & Bjaalie, J. G. (1995). Semi-automatic data acquisition for quantitative neuroanatomy. MicroTrace--computer programme for recording of the spatial distribution of neuronal populations. *Neurosci Res, 22*(2), 231-243. doi:10.1016/0168-0102(95)00899-6

Leutgeb, J. K., Leutgeb, S., Moser, M. B., & Moser, E. I. (2007). Pattern separation in the dentate gyrus and CA3 of the hippocampus. *Science, 315*(5814), 961-966. doi:10.1126/science.1135801

Lever, C., Burton, S., Jeewajee, A., O'Keefe, J., & Burgess, N. (2009). Boundary vector cells in the subiculum of the hippocampal formation. *J Neurosci, 29*(31), 9771-9777. doi:10.1523/jneurosci.1319-09.2009

Li, X. G., Somogyi, P., Ylinen, A., & Buzsáki, G. (1994). The hippocampal CA3 network: an in vivo intracellular labeling study. *J Comp Neurol, 339*(2), 181-208. doi:10.1002/cne.903390204

Lorente De Nó, R. (1934). Studies on the structure of the cerebral cortex. II. Continuation of the study of the ammonic system. *Journal für Psychologie und Neurologie, 46*, 113-177.

Lysetskiy, M., Földy, C., & Soltesz, I. (2005). Long- and short-term plasticity at mossy fiber synapses on mossy cells in the rat dentate gyrus. *Hippocampus, 15*(6), 691-696. doi:10.1002/hipo.20096

Ma, Y., Bayguinov, P. O., McMahon, S. M., Scharfman, H. E., & Jackson, M. B. (2021). Direct synaptic excitation between hilar mossy cells revealed with a targeted voltage sensor. *Hippocampus, 31*(11), 1215-1232. doi:10.1002/hipo.23386

Maguire, E. A., Frackowiak, R. S., & Frith, C. D. (1997). Recalling routes around london: activation of the right hippocampus in taxi drivers. *J Neurosci, 17*(18), 7103-7110.

Marqués-Marí, A. I., Nacher, J., Crespo, C., Gutièrrez-Mecinas, M., Martínez-Guijarro, F. J., & Blasco-Ibáñez, J. M. (2007). Loss of input from the mossy cells blocks maturation of newly generated granule cells. *Hippocampus, 17*(7), 510-524. doi:10.1002/hipo.20290

Morris, R. G., Garrud, P., Rawlins, J. N., & O'Keefe, J. (1982). Place navigation impaired in rats with hippocampal lesions. *Nature, 297*(5868), 681-683. doi:10.1038/297681a0

Moser, E. I., Kropff, E., & Moser, M. B. (2008). Place cells, grid cells, and the brain's spatial representation system. *Annu Rev Neurosci, 31*, 69-89. doi:10.1146/annurev.neuro.31.061307.090723

Moser, E. I., Moser, M. B., & McNaughton, B. L. (2017). Spatial representation in the hippocampal formation: a history. *Nat Neurosci, 20*(11), 1448-1464. doi:10.1038/nn.4653

Myers, C. E., & Scharfman, H. E. (2009). A role for hilar cells in pattern separation in the dentate gyrus: a computational approach. *Hippocampus, 19*(4), 321-337. doi:10.1002/hipo.20516

Naber, P. A., Lopes da Silva, F. H., & Witter, M. P. (2001). Reciprocal connections between the entorhinal cortex and hippocampal fields CA1 and the subiculum are in register with the projections from CA1 to the subiculum. *Hippocampus, 11*(2), 99-104. doi:10.1002/hipo.1028

Naber, P. A., & Witter, M. P. (1998). Subicular efferents are organized mostly as parallel projections: a double-labeling, retrograde-tracing study in the rat. *J Comp Neurol, 393*(3), 284-297.

Nakazawa, K. (2017). Dentate Mossy Cell and Pattern Separation. *Neuron, 93*(3), 465-467. doi:10.1016/j.neuron.2017.01.021

O'Keefe, J. (1976). Place units in the hippocampus of the freely moving rat. *Exp Neurol, 51*(1), 78-109.

O'Keefe, J., & Dostrovsky, J. (1971). The hippocampus as a spatial map. Preliminary evidence from unit activity in the freely-moving rat. *Brain Res, 34*(1), 171-175.

O'Keefe, J., & Nadel, L. (1978). *The hippocampus as a cognitive map*: Clarendon Press.

O'Mara, S. M., Commins, S., Anderson, M., & Gigg, J. (2001). The subiculum: a review of form, physiology and function. *Prog Neurobiol, 64*(2), 129-155. doi:10.1016/s0301-0082(00)00054-x

Olson, J. M., Tongprasearth, K., & Nitz, D. A. (2017). Subiculum neurons map the current axis of travel. *Nat Neurosci, 20*(2), 170-172. doi:10.1038/nn.4464

Penfield, W., & Milner, B. (1958). Memory deficit produced by bilateral lesions in the hippocampal zone. *AMA Arch Neurol Psychiatry, 79*(5), 475-497.

Pfeiffer, B. E., & Foster, D. J. (2013). Hippocampal place-cell sequences depict future paths to remembered goals. *Nature, 497*(7447), 74-79. doi:10.1038/nature12112

Poulter, S., Lee, S. A., Dachtler, J., Wills, T. J., & Lever, C. (2021). Vector trace cells in the subiculum of the hippocampal formation. *Nature Neuroscience, 24*(2), 266-275. doi:10.1038/s41593-020-00761-w

Ramón y Cajal, S. (1893). Estructura del asta de Ammon y fascia dentata. *Ann Soc Esp Hist, Nat 22*.

Ranck, J. B. (1984). Head direction cells in the deep layer of dorsal presubiculum in freely moving rats. *Soc Neurosci Abstr 10:599.* .

Ratzliff, A., Howard, A. L., Santhakumar, V., Osapay, I., & Soltesz, I. (2004). Rapid deletion of mossy cells does not result in a hyperexcitable dentate gyrus: implications for epileptogenesis. *J Neurosci, 24*(9), 2259-2269. doi:10.1523/jneurosci.5191-03.2004

Ribak, C. E., Seress, L., & Amaral, D. G. (1985). The development, ultrastructure and synaptic connections of the mossy cells of the dentate gyrus. *J Neurocytol, 14*(5), 835-857.

Rose, J. E. (1942). A cytoarchitectural study of the sheep cortex. *Journal of Comparative Neurology, 76*(1), 1-55. doi:https://doi.org/10.1002/cne.900760102

Sarel, A., Finkelstein, A., Las, L., & Ulanovsky, N. (2017). Vectorial representation of spatial goals in the hippocampus of bats. *Science, 355*(6321), 176-180. doi:10.1126/science.aak9589

Sargolini, F., Fyhn, M., Hafting, T., McNaughton, B. L., Witter, M. P., Moser, M. B., & Moser, E. I. (2006). Conjunctive representation of position, direction, and velocity in entorhinal cortex. *Science, 312*(5774), 758-762. doi:10.1126/science.1125572

Scharfman, H. E. (1991). Dentate hilar cells with dendrites in the molecular layer have lower thresholds for synaptic activation by perforant path than granule cells. *J Neurosci, 11*(6), 1660-1673. doi:10.1523/jneurosci.11-06-01660.1991

Scharfman, H. E. (2007). The CA3 "backprojection" to the dentate gyrus. *Prog Brain Res, 163*, 627-637. doi:10.1016/s0079-6123(07)63034-9

Scharfman, H. E. (2016). The enigmatic mossy cell of the dentate gyrus. *Nat Rev Neurosci, 17*(9), 562-575. doi:10.1038/nrn.2016.87

Scharfman, H. E. (2018). Advances in understanding hilar mossy cells of the dentate gyrus. *Cell Tissue Res, 373*(3), 643-652. doi:10.1007/s00441-017-2750-5

Scharfman, H. E., & Bernstein, H. L. (2015). Potential implications of a monosynaptic pathway from mossy cells to adult-born granule cells of the dentate gyrus. *Front Syst Neurosci, 9*, 112. doi:10.3389/fnsys.2015.00112

Scharfman, H. E., & Myers, C. E. (2012). Hilar mossy cells of the dentate gyrus: a historical perspective. *Front Neural Circuits, 6*, 106. doi:10.3389/fncir.2012.00106

Schwerdtfeger, W. K., & Sarvey, J. M. (1983). Connectivity of the hilar region of the hippocampal formation in the rat. *J Hirnforsch, 24*(2), 201-207.

Scoville, W. B., & Milner, B. (1957). Loss of recent memory after bilateral hippocampal lesions. *J Neurol Neurosurg Psychiatry, 20*(1), 11-21. doi:10.1136/jnnp.20.1.11

Senzai, Y., & Buzsaki, G. (2017). Physiological Properties and Behavioral Correlates of Hippocampal Granule Cells and Mossy Cells. *Neuron, 93*(3), 691-704.e695. doi:10.1016/j.neuron.2016.12.011

Seress, L. (2007). Comparative anatomy of the hippocampal dentate gyrus in adult and developing rodents, non-human primates and humans. *Prog Brain Res, 163*, 23-41. doi:10.1016/s0079-6123(07)63002-7

Sloviter, R. S. (1991). Permanently altered hippocampal structure, excitability, and inhibition after experimental status epilepticus in the rat: the "dormant basket cell" hypothesis and its possible relevance to temporal lobe epilepsy. *Hippocampus, 1*(1), 41-66. doi:10.1002/hipo.450010106

Sloviter, R. S., Zappone, C. A., Harvey, B. D., Bumanglag, A. V., Bender, R. A., & Frotscher, M. (2003). "Dormant basket cell" hypothesis revisited: relative vulnerabilities of dentate gyrus mossy cells and inhibitory interneurons after hippocampal status epilepticus in the rat. *J Comp Neurol, 459*(1), 44-76. doi:10.1002/cne.10630

Šmejda Haug, F.-M. (1974). Light microscopical mapping of the hippocampal region, the pyriform cortex and the corticomedial amygdaloid nuclei of the rat with Timm's sulphide silver method. *Zeitschrift für Anatomie und Entwicklungsgeschichte, 145*(1), 1-27. doi:10.1007/BF00519123

Smejda Haug, F. M. (1973). Heavy metals in the brain. A light microscope study of the rat with Timm's sulphide silver method. Methodological considerations and cytological and regional staining patterns. *Adv Anat Embryol Cell Biol, 47*(4), 1-71.

Solstad, T., Boccara, C. N., Kropff, E., Moser, M. B., & Moser, E. I. (2008). Representation of geometric borders in the entorhinal cortex. *Science, 322*(5909), 1865-1868. doi:10.1126/science.1166466

Soriano, E., & Frotscher, M. (1994). Mossy cells of the rat fascia dentata are glutamate-immunoreactive. *Hippocampus, 4*(1), 65-69. doi:10.1002/hipo.450040108

Spruston, N., & McBain, C. (2006). Structural and Functional Properties of Hippocampal Neurons. In P. Andersen, R. Morris, D. G. Amaral, T. Bliss, &

J. O'Keefe (Eds.), *The Hippocampus Book* (pp. 133-201). Oxford: Oxford University Press.

Stensola, H., Stensola, T., Solstad, T., Frøland, K., Moser, M. B., & Moser, E. I. (2012). The entorhinal grid map is discretized. *Nature, 492*(7427), 72-78. doi:10.1038/nature11649

Steward, O. (1976). Topographic organization of the projections from the entorhinal area to the hippocampal formation of the rat. *J Comp Neurol, 167*(3), 285-314. doi:10.1002/cne.901670303

Stewart, S., Jeewajee, A., Wills, T. J., Burgess, N., & Lever, C. (2014). Boundary coding in the rat subiculum. *Philos Trans R Soc Lond B Biol Sci, 369*(1635), 20120514. doi:10.1098/rstb.2012.0514

Strange, B. A., Witter, M. P., Lein, E. S., & Moser, E. I. (2014). Functional organization of the hippocampal longitudinal axis. *Nat Rev Neurosci, 15*(10), 655-669. doi:10.1038/nrn3785

Sun, Y., Grieco, S. F., Holmes, T. C., & Xu, X. (2017). Local and Long-Range Circuit Connections to Hilar Mossy Cells in the Dentate Gyrus. *eNeuro, 4*(2). doi:10.1523/eneuro.0097-17.2017

Sutula, T., Cascino, G., Cavazos, J., Parada, I., & Ramirez, L. (1989). Mossy fiber synaptic reorganization in the epileptic human temporal lobe. *Ann Neurol, 26*(3), 321-330. doi:10.1002/ana.410260303

Swanson, L., Sawchenko, P., & Cowan, W. (1981). Evidence for collateral projections by neurons in Ammon's horn, the dentate gyrus, and the subiculum: a multiple retrograde labeling study in the rat. *The Journal of Neuroscience, 1*(5), 548-559. doi:10.1523/jneurosci.01-05-00548.1981

Swanson, L. W., Wyss, J. M., & Cowan, W. M. (1978). An autoradiographic study of the organization of intrahippocampal association pathways in the rat. *J Comp Neurol, 181*(4), 681-715. doi:10.1002/cne.901810402

Tamamaki, N., Abe, K., & Nojyo, Y. (1987). Columnar organization in the subiculum formed by axon branches originating from single CA1 pyramidal neurons in the rat hippocampus. *Brain Res, 412*(1), 156-160. doi:10.1016/0006-8993(87)91452-1

Tamamaki, N., & Nojyo, Y. (1993). Projection of the entorhinal layer II neurons in the rat as revealed by intracellular pressure-injection of neurobiotin. *Hippocampus, 3*(4), 471-480. doi:10.1002/hipo.450030408

Tamamaki, N., & Nojyo, Y. (1995). Preservation of topography in the connections between the subiculum, field CA1, and the entorhinal cortex in rats. *J Comp Neurol, 353*(3), 379-390. doi:10.1002/cne.903530306

Taube, J. S., Muller, R. U., & Ranck, J. B., Jr. (1990). Head-direction cells recorded from the postsubiculum in freely moving rats. I. Description and quantitative analysis. *J Neurosci, 10*(2), 420-435.

Treves, A., Tashiro, A., Witter, M. P., & Moser, E. I. (2008). What is the mammalian dentate gyrus good for? *Neuroscience, 154*(4), 1155-1172. doi:10.1016/j.neuroscience.2008.04.073

van Groen, T., van Haren, F. J., Witter, M. P., & Groenewegen, H. J. (1986). The organization of the reciprocal connections between the subiculum and the entorhinal cortex in the cat: I. A neuroanatomical tracing study. *Journal of Comparative Neurology, 250*(4), 485-497. doi:https://doi.org/10.1002/cne.902500407

van Strien, N. M., Cappaert, N. L., & Witter, M. P. (2009). The anatomy of memory: an interactive overview of the parahippocampal-hippocampal network. *Nat Rev Neurosci, 10*(4), 272-282. doi:10.1038/nrn2614

Vivar, C., Potter, M. C., Choi, J., Lee, J. Y., Stringer, T. P., Callaway, E. M., . . . van Praag, H. (2012). Monosynaptic inputs to new neurons in the dentate gyrus. *Nat Commun, 3*, 1107. doi:10.1038/ncomms2101

Voogd, J., & Glickstein, M. (1998). The anatomy of the cerebellum. *Trends in Neurosciences, 21*(9), 370-375. doi:https://doi.org/10.1016/S0166-2236(98)01318-6

Vyleta, N. P., Borges-Merjane, C., & Jonas, P. (2016). Plasticity-dependent, full detonation at hippocampal mossy fiber-CA3 pyramidal neuron synapses. *Elife, 5*. doi:10.7554/eLife.17977

Wang, C., Chen, X., & Knierim, J. J. (2020). Egocentric and allocentric representations of space in the rodent brain. *Current Opinion in Neurobiology, 60*, 12-20. doi:https://doi.org/10.1016/j.conb.2019.11.005

Williams, P. A., Larimer, P., Gao, Y., & Strowbridge, B. W. (2007). Semilunar granule cells: glutamatergic neurons in the rat dentate gyrus with axon collaterals in the inner molecular layer. *J Neurosci, 27*(50), 13756-13761. doi:10.1523/jneurosci.4053-07.2007

Witter, M. P. (2006). Connections of the subiculum of the rat: topography in relation to columnar and laminar organization. *Behav Brain Res, 174*(2), 251-264. doi:10.1016/j.bbr.2006.06.022

Witter, M. P., & Amaral, D. G. (1991). Entorhinal cortex of the monkey: V. Projections to the dentate gyrus, hippocampus, and subicular complex. *J Comp Neurol, 307*(3), 437-459. doi:10.1002/cne.903070308

Witter, M. P., Griffioen, A. W., Jorritsma-Byham, B., & Krijnen, J. L. M. (1988). Entorhinal projections to the hippocampal CA1 region in the rat: An

underestimated pathway. *Neuroscience Letters, 85*(2), 193-198. doi:https://doi.org/10.1016/0304-3940(88)90350-3

Witter, M. P., & Groenewegen, H. J. (1990). The subiculum: cytoarchitectonically a simple structure, but hodologically complex. *Prog Brain Res, 83*, 47-58. doi:10.1016/s0079-6123(08)61240-6

Witter, M. P., Kleven, H., & Kobro Flatmoen, A. (2017). Comparative Contemplations on the Hippocampus. *Brain Behav Evol, 90*(1), 15-24. doi:10.1159/000475703

Witter, M. P., Ostendorf, R. H., & Groenewegen, H. J. (1990). Heterogeneity in the Dorsal Subiculum of the Rat. Distinct Neuronal Zones Project to Different Cortical and Subcortical Targets. *Eur J Neurosci, 2*(8), 718-725. doi:10.1111/j.1460-9568.1990.tb00462.x

Witter, M. P., Van Hoesen, G. W., & Amaral, D. G. (1989). Topographical organization of the entorhinal projection to the dentate gyrus of the monkey. *J Neurosci, 9*(1), 216-228. doi:10.1523/jneurosci.09-01-00216.1989

Witter, M. P., Wouterlood, F. G., Naber, P. A., & Van Haeften, T. (2000). Anatomical organization of the parahippocampal-hippocampal network. *Ann N Y Acad Sci, 911*, 1-24. doi:10.1111/j.1749-6632.2000.tb06716.x

Yeckel, M. F., & Berger, T. W. (1990). Feedforward excitation of the hippocampus by afferents from the entorhinal cortex: redefinition of the role of the trisynaptic pathway. *Proc Natl Acad Sci U S A, 87*(15), 5832-5836. doi:10.1073/pnas.87.15.5832

Yeh, C. Y., Asrican, B., Moss, J., Quintanilla, L. J., He, T., Mao, X., . . . Song, J. (2018). Mossy Cells Control Adult Neural Stem Cell Quiescence and Maintenance through a Dynamic Balance between Direct and Indirect Pathways. *Neuron, 99*(3), 493-510.e494. doi:10.1016/j.neuron.2018.07.010

Zimmer, J. (1971). Ipsilateral afferents to the commissural zone of the fascia dentata, demonstrated in decommissurated rats by silver impregnation. *J Comp Neurol, 142*(4), 393-416. doi:10.1002/cne.901420402

Zimmer, J., & Haug, F. M. (1978). Laminar differentiation of the hippocampus, fascia dentata and subiculum in developing rats, observed with the Timm sulphide silver method. *J Comp Neurol, 179*(3), 581-617. doi:10.1002/cne.901790309

APPENDIX (PAPER 1-4)

PAPER 1

Observations on Hippocampal Mossy Cells in Mink (*Neovison vison*) with Special Reference to Dendrites Ascending to the Granular and Molecular Layers

Jan Sigurd Blackstad,[1] Kirsten K. Osen,[1] Helen E. Scharfman,[2] Jon Storm-Mathisen,[1] Theodor W. Blackstad,[3†] and Trygve B. Leergaard[1]*

ABSTRACT: Detailed knowledge about the neural circuitry connecting the hippocampus and entorhinal cortex is necessary to understand how this system contributes to spatial navigation and episodic memory. The two principal cell types of the dentate gyrus, mossy cells and granule cells, are interconnected in a positive feedback loop, by which mossy cells can influence information passing from the entorhinal cortex via granule cells to hippocampal pyramidal cells. Mossy cells, like CA3 pyramidal cells, are characterized by thorny excrescences on their proximal dendrites, postsynaptic to giant terminals of granule cell axons. In addition to disynaptic input from the entorhinal cortex and perforant path via granule cells, mossy cells may also receive monosynaptic input from the perforant path via special dendrites ascending to the molecular layer. We here report qualitative and quantitative descriptions of Golgi-stained hippocampal mossy cells in mink, based on light microscopic observations and three-dimensional reconstructions. The main focus is on the location, branching pattern, and length of dendrites, particularly those ascending to the granular and molecular layers. In mink, the latter dendrites are more numerous than in rat, but fewer than in primates. They form on average 12% (and up to 29%) of the total dendritic length, and appear to cover the terminal fields of both the lateral and medial perforant paths. In further contrast to rat, the main mossy cell dendrites in mink branch more extensively with distal dendrites encroaching upon the CA3 field. The dendritic arbors extend both along and across the septotemporal axis of the dentate gyrus, not conforming to the lamellar pattern of the hippocampus. The findings suggest that the afferent input to the mossy cells becomes more complex in species closer to primates. © 2015 Wiley Periodicals, Inc.

KEY WORDS: hippocampus; Golgi stain; mossy cell; dendrites; dentate gyrus; hilus; fascia dentata

[1] Department of Molecular Medicine, Institute of Basic Medical Sciences, University of Oslo, Oslo, Norway; [2] Center for Dementia Research, The Nathan Kline Institute for Psychiatric Research, Orangeburg New York and Departments of Psychiatry, Physiology & Neuroscience, New York University Langone Medical Center, New York, New York; [3] Department of Anatomy, Institute of Basic Medical Sciences, University of Oslo, Oslo, Norway

INTRODUCTION

The hippocampal mossy cells, first named so by Amaral (1978), are thought to be a key element in hippocampal function (Buckmaster and Schwartzkroin, 1994; Henze and Buzsáki, 2007; Scharfman and Myers, 2012; Jinde et al., 2013). In all mammals that have been examined, including humans, mossy cells constitute a major component of the neurons located in the polymorph layer (also referred to as the hilus, or Z zone as used by Blackstad, 1963) of the dentate gyrus (Amaral, 1978; Ribak et al., 1985; Frotscher et al., 1991; Seress and Mrzljak, 1992; Amaral et al., 2007). It is well established that perforant path projections from the entorhinal cortex terminate on granule cells in the dentate gyrus, and that these project to CA3 pyramidal cells, which in turn project back to the entorhinal cortex via CA1 pyramidal cells. The mossy cells of the dentate gyrus receive disynaptic input from the entorhinal cortex via collaterals from dentate granule cell axons (Ramón y Cajal, 1911/1955; Blackstad et al., 1970; Claiborne et al., 1986). Besides contacting local interneurons (Scharfman and Schwartzkroin, 1988; Sloviter, 1994; Scharfman, 1995; Zappone and Sloviter, 2004; Larimer and Strowbridge, 2008; Scharfman and Myers, 2012), the mossy cells project back to the granule cells at other septotemporal levels both ipsilaterally and contralaterally (Zimmer, 1971; Swanson et al., 1978; Laurberg and Sørensen, 1981; Ribak et al., 1985; Scharfman, 1999; Scharfman and Myers, 2012). It is suggested that through this circuitry the mossy cells modulate the stream of information passing from the entorhinal cortex via the granule cells to the hippocampus proper, and thus contribute to spatial navigation, memory, or other functions of this network (Buckmaster and Schwartzkroin, 1994; Lisman, 1999; Henze and Buzsáki, 2007; Myers and Scharfman, 2009; Scharfman and Myers, 2012; Jinde et al., 2013).

A less emphasized, but conspicuous feature of hippocampal mossy cells is the additional monosynaptic input from the perforant path to dendrites ascending to the granular and molecular layers. Such dendrites are reported occasionally in rodents (rat: Amaral, 1978; Scharfman, 1991; Scharfman and Myers, 2012; Buckmaster, 2012; guinea pig: Blackstad, 1985) and

Origin of the Reconstructed and Measured Mossy Cells and Dendrites

Animal ID	Animal 84	Animal 85	Animal 87	Animal 88
Sex	Male	Male	Male	Female
Body weight	~2 kg	~2 kg	~2 kg	~1 kg
Age	6 months	6 months	6 months	6 months
Mean section thickness	100 µm	120 µm	190 µm	114 µm
Number of consecutive sections used for reconstruction	18	6	1	10
Section stack thickness	1,800 µm	720 µm		1,140 µm
Number of elements studied	12 cells	2 cells	34 gm-dendrites	3 cells
Nick names of cells	mc#1-12	mc#13-14		mc#15-17

routinely in primates including humans (monkey: Buckmaster and Amaral, 2001; human: Frotscher et al., 1991; Seress and Mrzljak, 1992). In hippocampal slices of rat, evidence of both a disynaptic and monosynaptic excitation of mossy cells by stimulation of perforant path fibers has been described (Scharfman, 1991; Buckmaster and Schwartzkroin, 1994). The dentate gyrus is the part of the hippocampus that shows the largest differences across species (Seress, 2007). To advance our understanding of the functional role of the hippocampal circuitry, detailed characterization of mossy cells and their dendrites in the granular and molecular layers are needed from additional species. The American mink (Neovison vison) is a carnivore with a larger and more complex gyrencephalic brain, relative to the lissencephalic rodents. It shares a later common ancestor with primates and has a relatively high learning capacity (Doty et al., 1967), and is more interesting than rat for studies of complex behavior (e.g., Malmkvist et al., 2012; Svendsen et al., 2012; Brandt et al., 2013). But so far little is known about the anatomy of the mink hippocampus (Gościcka et al., 1993; Malmkvist et al., 2012).

Theodor W. Blackstad (TWB), a pioneer in hippocampal anatomical research with profound interest in comparative studies across species, observed in the 1980s that, in mink, the mossy cells extend dendrites into the granular and molecular layers more frequently than apparent in published reports at that time about other mammals. TWB worked for several years on a computer-aided quantitative study of Golgi-impregnated mossy cells in mink. Many years after his death we, his grandson and near colleagues, have completed this work. We here present a detailed qualitative and quantitative characterization of hippocampal mossy cells in mink with material preserved from TWB's laboratory, with particular emphasis on dendrites of mossy cells extending into the granular and molecular layers.

MATERIALS AND METHODS

Material

The brains of nine healthy young adult mink (Neovison vison), 6-month old, weight ~2 kg (males) and 1 kg (females)

were used (Table 1). The animals were obtained from and euthanized at the experimental breeding facility (at Dal, Asker, Norway) of the Norwegian Veterinary College. The animals had been selected by the staff for other purposes, and were euthanized according to standard procedures employed in fur industry in the 1980s: In brief, unconsciousness was produced with an electrical shock, the neck was broken, and the animal exsanguinated. The brain was removed within 0.5–2 h and immersion-fixed (see below). To facilitate access of the fixative to the hippocampal region, some brain tissue around the hippocampus was removed. Five brains were used for Golgi impregnation, and four brains for Timm-thionin staining. Additional documentation about the general morphology of the mink hippocampus was derived from Gościcka et al. (1993), and the public comparative mammalian brain collection (http://brainmuseum.org/).

Histological Processing and Staining

The brains destined for Timm-thionin staining were fixed in 3% glutaraldehyde, 30% sucrose, and 0.3–0.4% Na_2S in 0.15M phosphate buffer at pH 7.4 for 24 h, transferred to 30% sucrose in 0.1M phosphate buffer at pH 7.4 for 28 h, and then frozen. Cryostat sections (40 µm thick) were made and subjected to Timm staining (Haug, 1973; Zimmer and Haug, 1978). The sections were counterstained with thionin to visualize cell bodies.

Brains for Golgi impregnation (three males, animals 84, 85, 87; one female, animal 88; Table 1) were fixed at room temperature, in 3% paraformaldehyde, 1.25% glutaraldehyde, and 1% sucrose in 0.1M phosphate buffer at pH 7.4. After 3 weeks in the fixative, the brains were trimmed again to further facilitate penetration of liquids. In some brains, the entire (banana-shaped) hippocampus was isolated. The left hippocampus of animal 88 was embedded in one piece, while the others were cut across their longitudinal (septotemporal) axis into 2 to 3 mm thick blocks. Other blocks were cut from whole hemispheres or parts of hemispheres, in various, selected planes. The location of the blocks along the septotemporal axis was determined post hoc by evaluation of the shape of the dentate gyrus and its surroundings.

Chromation was done in 2.4% potassium dichromate with 0.2% osmium tetroxide for 2 days, and 3.0% potassium dichromate for a further few days. Following silver impregnation in 0.75% silver nitrate for 2 days, blocks were taken through a series of ascending ethanol concentrations (1 day) followed by propylene oxide and a propylene oxide-epoxy resin (Araldite) mixture and pure Araldite (1 day), similar to processing for electron microscopy. The next step was polymerization. Dehydration liquids were saturated with silver chromate to prevent precipitated silver chromate (i.e., Golgi impregnation) in fine structures to be washed out. Blocks were covered in a thin shell of agar before silver impregnation to reduce unwanted precipitates on the surface. The agar was removed after the silver impregnation since it impedes penetration of epoxy resin.

Polymerized Golgi blocks were sectioned with a steel knife on a sledge microtome with electronically regulated heating elements in the knife holder, keeping the knife at a temperature of about 70°C. At this temperature, the knife cut compression-free serial sections from hard epoxy resin blocks. Serial sections cut at 100–190 μm were mounted on slides under a coverslip, in unpolymerized resin used for embedding. The slides were then covered with heavy weights to secure flattened sections, and cured at about 60°C.

Microscopy and 3D Reconstruction

Golgi-stained sections were inspected and measured using a Leitz Ortholux microscope equipped with a Leitz drawing tube and a 1–3.2× Leitz Variomat zooming device, using (1) an oil immersion objective with 650 μm working distance (Leitz KS 100×, NA 1.32), (2) a dry objective with working distance of 1,000 μm (Leitz KS 53×, NA 0.95), and (3) a water immersion objective with a working distance of 1.8 mm (Zeiss Ortholplan 40×, NA 0.75). Camera lucida drawings of Golgi-impregnated cells, laminar borders, and fiducial points were made on moisture resistant paper at a magnification of 580× in most cases or 1,524× in rare instances. Drawings of consecutive sections were manually aligned, joining upper and lower ends of cut dendrites at section surfaces, a process much facilitated by the embedding and sectioning procedures. The x and y coordinates of regularly spaced points along mossy cell dendrites were collected from the drawings using a digitizing table (Calcomp 9680) and a custom software tool MicroTrace (Leergaard and Bjaalie, 1995). The z coordinates of the points were read from an enlarged dial on the fine focus knob of the microscope, registered on the drawings, and entered interactively during digitization. Cells located within the same resin block were recorded in the same coordinate system. Z values were corrected for the effects of the difference in refractive indexes of the embedding and immersion media. For resin embedded tissue studied with a 40× water immersion lens an empirically determined factor of 1.167 (Blackstad et al., 1984) was used. This correction was also applied for measurements of section thickness.

Several unpublished custom software tools (developed by TWB) were used for editing of spatial coordinate values and calculation of segment lengths, numbers, and topological order. Three-dimensional (3D) reconstructions were viewed using custom software running on Silicon Graphics Indigo computers, exploiting OpenGL graphic library for rotation, scaling, translation, coloring, and control of vector appearance. Stereoscopic image pairs were generated by applying ~8 degree rotation along one axis. High-resolution digital images of histological sections were acquired using an automated slide scanner system (Axio Scan Z1, Carl Zeiss MicroImaging, Jena, Germany). Images were captured at multiple focal depths, and merged using the extended focus depth tools provided in the Zen Blue software from Carl Zeiss.

Morphological Measurements and Statistical Analyses

Seventeen Golgi-stained mossy cells (Table 2) were selected by TWB and reconstructed from up to 1,800 μm thick stacks of consecutive sections cut from three tissue blocks, one block from each of three animals (Table 1). The cells were sampled from sections cut transverse to the septotemporal axis of the dentate gyrus. Sections were taken from caudal (animal 88) and progressively more rostral locations (animals 85 and 84) in the temporal limb of the left dentate gyrus (Fig. 1). In addition, a group of 34 mossy cell dendrites extending into the granular and molecular layers (in the following referred to as gm-dendrites) was reconstructed from a single 190 μm thick section (also cut transverse to the septotemporal axis of the dentate gyrus) from animal 87 (Table 1). Of these, 21 could be traced microscopically to characteristic main mossy cell dendrites in the polymorph layer within the same section, and were used for quantitative analysis.

Morphological measurements, including total dendritic lengths, were derived from 3D reconstructions of camera lucida drawings. The length of gm-dendrites were in part estimated on the basis of additional manual measurements derived from two-dimensional (2D) camera lucida drawings. These measurements were confirmed in digital section images. For 12 of the cells, two-dimensional dendritic diagrams (Claiborne et al., 1990) were generated, providing linear representations of single stem dendrites from the cell body through branch points to the observed end points, with "straightened" individual dendritic segment lengths, i.e., distance between branch points, measured in 3D space along the dendrite. Descriptive statistical measures were generated using Microsoft Excel. Measurements are reported as mean values with standard deviation (SD). No corrections were made for possible shrinkage of tissue.

Nomenclature

The hippocampal region is anatomically complex, and variable use of terminology and boundary definitions poses researchers with additional challenges. We have adopted the nomenclature of the Terminologia Anatomica (Federative Committee on Anatomical Terminology, 1998) for the dentate

Measurements of the 17 Golgi-stained Mossy Cells

Cell names	Start point #	Branch point #	End point #	Segm. #	Mean segm. length (µm)	Total dendr. length (µm)	Gm-dendr. #	Summed length gm-dendr. (µm)	Summed gm-dendr. length/total dendr. length (%)
mc #1	4	41	45	86	86	7,917	0	0	0
mc #2	7	60	67	127	97	12,349	2	771	6
mc #3	3	26	29	55	104	5,765	1	250	4
mc #4	3	28	31	59	78	4,403	3	1,153	26
mc #5	3	21	24	45	134	5,353	3	1,217	23
mc #6	2	36	38	74	100	7,236	0	0	0
mc #7	6	44	50	94	103	9,684	5	2,767	29
mc #8	5	36	41	77	107	8,218	4	1,775	22
mc #9	9	61	70	131	102	9,700	1	339	3
mc #10	7	30	37	67	130	7,144	2	946	13
mc #11	7	47	54	101	110	10,933	3	735	7
mc #12	6	41	47	88	123	10,189	2	624	6
mc #13	5	64	69	133	118	15,192	5	1,881	12
mc #14	3	49	52	101	107	10,622	5	2,013	19
mc #15	4	44	48	92	139	12,758	8	3,379	26
mc #16	4	22	26	48	116	5,603	2	761	14
mc #17	4	35	39	74	117	8,687	1	167	2
Mean	**4.8**	**40.3**	**44.5**	**85.3**	**110.1**	**8,926.6**	**2.8**	**1,104.5**	**12**
SD	1.9	13.1	14.5	27.4	16.1	2,928.3	2.1	971.1	10

gyrus, which is in agreement with Amaral et al. (2007). Also, in accordance with Terminologia Anatomica, we use the term "granular layer" for the layer of granule cell somata, rather than "granule cell layer" which logically would include also the granule cell dendrites, but these dendrites are located in the molecular layer. In contrast to Terminologia Anatomica, we use the term CA3 to include the end portion of the hippocampus proper, instead of the term CA4, which is ill defined with respect to the polymorph layer of the dentate gyrus (Cappaert et al., 2014).

RESULTS

The mink dentate gyrus shares its basic morphology with other mammals, but with some specific traits that to our knowledge have not been described earlier. Therefore, before presenting the mossy cells, we give a brief orientation of the mink hippocampus, with a comparative perspective and focus on the dentate gyrus.

Main Features of the Mink Dentate Gyrus

The mink hippocampus has a c-shaped longitudinal (septo-temporal) axis (Gościcka et al., 1993) (Fig. 1A), and therefore occurs twice in frontal sections at certain rostrocaudal levels (Fig. 1B). The septal (dorsal) limb forms a caudally convex curvature extending from near the midline dorsally toward the

incipient temporal lobe ventrolaterally. The slightly longer and straighter temporal (ventral) limb (Fig. 1C), from where our cells are sampled, extends rostrally, medially, and ventrally. The dentate gyrus caps the end of CA3. It is curved both along its septotemporal and transverse axis and is located medially in the hippocampus with its concavity toward the fimbria (Figs. 1C,D,F). In sections cut transverse to the septotemporal axis, instead of forming a simple V-shape septally, and a U-shape temporally, as seen in rat (Scharfman and Witter, 2007; Kjonigsen et al., 2015), the mink dentate gyrus at all septotemporal levels forms two crests (one hidden and one exposed), and three blades, here defined as the hidden blade (corresponding to the suprapyramidal blade of rat), the middle blade, and the exposed blade (corresponding to the infrapyramidal blade of rat) (Figs. 1D,F). The crests are about 2 mm apart. Only the exposed blade is exposed to the (medial) surface of the hemisphere, the others line the obliterated hippocampal fissure.

The mammalian dentate gyrus is a three-layered cortex which besides other types of neurons contains two types of interconnected, excitatory glutamatergic projection neurons, granule cells and mossy cells (Amaral and Lavenex, 2006). The granule cell somata are densely packed in the granular layer while the unipolar dendritic trees permeate the molecular layer (Figs. 1D, 5, and 7B). The mossy cells with their somata and main dendrites occupy the polymorph layer (Figs. 2B and 4). In Golgi impregnated sections from mink, cut transverse to the septotemporal axis, the granular layer is roughly 100-µm thick and the molecular layer about 270 µm thick (Fig. 1D). The two layers together are sometimes referred as fascia dentata
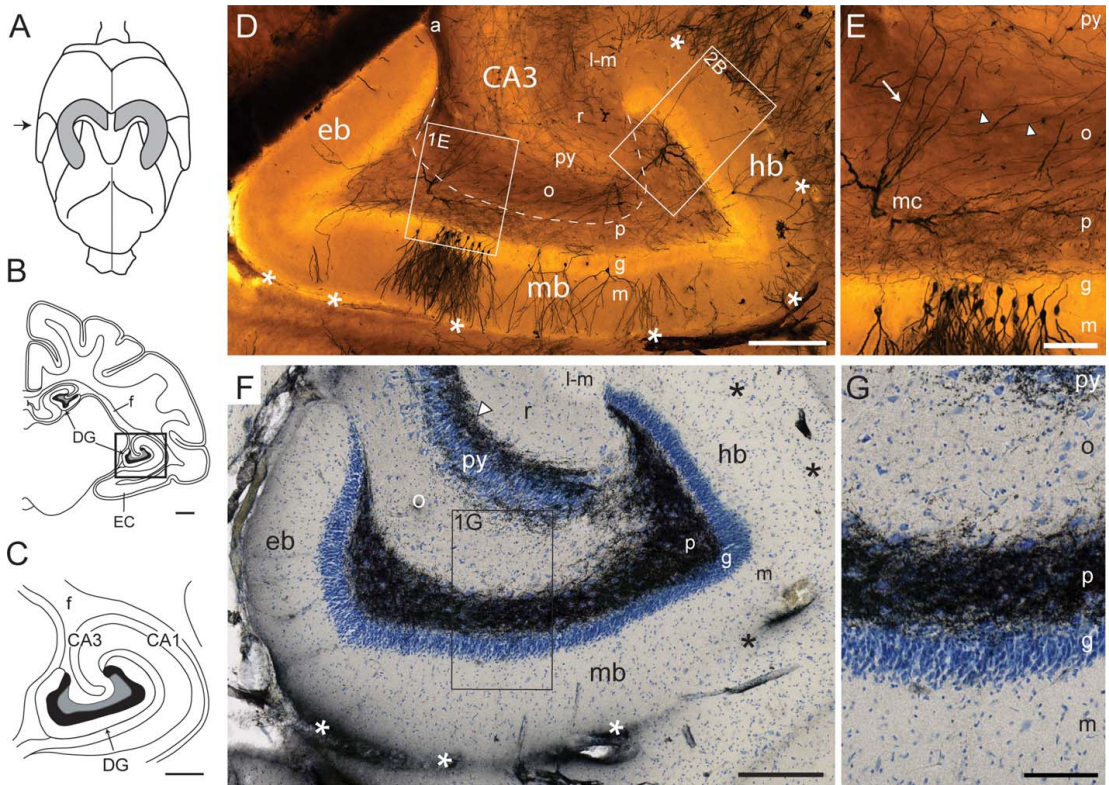
FIGURE 1. **Gross anatomy of the mink hippocampus. (A–C)** **Illustration of mink brain redrawn from photographs (www.brain-museum.org, Neovison vison, #58-324): (A) The whole brain seen from above with the outlines of the hippocampus (in grey, derived from Gościcka et al., 1993) superimposed. (B) A frontal section (approximate position indicated with arrow in A), with the septal and temporal limbs of the hippocampus interconnected by the fimbria (f). (C) Higher magnification of the boxed area in B with the hippocampal region. (D–G) Microphotographs of the temporal limb of the hippocampus with the dentate gyrus cut transverse to its septotemporal axis from levels approximately corresponding to B and C. (D,E) Golgi impregnation. (D) Border of polymorph layer (p) with CA3 is marked by stippled line. (E) Higher magnification of boxed area (E) in (D), shows the plexus of mossy fiber collaterals** in the polymorph layer versus the parallel mossy fibers (arrowheads) in the oriens layer. Mossy cell dendrites crossing the border are indicated by arrow. (F,G) Timm-thionin stain. Mossy fiber bundle marked by arrowhead. (G) Higher magnification of boxed area in (F). The boxed area marked "2B" in (D) is shown at higher magnification in Figure 2B. Fissura hippocampi is indicated by asterisks. Abbr.: a, alveus; CA1, cornu ammonis area 1; CA3, cornu ammonis area 3; DG, dentate gyrus; eb, exposed blade; EC, entorhinal cortex; f, fimbria; g, granular layer; hb, hidden blade; l-m, lacunar-molecular layer; m, molecular layer; mb, middle blade; mc, mossy cell; o, oriens layer; p, polymorph layer; py, pyramidal layer; r, radiate layer. Calibration bars: B, 1 mm; C, 500 μm; D & F, 250 μm; E & G, 100 μm.

(Blackstad, 1956, 1958). Microscopic examination of mink granule cells reveals that the thickness and spine density of dendrites vary between cells (Figs. 5 and 7B). The thin granule cell axon (mossy fiber), extends from the cell body to the mossy fiber bundle in CA3 (Figs. 1F and 9). Within the polymorph layer, the axon is seen to give off collaterals (Fig. 2A), which feature large terminals (Figs. 7A,B), somewhat smaller than those of the parent fiber (Fig. 2A). These collaterals form a dense plexus throughout the polymorph layer (Figs. 1D,E), as also observed in other species (Blackstad, 1963, his Figs. 12B and 17C; Claiborne et al., 1986), and used here to define

the dentate gyrus/CA3 borderline. The terminals are rich in zinc, and thus responsible for the dense, black staining of the polymorph layer and mossy fiber bundle observed in Timm-thionin sections (Figs. 1F,G; see, also Blackstad, 1963, 1985; Haug, 1967, 1974; Wenzel et al., 1997; Blaabjerg and Zimmer, 2007). In Golgi-impregnated sections, the density and extent of the plexus depends on the number of impregnated granule cells (Figs. 1D,E and 7A,B).

In mink, the polymorph layer is slimmer and more concave than in rat. At the center of the middle blade, it is only about 100- to 150-μm thick, i.e., only slightly thicker than the
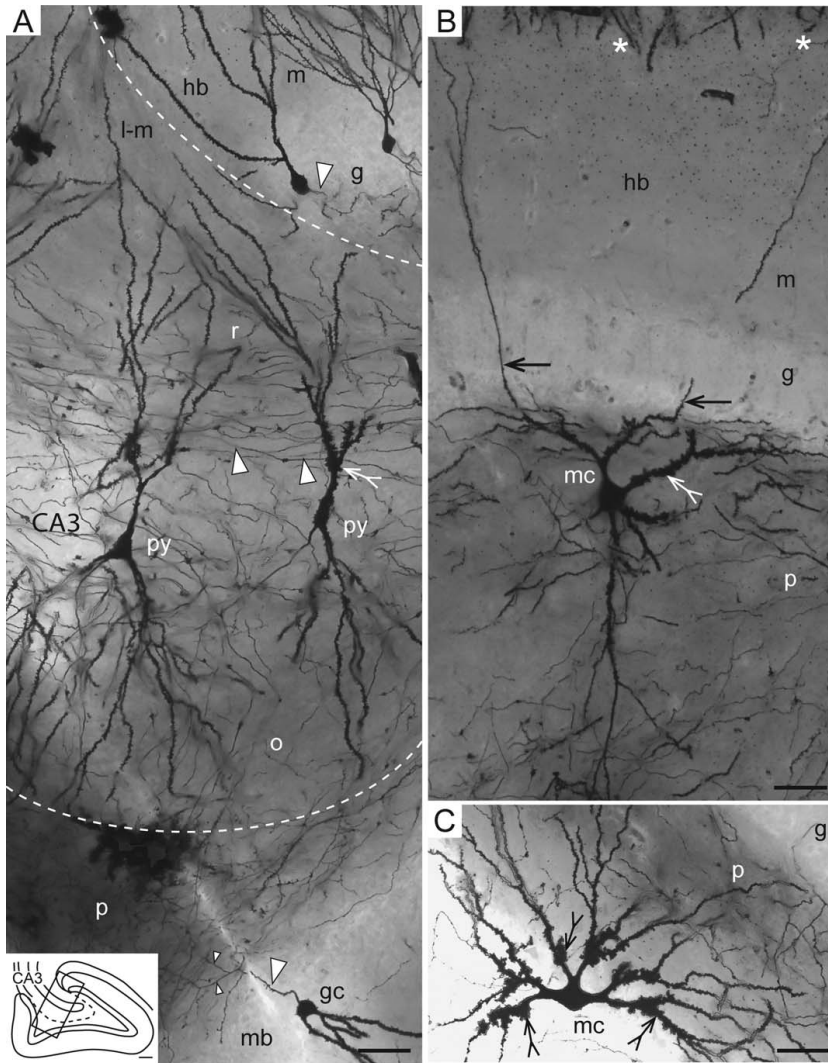
FIGURE 2. Comparison of mossy cells and CA3 pyramidal cells. Photomicrographs of Golgi sections, (A) two pyramidal cells (py) in CA3 near its end (see, inset), and granule cells (gc) in the hidden (hb) and middle blades (mb) of the dentate gyrus. (B) Higher magnification of boxed area 2B in Figure 1D. Mossy cell mc#13 with two gm-dendrites (arrows) in this section (same cell as in Fig. 3A). (C) A mossy cell from animal 84 (not in the sample used for quantitative analysis). Both mossy cells are from the hidden blade of the dentate gyrus. Excrescences are marked by tailed arrows, mossy fibers by large arrowheads, mossy fiber collaterals by small arrowheads, and the hippocampal fissure by asterisks. Stippled lines indicate border of CA3. Abbr.: g, granular layer; gc, granule cell; hb, hidden blade; l-m, lacunar-molecular layer; m, molecular layer; mb, middle blade; o, oriens layer; p, polymorph layer; py, pyramidal cell; r, radiate layer. Calibration bars: A–C, 50 μm.

granular layer (Figs. 1D–G). Although a subgranular germinal matrix has been identified also in mink (Malmkvist et al., 2012), there is no consistent Timm-negative "subgranular zone" immediately beneath the granular layer (Figs. 1F,G) as described, e.g., in guinea pig (Blackstad, 1963, his Fig. 12C).

As in rat, but in contrast to many other species including primates (Amaral et al., 2007), CA3 in mink remains stratified with a distinct pyramidal layer until its end. Because in mink, the tip of the CA3 pyramidal layer bends toward the hidden blade, the cell- and zinc-poor oriens layer becomes situated adjacent to the

cell- and zinc-rich polymorph layer, with a sharp borderline (Figs. 1F,G). In Golgi sections, the border between the polymorph layer and CA3 is also demarcated by the fading root of the alveus (Fig. 1D), through which fibers pass to and from the fimbria. The basal dendrites of CA3 pyramidal cells do not seem to extend beyond the oriens layer and alveus (Figs. 2A and 9). The apical dendrites of the pyramidal cells also avoid the polymorph layer, but achieve this by bending around the tip of the granular and molecular layers of the dentate gyrus, on their way to the lacunar-molecular layer of CA3, as also observed in rat (Amaral, 1978; Buckmaster et al., 1993). The transition between the CA3 and the polymorph layer in mink seems indistinct only at the tip of the pyramidal layer (Fig. 1F), where some modified cell forms occur, as also described in rat (Amaral, 1978; Scharfman, 1993). We have not reconstructed or measured pyramidal cells, but their main features are shown in Figure 2A.

Mossy Cells

Because of certain structural similarities with CA3 pyramidal cells, the mossy cells were originally classified as "modified pyramids" (Lorente de Nó, 1934; Blackstad et al., 1970). As later research has shown, mossy cells and CA3 pyramidal cells are distinct cell types (Amaral, 1978; Buckmaster et al., 1993; Seress, 2007) although they share some conspicuous structural features, notably the thorny excrescences which are postsynaptic to the large mossy fiber terminals. In Golgi impregnated sections, the mossy cells in mink are readily identified by their relatively large soma and their thick proximal dendrites covered with thorny excrescences, with both soma and excrescences slightly larger than those of CA3 pyramidal cells (Figs. 2A–C). There may be some smaller mossy cells without exuberant excrescences (see Scharfman and Myers, 2012 for discussion), but for the purposes of this study, mossy cells were defined by anatomical criteria that could be determined by Golgi staining, which included excrescences. Interneurons (here defined by their lack of excrescences) are scattered between the mossy cells, some with spiny, others with aspiny dendrites (Amaral, 1978; Freund and Buzsáki, 1996; Houser, 2007). We have inspected a large number of Golgi impregnated mossy cells in mink, but the quantitative data are based on the 17 cells sampled by TWB and measured using camera lucida drawings, and computerized 3D reconstructions.

Mossy Cell Somata with Primary Dendrites

Both bi- and multipolar mossy cell somata were observed, depending on the number of primary dendrites (Figs. 3 and 4), which in our sample ($n = 17$) varies between 2 and 9 per cell (average 4.8, SD 1.9; Table 2). The somata appear to be of the same size or possibly slightly larger than in CA3 pyramidal cells (Fig. 2). Nearly all somata observed (∼250) had smooth surfaces (Fig. 2C), but for occasional irregularities (Fig. 3C). The primary dendrites have a broad tapering base that makes it difficult to set a border between soma and dendrite. The initial part of primary dendrites also has a smooth surface, before the characteristic excrescences occur (see below).

Dendritic Arbors

Complete or nearly complete mossy cell dendritic arbors were reconstructed from several consecutive sections about 100 to 120 μm thick from the temporal limb of the hippocampus in three animals. The mossy cells exhibit a space-filling type of arborization (Fiala and Harris, 1999), with the shapes of the somata and arbors varying with the number of primary dendrites, and the space available in the polymorph layer (Fig. 4). At the two crests, the mossy cell dendrites tend to radiate from the soma in all directions, the arbors filling the polymorph layer, and often extending throughout half of the hidden—exposed dimension of the dentate gyrus, i.e., up to about 1 mm in the transverse dimension (Fig. 4B). In the narrow portion of the polymorph layer at the middle of the dentate gyrus, however, the arbor appears as if it were flattened to fit between the granular layer and CA3 (Fig. 4A).

Upon reaching the deep border of the granular layer (the border with the polymorph layer), the mossy cell dendrites bend and run parallel to the border, indicating a barrier limiting entry of the main dendrites (Figs. 2B and 4), as also described in rat (Scharfman, 1991). It is from these dendrites that we frequently observe special, perpendicularly oriented branches extending into the granular and molecular layers. In the following, we will refer to the granular-molecular mossy cell dendrites as gm-dendrites. At the deep border of the polymorph layer (the border with CA3), on the other hand, the distal end of regular mossy cell dendrites often extend into CA3 (Figs. 1E, 4B, and 9). The excrescence covered proximal parts of the dendrites, however, are confined to the polymorph layer with its plexus of mossy fiber collaterals.

Arbors also extend for a considerable distance in the septo-temporal dimension. The arbor of the mossy cell shown in Figure 5 was measured in a single longitudinal section to extend septotemporally for about 900 μm, which is in accordance with data for cells reconstructed from a series of transverse sections. This explains the smaller and less dense appearance of arbors in images of single sections compared to reconstructions of the same arbors, based on several sections (Figs. 2B versus 3A).

Mossy cell dendrites in mink have brush-like arborizations with several generations of branch points close to the cell body, giving rise to long, undivided or sparsely branched distal dendrites (Figs. 2C, 3A,B, and 4A,B). The primary segments are short and the majority of branch points are located within about 200 μm from the cell body (Figs. 6A,B).

In our sample, the total dendritic length per mossy cell ranges from 4,403 to 15,192 μm ($n = 17$), with an average of 8,927 μm (SD 2,928; Table 2). This average may be an underestimate since at least in five of the 3D-reconstructed cells the shape of the impregnated soma indicated the existence of an unimpregnated dendritic stem. Incomplete impregnation of minor, distal dendrites cannot be excluded. In agreement with the presence of many miniature segments proximally at the base of the brush (Fig. 6B), the total dendritic length is more closely related to the number of branch points (Fig. 6D)
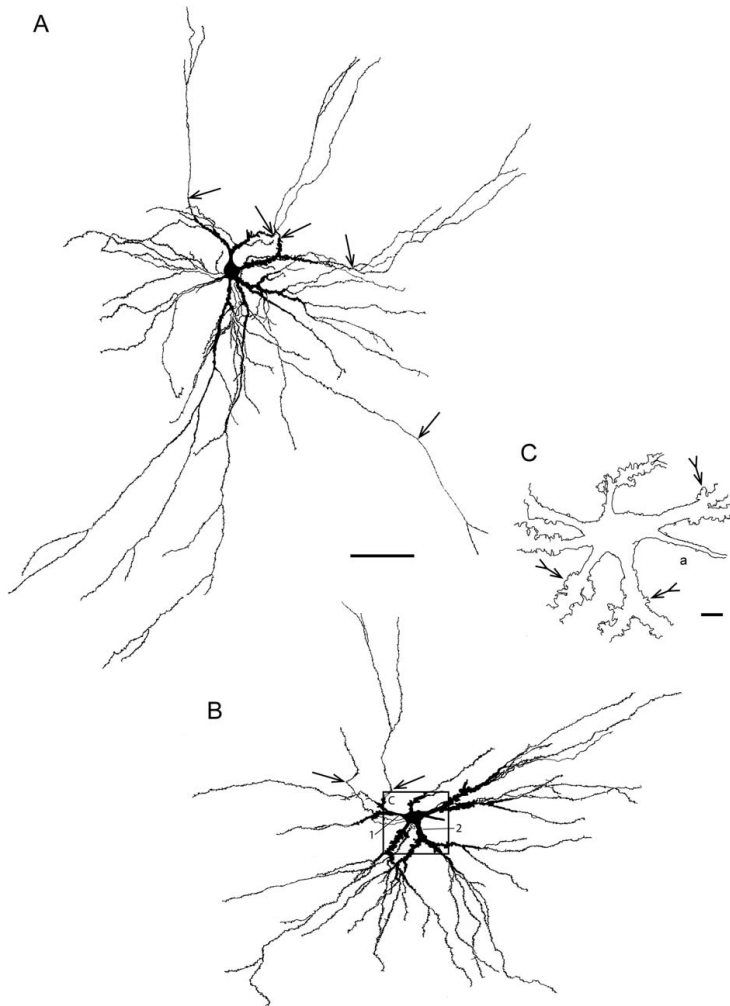
FIGURE 3.   Camera lucida drawings of complete mossy cell arbors. (A, B) Two mossy cell arbors drawn at 580× from several sections and projected onto a single plane, (A): mc #13 (same cell as shown in Fig. 2B). (B), mc #2 (caricatured in Fig. 9). The soma and proximal dendrites with excrescences are filled apart from a few dendrites that course perpendicular to the main plane of the drawing. The proximal dendrites are covered with coarse excres- cences which are replaced distally by regular spines. The gm- dendrites are marked by arrows. (C) Represents roughly the squared area in (B) drawn at higher magnification (1,524×). Excrescences are indicated by tailed arrows. Dendrites 1 and 2 in B are represented as stem dendritic diagrams in Figure 6B. Abbr.: a, axon. Calibration bars: A, 100 μm (also applies to B); C, 10 μm.

than to the mean segment length (Fig. 6C), which is remark- ably short (110 μm, SD 16, Table 2) in view of the long "brushes."

In our material, thorny excrescences occur on primary den- drites (Figs. 2B,C and 3) on average 18 μm ($n = 36$, SD 8) from the soma, and continue past two to five branch points (average 2.74, SD 1.27, $n = 36$; Fig. 6B), usually covering a branch point before they decrease in size and are replaced by regular spines on the distal dendrites, which are thinner and non-tapering (Figs. 2B,C and 3A,B). An exact border between the excrescence-covered and spine-covered portions was not set. We estimate that the excrescences typically extend about 110 μm from the soma, to a large extent including the parts of the dendrites with extensive branching (Fig. 6A,B). The width of the excrescences over the dendritic shaft is difficult to measure accurately due to the dense Golgi impregnation.
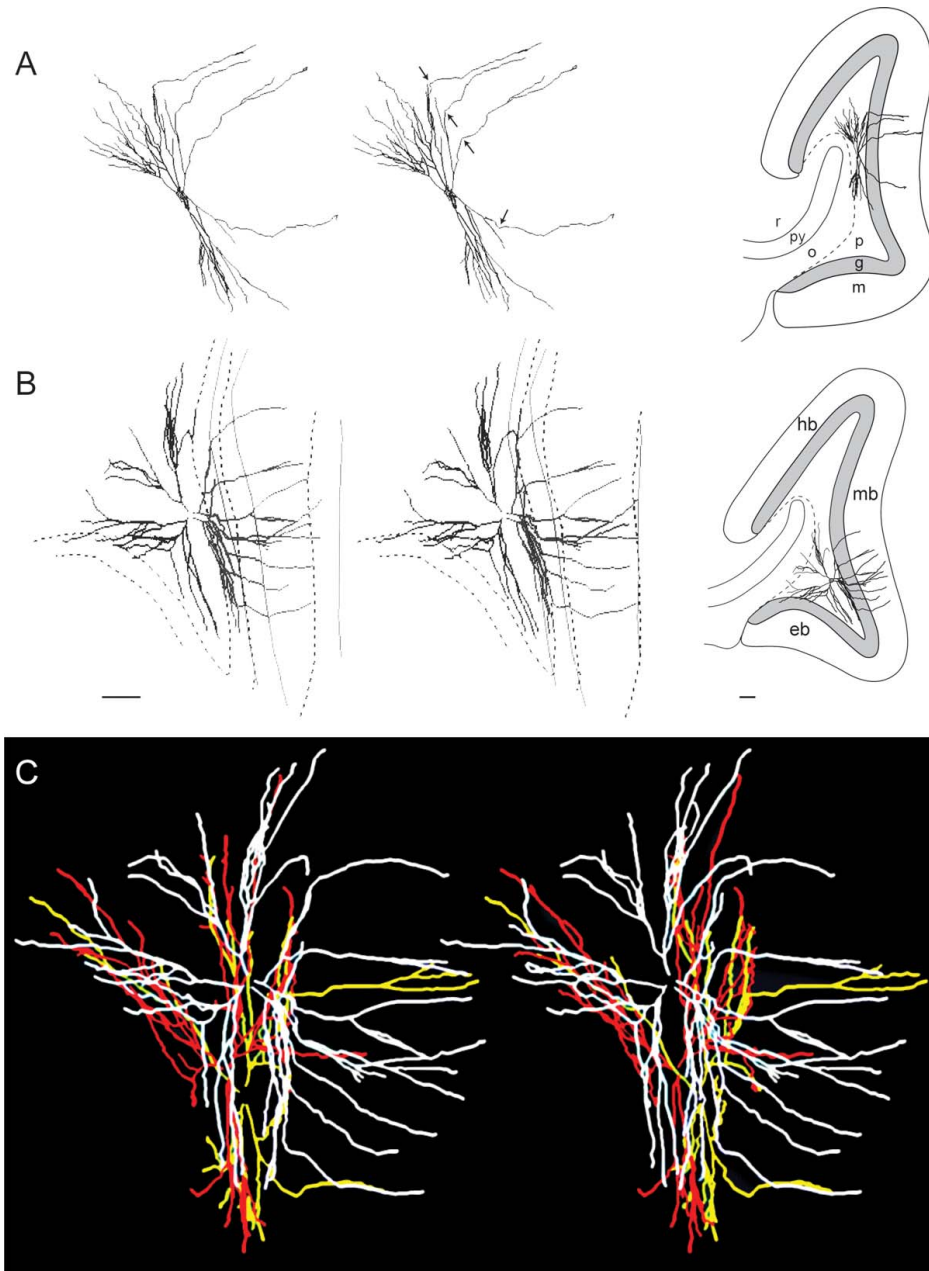
FIGURE 4. Shape and location of mossy cell arbors in stereo view. (A–C) Reconstructed dendritic arbors of four mossy cells shown as stereo pairs. (A) mc #8, (B) mc #15 (also shown in C), and (C): mc #15 (white), #16 (yellow) and #17 (red). Inset figures (right hand side) show the cells reconstructed in A and B projected onto a drawing of the dentate gyrus. In (A) the entrance of gm-dendrites into the granular layer is indicated by arrows, while in (B) both the inner and outer border of the granular layer and the hippocampal fissure are traced at two levels with the upper contours stippled. Borders in (B) also apply to (C). All four cells have gm-dendrites. Together the cells illustrate the space-filling type of arborization of the main dendrites within the polymorph layer. Abbr.: eb, exposed blade; g, granular layer; hb, hidden blade; m, molecular layer; mb, middle blade; o, oriens layer; p, polymorph layer; py, pyramidal layer; r, radiate layer. Calibration bars in B (100 μm) are valid also for A.
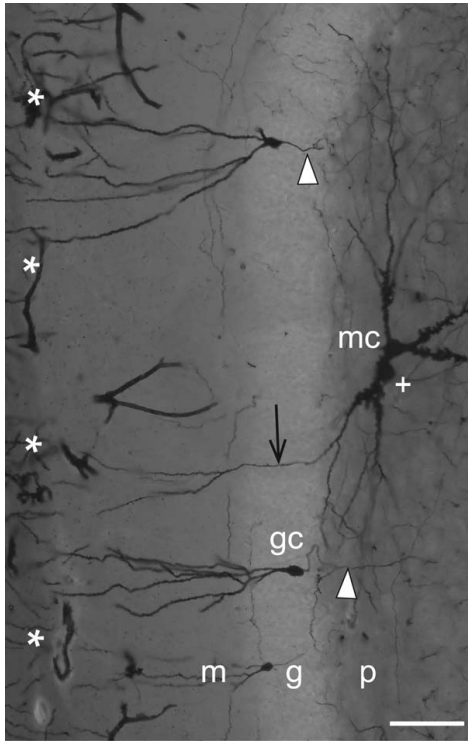
FIGURE 5.   Mossy cell in septotemporally cut section. Photomicrograph of a Golgi section cut parallel to the septotemporal axis of the dentate gyrus, with an impregnated mossy cell (mc) (not in the sample used for quantitative analysis) showing a gm-dendrite (arrow), and a few granule cells (gc) with axons (arrowheads). A dendrite oriented perpendicular to the plane of sectioning is marked by a plus symbol, the hippocampal fissure by asterisks. Abbr.: g, granular layer; gc, granule cell; m, molecular layer; mc, mossy cell; p, polymorph layer. Calibration bar, 100 μm.

Granular-Molecular Mossy Cell Dendrites (gm-Dendrites)

Fifteen of the 17 sampled mossy cells (88%) were found to have one or more gm-dendrites (Table 2). Typically a distal mossy cell dendrite courses in the polymorph layer close to the border with the granular layer, and upon reaching the border makes an abrupt, often Z-shaped turn, reducing its spine density, and penetrating the granular layer (*Figs*. 2B, 3A,B, 4, 5, and 7A), similar to the situation described in rats (Scharfman, 1991), guinea pig (Blackstad, 1985), and primates (Buckmaster and Amaral, 2001; Seress, 2007). The gm-dendrites are remarkably slim and straight, and are directed toward the hippocampal fissure. They typically ramify once or twice within the molecular layer. Some gm-dendrites appear to end within the granular or molecular layers (perhaps because of incomplete impregnation?), while others reach the hippocampal fissure.

Within the granular layer, the gm-dendrites may be devoid of spines for a shorter or longer distance (Fig. 7A). The spine density increases toward the molecular layer, but they remain thinner with less spine density than most granule cell dendrites. If viewed in isolation from their dendrites of origin, gm-dendrites may be difficult to distinguish from the thinner variety of granule cell dendrites (Fig. 7B). The number of gm-dendrites per mossy cell ($n = 17$ cells) in our sample ranges from 0 to 8, with an average of 2.8 gm-dendrites (SD 2.1) per cell (Table 2). The summed length of gm-dendrites per mossy cell ranges from 0 to 3,379 μm, on average 1,105 μm (SD 971) per cell (Table 2). The number and summed length of gm-dendrites per cell are strongly correlated (Fig. 8B), consistent with their uniform structure. The summed length of gm-dendrites per cell constitutes up to 29% of the total dendritic length, but the average is 12% (SD 10; Table 2).

The summed length of the part of the gm-dendrites within the molecular layer (molecular sectors) was measured in one cell (mc#15, Fig. 4B) with 8 gm-dendrites and found to be 2,569 μm, which is one fourth the summed length of the gm-dendrites (3,379 μm, Table 2) and 321 μm per gm-dendrite. This is consistent with measurements in 21 reconstructed gm-dendrites from a single 190 μm thick section (animal 87), where the mean summed length of the molecular sectors was found to be 373 μm. Because the molecular layer is only about 270-μm thick, the calculated mean lengths of the molecular sectors reflect branching, as also visualized in Figure 7C. In this figure, the 21 gm-dendrites are seen intermingled with 13 others which were excluded from the quantitation because, as apparent from the stereo image, their connection with the main mossy cell dendrites in the polymorph layer was not within the section.

Relationship of gm-Dendrite Number and Soma Location

Our cell sample represents all depths and the entire hidden-exposed axis of the polymorph layer (Fig. 8A). Cells feature gm-dendrites irrespective of the depth of their soma in the polymorph layer. The occurrence of gm-dendrites could, however, be influenced by the position of the soma along the hidden-exposed axis. In our sample, the only cells without gm-dendrites were located in the exposed crest and none of the sampled cells had dendrites in the exposed blade. We have observed other mossy cells with gm-dendrites in the exposed blade, but in a systematic registration of gm-dendrites in a series of 15 sections (about 120 μm thick) from animal 85, and 12 sections (about 190 μm thick) from animal 87, we found four times as many gm-dendrites both in the hidden and middle blade as in the exposed blade. The three cells in the exposed crest that are reconstructed together in Figure 4C all had dendrites in the middle blade, but none in the exposed blade. On the contrary, four of the five sampled cells in the hidden crest had gm-dendrites in both the hidden and the middle blade (Fig. 8A), although with a larger number in the nearest blade.
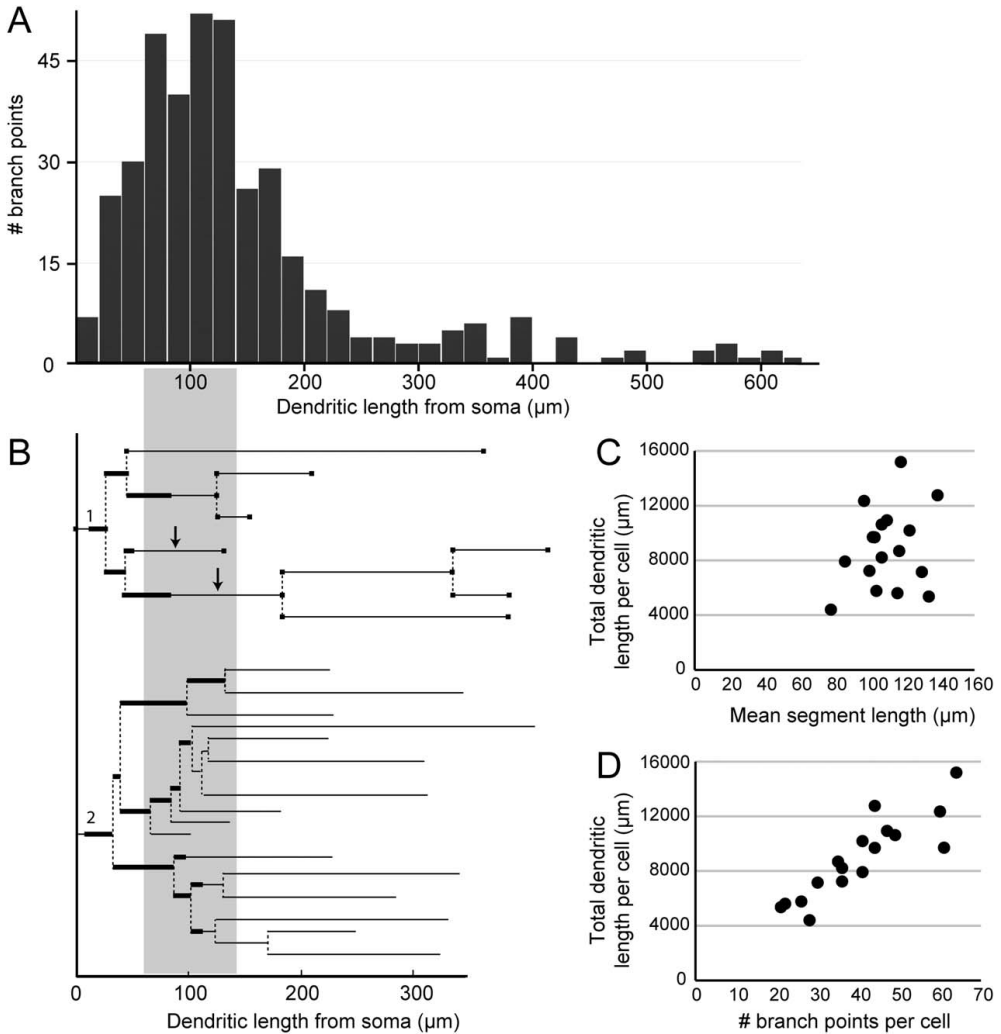
FIGURE 6. Dendritic measurements. **(A)** Graphic representation of the total number of dendritic branch points as a function of dendritic length from soma estimated for 54 stem dendritic diagrams from 12 mossy cells. Most of the branch points are within 200 μm from the soma with the highest frequency of branching between 60 and 140 μm. This trend is visualized by the grey area interconnecting **(A)** with **(B)**, the latter figure showing two stem dendritic diagrams (dendrite 1 and 2 from Fig. 3B, mc#2) with branch points. The thicker lines in **(B)** indicate the stretches covered with excrescences, arrows point to gm-dendrites. **(C,D)** The total dendritic length per cell seems to be largely independent of the mean segment length per cell **(C)**, but positively correlated with the number of branch points per cell **(D)**.

DISCUSSION

We have investigated Golgi-impregnated sections from the mink hippocampus and provided detailed qualitative and quantitative morphological descriptions of the mossy cells in the dentate gyrus, with particular focus on gm-dendrites. We have found that (1) the somata and excrescence-covered proximal dendrites of mossy cells are confined to the polymorph layer, (2) there seems to be a barrier for mossy cell dendrites to enter the granular and molecular layers, except for the special gm-dendrites, (3) the shape of the dendritic arbors depends upon the space available in the polymorph layer, although distal dendrites may cross the border to the subjacent CA3, (4) the total
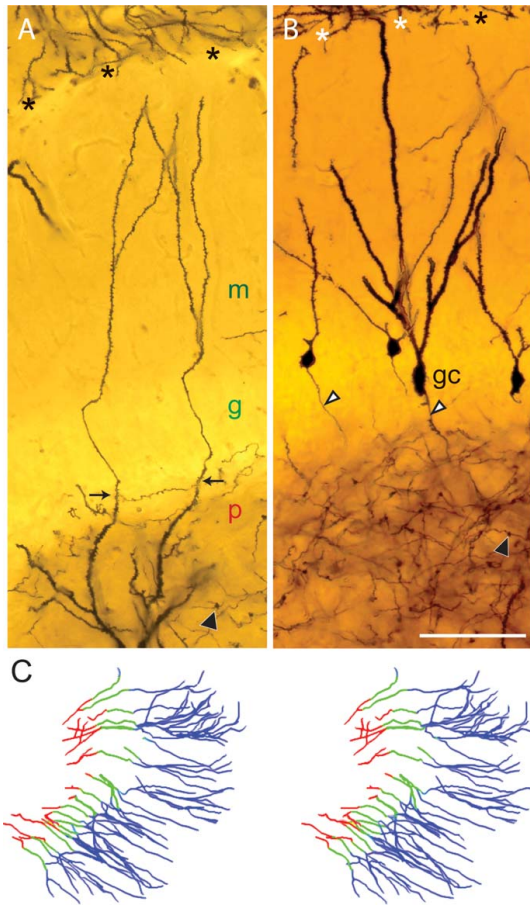
FIGURE 7.   Gm-dendrites. Photomicrographs of Golgi sections, (A) two gm-dendrites (arrows) from one mossy cell, with color-coded labels for the polymorph (red), granular (green), and molecular (blue) layers. (B) Four granule cells (gc) with dendrites of various thickness and spine density. Granule cell axons are marked by white arrowheads, their terminals by black arrowheads. Both fields are from the hidden blade. (C) Stereo view of 34 gm-dendrites reconstructed from the hidden blade, with sectors color-coded corresponding to (A). The hippocampal fissure is marked by asterisks. Abbr.: g, granular layer; gc, granule cell; m, molecular layer; p, polymorph layer. Calibration bar in B (100 µm) is also valid for A.

FIGURE 8.   Relation between cell soma location and gm-dendrites; summed gm-dendritic length per cell. (A) Contour of the mink dentate gyrus with the location of the somata (black dots) of the 17 mossy cells sampled for the present study, with cell numbers (Table 2). The deep border of the polymorph layer is indicated by a stippled line. Cells with gm-dendrites extending to two opposing blades are marked by a triangle around the dot, cells with gm-dendrites to one blade by the dot only, while cells without registered gm-dendrites are indicated by a circle around the dot. Abbr.: eb, exposed blade; hb, hidden blade; mb, middle blade. Calibration bar, 100 µm. (B) The number and summed length of gm-dendrites per cell are closely related.

of granule cells, mossy cells, and pyramidal cells, the relation of the three cell types to the mossy fibers as well as the relation of their dendritic arbors to subdivision boundaries are summarized in Figure 9.

Methodological Considerations

The Golgi method allows impregnation of a limited, and possibly random, fraction of cells and unmyelinated fibers (Spielmeyer, 1924; Baloyannis, 2015). Topographic relationships between cell types and their locations within subfields may be studied, and it occasionally happens that elements of a circuit (such as granule cells and mossy cells, Fig. 5) are found together without other disturbing elements. Because of incomplete impregnation and sampling problems, however, the quantitative results will be uncertain. Consequently, the total dendritic lengths reported here may be underestimated. In our study, a bias in cell sampling with respect to the proportion of

dendritic lengths of Golgi impregnated mossy cells vary considerably, (5) 88% of them have gm-dendrites, which constitute on average 12% of the total dendritic length, while (6) the frequency of gm-dendrites per cell may be less in the exposed blade than in the middle and hidden blades. The overall shape of the dentate gyrus in mink, the relative size and shape of its three layers, the topographic relation of the dentate gyrus to CA3, the topographic relationship between the dendritic arbors
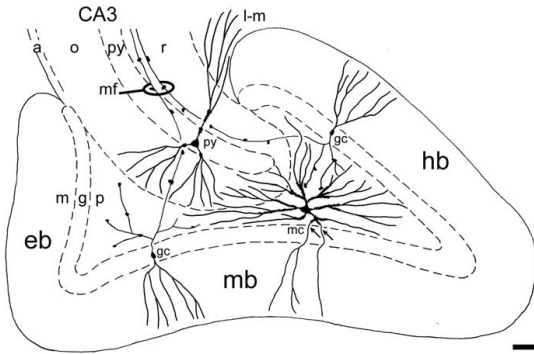
FIGURE 9.   Concluding diagram. Semidiagrammatic drawing of the dentate gyrus and adjacent part of CA3 with focus on the shape of the dendritic arbors of granule cells (gc), mossy cells (mc) and CA3 pyramidal cells (py) and their relation to subdivision boundaries. Axons are not included except for the granule cell axons (mossy fibers, mf), which feature giant terminals synapsing with the thorny excrescences of both mossy and pyramidal cells. The somata and excrescence covered proximal dendrites of mossy cells are confined to the polymorph layer. Special, so-called gm-dendrites (arrows), extend into the granule and molecular layers. Distal dendrites of mossy cells may extend into the subjacent CA3, while dendrites of pyramidal cells seem to respect the border. Abbr.: a, alveus; g, granular layer; eb, exposed blade; gc, granule cell; hb, hidden blade; l-m, lacunar-molecular layer; m, molecular layer; mb, middle blade; mc, mossy cell; mf, mossy fibers; o, oriens layer; p, polymorph layer; py, pyramidal layer/cell; r, radiate layer. Calibration bar, 100 μm.

cells with gm-dendrites cannot be excluded. Furthermore, we cannot exclude that some morphological changes may have occurred during the up to 2 h interval between time of death and immersion fixation, but the absence of obvious artifacts indicates that such changes, if any, are subtle. A strength of our approach is that resin embedding minimizes distortion of the tissue and makes 3D reconstructions and measurements more accurate. A comparison of our quantitative data with previous studies in other species based on different methods may be subject to systematic errors, but as a whole, the results seem coherent and consistent with other information. As the cells are all sampled from the temporal limb of the dentate gyrus, possible septotemporal gradients are not addressed.

General Morphology of Mossy Cells

Mossy cells are characterized by the same morphological features in mink as in other mammals, with a relatively large soma and thick dendrites covered proximally with thorny excrescences (rat: Amaral, 1978; Buckmaster, 2012; Scharfman and Myers, 2012; hamster: Murakawa and Kosaka, 2001; guinea pig; Blackstad, 1985; rat and monkey: Frotscher et al., 1991; monkey: Seress and Ribak, 1995; Buckmaster and Amaral, 2001; human: Seress and Mrzljak, 1992). The width and extension of the excrescences vary somewhat across species. Although not measured systematically, the excrescences in mink

seem to be intermediate in size to those of rodents and primates. In mink, the soma and initial part of the primary segments have a smooth surface, as in guinea pig (Blackstad, 1985), monkey (Seress and Ribak, 1995; Buckmaster and Amaral, 2001), and human (Seress and Mrzljak, 1992), while in hamster the excrescences also cover these parts of the cell (Murakawa and Kosaka, 2001). In rat, likewise the vast majority of excrescences are on the proximal portions of the dendrites, but a few may also occur on the soma (Amaral, 1978; Frotscher et al., 1991; Buckmaster and Schwartzkroin, 1994; Buckmaster et al., 1996; Scharfman and Myers, 2012).

Buckmaster et al. (1993) found that in rat the mean total length of segments covered with excrescences measured 912 μm (SEM 72), with a range of 676–1,102 μm ($n = 6$). We did not do corresponding measurements in mink, but we found that the excrescences extended on average to about 110 μm from the cell soma, covering part of the zone of most heavy branching. In rat, Amaral (1978) described a "total encrustation of 40–80 μm of the proximal dendrites with thorny excrescences."

Mossy Cell Dendritic Arbors

Our findings indicate that mossy cell dendritic arbors in mink largely adapt to the available space within the polymorph layer, as also observed in rat (Amaral, 1978; Claiborne et al., 1986; Scharfman and Myers, 2012) and monkey (Seress and Ribak, 1995), with distal dendrites often extending into the CA3 as in monkey (Buckmaster and Amaral, 2001) and sheep (K.K. Osen, unpublished observation). Unlike mossy cells, the pyramidal cells in the subjacent CA3 do not appear to extend dendrites across the polymorph layer/CA3 border, an observation consistent with findings at least in the rat (Buckmaster et al., 1993; Buckmaster, 2012). It is tempting to speculate that the difference might be related to the source of afferents, based on the idea that pre- and postsynaptic processes provide mutual trophic support during development, but further studies are needed to answer the question.

The size of the dentate gyrus and the mossy cell dendritic arbors (Table 3) vary across species both in absolute and relative terms. Accordingly, while in rat a single mossy cell arbor may span the entire hidden-exposed (transverse) dimension of the polymorph layer (Amaral, 1978; Scharfman and Schwartzkroin, 1988; Buckmaster et al., 1996; Amaral et al., 2007), in mink it may span only one-half of it, and in primates merely a small fraction (Buckmaster and Amaral, 2001).

Mossy cell axons, besides innervating the polymorph layer locally, project to the deep molecular layer at distances 1–2 mm from the soma in the septal and temporal directions (Ribak et al., 1985; Buckmaster et al., 1996; Scharfman and Myers, 2012). This commissural/associational pathway is bilateral in rodents (Blackstad, 1956). As shown in mink, the mossy cell dendrites may extend up to 1 mm in the septotemporal dimension. Therefore these cells do not conform to the anisotropic, lamellar organization typical of hippocampal structures (Sloviter and Lømo, 2012), neither with respect to axons nor dendrites.

Mossy Cell Total Dendritic Lengths in Various Species

Species	Range (μm)	Mean of total dendritic length (μm)
Mouse[a]	NA	5,392 (SEM 313)
Rat[b]	7,428–10,924	8,292 (SD 1,200)
Mink[c]	4,403–15,192	8,927 (SD 2,928)
Monkey[d]	7,338–15,339	12,101 (SEM)

[a]Data from Kowalski et al., 2010 ($n = 13$).
[b]Based on data from Buckmaster, 2012 ($n = 12$).
[c]Present study ($n = 17$).
[d]Data from Buckmaster and Amaral, 2001 ($n = 6$).

Accordingly, as pointed out by Buckmaster and Amaral (2001), both mossy cell axons and dendrites may be severely amputated by the hippocampal slice procedure.

Total Dendritic Length

In the 17 mink mossy cells the total dendritic length varied between 15,192 and 4,403 μm, mean 8,927 μm. Previous measurements of total dendritic length of mossy cells are available from 12 rat cells intracellularly labelled with biocytin in vivo (Buckmaster, 2012), as well as in 6 monkey cells (Buckmaster and Amaral, 2001), and 13 wild type mouse cells (Kowalski et al., 2010) filled with biocytin in acute slices. In Table 3, these data are compared with the present findings from mink. All groups show variability. The mean total length of mossy cell dendrites in mink (8,927 μm, SD 2,928) is about the same as in rat (8,292 μm, SD 1,200), larger than in mice (5,392 μm, SEM 313 μm) and smaller than in monkey (12,101 μm, SEM 1,265). However, the largest arbor in mink (15,192 μm) is about the same size as the largest arbor in monkey (15,339 μm), both being considerably larger than the largest arbor in rat (10,924 μm). At the same time, the smallest arbor in mink (4,403 μm) is considerably smaller than the smallest arbor both in rat (7,428 μm) and monkey (7,338 μm). It seems reasonable to assume that the larger variability in the total dendritic length of mossy cells in mink, compared to both rat and monkey, is due to the capriciousness of the Golgi method, and that the mossy cells in mink in reality may have a larger mean total dendritic length than in rat, somewhat between rat and monkey despite the relatively small calculated mean.

In rat, the total dendritic lengths of mossy cells and CA3 pyramidal cells are about equal (8,292 μm vs. 8,805 μm; Buckmaster, 2012), whereas in monkey, mossy cells have a larger total dendritic length than the "classical" proximal CA3 pyramidal cells (12,101 μm vs. 9,375 μm; Buckmaster and Amaral, 2001). Mossy cell arbors thus are 1.5 times larger in monkey than in rat, while CA3 pyramidal cell arbors are only 1.1 times larger, which supports the notion of larger species differences in the dentate gyrus than in the hippocampus proper (Seress, 2007). We have not provided quantitative data

for CA3 pyramidal cells in mink, but by mere inspection, the mossy cells seem to have a somewhat larger soma and total dendritic length than the CA3 pyramidal cells. The granule cells obviously have smaller total dendritic length than both mossy cells and CA3 pyramidal cells in all of the three species, as also documented quantitatively in rat (Pierce et al., 2011; Buckmaster, 2012).

Branching Pattern

The branching of mossy cell dendrites in mink appears more extensive than in rat. While the mean number of primary dendrites is only slightly larger in mink than in rat (4.8 in mink versus 4 in rat, Buckmaster, 2012), the mean number of dendritic segments per cell is almost three times larger in mink than in rat (85 in mink versus 31 in rat, Buckmaster, 2012), but interestingly enough similar to mouse (80 segments per cell, Kowalski et al., 2010). In addition, the majority of branch points are located closer to the soma in mink than in rat, most branch points occurring within 200 μm (peak at 60–140 μm) from the soma in mink (Fig. 6A), against 400 μm (peak at 180 μm) in rat (Buckmaster, 2012, his Fig. 5E). Although the measures may be influenced by different quantitative methods, i.e., dendritic diagrams (in the present study) versus Sholl analyses (Buckmaster, 2012), the numerical data support our visual impression of a more brush-like arborization of mossy cell dendrites in mink compared with rat, a pattern reminiscent of CA3 pyramidal cells in both species. The extensive branching of mossy cell dendrites in mink is reflected in the fact that the total dendritic length is more strongly correlated with number of branch points than with mean segment length (Fig. 6C,D).

Gm-Dendrites

Special mossy cell dendrites extending into the granular and molecular layers seem to be a general phenomenon, but with some variation across species. In mink, most of the observed mossy cells (88%), had from 1 to 8 gm-dendrites each, on average 2.8 gm-dendrites per cell. According to Buckmaster and Amaral (2001), 90% of mossy cells in monkey have at least one dendritic branch that projects into the molecular layer, on average five per cell. Such dendrites also occur regularly in human (Seress and Mrzljak, 1992). In rodents they may occur less frequently. Amaral (1978) found them only in Golgi material of very young rats, while Blackstad (1985) observed some in guinea pig. In rat studies based on intracellular labelling, Scharfman (1991) found at least one gm-dendrite in many so-called spiny hilar cells (i.e., mossy cells) particularly when the cell body was close to the granular layer. Buckmaster et al. (1993) found a gm-dendrite in 4 out of 34 (12%) biocytin-labelled mossy cells in acute slices, and Buckmaster (2012) found one gm-dendrite in 3 out of 12 (25%) in vivo labelled mossy cells. In wild type mice 2 of 13 (15%) mossy cells labelled with biocytin in acute slices had "two short" dendrites extending into the granular and molecular layers (Kowalski et al., 2010). The diverging results with respect to the frequency of gm-dendrites could perhaps be due to sampling from

different septotemporal or hidden-exposed parts of the dentate gyrus. As mentioned, the present material does not provide information on septotemporal gradients. A possible hidden-exposed gradient is discussed below.

In mink, the gm-dendrites constitute on average 12% of the total dendritic length of mossy cells, with about three fourth of the length being located within the molecular layer. Corresponding measures have, as far as we know, not been published in other species. The main afferents to the molecular layer are organized in three levels, the outer third being supplied by the lateral perforant path, the middle third by the medial perforant path, and the inner third by the commissural/associational pathway (Blackstad, 1956; Amaral et al., 2007). While some branches of gm-dendrites do not reach the outer levels, other branches provide gm-dendrites to these levels, right out to the dentate surface (Fig. 7C). Mossy cells, thus, have dendrites in the terminal area of the medial as well as the lateral perforant path. It is noteworthy that at the inner level of the molecular layer, where the mossy cell axons synapse with granule cell dendrites (Ribak et al., 1985; Amaral and Witter, 1989; Buckmaster et al., 1996), they are in a position also to synapse on gm-dendrites belonging to mossy cells of a different septotemporal level than their own level of origin.

Spatial Distribution Gradients in the Dentate Gyrus

In spite of the large variation in arbor shape and total dendritic length, we found no indication of specific subgroups of mossy cells. Mink mossy cells, however, appear to have more gm-dendrites in the hidden (suprapyramidal) and middle blades than in the exposed (infrapyramidal) blade. A difference between the supra- and infrapyramidal blades has been described in rat with respect to granule cells, which have greater total dendritic length, greater number of dendritic segments, and more flattened dendritic arbors in the suprapyramidal blade (Claiborne et al., 1990). In rat, gm-dendrites are found in mossy cells throughout the polymorph layer and both blades (H.E. Scharfman, unpublished data), which is actually also true in mink where it is the frequency that seems to differ.

Spine Density of Granule Cell Dendrites

The differences between granule cells with respect to dendritic spine density observed by us in mink, agree with Golgi studies in mouse (Williams and Matthysse, 1983) and primates (Seress and Frotscher, 1990; Seress, 1992) in which two types of granule cells have been defined, spine rich and spine poor. Because in these studies, the animals were fixed by transcardial perfusion, the findings are unlikely to be an artifact of postmortem changes. Similar variations in granule cell dendrites have been observed by us in either perfusion- or immersion-fixed Golgi material of rat, guinea pig, cat, pig, and sheep (K.K. Osen, unpublished observations). Variation in granule cell spine density has been related to animal age (Duffy and Rakic, 1983). Dentate granule cells are generated throughout life from a germinal center deep to the granular layer (Deshpande et al., 2013; Liu

et al., 2014; Pallotto and Deprez, 2014; Yamada et al., 2015), as also demonstrated in mink (Malmkvist et al., 2012), suggesting a relation between spine density, cell age, and functional properties (see e.g., Brunner et al., 2014). This warrants further investigation.

Implications and Perspectives

It seems reasonable to conclude from the available data that mossy cells have more gm-dendrites in mink (about 3 per cell in 88% of the cells) than in rat (1 per cell in <25% of the cells, Buckmaster, 2012), but fewer than in monkey (about 5 per cell in 90% of the cells, Buckmaster and Amaral, 2001). Interestingly, the threshold of mossy cells to perforant path stimulation may be lower when thin distal gm-dendrites are present (Scharfman, 1991). Mossy cells, thus, may be under a more direct influence from the entorhinal cortex in mink than in the much studied rat, but less than in primates. It remains to be elucidated whether the number of gm-dendrites, together with the extensive branching of mossy cell dendrites in general, relates to the relatively high learning capability in mink which in certain aspects approaches that of primates (Doty et al., 1967).

It is also an open question, why gm-dendrites normally are the only mossy cell dendrites that enter the granular layer. The border is open for certain interneurons (Amaral, 1978) and in monkey for the so-called dentate pyramidal cells (Buckmaster and Amaral, 2001). In reeler mutant mice the stratification of the dentate gyrus is disturbed, with both somata and main dendrites of mossy cells being intermingled with granule cells throughout the structure (Kowalski et al., 2010). It also remains to be unresolved why mossy cell dendrites become thinner when they enter into the granular and molecular layer, i.e., the domain of the granule cells, and why the change in diameter is so abrupt.

The new data presented here thus highlight important aspects of the mossy cells in the dentate gyrus of the hippocampus, and emphasize that these cells should be taken into account in attempts to construct computational models of hippocampal function. The structural data about mossy cells in mink support the notion that mossy cells may play a more important role in the hippocampal circuitry in primates and humans than in rat. Increased knowledge about mossy cells is needed, and to this end the mink may provide an interesting model.

Acknowledgments

acquired at the Norbrain Slidescanning Facility at the Institute of Basic Medical Sciences, University of Oslo.

REFERENCES

Amaral DG. 1978. A Golgi study of cell types in the hilar region of the hippocampus in the rat. J Comp Neurol 182:851–914.

Amaral DG, Lavenex P. 2006. Hippocampal neuroanatomy. In: Andersen P, Morris R, Amaral D, Bliss T, O'Keefe J, editors. The Hippocampus Book, New York: Oxford University Press, pp 37–114.

Amaral DG, Witter MP. 1989. The three-dimensional organization of the hippocampal formation: A review of anatomical data. Neuroscience 31:571–591.

Amaral DG, Scharfman HE, Lavenex P. 2007. The dentate gyrus: Fundamental neuroanatomical organization (dentate gyrus for dummies). Prog Brain Res 163:3–22.

Baloyannis SJ. 2015. Staining of dead neurons by the Golgi method in autopsy material. Methods Mol Biol 1254:167–179.

Blaabjerg M, Zimmer J. 2007. The dentate mossy fibers: Structural organization, development and plasticity. Prog Brain Res 163:85–107.

Blackstad TW. 1956. Commissural connections of the hippocampal region in the rat, with special reference to their mode of termination. J Comp Neurol 105:417–537.

Blackstad TW. 1958. On the termination of some afferents to the hippocampus and fascia dentata: An experimental study in the rat. Acta Anatom 35:202–214.

Blackstad TW. 1963. Ultrastructural studies on the hippocampal region. Prog Brain Res 3:122–148.

Blackstad TW. 1985. Laminar specificity of dendritic morphology: Examples from the guinea pig hippocampal region. In: Agnati L, Fuxe K, editors. Quantitative Neuroanatomy in Transmitter Research, Vol. 42. New York and London: Plenum Press, pp 55–69.

Blackstad TW, Brink K, Hem J, Jeune B. 1970. Distribution of hippocampal mossy fibers in the rat. An experimental study with silver impregnation methods. J Comp Neurol 138:433–449.

Blackstad TW, Osen KK, Mugnaini E. 1984. Pyramidal neurones of the dorsal cochlear nucleus: A Golgi and computer reconstruction study in cat. Neuroscience 13:827–854.

Brandt C, Malmkvist J, Nielsen RL, Brande-Lavridsen N, Surlykke A. 2013. Development of vocalization and hearing in American mink (*Neovison vison*). J Exp Biol 216:3542–3550.

Brunner J, Neubrandt M, Van-Weert S, Andrasi T, Kleine Borgmann FB, Jessberger S, Szabadics J. 2014. Adult-born granule cells mature through two functionally distinct states. eLife 3:e03104.

Buckmaster PS. 2012. Mossy cell dendritic structure quantified and compared with other hippocampal neurons labeled in rats in vivo. Epilepsia 53 (Suppl 1):9–17.

Buckmaster PS, Amaral DG. 2001. Intracellular recording and labeling of mossy cells and proximal CA3 pyramidal cells in macaque monkeys. J Comp Neurol 430:264–281.

Buckmaster PS, Schwartzkroin PA. 1994. Hippocampal mossy cell function: A speculative view. Hippocampus 4:393–402.

Buckmaster PS, Strowbridge BW, Schwartzkroin PA. 1993. A comparison of rat hippocampal mossy cells and CA3c pyramidal cells. J Neurophysiol 70:1281–1299.

Buckmaster PS, Wenzel HJ, Kunkel DD, Schwartzkroin PA. 1996. Axon arbors and synaptic connections of hippocampal mossy cells in the rat in vivo. J Comp Neurol 366:271–292.

Cappaert N, Van Strien N, Witter M. 2014. Hippocampal formation. In: Paxinos G, editor. The Rat Brain. San Diego: Elsevier Academic Press. pp 511–574.

Claiborne BJ, Amaral DG, Cowan WM. 1986. A light and electron microscopic analysis of the mossy fibers of the rat dentate gyrus. J Comp Neurol 246:435–458.

Claiborne BJ, Amaral DG, Cowan WM. 1990. Quantitative, three-dimensional analysis of granule cell dendrites in the rat dentate gyrus. J Comp Neurol 302:206–219.

Deshpande A, Bergami M, Ghanem A, Conzelmann KK, Lepier A, Götz M, Berninger B. 2013. Retrograde monosynaptic tracing reveals the temporal evolution of inputs onto new neurons in the adult dentate gyrus and olfactory bulb. Proc Natl Acad Sci USA 110:E1152–E1161.

Doty BA, Jones CN, Doty LA. 1967. Learning-set formation by mink, ferrets, skunks, and cats. Science 155:1579–1580.

Duffy CJ, Rakic P. 1983. Differentiation of granule cell dendrites in the dentate gyrus of the rhesus monkey: A quantitative Golgi study. J Comp Neurol 214:224–237.

Federative Committee on Anatomical Terminogy. 1998. Terminologia Anatomica: International Anatomical Terminology. Stuttgart: Thieme.

Fiala J, Harris K. 1999. Dendrite structure. In: Stuart G, Spruston N, Häusser M, editors. Dendrites. Oxford, UK: Oxford University Press, pp 1–34.

Freund TF, Buzsáki G. 1996. Interneurons of the hippocampus. Hippocampus 6:347–470.

Frotscher M, Seress L, Schwerdtfeger WK, Buhl E. 1991. The mossy cells of the fascia dentata: A comparative study of their fine structure and synaptic connections in rodents and primates. J Comp Neurol 312:145–163.

Gościcka D, Stankiewicz W, Szpinda M. 1993. Hippocampus in the N. American mink (*Mustela vison* Brisson, 1756). Arch Vet Polonicum 33:129–34.

Haug FM. 1967. Electron microscopical localization of the zinc in hippocampal mossy fibre synapses by a modified sulfide silver procedure. Histochemie 8:355–368.

Haug FM. 1973. Heavy metals in the brain. A light microscope study of the rat with Timm's sulphide silver method. Methodological considerations and cytological and regional staining patterns. Adv Anat Embryol Cell Biol 47:1–71.

Haug FM. 1974. Light microscopical mapping of the hippocampal region, the pyriform cortex and the corticomedial amygdaloid nuclei of the rat with Timm's sulphide silver method. I. Area dentata, hippocampus and subiculum. Zeitschrift Für Anatomie Und Entwicklungsgeschichte 145:1–27.

Henze DA, Buzsáki G. 2007. Hilar mossy cells: Functional identification and activity in vivo. Prog Brain Res 163:199–216.

Houser CR. 2007. Interneurons of the dentate gyrus: An overview of cell types, terminal fields and neurochemical identity. Prog Brain Res 163:217–232.

Jinde S, Zsiros V, Nakazawa K. 2013. Hilar mossy cell circuitry controlling dentate granule cell excitability. Front Neural Circ 7:14.

Kjonigsen LJ, Lillehaug S, Bjaalie JG, Witter MP, Leergaard TB. 2015. Waxholm Space atlas of the rat brain hippocampal region: Three-dimensional delineations based on magnetic resonance and diffusion tensor imaging. Neuroimage 108:441–449.

Kowalski J, Geuting M, Paul S, Dieni S, Laurens J, Zhao S, Vida I. 2010. Proper layering is important for precisely timed activation of hippocampal mossy cells. Cereb Cortex 20:2043–2054.

Larimer P, Strowbridge BW. 2008. Nonrandom local circuits in the dentate gyrus. J Neurosci 28:12212–12223.

Laurberg S, Sørensen KE. 1981. Associational and commissural collaterals of neurons in the hippocampal formation (hilus fasciae dentatae and subfield CA3). Brain Res 212:287–300.

Leergaard TB, Bjaalie JG. 1995. Semi-automatic data acquisition for quantitative neuroanatomy. MicroTrace–computer programme for recording of the spatial distribution of neuronal populations. Neurosci Res 22:231–243.

Lisman JE. 1999. Relating hippocampal circuitry to function: Recall of memory sequences by reciprocal dentate-CA3 interactions. Neuron 22:233–242.

Liu S, Li C, Xing Y, Tao F. 2014. Effect of transplantation of human embryonic stem cell-derived neural progenitor cells on adult neurogenesis in aged hippocampus. Am J Stem Cells 3:21–26.

Lorente de Nó R. 1934. Studies of the structure of the cerebral cortex. II. Continuation of the study of the ammonic system. J Psychol Neurol 46:113–177.

Malmkvist J, Brix B, Henningen K, Wiborg O. 2012. Hippocampal neurogenesis increase with stereotypic behavior in mink (*Neovison vison*). Behav Brain Res 229:359–364.

Murakawa R, Kosaka T. 2001. Structural features of mossy cells in the hamster dentate gyrus, with special reference to somatic thorny excrescences. J Comp Neurol 429:113–126.

Myers CE, Scharfman HE. 2009. A role for hilar cells in pattern separation in the dentate gyrus: A computational approach. Hippocampus 19:321–337.

Pallotto M, Deprez F. 2014. Regulation of adult neurogenesis by GABAergic transmission: Signaling beyond GABAA-receptors. Front Cell Neurosci. 8:166.

Pierce JP, McCloskey DP, Scharfman HE. 2011. Morphometry of hilar ectopic granule cells in the rat. J Comp Neurol 519:1196–1218.

Ramón y Cajal SS. 1955. Histologie du systeme nerveux de l'homme et des vertebres. T.II. Paris: A. Maloine 1911; reprinted Madrid: Instituto Cajal 1955.

Ribak CE, Seress L, Amaral DG. 1985. The development, ultrastructure and synaptic connections of the mossy cells of the dentate gyrus. J Neurocytol 14:835–857.

Scharfman HE. 1991. Dentate hilar cells with dendrites in the molecular layer have lower thresholds for synaptic activation by perforant path than granule cells. J Neurosci 11:1660–1673.

Scharfman HE. 1993. Spiny neurons of area CA3c in rat hippocampal slices have similar electrophysiological characteristics and synaptic responses despite morphological variation. Hippocampus 3:9–28.

Scharfman HE. 1995. Electrophysiological evidence that dentate hilar mossy cells are excitatory and innervate both granule cells and interneurons. J Neurophysiol 74:179–194.

Scharfman HE. 1999. The role of nonprincipal cells in dentate gyrus excitability and its relevance to animal models of epilepsy and temporal lobe epilepsy. Adv Neurol 79:805–820.

Scharfman HE, Myers CE. 2012. Hilar mossy cells of the dentate gyrus: A historical perspective. Front Neural Circ 6:106.

Scharfman HE, Schwartzkroin PA. 1988. Electrophysiology of morphologically identified mossy cells of the dentate hilus recorded in guinea pig hippocampal slices. J Neurosci 8:3812–3821.

Scharfman HE, Witter MP. 2007. Preface. The Dentate Gyrus: A Comprehensive Guide to Structure, Function and Clinical Implications. New York, NY: Elsevier.

Seress L. 1992. Morphological variability and developmental aspects of monkey and human granule cells: Differences between the rodent and primate dentate gyrus. Epilepsy Res Suppl 7:3–28.

Seress L. 2007. Comparative anatomy of the hippocampal dentate gyrus in adult and developing rodents, non-human primates and humans. Prog Brain Res 163:23–41.

Seress L, Frotscher M. 1990. Morphological variability is a characteristic feature of granule cells in the primate fascia dentata: A combined Golgi/electron microscope study. J Comp Neurol 293:253–267.

Seress L, Mrzljak L. 1992. Postnatal development of mossy cells in the human dentate gyrus: A light microscopic Golgi study. Hippocampus 2:127–141.

Seress L, Ribak CE. 1995. Postnatal development and synaptic connections of hilar mossy cells in the hippocampal dentate gyrus of rhesus monkeys. J Comp Neurol 355:93–110.

Sloviter RS. 1994. The functional organization of the hippocampal dentate gyrus and its relevance to the pathogenesis of temporal lobe epilepsy. Ann Neurol 35:640–654.

Sloviter RS, Lømo T. 2012. Updating the lamellar hypothesis of hippocampal organization. Front Neural Circ 6:102.

Spielmeyer W. 1924. Technik der mikroskopischen Untersuchung des Nervensystems, 3rd ed. Berlin: Verlag von Julius Springer. 77p.

Svendsen PM, Malmkvist J, Halekoh U, Mendl M. 2012. Responses of mink to auditory stimuli: Prerequisites for applying the "cognitive bias" approach. Behav Process 91:291–297.

Swanson LW, Wyss JM, Cowan WM. 1978. An autoradiographic study of the organization of intrahippocampal association pathways in the rat. J Comp Neurol 181:681–715.

Wenzel HJ, Cole TB, Born DE, Schwartzkroin PA, Palmiter RD. 1997. Ultrastructural localization of zinc transporter-3 (ZnT-3) to synaptic vesicle membranes within mossy fiber boutons in the hippocampus of mouse and monkey. Proc Natl Acad Sci USA 94: 12676–12681.

Williams RS, Matthysse S. 1983. Morphometric analysis of granule cell dendrites in the mouse dentate gyrus. J Comp Neurol 215: 154–164.

Yamada M, Clark J, McClelland C, Capaldo E, Ray A, Iulianella A. 2015. Cux2 activity defines a subpopulation of perinatal neurogenic progenitors in the hippocampus. Hippocampus 25:253–267.

Zappone CA, Sloviter RS. 2004. Translamellar disinhibition in the rat hippocampal dentate gyrus after seizure-induced degeneration of vulnerable hilar neurons. J Neurosci 24:853–864.

Zimmer JJ. 1971. Ipsilateral afferents to the commissural zone of the fascia dentata, demonstrated in decommissurated rats by silver impregnation. J Comp Neurol 142:393–416.

Zimmer J, Haug FM. 1978. Laminar differentiation of the hippocampus, fascia dentata and subiculum in developing rats, observed with the Timm sulphide silver method. J Comp Neurol 179:581–617.

PAPER 2

Title:

The fibro- and cytoarchitecture demarcating the boundary between the dentate gyrus and CA3 end in sheep (Ovis aries) and domestic pig (Sus scrofa domesticus)

Running title: The dentate-ammonic boundary in sheep and pig

Jan Sigurd Blackstad[1,2], Kirsten K. Osen[1], Trygve B. Leergaard[1]

1. Department of Molecular Medicine, Institute of Basic Medical Sciences, University of Oslo, Oslo, Norway

2. Kavli Institute for Systems Neuroscience and Center for Biology of Memory, Norwegian University of Science and Technology, Trondheim, Norway

ABSTRACT (< 300 ord)

The hippocampal formation is essential for spatial navigation and episodic memory. The anatomical structure is largely similar across mammalian species, apart from the deep polymorphic layer of the dentate gyrus and the adjacent part of cornu Ammonis 3 (CA3) which feature substantial variations. In rodents, the polymorphic layer has a triangular cross section abutting on the end of the CA3 pyramidal layer, while in primates it is long and band-shaped capping the expanded CA3 end which here lacks a distinct pyramidal layer. This structural variation has resulted in a confusing nomenclature and unclear anatomical criteria for definition of the dentate-ammonic boundary. Seeking to clarify the boundary, we present here a light microscopic investigation based on Golgi-impregnated and Timm-thionin-stained sections of the artiodactylae sheep and domestic pig, in which the dentate gyrus and CA3 end have some topographical features in common with primates. In short, the band-shaped polymorphic layer coincides with the Timm-positive mossy fibre collateral plexus and the Timm-negative subgranular zone. While the soma and excrescence-covered proximal dendrites of the mossy cells are localized within the plexus, the peripheral mossy cell dendrites extend outside the plexus also into the CA3. The main mossy fibres leave the collateral plexus in a scattered formation to converge slowly through the CA3 end in between the dispersed pyramidal cells, which are of three subtypes, as in monkey, with the classical apical subtype dominating near the hidden blade, the non-apical subtype near the exposed blade, and the dentate subtype being the only pyramidal cells that extend dendrites into the dentate gyrus. In agreement with our previous study in mink, the findings show that the boundary between the dentate gyrus and the CA3 end can be more accurately localized by the mossy fibre system than by cytoarchitecture alone.

INTRODUCTION

The dentate gyrus (DG) and the cornu Ammonis 3 (CA3) are two adjacent allocortical areas in the hippocampal formation of mammalian brains with particular importance for spatial navigation and episodic memory (Scoville & Milner, 1957; O'Keefe & Nadel, 1978; Squire, 1992; Maguire et al., 1997; Leutgeb et al., 2007; Moser et al., 2017; Senzai, 2019). The two areas are integral parts of the parahippocampal-hippocampal circuitry that forms a largely unidirectional, multisynaptic neuronal pathway from the entorhinal cortex in the parahippocampal region through the hippocampal formation and back again (Amaral & Witter, 1989; Witter et al., 1989; van Strien et al., 2009; Cappaert et al., 2015).

The DG and CA3 are interconnected by mossy fibre axons from DG granule cells (Ramón y Cajal, 1911; Lorente de Nó, 1934; Blackstad et al., 1970; Gaarskjaer, 1978; Swanson et al., 1978; Claiborne et al., 1986). The granule cell dendrites are supplied by perforant fibres from the entorhinal cortex of the parahippocampal region in the molecular layer (Blackstad, 1958; Hjorth-Simonsen, 1972; Hjorth-Simonsen & Jeune, 1972; Steward, 1976), while the mossy fibres, after having emitted collaterals (Golgi, 1886) to the deep polymorphic layer of the DG (Claiborne et al., 1986; Acsády et al., 1998), project to the CA3 where they are oriented in the perpendicular plane (Andersen et al., 1969; Blackstad et al., 1970; Andersen et al., 1971), being unbranched with en passant collaterals and largely oriented in parallel like axons of other granule cell systems (Ramón y Cajal, 1909, 1911; Mugnaini et al., 1980b; Osen et al., 1995; Voogd & Glickstein, 1998; D'Angelo et al., 2011). Cells of the polymorphic layer, by their projection to the inner third of the molecular layer (Blackstad, 1956; Zimmer, 1971; Laurberg, 1979; Laurberg & Sorensen, 1981; Swanson et al., 1981; Blackstad, 1985; Soriano & Frotscher, 1994) constitute a modulatory feedback link to the granule cells (Ribak et al., 1985; Buckmaster et al., 1996; Scharfman & Myers, 2012), while pyramidal cells of the CA3 have a widespread collateral projection to the CA1

(Schaffer, 1892; Ishizuka et al., 1990), which in turn projects to the entorhinal cortex, partly via the subiculum, thus completing the circuitry (Amaral & Witter, 1989; Witter et al., 1989; van Strien et al., 2009; Cappaert et al., 2015).

Even thought the hippocampus as a whole appears surprisingly similar across mammalian species, comparative studies are complicated by significant species differences in the shape and relative size of the DG and the CA3 (Amaral et al., 2007; Seress, 2007) . A common understanding of how the DG and the CA3 can be reproducibly identified in different species is, therefore, of crucial importance for our ability to compare and integrate results across experimental studies.

The location of the DG/CA3 border has long been a matter of dispute, not least because of the transformation of the DG polymorphic layer from a triangular cross section (usually referred to as the hilus), abutting on the CA3 pyramidal layer in the much-studied rat (Haug, 1974), to a long, thin band capping the expanded non-stratified CA3 end in primates (Buckmaster & Amaral, 2001)). The descriptive term "CA3 end", which is used here for the DG-near end of the CA3, corresponds approximately to the terms ¨proximal CA3" (Ishizuka et al., 1990) and "CA3c" (Lorente de Nó, 1934). The long, curved, and twisted shape of the hippocampus as a whole adds to the difficulties in distinguishing the DG/CA3 border in conventional planes of sectioning.

Historical examples of misleading DG/CA3 border definitions include 1) the classical Golgi-study of Lorente de Nó (1934) in mouse, rabbit, monkey and man, in which the polymorphic layer is regarded as an extension of the Ammon's horn termed "CA4", and 2) a series of histochemical studies in domestic pig (Holm & Geneser, 1989, 1991b, 1991a), guinea pig (Jensen, 1975), and rabbit (Geneser, 1987a, 1987b), in which the CA3 end is included in an extended DG named "area dentata". In these examples, the different connectivity of the CA3 and the polymorphic layer were apparently not taken into account.

Thanks to detailed cytoarchitectural studies in rat (Amaral, 1978) and monkey (Buckmaster & Amaral, 2001), there is now a general agreement about the key cytological features of the DG and the CA3 (Amaral et al., 2007; Seress, 2007). Yet a precise and operational definition of the DG/CA3 borderline that is applicable across species, is still missing (Cappaert et al., 2015). Since part of the problem may be ascribed to certain cytoarchitectonic similarities between the polymorphic layer and the unstratified expanded CA3 end, we here propose to base the DG/CA3 borderline on the mossy fibre collateral plexus rather than on the cytoarchitecture alone.

To elucidate this option, we investigated the DG/CA3 boundary in the artiodactylae sheep and domestic pig, in which the band-shaped polymorphic layer and the subjacent expanded non-stratified CA3 end have many features in common with monkey (Buckmaster & Amaral, 2001). To our knowledge, the only available morphological descriptions of the sheep hippocampus are the study by J.E. Rose (1942) and a study of fetal sheep by Godina and Barasa (1964). Although Rose (1942) reported on some basic features of the structure, we here may provide the first detailed anatomical description of the DG and CA3 end in adult sheep. A reappraisal of the DG/CA3 boundary in pig was also warranted, since previous studies in this species, as mentioned above (Holm & Geneser, 1989, 1991b, 1991a), are at odds with the currently accepted distinction between the DG and the CA3 (Amaral et al., 2007; Seress, 2007).

We utilized a sparse, but unique archive histological material prepared by late T.W. Blackstad and F. Geneser for comparison of Timm-thionin- and Golgi-stained sections from adjacent blocks of the same hippocampus, cut perpendicular to its curved long axis, *i.e.*, approximately in parallel with the main mossy fibres and the so-called hippocampal lamellae (Blackstad et al., 1970; Sloviter & Lømo, 2012). The Golgi-method, besides staining cell bodies and dendrites of randomly sampled neurons, stains unmyelinated axons like the mossy

fibres and their collaterals, while the Timm-method (Timm, 1958; Haug, 1973; Danscher, 1981) relatively specifically stains the zinc-containing terminals which occur scattered along the entire length of both main fibres and collaterals, thus making them distinguishable and traceable to a certain extent. The combination of Timm- and thionin-staining enabled a direct comparison between cyto- and fibroarchitecture in the same tissue section.

Our findings support the use of the mossy fibre collateral plexus in localizing the DG/CA3 borderline, which in principle also should provide a general key to comparing the two adjacent areas across mammals.

MATERIAL & METHODS

The present study is based on a historical histological material created from sheep and domestic pig hippocampi by late professor Theodor W. Blackstad (1925-2003), in collaboration with the late professor Finn Geneser (1938-2018), who permitted the use of the material (F. Geneser, personal communication to K.K. Osen, 2003). Their notes on several initial observations have served as an inspiration and starting point for the present study.

The material includes the hippocampi of two 8 week old sheep (Ovis aries, TBL75 and TBL76; Table 1) obtained by T. W. Blackstad from the Norwegian School of Veterinary Science (Dal, Asker, Norway), and three domestic pigs (Sus scrofa, TBL80, FIJ2, FIJ3) partly or fully procured by F. Geneser at the University of Aarhus Denmark (Table 1). The brains were processed using standard laboratory routines employed at the Universities of Oslo and Aarhus in the 1980s, with local institutional approvals in line with national legislation and practice at that time. For information about animals and histological processing, as summarized below, we have relied on notes and protocols left by T.W. Blackstad. The protocols of F. Geneser are no longer available.

Both sheep were euthanized with an overdose of pentobarbital (Nebumal). Within 1 hour, the brains were removed and immersed in 3 % glutaraldehyde and 0.4% sodium sulphide in 0.15 M Sørensen phosphate buffer for 10 hrs. During this period each hemisphere was gradually dissected to expose the hippocampus to view, bilaterally, leaving some minor physical artifacts at the pial surface (Figs. 2A,B, 3A, 7A). Each hippocampus was subdivided into five blocks cut perpendicular to the curved long septotemporal axis of the hippocampus, excluding the extreme ends**.** The blocks were labelled A-E, starting from septal. Blocks A, C, and E were used for Golgi-staining, and blocks B and D for Timm-thionin-staining (see below).

The brain of one domestic pig, most probably perfusion-fixed at the University of Aarhus, was shipped to Oslo in an aldehyde solution for further processing. The left hippocampus was exposed and cut perpendicular to its long axis in five blocks numbered 1-5 from septal to temporal. All blocks were subjected to Golgi-staining together with the sheep material (see below).

Tissue blocks of both species destined for Golgi-staining (those from sheep after the 10 hrs in the sulphide solution) were immersed in 1% paraformaldehyde in 0.1 M Sørensen phosphate buffer, pH 7.4, for 10 days, followed by 2.4% potassium dichromate with 0.2% osmium tetroxide for 2 days, and then 3.0% potassium dichromate for a few days. After covering the blocks with 2-4% agar, silver impregnation was carried out with 0.75% silver nitrate for two days. Finally, the agar was removed before dehydration and embedding in Araldite. Sections 100 μm thick were cut on a sliding microtome with a hot steel knife.

Tissue blocks of sheep destined for Timm-thionin-staining were, after the 10 hrs in sulphide solution, immersed in 30% sucrose in 0.1M phosphate buffer at pH 7.4 for another 13-15 hours, and cut in 40 μm thick sections using a cryostat. Sections were mounted and subjected to Timm-staining (Holm & Geneser, 1989) before being counterstained with thionin to visualize cell bodies. The stronger Timm-staining of the subpial brain tissue in Figure 2A,B may be due to a more direct exposure to the sulphide solution peripherally in the block.

All sections were cut perpendicular to the long axis of the hippocampus, in the following referred to as the perpendicular plane, which is approximately parallel to the so-called lamellar plane (Andersen et al., 1969; Blackstad et al., 1970; Andersen et al., 1971; Sloviter & Lømo, 2012). Because of the curvature of the hippocampus, the orientation of the sections with respect to the axes of the brain differs between the blocks. In addition, three thionin-stained sections and three Timm-thionin-stained sections from two other pigs were received from the University of Aarhus in the late 1980s. These ~40 μm thick sections had

apparently been cut horizontally with the hippocampus in situ in the brain, not adjusting for the curvature and orientation of the hippocampus, and thus not exactly perpendicular to its long axis. Details of the Timm-method used in these cases were not available.

High-resolution microscopic images were acquired at multiple depths of focus using an automated slide scanner system (Axio Scan Z1, Cark Zeiss MicroImaging, Jena, Germany) employing the extended depth of focus function module provided in the Zen software (Carl Zeiss MicroImaging, Jena, Germany). The ensuing 2-D images show cellular structures from different depths in the section projected into one plane, thus hampering differensiation between various focus depths and making strongly stained adjacent elements appear to be merge. Septotemporal differences are reflected in the diagrams of Figure 1, but were otherwise not evaluated.

Data availability

Selected images from the collection of high-resolution microscopic images utilized in the present study will be shared via the EBRAINS research infrastructure (http://ebrains.eu).

RESULTS

We here present observations on the cyto- and fibroarchitecture of the DG and CA3 end in sheep and pig, with special emphasis on the mossy fibre system and its significance for the definition of the borderline between the polymorphic layer and the subjacent expanded CA3 end, here referred to as the DG/CA3 border. Considering the mossy fibre system as the principal organizing element, the polymorphic layer was defined as the area covered by the plexus of mossy fibre collaterals plus the superjacent subgranular zone free of zinc-containing mossy fibre terminals, observed previously among others in guinea pig (Geneser-Jensen et al., 1974) and rabbit (Geneser, 1987b) under the name "outer plexiform layer". The term CA3 end, on the other hand, was used for the area of scattered pyramidal cells deep to the mossy fibre collateral plexus, found also in monkey and human (Amaral et al., 2007; Lavenex et al., 2007). The cellular area proved to coincide with the area of scattered main mossy fibres gradually converging into the dense mossy fibre bundle adjacent to the pyramidal layer of the main CA3. The present definition of the DG/CA3 borderline is compatible with the generally accepted perception of the border (Amaral et al., 2007), while at the same time it underlines the relationship of the polymorphic layer with the mossy fibre collaterals and of the CA3 end with the main mossy fibres (Claiborne et al., 1986; Acsády et al., 1998). It also supports the feasibility of the Timm-staining method for recognition of the DG/CA3 borderline in cases where this is difficult to set by the cytoarchitecture alone. Basing the borderline definition on the mossy fibre system, however, required a clarification of the topographic relationships of the somata and dendrites of the DG mossy cells and the CA3 pyramidal cells to the DG/CA3 borderline, as also attempted at in our previous study in mink (Blackstad et al., 2016).

Below, we first compare the overall organization of the DG and CA3 end in sheep and pig. We then describe the cyto-and fibroarchitecture of the polymorphic layer and the CA3 end in the two species separately, with emphasis on the sheep which has been subject to fewer

hippocampal studies than the pig. Our Discussion and conclusions build on observations from both species in relation to findings reported in the literature.

Overall organization of the DG and CA3 end in sheep and pig

Figure 1 presents diagrams of the sheep and pig hippocampus viewed in the perpendicular plane at three comparative septotemporal levels. The diagrams were constructed from *camera lucida* drawings of Golgi- stained sections, aided by Timm-thionin-sections to localize the deep border of the polymorphic layer and the transition between the CA3 end and the main CA3. The pattern appeared largely similar in the two species, both featuring a three-layered DG with a slim polymorphic layer (about 200 µm thick) deep to the molecular and granular layers. The three layers of the DG together form a concavity filled by the expanded, non-stratified CA3 end, much like the situation in monkey (Buckmaster & Amaral, 2001). Unfortunately, the concavity with the expanded CA3 end in these species is often referred to as the hilus (Holm & Geneser, 1991b) or the hilar region (Amaral et al., 2007). This is confusing since the term hilus is originally used in rodents for the polymorphic layer, which in cross sections in these species forms a triangular cellular field filling the larger part of the concavity formed by the molecular and granular layers. In sheep and pig, the cell-rich CA3 end gradually tapers into the pyramidal layer flanked by the cell poor radiate and oriens layers of the main CA3. The transition appeared more gradual in sheep, in which the entire hippocampal region was smaller, in agreement with the generally ~40 % smaller brain weight compared to pig (Minervini et al., 2016; Steinhausen et al., 2016).

In both sheep and pig, the molecular layer, which runs deep to the obliterated hippocampal fissure (Fig.1, asterisks), is contiguous with the CA3 lacunar-molecular layer close to the U-turn of the latter near the bottom of the fissure (Fig. 1, dotted borderline between the two). Compared to mink (Blackstad et al., 2016, their Fig. 1), the DG in sheep

and pig features a more rounded surface with less marked crests apart from an exposed crest at the outlet of the hippocampal fissure and a middle crest at the septal level (Fig. 1A,D) reminiscent of the V-shaped DG at this level in rat (Amaral et al., 2007; Kjonigsen et al., 2011; Boccara et al., 2015; Kjonigsen et al., 2015). Despite the lack of a distinct hidden crest, we roughly divide the DG in an exposed, middle and hidden blade for descriptive purposes, and in the following use these terms to indicate approximate locations within the DG and the CA3 end.

Cyto- and fibroarchitecture of the polymorphic layer and CA3 end in sheep
The spatial organization of mossy fibres and related cells in sheep were observed in Timm-thionin- and Golgi-stained sections, oriented in the perpendicular plane (Figs. 2, 3). In the lack of a plain thionin-stained section in sheep, we utilized a very special Timm-thionin-stained section, in which the cellular pattern was clearly visible because of a failure of the Timm-staining throughout most of the section except in and near to the exposed blade of the DG (Fig. 2A,C,D).

Cytoarchitecture of the sheep dentate gyrus and CA3 end in thionin-stained sections
In the thionin-dominated part of the above mentioned section, the densely packed granular layer appeared sharply delimited against the polymorphic layer, which, apart from the narrow subgranular zone, exhibited scattered somata of large multipolar neurons perceived by us as mossy cells (Fig. 2A,C,D). The CA3 end was composed of two indistinctly separated zones, a narrow cell poor zone next to the polymorphic layer and a larger cell rich zone gradually tapering into the CA3 pyramidal layer. The CA3 cells, perceived by us mostly as pyramidal cells, appeared slightly smaller and in part more oval than the mossy cells. In the hidden part, the cells tended to be elongated and oriented with their long axis across the extension of the

long axis of the pyramidal layer, which here curved towards the hidden blade (Fig. 2A,C), in agreement with the illustrations of Godina and Barasa (1964, their Fig. 9) in fetal sheep. In the exposed part of the CA3 end, the cells appeared more multipolar (Fig. 2A,D).

The polymorphic layer and the CA3, besides the mossy cells and the pyramidal cells, contained numerous smaller interneurons (Amaral, 1978; Freund & Buzsáki, 1996) , that were not further considered in our study.

Architecture of the sheep mossy fibre system in Timm- and Golgi-staining

The mossy fibre collateral plexus in our Timm-stained sections of sheep appeared almost homogeneously black, occupying the polymorphic layer, except for the Timm-negative subgranular zone which appeared very slim, particularly in the exposed blade where it was barely visible (Fig. 2). The plexus exhibited distinct, but somewhat grainy borders with occasional minor excavations next to the CA3 (Fig. 2D,E). Within the CA3 end, the neuropil appeared studded with black, irregularly shaped mossy fibre giant terminals (Fig. 2D,E, black arrowheads), which at all hidden-exposed levels were less numerous in the cell poor zone than in the cell rich zone. In the latter site, the terminals tended to be oriented in rows apparently representing mossy fibres converging towards the dense mossy fibre bundle on the radiate side of the pyramidal layer (Fig. 2B; see also Holm & Geneser, 1991b, their Fig. 6), consistent with the bundling of unmyelinated thin fibres observed electron microscopically in rat both in the deep polymorphic layer (Laatsch & Cowan, 1966) and in the mossy fibre bundle (Blackstad & Kjaerheim, 1961). The rows of fibres with giant terminals were apparently orientated in the perpendicular plane, as previously shown for the fibres of the densely packed mossy fibre bundle in rat (Blackstad et al., 1970; Acsády et al., 1998). At the end of the mossy fibre bundle and the corresponding stratum lucidum, the CA3-CA2 border is marked by a bend of the pyramidal layer (Fig. 2A) also shown in the rat (Ishizuka et al., 1990, his Figs. 1-

4). In contrast to the abrubt end of the mossy fibre bundle in rat (Gaarskjaer, 1978; Cappaert et al., 2015), however, some mossy fibres (in both of our sheep) continue beyond CA3 into CA2, and apparently also within CA1 (Fig. 2B). Similar uncommon observations have previously been reported in hedgehog (Gaarskjaer et al., 1982).

In Golgi-stained sections, the brighter granular layer contrasted with the darker polymorphic layer (Fig. 3). The few impregnated granule cells varied in soma size and dendritic thickness (Fig. 3B), in agreement with previous reports in mink (Blackstad et al., 2016) and monkey (Seress & Frotscher, 1990), as well as with personal observations (K.K. Osen) in Golgi-stained sections from rat, guinea pig, and cat. The mossy fibre collateral plexus, which featured a vaguely fibrillar texture, seemed to have a more distinct border with the CA3 than with the subgranular zone (Fig. 3B). Mossy fibres could be traced from the base of the impregnated granule cells, but were lost to view in the collateral plexus, to occur again scattered at its deep border with the CA3 end within which they continued without further branching. In their initial course, the fibres had only few giant terminals (Fig. 3B) in accordance with the scarcity of Timm-positive structures in the cell poor zone (Fig. 2). The uniform appearance of this zone throughout its entire hidden-exposed span in Timm-stained sections, favoured an evenly spaced transition of mossy fibres from the entire collateral plexus.

Mossy cells in the sheep dentate gyrus in Golgi staining
Mossy cells represent the major glutamatergic (excitatory) type of neuron in the polymorphic layer (Amaral, 1978; Scharfman & Myers, 2012; Scharfman, 2018). The few impregnated mossy cells found in the Golgi-stained sections of sheep, featured short, thick primary dendrites studded with large excrescences (Fig. 4C), and a brush-like type of arborization with long straight, unbranched distal dendrites (Fig. 4A,B). The excrescences were located closer

to the soma than in mink (Blackstad et al., 2016 , their Fig. 2C) and monkey (Buckmaster and Amaral, 2001, their Figs. 3A, 4C), possibly also encroaching upon the soma, but considerably less so than in hamster (Murakawa & Kosaka, 2001). In the Golgi-stained fetal sheep material of Godina and Barasa (1964), no mention is made of mossy cells with excrescences, but also in human the excrescences do not develop until after birth (Seress & Mrzljak, 1992; Seress, 2007). While the somata and excrescence-covered proximal dendrites of mossy cells in sheep appeared to be confined to the territory of the mossy fibre collateral plexus, in agreement with the synapses of large collateral terminals with the mossy cell excrescences in rat (Acsády et al., 1998; Scharfman & Myers, 2012), many distal mossy cell dendrites clearly extended outside the plexus, as also shown previously in mink (Blackstad et al., 2016). On approaching the granular layer, the mossy cell dendrites tended to bend and continue beneath the granular layer (Fig. 4B), as also shown in guinea pig (Scharfman & Schwartzkroin, 1988) and mink (Blackstad et al., 2016), running partly within the subgranular zone. At least one dendrite per cell ascended into the granular and molecular layer as a typical gm-dendrite (Fig. 4A,B), in agreement with observations from several other species (guinea pig: T.W. Blackstad, 1985; rat: Scharfman, 1991; Buckmaster et al., 1993, Buckmaster, 2012 ; monkey: Buckmaster and Amaral , 2001; mouse: Kowalski et al., 2010 ; mink: J.S. Blackstad et al., 2016; human: Seress and Mrzljak, 1992). The exact number of gm-dendrites per cell in sheep could not be determined, but it is clearly less than in human (where the mean number is 5 per cell; (Buckmaster & Amaral, 2001) and in mink (mean = 2,8 per cell; (Blackstad et al., 2016), although with a large span in both species. In rat, only few mossy cells exhibit a gm-dendrite (Buckmaster, 2012). At the deep border of the polymorphic layer, many distal mossy cell dendrites continued into the subjacent CA3 end, as also observed in monkey (Buckmaster and Amaral, 2001, their Figs. 4, 5) and mink (J.S. Blackstad et al., 2016, their Figs. 1E, 9), but considerably deeper in sheep than in mink.

Pyramidal cells in the sheep CA3 end in Golgi-staining

The majority of Golgi-impregnated cells within the CA3 end were found to meet the criteria

of pyramidal cells with a brush-like type of arborization with long straight distal dendrites

slightly thicker than in mossy cells and with postsynaptic excrescences that are smaller and

located farther from the soma, usually around the first and second dendritic branching point

(Fig. 5D), as also shown by Ishizuka et al. (1995, their Fig.1) in the DG-near end of the CA3

pyramidal layer in rat. In accordance with the intracellular labelling study by Buckmaster and

Amaral (2001) in monkey, we found three subtypes of pyramidal cells in sheep: apical, non-

apical and dentate.

   Apical pyramidal cells, (called classical by Buckmaster & Amaral, 2001) with a

bipolar soma and apical dendrites reaching the lacunar-molecular layer like CA3 pyramidal

cells in general (Blackstad, 1985; Ishizuka et al., 1995, their Figs. 1, 15), occurred near the

hidden blade (Figs. 5A-C). In Figure 5C, from the surface of a sheep tissue block with heavy

impregnation, numerous apical dendrites were seen to converge towards the u-turn of the

lacunar-molecular layer while clearly avoiding the polymorphic layer, reminiscent of the

classical Golgi-drawing of Lorente de Nó (1934, his Fig. 24) from the monkey hippocampus.

   Non-apical pyramidal cells, appearing more or less multipolar without dendrites to

the lacunar-molecular layer (Fig. 5D), seemed to predominate in the exposed part of the CA3

end, but might also have been scattered between the apical pyramidal cells in the hidden part

(Fig. 5A). Apical dendrites of these cells might have gone undetected, but it is reason to doubt

whether dendrites could reach the long distance from the exposed part of the CA3 end to the

lacunar-molecular layer.

   Dentate pyramidal cells, characterized by one or more dendrites extending into the

polymorphic, granular and molecular layers (Fig. 5E), like gm-dendrites of mossy cells, were

rarely found. They typically occurred in the hidden blade, but were also observed in the exposed crest. Near the end of the hidden blade, where the borders of the granular and molecular layers with the lacunar-molecular layer sometimes appeared indistinct, it was less obvious whether a pyramidal cell should be classified as apical or dentate.

Since both the molecular and the lacunar-molecular layers are supplied by the perforant path (T.W. Blackstad, 1956, his Fig. 13), the non-apical pyramidal cells may be the only of the three subtypes that lacks a direct access to perforant path fibres, while only the dentate pyramidal cells traverse the border with the polymorphic layer to reach these afferents.

Cyto- and fibroarchitecture of the polymorphic layer and CA3 end in domestic pig
Our observations were made in Golgi-, thionin-, and Timm-thionin- stained pig brain sections. The Golgi-stained sections (Figs. 7-9) were oriented in the perpendicular plane, while the thionin- and Timm-thionin- sections (Fig. 6) were cut in a conventional horizontal plane, as in the pig studies of Holm and Geneser (1989, 1991a,b), resulting in a slightly different shape and intrinsic structure of the dentate gyrus and the CA3 end (compare Figs. 2A and 6A,D). The main pattern of layering, nevertheless, appeared principally similar.

Cytoarchitecture of the pig dentate gyrus and CA3 end in thionin-staining
In the thionin-stained sections, the mossy cell somata of the polymorphic layer appeared located deep to the subgranular zone (Fig. 6A-C), as in sheep. Due to the better tissue preservation, the cell rich neuropil of the polymorphic layer appeared more striking, particularly in the subgranular zone where numerous minute cells adjacent to the basalmost granular cells (Fig. 6B,C) might have included both glial cells with processes to the granular layer as shown in monkey (Eckenhoff and Rakic, 1984, their Fig. 10), and granule cell

precursor as shown in rabbit (Guéneau et al., 1982). In the CA3 end, the transition between the cell rich and the cell poor zone appeared less distinct than in sheep. Next to the hidden blade, there was a slight tendency for the pyramidal cells to be oriented in parallel across the continuation of the curved long axis of the CA3 pyramidal layer, but less clearly so than in sheep, a difference that might be ascribed to the diverging planes of sectioning.

The mossy fibre system of pig in Timm- and Golgi staining

As in sheep, the band-shaped polymorphic layer in pig exhibited a Timm-positive collateral plexus covering the mossy cell somata, as well as a thin Timm-negative subgranular zone (Fig. 6D,E). In accordance with the better tissue preservation, the plexus at higher magnification of the Timm-stained sections, featured a grainy texture compatible with stained tiny terminals, as well as indistinct black silhouettes of large multipolar cells with an unstained centre, most likely representing somata and proximal dendrites of mossy cells surrounded by Timm-positive collateral terminals (Fig. 6E,F). Deep to the exposed crest, a few such cells also appeared immediately deep to the polymorphic layer (Fig. 6D). Small bright spots surrounded by black material in the plexus likely represented crosscut dendrites surrounded by afferents (Fig. 6F, marked d), while the serrated appearance of the borders of the plexus as a whole reflected cellular processes covered in Timm-positive terminals.

As in sheep, the cell poor zone of the CA3 end exhibited fewer Timm-positive mossy fibre giant terminals than the cell rich zone (Fig. 6D,E). Within the cell rich zone, the giant terminals, which here appeared connected by tiny, faintly stained fibres, were clearly located *between* the cell bodies (Fig. 6E,G), rather than enveloping the somata as seen for mossy cells within the collateral plexus. The observation is consistent with the location of the pyramidal cell postsynaptic excrescences farther from the cell body (Ishizuka et al., 1995) than in the

mossy cells, but not on the distal dendrites which apparently constitute the major part of the cell poor zone.

In contrast to the perpendicularly oriented Timm-stained sections in sheep, where the giant terminals in the CA3 end appeared collected into converging bundles, the terminals in the horizontal sections of pig were collected into tiny, randomly arranged groups increasing in size with the distance from the polymorphic layer (compare Figs. 2B and 6D). Judged by the different orientation of the sections, it is reasonable to regard the groups of terminals in pig as crosscut rows of mossy fibre terminals oriented in the perpendicular plane, like the fibres of the mossy fibre bundle in rat (Blackstad et al., 1970). The random distribution of the crosscut rows, however, speaks against an arrangement of the mossy fibres in physically separate lamellae, as also questioned by others (Amaral & Witter, 1989; Sloviter & Lømo, 2012).

In Golgi-sections from pig, the collateral plexus of the polymorphic layer featured an irregular network of tiny branching collaterals with scattered small "giant" terminals (Fig. 7B) and *én passage* varicosities, which were visible only at higher magnification. The network was too complex for identification of single mossy fibres with collaterals. As in sheep, and in agreement with our Timm-sections and the drawings of Ramon y Cajal (1911, his Figs. 478, 482) from guinea pig and rabbit, the main mossy fibres with occasional giant terminals were found to leave the deep border of the plexus in a scattered formation, to course within the CA3 end (Figs. 7B, 9).

Mossy cells in the pig dentate gyrus in Golgi-staining
In pig, as in sheep, thionin- stained mossy cell bodies appeared slightly larger than those of pyramidal cells (Fig. 6B). In Golgi sections, the mossy cell excrescences were as prominent as in sheep, being located on the soma and secondary dendrites as well as on primary dendrites (Fig. 8B). As in sheep, the mossy cells had at least one gm-dendrite each ascending to the

granular and molecular layers, while distal dendrites were seen to enter the CA3 end (Fig. 8A).

Pyramidal cells in the pig CA3 end in Golgi-staining

In Golgi sections from pig, as in sheep, apical pyramidal cells with dendrites to the lacunar-molecular layer were found next to the hidden blade, while non-apical pyramidal cells appeared to dominate near the exposed blade (Fig. 9A). In our relatively restricted Golgi-material, we only found a single cell that may represent an incomplete dentate pyramidal cell, with a dendrite penetrating into, but not beyond the polymorphic layer (Fig. 9B). Overall, the dendrites of the pyramidal cells, with the exception of the dentate subtype, seemed to respect the border with the polymorphic layer/collateral plexus. Close to the border with the polymorphic layer, the pyramidal cells seemed to adapt the shape of their dendritic tree to the border, occasionally forming an excavation into the DG polymorphic layer (marked "x" in Fig. 9A). However, as also demonstrated in the Timm-stained sections, a borderline composed of cellular elements can hardly be strictly linear.

DISCUSSION

We have studied the DG and CA3 end of sheep and domestic pig, with focus on the DG/CA3 border defined by the mossy fibre system. We compared Timm-thionin- and Golgi-stained sections, which in sheep were from adjacent blocks of the same hippocampus cut perpendicular to its long curved axis, approximately parallel to the main mossy fibres (= granule cell axons). The perpendicular (or "lamellar") plane of sectioning highlighted the relatively simple shape and pattern of the DG and CA3 end, which because of the curved, twisted long axis of the hippocampus may appear rather confusing in conventional planes of sectioning. The main findings, which were largely similar in the two species, are summarized in a common diagram (Fig. 10), featuring the long and slim polymorphic layer with mossy fibre collaterals and mossy cells capping the expanded CA3 end with scattering of mossy fibres and pyramidal cells. A single granule cell with mossy fibre and collaterals is shown in a slightly different view to visualize the "non-lamellar" orientation of the collateral tree.

Notably, our Figure 10 resembles the otherwise much more sophisticated and 110 years older diagram of the Ammon's horn by Ramon y Cajal (1911/1955, his Fig. 479) in young rabbits, both with respect to the mossy fibre collaterals in the polymorphic layer and the convergence of the scattered main mossy fibres through the CA3 end. Ramon y Cajal's diagram, however, just missed the expansion of the CA3 end, and the three other topics that were central in our study, namely a DG/CA3 borderline, mossy cells in the polymorphic layer, and pyramidal cells of various subtypes in the CA3 end.

The comparative architecture of the polymorphic layer with its mossy fibre collateral plexus

With its long, band-shaped polymorphic layer capping the expanded CA3 end, the DG in sheep and domestic pig (Fig. 10) resembles the DG in monkey (Buckmaster & Amaral, 2001)

and human (Cassell & Brown, 1984). It is distinctly different from the polymorphic layer in rat, which exhibits a triangular cross section filling the larger part of the so-called hilus deep to the molecular and granular layers, abutting on the end of the pyramidal layer of the CA3 (Boccara et al., 2015; Kjonigsen et al., 2015). Jugded by our material and consistent with observations in other mammals (guinea pig: Geneser-Jensen et al., 1974; rabbit: Geneser 1987), the polymorphic layer in sheep and pig consists of a minor Timm-negative subgranular zone and a major Timm-positive zone corresponding to the mossy fibre collateral plexus which according to our definition constitutes the border of the polymorphic layer with the subjacent CA3 end. The two zones correspond to the inner plexiform layer and the inner cellular layer, respectively, of the so-called "area dentata" defined by Holm and Geneser (1991b) in pig.

The mossy fibre collaterals were observed already by Camillo Golgi in 1886. The mossy fibres and their collateral plexus were illustrated in more detail by Ramon y Cajal (1911, his Figs. 478, 479, 482) in Golgi-stained sections of rabbit and guinea pig. Although Ramon y Cajal labelled the collateral plexus as "*l'assise des cellules polymorphes*", it is not clear if he regarded the plexus to define the border of the polymorphic layer with the CA3, as concluded by us. He did not, however, have at hand the Timm-method that was developed half a century later (Timm, 1958), enabling identification of the collaterals by their zinc-containing boutons, which inspired T.W. Blackstad (1963) to name the plexus "*the Z-zone*".

Despite the dense Timm-staining indicating a packing density of terminals in the plexus on a par with the mossy fibre bundle, the collateral plexus has been paid remarkably little attention in recent literature. Noteworthy exceptions are the brilliant studies by Claiborne et al. (1986) and Acsády et al. (1998) based on intracellular labeling of granule cells in rat. According to Claiborne et al. (1986), each mossy fibre in rat gives rise to 5-12 extremely thin branching and winding collaterals about 100-350 μm long extending in all directions. The

corresponding estimates of Acsády et al. (1998) are 5-8 and 400-700. Consistent with our observations in Golgi-sections from sheep and pig, both studies found the collaterals to be endowed with a few larger terminals, somewhat smaller than the giant terminals of the main fibres, as well as numerous smaller *en passant* presynaptic varicosities. Electron microscopically, the larger terminals have been found to be presynaptic to the mossy cell excrescences, while the *en passant* terminals synapse mainly on GABA-ergic interneurons (Laatsch & Cowan, 1966; Acsády et al., 1998), including basket cells. The numbers per granule cell are according to Claiborne et al. (1986) about 7 "giant" terminals (viz., about one per collateral) and 160 small varicosities; according to Acsády et al. (1998) 7-12 and 147, respectively, with some intermediate forms. In view of the high number of *en passant* terminals, the collaterals may be Timm-positive throughout most of their length, consistent with the density of the plexus in our Timm-stained sections.

Because in our Golgi-sections, the impregnated granule cells tended to occur in groups, single collaterals were seldom observed. Exact counts and measurements of the mossy fibre collaterals, therefore, were not possible. The number of 4 collaterals per mossy fibre measureing about 400 μm in the hidden-exposed dimension, as indicated in Figure 10A,C are only rough estimates based on the above mentioned data in rat adjusted by observations in Golgi-stained sections of sheep and pig at the periphery of areas with many impregnated granule cells. Interestingly, the estimated collaterals are compatible also with the hippocampal scheme by Ramon y Cajal (1911/1955, his Fig. 479). The intention with our Figure 10A, was to give an impression of the size of a collateral tree releative to the hidden-exposed length of the polymorphic layer, which in sheep and pig, thus, may give space for about eight segregated collateral trees side by side, in sharp contrast to the situation in rat where a single collateral tree covers almost the entire cross section of the polymorphic layer at septal levels (Claiborne et al.,1986, their Fig.7). In the perpendicular plane, thus, the degree of

overlap between collateral trees originating in the hidden and exposed parts of the granular layer must be considerably less in sheep and pig than in rat.

The mossy cells in sheep and pig are, largely in agreement with observations in other species (rat: Amaral, 1978; Scharfman & Myers, 2012; monkey: Buckmaster and Amaral, 2001; mink, Blackstad et al., 2016), located with their soma and excrescence-covered proximal dendrites within the collateral plexus while distal dendrites extend to areas outside the plexus including the granular and molecular layers (gm-dendrites), the subgranular zone, and the CA3 end (Fig. 10B). As indicated in Fig. 10B, the dendritic tree of each mossy cell in sheep and pig covers about 1/6 the length of the polymorphic layer, beeing in the same order of magnitude as the collateral trees. In rat, each mossy cell dendritic tree, like each collateral tree, fills in about the whole cross section of the polymorphic layer. In view of the length of the hippocampus, the overlap, may be less in the septotemporal dimension, even in rat.

By their the gm-dendrites, which increase in number from rat to human, the mossy cells may get direct, monosynaptic input from the perforant path (Scharfman, 1991, 2016), in addition to the disynaptic input to the excrescences from the mossy fibre collaterals (Scharfman, 1991; Acsády et al., 1998), and the three-synaptic back-projection from the CA3 pyramidal cells (Ishizuka et al., 1990; Buckmaster et al., 1993; Li et al., 1994; Scharfman, 1994; Wittner et al., 2007; Vivar et al., 2012). The strong glutamatergic input from the mossy fibre collaterals to the mossy cell excresences (Acsády et al., 1998), is potentially relevant in the context of possible exitotoxic death of mossy cells in epileptic rats (Blümcke et al., 1999; Blümcke et al., 2000).

The extension of distal mossy cell dendrites into the CA3 end, is a feature of particular relevance to the DG/CA3 border. Such extensions may be missing in rat (Amaral, 1978), minimal in mink (Blackstad et al., 2016), and extensive in monkey (Buckmaster & Amaral, 2001) as in sheep and pig, perhaps related to the phylogenetically shrinking depth of

the polymorphic layer and the "space-filling type of arborization" (Fiala & Harris, 2012) of

the mossy cells (Blackstad et al., 2016). The mossy cells, which also receive a rich supply

from subcortical regions through the fimbria (Scharfman, 2016, 2018), are thought to play an

integral part in the hippocampal circuitry by modulating the mossy fibre signals to the CA3

that are thought to be essential for episodic memory formation (Leutgeb et al., 2007; Treves et

al., 2008; Myers & Scharfman, 2009).

The subgranular zone of the polymorphic layer varies much in relative depth between

species, from being non-existent in rat (Haug, 1974), to barely visible in mink (Blackstad et

al., 2016), slim in human (Cassell & Brown, 1984) as in sheep and pig (present study), and

about 1/3 the thickness of the polymorphic layer in guinea pig (Geneser-Jensen et al., 1974)

and rabbit (Geneser, 1987b). Interestingly, it can also be observed in monkey (Kondo et al.,

2008; their Fig. 2). The zone constitutes the secondary germinal matrix of adult-born granule

cells (Guéneau et al., 1982; Deshpande et al., 2013), one of the few neuronal types reproduced

throughout life in mammals, which means that also the mossy fibres must in part be

transitory. The histological variation in soma size and dendritic thickness of granule cells

observed in sheep and pig, as well as in mink and other species (Blackstad et al., 2016), thus,

could possibly relate to different functional stages of a life cycle (Guéneau et al., 1982;

Brunner et al., 2014).. In species with an inconspicuous subgranular zone, the germinal cells

may possibly be intermingled with other cells in the polymorphic layer as during early

ontogenesis (Altman & Bayer, 1990a, 1990b, 1990c).

Scattered fibres and cells in the CA3 end

The expanded CA3 end in sheep and pig differs from the main part of the CA3 by the absence

of a dense mossy fibre bundle and a distinct pyramidal layer both of which are gradually

restored at the transition to the main CA3 (Fig. 10A,B). This special fibro-and

cytoarchitecture seems to be a function of the scattered transition of main mossy fibres from the collateral plexus with a corresponding scattering of main mossy fibres and pyramidal cells throughout the CA3 end.

The scattering of main mossy fibres is clearly consistent with previous Golgi-studies in guinea pig and rabbit (Ramon y Cajal, 1911, his Figs. 478, 480, 479) as well as with illustrations in previous Timm-studies in human (Sutula et al., 1989), domestic pig (Holm & Geneser, 1989, 1991b, 1991a) and guinea pig (Geneser-Jensen et al., 1974; Blackstad, 1985). In rat (Haug, 1974, his Fig.2e) and mink (Blackstad et al., 2016, their Fig. 1F), where the CA3 is stratified to its end, the mossy fibres in Timm-stained sections seem to enter the CA3 largely at the tip of the pyramidal layer. However, in the intracellular HRP-labelling experiments in rat (Claiborne et al 1986, their Fig. 14), and in Golgi-stained sections of mink (J.S. Blackstad et al., 2016, their Fig. 2A), additional main mossy fibres reach the pyramidal layer by passing through the adjacent radiate and oriens layers. The reason why these fibres don't show up in Timm-staining, is probably that the layers are composed mainly of distal pyramidal cell dendrites without postsynaptic excrescences, a feature also reflected in the fewer Timm-positive terminals in the cell poor zone of the CA3 end in sheep and pig compared to the cell rich zone A scattered transition of the main mossy fibres into the CA3 end, thus, may be a rule rather than an exception.

As shown electron microscopically in rat, the mossy fibres, which are unmyelinated with a diameter < 1 μm, tend to form minor bundles both within the deep portion of the polymorphic layer (Laatsch & Cowan, 1966) and the mossy fibre bundle (Blackstad & Kjaerheim, 1961). Despite the scattering of the mossy fibres in our Golgi-sections, a certain tendency to bundling might explain the distribution pattern of Timm-positive terminals within the CA3 end and the transitional region reminiscent of the infra- and suprapyramidal bundles in rat (Cappaert et al., 2015).

The scattering of the pyramidal cells in the CA3 end in sheep and pig is clearly related to the scattering of mossy fibres (Fig. 10A,B). The distribution of the pyramidal cells as well as the existence of three subtypes, resemble the pattern reported in monkey (Buckmaster & Amaral, 2001). It is unclear, however, whether the hidden-exposed gradient in the distribution of the apical and non-apical subtypes in sheep and pig applies also to monkey. The apical and dentate pyramidal cells, besides the disynaptic input through the mossy fibres, may also get monosynaptic input from the entorhinal cortex. The apical subtype receives perforant path input to their dendrites in the lacunar-molecular layer of the CA3, while the dentate subtype receives perforant path input to their gm-dendrites in the molecular layer of the DG (Ramon y Cajal, 1911/1955; Blackstad, 1956, his Fig. 13). The non-apical pyramidal cells, on the contrary, which dominate in the exposed part of the CA3 end, do not have dendrites to layers directly supplied by perforant path fibres, and thus may get only disynaptic input from the entorhinal cortex through the mossy fibres. With the exception of the dentate subtype, the pyramidal cells in the CA3 end of sheep and pig respect the border with the collateral plexus, like pyramidal cells in rat (Amaral, 1978; Ishizuka et al., 1995; Acsády et al., 1998) and mink (Blackstad et al., 2016).

It is reasonable to assume that the scattering of mossy fibres and pyramidal cells, coupled with the differentiation of the latter into subtypes, may promote a differentiated response to the perforant path signals conveyed to the CA1. The conditions for a differentiated response may be brought a step further in the human brain, where in addition to the larger CA3 end, the granular and molecular layers of the dentate gyrus become elongated and heavily folded (Cassell & Brown, 1984; Sutula et al., 1989) in accord with the term *fascia dentata* often used for the molecular and granular layers together also in sub-primate species (Blackstad, 1956, 1958).

By its loose packing of the pyramidal layer and concomitant splitting of the mossy

fibre bundle, the transitional region from the CA3 end to main CA3 in sheep resembles the

DG near end of the pyramidal layer in rat, referred to as CA3c (Lorente de Nó, 1934).In

sheep, the CA3 end and the transitional region together constitute about 2/3 the total length of

the CA3, while the remaining 1/3 exhibits a dense pyramidal layer with a compact mossy

fibre bundle. In human, the CA3, which also appears relatively shorter than in rat, is made up

entirely of an expanded CA3 end and a loose pyramidal layer with only traces of a dense

mossy fibre bundle (Cassell & Brown, 1984; Sutula et al., 1989). In view of the various

subtypes of pyramidal cells described by Amaral (1978, his Fig. 1A) in his looser zone 1 of

the rat pyramidal layer, it is tempting to regard this as a precursor of the expanded CA3 end.

Geometry of granule cell systems

The so-called lamellar organization of the hippocampal mossy fibres (Andersen et al., 1969;

Blackstad et al., 1970; Andersen et al., 1971), in the sense of a parallel orientation of the main

granule cell axons, is a feature shared with the granule cell systems in the cerebellum (see,

e.g. Voogd and Glickstein, 1998; D'Angelo, 2018) and the cochlear nuclear complex (Oertel

& Young, 2004; Yaeger & Trussell, 2015). The three systems are all characterized by a large

amount of minute granule cell bodies exhibiting unramified, unmyelinated axons endowed

with *én passage* synapses, and coursing in parallel perpendicular to the target neurons which

are also oriented in parallel, thus forming a strict geometrical pattern. While in all three sites,

the granule cell somata are situated deep to the molecular layer, the location of the granule

cell dendrites and axons differs. In the cerebellum and the cochlear nuclear complex (which

both originate from the rhombic lip; see, e.g. Leto et al., 2016; Wullimann et al., 2011;

Giacomo Consalez et al., 2020), the short granule cell dendrites are situated in between the

somata in the granule cell layer, while the axons and their target cells, Purkinje and pyramidal

cells respectively, occupy the molecular layer (Mugnaini et al., 1980a; Mugnaini et al., 1980b; Blackstad et al., 1984; Voogd & Glickstein, 1998). In the hippocampus, on the contrary, the granule cell dendrites extend into the molecular layer while the axons and their target pyramidal neurons occupy the neighbouring brain area CA3 (van Strien et al., 2009; Cappaert et al., 2015). The difference might possibly relate to the phylogenetically late development of the DG granule cell system , with the granule cell dendrites growing towards the afferent perforant path fibers and the mossy fibres invading the CA3 (Bayer, 1980; Altman & Bayer, 1990a, 1990b, 1990c; Donato et al., 2017).

The granule cell system of the DG is unique also by its mossy fibre collateral plexus and the related polymorphic layer with mossy cells and other cells contributing to the back projection to the granule cells (Blackstad, 1956; Zimmer, 1971; Laurberg, 1979; Claiborne et al., 1986; Acsády et al., 1998; Scharfman & Myers, 2012). The location of the granule cell somata, dendrites and the majority of related interneurons in separate layers in the DG, is consistent with the higher packing density of the granular layer in the DG, compared to the other regions, as reflected in the official name "granular layer" in the DG as opposed to "granule cell layer" in the cerebellum and cochlear nucleus.

The three regions with a granule cell system are all characterized by an extensive contact with other brain regions indicative of the integration and analysis of a large amount of information from different sources as expected for the "pattern separation" or "filtering" of signals. In analogy with the hippocampal circuitry, one may, with some imagination, define circuitries reciprocally interconnecting the granule cell systems with the cerebral cortex also for the cerebellum and the cochlear nuclear complex.

Conclusion

Our findings lend support to the notion that a DG/CA3 boundary defined by the plexus of mossy fibre collaterals, is of general validity in mammals despite the interspecies variation in the topography of the polymorphic layer and the CA3 end. The borderline coincides largely with the generally accepted one, but it is more precise, and it is valid irrespective of whether the polymorphic layer has a triangular cross section as in rat (Haug, 1974) or a thin band capping the expanded CA3 end as in sheep, pig, monkey (Buckmaster & Amaral, 2001) and human (Cassel and Brown, 1984; Sutula et al., 1989). There is, however, still a need for further phylogenetic studies of the DG and CA3 end in an ontogenetic perspective with attention to the late development of granule cells, mossy cells and perforant path enabling input to the hippocampus proper from the entorhinal cortex via the dentate gyrus, in addition to the direct input to the lacunar-molecular layer of the CA3 and CA1 (Blackstad, 1956 his fig.13; Ramon y Cajal, 1911, his Fig. 479), and the original input to the CA3 from subcortical regions through the fimbria (emphasized by Scharfman, 2007).

REFERENCES

Acsády, L., Kamondi, A., Sík, A., Freund, T., & Buzsáki, G. (1998). GABAergic cells are the major postsynaptic targets of mossy fibers in the rat hippocampus. *J Neurosci, 18*(9), 3386-3403. doi:10.1523/jneurosci.18-09-03386.1998

Altman, J., & Bayer, S. A. (1990a). Migration and distribution of two populations of hippocampal granule cell precursors during the perinatal and postnatal periods. *J Comp Neurol, 301*(3), 365-381. doi:10.1002/cne.903010304

Altman, J., & Bayer, S. A. (1990b). Mosaic organization of the hippocampal neuroepithelium and the multiple germinal sources of dentate granule cells. *J Comp Neurol, 301*(3), 325-342. doi:10.1002/cne.903010302

Altman, J., & Bayer, S. A. (1990c). Prolonged sojourn of developing pyramidal cells in the intermediate zone of the hippocampus and their settling in the stratum pyramidale. *J Comp Neurol, 301*(3), 343-364. doi:10.1002/cne.903010303

Amaral, D. G. (1978). A Golgi study of cell types in the hilar region of the hippocampus in the rat. *J Comp Neurol, 182*(4 Pt 2), 851-914.

Amaral, D. G., Scharfman, H. E., & Lavenex, P. (2007). The dentate gyrus: fundamental neuroanatomical organization (dentate gyrus for dummies). *Prog Brain Res, 163*, 3-22. doi:10.1016/s0079-6123(07)63001-5

Amaral, D. G., & Witter, M. P. (1989). The three-dimensional organization of the hippocampal formation: a review of anatomical data. *Neuroscience, 31*(3), 571-591. doi:10.1016/0306-4522(89)90424-7

Andersen, P., Bliss, T. V., Lomo, T., Olsen, L. I., & Skrede, K. K. (1969). Lamellar organization of hippocampal excitatory pathways. *Acta Physiol Scand, 76*(1), 4a-5a. doi:10.1111/j.1748-1716.1969.tb04499.x

Andersen, P., Bliss, T. V., & Skrede, K. K. (1971). Lamellar organization of hippocampal pathways. *Exp Brain Res, 13*(2), 222-238. doi:10.1007/bf00234087

Bayer, S. A. (1980). Development of the hippocampal region in the rat. II. Morphogenesis during embryonic and early postnatal life. *J Comp Neurol, 190*(1), 115-134. doi:10.1002/cne.901900108

Blackstad, J. S., Osen, K. K., Scharfman, H. E., Storm-Mathisen, J., Blackstad, T. W., & Leergaard, T. B. (2016). Observations on hippocampal mossy cells in mink (Neovison vison) with special reference to dendrites ascending to the granular and molecular layers. *Hippocampus, 26*(2), 229-245. doi:10.1002/hipo.22518

Blackstad, T. W. (1956). Commissural connections of the hippocampal region in the rat, with special reference to their mode of termination. *J Comp Neurol, 105*(3), 417-537. doi:10.1002/cne.901050305

Blackstad, T. W. (1958). On the termination of some afferents to the hippocampus and fascia dentata. *Cells Tissues Organs, 35*(3), 202-214. doi:10.1159/000141409

Blackstad, T. W. (1963). Ultrastructural Studies on the Hippocampal Region. In W. Bargmann & J. P. Schadé (Eds.), *Prog Brain Res* (Vol. 3, pp. 122-148): Elsevier.

Blackstad, T. W. (1985). Laminar specificity of dendritic morphology: Examples from the guinea pig hippocampal region. In F. K. Agnati L (Ed.), *Quantitative Neuroanatomy in Transmitter Research* (pp. 55–69.). New York and London: Plenum Press.

Blackstad, T. W., Brink, K., Hem, J., & Jeune, B. (1970). Distribution of hippocampal mossy fibers in the rat. An experimental study with silver impregnation methods. *J Comp Neurol, 138*(4), 433-449. doi:10.1002/cne.901380404

Blackstad, T. W., & Kjaerheim, A. (1961). Special axo-dendritic synapses in the hippocampal cortex: electron and light microscopic studies on the layer of mossy fibers. *J Comp Neurol, 117*, 133-159. doi:10.1002/cne.901170202

Blackstad, T. W., Osen, K. K., & Mugnaini, E. (1984). Pyramidal neurones of the dorsal cochlear nucleus: a Golgi and computer reconstruction study in cat. *Neuroscience, 13*(3), 827-854. doi:10.1016/0306-4522(84)90099-x

Blümcke, I., Suter, B., Behle, K., Kuhn, R., Schramm, J., Elger, C. E., & Wiestler, O. D. (2000). Loss of hilar mossy cells in Ammon's horn sclerosis. *Epilepsia, 41 Suppl 6*, S174-180. doi:10.1111/j.1528-1157.2000.tb01577.x

Blümcke, I., Zuschratter, W., Schewe, J. C., Suter, B., Lie, A. A., Riederer, B. M., . . . Wiestler, O. D. (1999). Cellular pathology of hilar neurons in Ammon's horn sclerosis. *J Comp Neurol, 414*(4), 437-453. doi:10.1002/(sici)1096-9861(19991129)414:4<437::aid-cne2>3.0.co;2-3

Boccara, C. N., Kjonigsen, L. J., Hammer, I. M., Bjaalie, J. G., Leergaard, T. B., & Witter, M. P. (2015). A three-plane architectonic atlas of the rat hippocampal region. *Hippocampus, 25*(7), 838-857. doi:10.1002/hipo.22407

Brunner, J., Neubrandt, M., Van-Weert, S., Andrási, T., Kleine Borgmann, F. B., Jessberger, S., & Szabadics, J. (2014). Adult-born granule cells mature through two functionally distinct states. *Elife, 3*, e03104. doi:10.7554/eLife.03104

Buckmaster, P. S. (2012). Mossy cell dendritic structure quantified and compared with other hippocampal neurons labeled in rats in vivo. *Epilepsia, 53 Suppl 1*(Suppl 1), 9-17. doi:10.1111/j.1528-1167.2012.03470.x

Buckmaster, P. S., & Amaral, D. G. (2001). Intracellular recording and labeling of mossy cells and proximal CA3 pyramidal cells in macaque monkeys. *J Comp Neurol, 430*(2), 264-281. doi:10.1002/1096-9861(20010205)430:2<264::aid-cne1030>3.0.co;2-3

Buckmaster, P. S., Strowbridge, B. W., & Schwartzkroin, P. A. (1993). A comparison of rat hippocampal mossy cells and CA3c pyramidal cells. *J Neurophysiol, 70*(4), 1281-1299. doi:10.1152/jn.1993.70.4.1281

Buckmaster, P. S., Wenzel, H. J., Kunkel, D. D., & Schwartzkroin, P. A. (1996). Axon arbors and synaptic connections of hippocampal mossy cells in the rat in vivo. *J Comp Neurol, 366*(2), 271-292. doi:10.1002/(sici)1096-9861(19960304)366:2<270::aid-cne7>3.0.co;2-2

Cajal, R. y. (1955). *Histologie du systeme nerveux de l'homme et des vertebres. T.II.* Paris: A. Maloine 1911; reprinted Madrid: Instituto Cajal.

Cappaert, N. L. M., van Strien, N., & Witter, M. (2015). Chapter 20. Hippocampal Formation (pp. 511-573).

Cassell, M. D., & Brown, M. W. (1984). The distribution of Timm's stain in the nonsulphide-perfused human hippocampal formation. *J Comp Neurol, 222*(3), 461-471. doi:10.1002/cne.902220311

Claiborne, B. J., Amaral, D. G., & Cowan, W. M. (1986). A light and electron microscopic analysis of the mossy fibers of the rat dentate gyrus. *J Comp Neurol, 246*(4), 435-458. doi:10.1002/cne.902460403

Consalez, G. G., Goldowitz, D., Casoni, F., & Hawkes, R. (2020). Origins, Development, and Compartmentation of the Granule Cells of the Cerebellum. *Front Neural Circuits, 14*, 611841. doi:10.3389/fncir.2020.611841

D'Angelo, E., Mazzarello, P., Prestori, F., Mapelli, J., Solinas, S., Lombardo, P., . . . Congi, L. (2011). The cerebellar network: From structure to function and dynamics. *Brain Research Reviews, 66*(1), 5-15. doi:https://doi.org/10.1016/j.brainresrev.2010.10.002

Danscher, G. (1981). Histochemical demonstration of heavy metals. A revised version of the sulphide silver method suitable for both light and electronmicroscopy. *Histochemistry, 71*(1), 1-16. doi:10.1007/bf00592566

Deshpande, A., Bergami, M., Ghanem, A., Conzelmann, K.-K., Lepier, A., Götz, M., & Berninger, B. (2013). Retrograde monosynaptic tracing reveals the temporal evolution of inputs onto new neurons in the adult dentate gyrus and olfactory bulb. *Proceedings of the National Academy of Sciences, 110*(12), E1152-E1161. doi:10.1073/pnas.1218991110

Donato, F., Jacobsen, R. I., Moser, M. B., & Moser, E. I. (2017). Stellate cells drive maturation of the entorhinal-hippocampal circuit. *Science, 355*(6330). doi:10.1126/science.aai8178

Eckenhoff, M. F., & Rakic, P. (1984). Radial organization of the hippocampal dentate gyrus: a Golgi, ultrastructural, and immunocytochemical analysis in the developing rhesus monkey. *J Comp Neurol, 223*(1), 1-21. doi:10.1002/cne.902230102

Fiala, J., & Harris, K. (2012). Dendrite structure. *Dendrites*. doi:10.1093/acprof:oso/9780198566564.003.0001

Freund, T. F., & Buzsáki, G. (1996). Interneurons of the hippocampus. *Hippocampus, 6*(4), 347-470. doi:10.1002/(sici)1098-1063(1996)6:4<347::Aid-hipo1>3.0.Co;2-i

Geneser-Jensen, F. A., Haug, F. M., & Danscher, G. (1974). Distribution of heavy metals in the hippocampal region of the guinea pig. A light microscope study with Timm's sulfide silver method. *Z Zellforsch Mikrosk Anat, 147*(4), 441-478. doi:10.1007/bf00307249

Geneser, F. A. (1987a). Distribution of acetylcholinesterase in the hippocampal region of the rabbit: II. Subiculum and hippocampus. *J Comp Neurol, 262*(1), 90-104. doi:10.1002/cne.902620108

Geneser, F. A. (1987b). Distribution of acetylcholinesterase in the hippocampal region of the rabbit: III. The dentate area. *J Comp Neurol, 262*(4), 594-606. doi:10.1002/cne.902620411

Godina, G., & Barasa, A. (1964). [MORPHOGENESIS AND HISTOGENESIS OF THE HORN OF AMMON]. *Z Zellforsch Mikrosk Anat, 63*, 327-355.

Golgi, C. (1886). *Sulla Fina Anatomia Degli Organi Centrali del Sistema Nervoso*. Milano: Hoepli.

Guéneau, G., Privat, A., Drouet, J., & Court, L. (1982). Subgranular zone of the dentate gyrus of young rabbits as a secondary matrix. A high-resolution autoradiographic study. *Dev Neurosci, 5*(4), 345-358. doi:10.1159/000112694

Gaarskjaer, F. B. (1978). Organization of the mossy fiber system of the rat studied in extended hippocampi. II. Experimental analysis of fiber distribution with silver impregnation methods. *J Comp Neurol, 178*(1), 73-88. doi:10.1002/cne.901780105

Gaarskjaer, F. B., Danscher, G., & West, M. J. (1982). Hippocampal mossy fibers in the regio superior of the European hedgehog. *Brain Res, 237*(1), 79-90. doi:10.1016/0006-8993(82)90558-3

Haug, F.-M. Š. (1973). Heavy metals in the brain. A light microscope study of the rat with Timm's sulphide silver method. Methodological considerations and cytological and regional staining patterns. *Adv Anat Embryol Cell Biol, 47*(4), 1-71.

Haug, F.-M. Š. (1974). Light microscopical mapping of the hippocampal region, the pyriform cortex and the corticomedial amygdaloid nuclei of the rat with Timm's sulphide silver method. *Zeitschrift für Anatomie und Entwicklungsgeschichte, 145*(1), 1-27. doi:10.1007/BF00519123

Hjorth-Simonsen, A. (1972). Projection of the lateral part of the entorhinal area to the hippocampus and fascia dentata. *J Comp Neurol, 146*(2), 219-232. doi:10.1002/cne.901460206

Hjorth-Simonsen, A., & Jeune, B. (1972). Origin and termination of the hippocampal perforant path in the rat studied by silver impregnation. *J Comp Neurol, 144*(2), 215-232. doi:10.1002/cne.901440206

Holm, I. E., & Geneser, F. A. (1989). Histochemical demonstration of zinc in the hippocampal region of the domestic pig: I. Entorhinal area, parasubiculum, and presubiculum. *J Comp Neurol, 287*(2), 145-163. doi:10.1002/cne.902870202

Holm, I. E., & Geneser, F. A. (1991a). Histochemical demonstration of zinc in the hippocampal region of the domestic pig: II. Subiculum and hippocampus. *J Comp Neurol, 305*(1), 71-82. doi:10.1002/cne.903050108

Holm, I. E., & Geneser, F. A. (1991b). Histochemical demonstration of zinc in the hippocampal region of the domestic pig: III. The dentate area. *J Comp Neurol, 308*(3), 409-417. doi:10.1002/cne.903080308

Ishizuka, N., Cowan, W. M., & Amaral, D. G. (1995). A quantitative analysis of the dendritic organization of pyramidal cells in the rat hippocampus. *J Comp Neurol, 362*(1), 17-45. doi:10.1002/cne.903620103

Ishizuka, N., Weber, J., & Amaral, D. G. (1990). Organization of intrahippocampal projections originating from CA3 pyramidal cells in the rat. *J Comp Neurol, 295*(4), 580-623. doi:10.1002/cne.902950407

Jensen, F. G. (1975). *Histochemical studies on the hippocampal region of the guinea pig*. Denmark: Aarhus [Denmark : s.n.], 1975.

Kjonigsen, L. J., Leergaard, T. B., Witter, M. P., & Bjaalie, J. G. (2011). Digital atlas of anatomical subdivisions and boundaries of the rat hippocampal region. *Front Neuroinform, 5*, 2. doi:10.3389/fninf.2011.00002

Kjonigsen, L. J., Lillehaug, S., Bjaalie, J. G., Witter, M. P., & Leergaard, T. B. (2015). Waxholm Space atlas of the rat brain hippocampal region: three-dimensional delineations based on magnetic resonance and diffusion tensor imaging. *Neuroimage, 108*, 441-449. doi:10.1016/j.neuroimage.2014.12.080

Kondo, H., Lavenex, P., & Amaral, D. G. (2008). Intrinsic connections of the macaque monkey hippocampal formation: I. Dentate gyrus. *J Comp Neurol, 511*(4), 497-520. doi:10.1002/cne.21825

Kowalski, J., Geuting, M., Paul, S., Dieni, S., Laurens, J., Zhao, S., . . . Vida, I. (2010). Proper layering is important for precisely timed activation of hippocampal mossy cells. *Cereb Cortex, 20*(9), 2043-2054. doi:10.1093/cercor/bhp267

Laurberg, S. (1979). Commissural and intrinsic connections of the rat hippocampus. *Journal of Comparative Neurology, 184*(4), 685-708. doi:https://doi.org/10.1002/cne.901840405

Laurberg, S., & Sorensen, K. E. (1981). Associational and commissural collaterals of neurons in the hippocampal formation (hilus fasciae dentatae and subfield CA3). *Brain Res, 212*(2), 287-300.

Lavenex, P., Banta Lavenex, P., & Amaral, D. G. (2007). Postnatal Development of the Primate Hippocampal Formation. *Developmental Neuroscience, 29*(1-2), 179-192. doi:10.1159/000096222

Leto, K., Arancillo, M., Becker, E. B., Buffo, A., Chiang, C., Ding, B., . . . Hawkes, R. (2016). Consensus Paper: Cerebellar Development. *Cerebellum, 15*(6), 789-828. doi:10.1007/s12311-015-0724-2

Leutgeb, J. K., Leutgeb, S., Moser, M. B., & Moser, E. I. (2007). Pattern separation in the dentate gyrus and CA3 of the hippocampus. *Science, 315*(5814), 961-966. doi:10.1126/science.1135801

Li, X. G., Somogyi, P., Ylinen, A., & Buzsáki, G. (1994). The hippocampal CA3 network: an in vivo intracellular labeling study. *J Comp Neurol, 339*(2), 181-208. doi:10.1002/cne.903390204

Lorente de Nó, R. (1934). Studies on the structure of the cerebral cortex. II. Continuation of the study of the ammonic system. *Journal für Psychologie und Neurologie, 46*, 113-177.

Laatsch, R. H., & Cowan, W. M. (1966). Electron microscopic studies of the dentate gyrus of the rat. I. Normal structure with special reference to synaptic organization. *J Comp Neurol, 128*(3), 359-395. doi:10.1002/cne.901280305

Maguire, E. A., Frackowiak, R. S., & Frith, C. D. (1997). Recalling routes around london: activation of the right hippocampus in taxi drivers. *J Neurosci, 17*(18), 7103-7110.

Minervini, S., Accogli, G., Pirone, A., Graïc, J. M., Cozzi, B., & Desantis, S. (2016). Brain Mass and Encephalization Quotients in the Domestic Industrial Pig (Sus scrofa). *PLoS One, 11*(6), e0157378. doi:10.1371/journal.pone.0157378

Moser, E. I., Moser, M. B., & McNaughton, B. L. (2017). Spatial representation in the hippocampal formation: a history. *Nat Neurosci, 20*(11), 1448-1464. doi:10.1038/nn.4653

Mugnaini, E., Osen, K. K., Dahl, A. L., Friedrich, V. L., Jr., & Korte, G. (1980a). Fine structure of granule cells and related interneurons (termed Golgi cells) in the cochlear nuclear complex of cat, rat and mouse. *J Neurocytol, 9*(4), 537-570. doi:10.1007/bf01204841

Mugnaini, E., Warr, W. B., & Osen, K. K. (1980b). Distribution and light microscopic features of granule cells in the cochlear nuclei of cat, rat, and mouse. *J Comp Neurol, 191*(4), 581-606. doi:10.1002/cne.901910406

Murakawa, R., & Kosaka, T. (2001). Structural features of mossy cells in the hamster dentate gyrus, with special reference to somatic thorny excrescences. *J Comp Neurol, 429*(1), 113-126. doi:10.1002/1096-9861(20000101)429:1<113::aid-cne9>3.0.co;2-d

Myers, C. E., & Scharfman, H. E. (2009). A role for hilar cells in pattern separation in the dentate gyrus: a computational approach. *Hippocampus, 19*(4), 321-337. doi:10.1002/hipo.20516

O'Keefe, J., & Nadel, L. (1978). *The hippocampus as a cognitive map*: Clarendon Press.

Oertel, D., & Young, E. D. (2004). What's a cerebellar circuit doing in the auditory system? *Trends Neurosci, 27*(2), 104-110. doi:10.1016/j.tins.2003.12.001

Osen, K. K., Storm-Mathisen, J., Ottersen, O. P., & Dihle, B. (1995). Glutamate is concentrated in and released from parallel fiber terminals in the dorsal cochlear nucleus: a quantitative immunocytochemical analysis in guinea pig. *J Comp Neurol, 357*(3), 482-500. doi:10.1002/cne.903570311

Ramón y Cajal, S. (1909). *Histologie du système nerveux de l'homme & des vertébrés* (Ed. française rev. & mise à jour par l'auteur, tr. de l'espagnol par L. Azoulay. ed. Vol. v. 1). Paris :: Maloine.

Ramón y Cajal, S. (1911). *Histologie du systéme nerveux de l'homme et des vertébrés. T.II.* Paris, Malonie.

Ribak, C. E., Seress, L., & Amaral, D. G. (1985). The development, ultrastructure and synaptic connections of the mossy cells of the dentate gyrus. *J Neurocytol, 14*(5), 835-857.

Rose, J. E. (1942). A cytoarchitectural study of the sheep cortex. *Journal of Comparative Neurology, 76*(1), 1-55. doi:https://doi.org/10.1002/cne.900760102

Schaffer, K. (1892). Beitrag zur Histologie der Ammonshornformation. *Arch mikroskop Anatomie, 39*, 611–632.

Scharfman, H. E. (1991). Dentate hilar cells with dendrites in the molecular layer have lower thresholds for synaptic activation by perforant path than granule cells. *J Neurosci, 11*(6), 1660-1673. doi:10.1523/jneurosci.11-06-01660.1991

Scharfman, H. E. (1994). EPSPs of dentate gyrus granule cells during epileptiform bursts of dentate hilar "mossy" cells and area CA3 pyramidal cells in disinhibited rat hippocampal slices. *J Neurosci, 14*(10), 6041-6057. doi:10.1523/jneurosci.14-10-06041.1994

Scharfman, H. E. (2016). The enigmatic mossy cell of the dentate gyrus. *Nat Rev Neurosci, 17*(9), 562-575. doi:10.1038/nrn.2016.87

Scharfman, H. E. (2018). Advances in understanding hilar mossy cells of the dentate gyrus. *Cell Tissue Res, 373*(3), 643-652. doi:10.1007/s00441-017-2750-5

Scharfman, H. E., & Myers, C. E. (2012). Hilar mossy cells of the dentate gyrus: a historical perspective. *Front Neural Circuits, 6*, 106. doi:10.3389/fncir.2012.00106

Scharfman, H. E., & Schwartzkroin, P. A. (1988). Electrophysiology of morphologically identified mossy cells of the dentate hilus recorded in guinea pig hippocampal slices. *J Neurosci, 8*(10), 3812-3821. doi:10.1523/jneurosci.08-10-03812.1988

Scoville, W. B., & Milner, B. (1957). Loss of recent memory after bilateral hippocampal lesions. *J Neurol Neurosurg Psychiatry, 20*(1), 11-21. doi:10.1136/jnnp.20.1.11

Senzai, Y. (2019). Function of local circuits in the hippocampal dentate gyrus-CA3 system. *Neuroscience Research, 140*, 43-52. doi:https://doi.org/10.1016/j.neures.2018.11.003

Seress, L. (2007). Comparative anatomy of the hippocampal dentate gyrus in adult and developing rodents, non-human primates and humans. *Prog Brain Res, 163*, 23-41. doi:10.1016/s0079-6123(07)63002-7

Seress, L., & Frotscher, M. (1990). Morphological variability is a characteristic feature of granule cells in the primate fascia dentata: a combined Golgi/electron microscope study. *J Comp Neurol, 293*(2), 253-267. doi:10.1002/cne.902930208

Seress, L., & Mrzljak, L. (1992). Postnatal development of mossy cells in the human dentate gyrus: a light microscopic Golgi study. *Hippocampus, 2*(2), 127-141. doi:10.1002/hipo.450020205

Sloviter, R. S., & Lømo, T. (2012). Updating the lamellar hypothesis of hippocampal organization. *Front Neural Circuits, 6*, 102. doi:10.3389/fncir.2012.00102

Soriano, E., & Frotscher, M. (1994). Mossy cells of the rat fascia dentata are glutamate-immunoreactive. *Hippocampus, 4*(1), 65-69. doi:10.1002/hipo.450040108

Squire, L. R. (1992). Memory and the hippocampus: A synthesis from findings with rats, monkeys, and humans. *Psychological Review, 99*(2), 195-231. doi:10.1037/0033-295X.99.2.195

Steinhausen, C., Zehl, L., Haas-Rioth, M., Morcinek, K., Walkowiak, W., & Huggenberger, S. (2016). Multivariate Meta-Analysis of Brain-Mass Correlations in Eutherian Mammals. *Frontiers in Neuroanatomy, 10*(91). doi:10.3389/fnana.2016.00091

Steward, O. (1976). Topographic organization of the projections from the entorhinal area to the hippocampal formation of the rat. *J Comp Neurol, 167*(3), 285-314. doi:10.1002/cne.901670303

Sutula, T., Cascino, G., Cavazos, J., Parada, I., & Ramirez, L. (1989). Mossy fiber synaptic reorganization in the epileptic human temporal lobe. *Ann Neurol, 26*(3), 321-330. doi:10.1002/ana.410260303

Swanson, L., Sawchenko, P., & Cowan, W. (1981). Evidence for collateral projections by neurons in Ammon's horn, the dentate gyrus, and the subiculum: a multiple retrograde labeling study in the rat. *The Journal of Neuroscience, 1*(5), 548-559. doi:10.1523/jneurosci.01-05-00548.1981

Swanson, L. W., Wyss, J. M., & Cowan, W. M. (1978). An autoradiographic study of the organization of intrahippocampal association pathways in the rat. *J Comp Neurol, 181*(4), 681-715. doi:10.1002/cne.901810402

Timm, F. (1958). Dtsch. Z. für Gerichtl. Med*., 46*, 706-711.

Treves, A., Tashiro, A., Witter, M. P., & Moser, E. I. (2008). What is the mammalian dentate gyrus good for? *Neuroscience, 154*(4), 1155-1172. doi:10.1016/j.neuroscience.2008.04.073

van Strien, N. M., Cappaert, N. L., & Witter, M. P. (2009). The anatomy of memory: an interactive overview of the parahippocampal-hippocampal network. *Nat Rev Neurosci, 10*(4), 272-282. doi:10.1038/nrn2614

Vivar, C., Potter, M. C., Choi, J., Lee, J. Y., Stringer, T. P., Callaway, E. M., . . . van Praag, H. (2012). Monosynaptic inputs to new neurons in the dentate gyrus. *Nat Commun, 3*, 1107. doi:10.1038/ncomms2101

Voogd, J., & Glickstein, M. (1998). The anatomy of the cerebellum. *Trends in Neurosciences, 21*(9), 370-375. doi:https://doi.org/10.1016/S0166-2236(98)01318-6

Witter, M. P., Van Hoesen, G. W., & Amaral, D. G. (1989). Topographical organization of the entorhinal projection to the dentate gyrus of the monkey. *J Neurosci, 9*(1), 216-228. doi:10.1523/jneurosci.09-01-00216.1989

Wittner, L., Henze, D. A., Záborszky, L., & Buzsáki, G. (2007). Three-dimensional reconstruction of the axon arbor of a CA3 pyramidal cell recorded and filled in vivo. *Brain Struct Funct, 212*(1), 75-83. doi:10.1007/s00429-007-0148-y

Wullimann, M., Mueller, T., Distel, M., Babaryka, A., Grothe, B., & Köster, R. (2011). The Long Adventurous Journey of Rhombic Lip Cells in Jawed Vertebrates: A Comparative Developmental Analysis. *Frontiers in Neuroanatomy, 5*(27). doi:10.3389/fnana.2011.00027

Yaeger, D. B., & Trussell, L. O. (2015). Single granule cells excite Golgi cells and evoke feedback inhibition in the cochlear nucleus. *J Neurosci, 35*(11), 4741-4750. doi:10.1523/jneurosci.3665-14.2015

Zimmer, J. (1971). Ipsilateral afferents to the commissural zone of the fascia dentata, demonstrated in decommissurated rats by silver impregnation. *J Comp Neurol, 142*(4), 393-416. doi:10.1002/cne.901420402
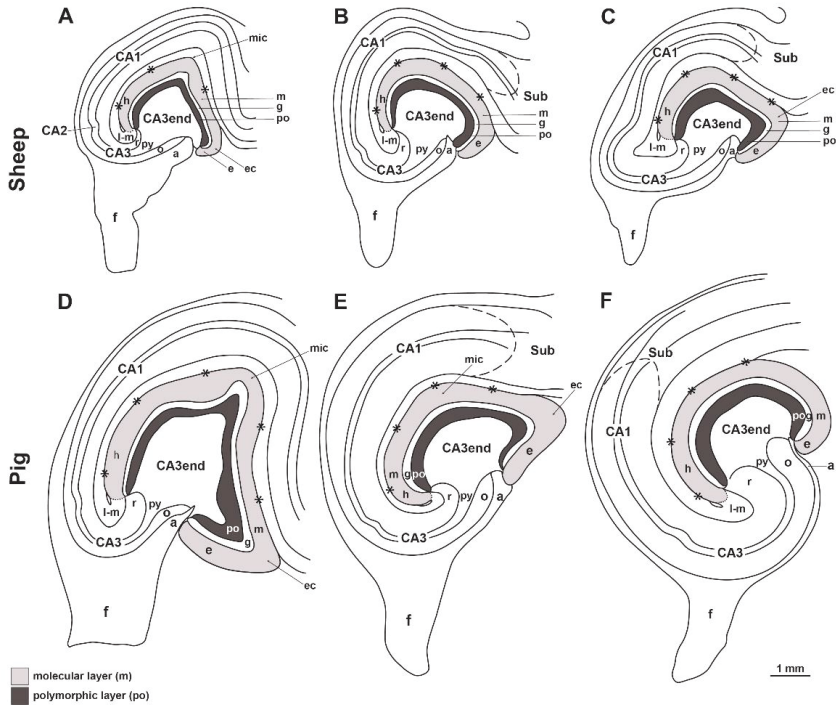
Figure 1. Diagrams of the dentate gyrus and the CA3 end in sheep and pig

Camera lucida drawings of the DG and the CA3 end in sheep (A-C) and pig (D-F) based on Golgi-stained sections cut perpendicular to the long septotemporal axis of the hippocampus at septal (A,D), middle (B,E), and temporal (C,F) levels, in sheep aided by Timm-thionin-stained sections from alternating tissue blocks. Being cut from different blocks, the sections are arbitrarily aligned with respect to each other. The hippocampal fissure is marked by asterisks and a loop in the end. **Abbr.**: a, alveus; CA1, cornu ammonis area 1; CA2, cornu ammonis area 2; CA3, cornu ammonis area 3; eb, exposed blade; ec, exposed crest; f, fimbria; g, granular layer; h, hidden blade; l-m: lacunar-molecular layer; m, molecular layer; mic, middle crest; o, oriens layer; po, polymorphic layer; py, pyramidal layer; r, radiate layer; Sub, subiculum.
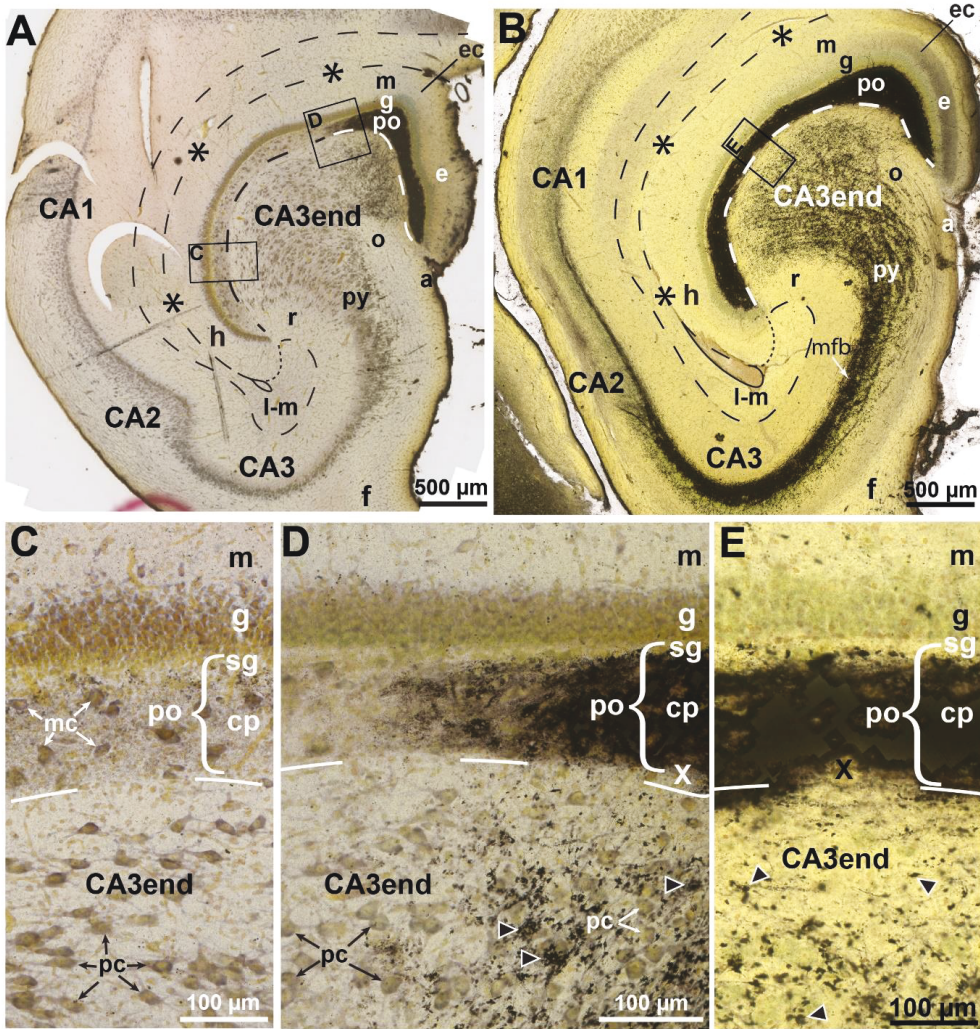
Figure 2. The sheep dentate gyrus and CA3 end in Timm-thionin-staining

Photomicrographs of Timm-thionin-stained sections cut perpendicular to the approximate middle of the long septotemporal axis of the hippocampus, (A,C,D) with predominance of thionin-staining except in the most exposed part. (C,D,E) are higher magnifications of the boxed areas in (A,B). In (B), a trace of the three-partition of the molecular layer (m) is seen in the exposed blade (e). The polymorphic layer (po) consists of the Timm-positive mossy fiber collateral plexus (cp) and the Timm-negative subgranular zone (sg) (C-E). The hippocampal fissure is marked by stipples and asterisks and a loop in the end, the po/CA3 border and the

lacunar-molecular layer (m-l) by stippling apart for the dotted border with the molecular layer (m), and mossy fiber giant terminals by black arrowheads. **Abbr**.: a, alveus; CA1, cornu ammonis area 1; CA2, cornu ammonis area 2; CA3, cornu ammonis area 3; e, exposed blade; ec, exposed crest; f, fimbria; g, granular layer; h, hidden blade; mc, mossy cell; mfb, mossy fibre bundle; o, oriens layer; pc, pyramidal cell; py, pyramidal layer; r, radiate layer; x, excavation in the cp.
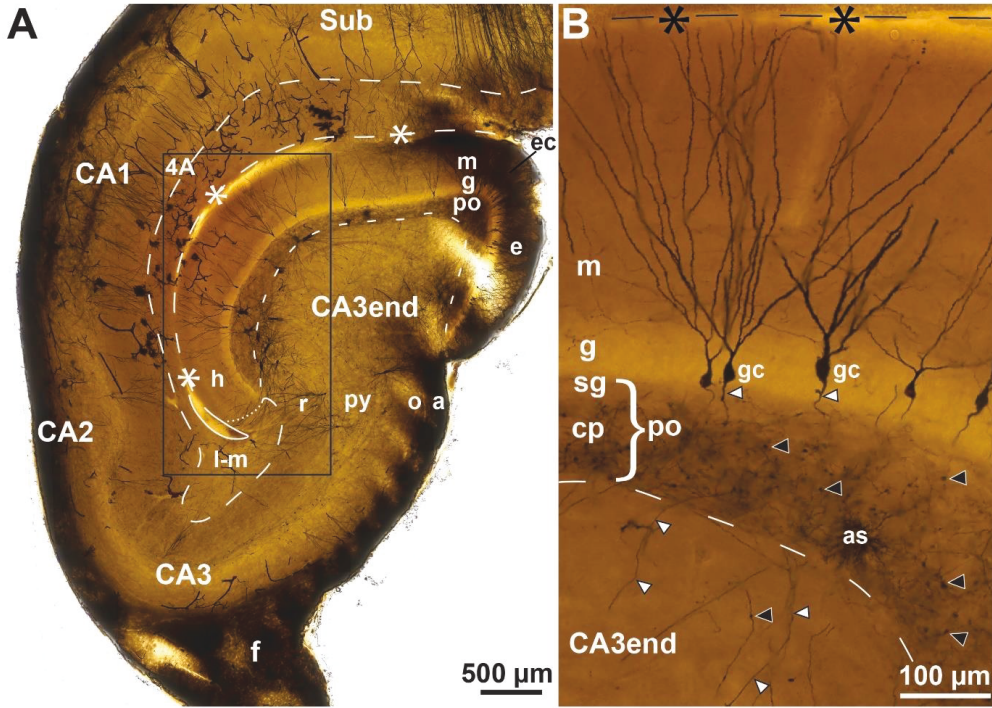
Figure 3. Collateral plexus in Golgi sections of sheep

Photomicrographs of Golgi-stained sections cut perpendicular to the long septotemporal axis
of the hippocampus, at temporal (A) and middle (B) levels. The boxed area in (A) is shown at
higher magnification in Fig. 4A. (B) features the three layers of the DG: the molecular layer
(m), the granular layer (g), the polymorphic layer (po) with the subgranular zone (sg) and the
mossy fiber collateral plexus (cp), and some of the subjacent CA3 end. The granule cells (gc)
differ with respect to dendritic thickness and soma size. Mossy fibers are marked by white
arrowheads, mossy fiber giant terminals by black arrowheads, the hippocampal fissure by
stipples and asterisks and a loop in the end, the po/CA3 border and the lacunar-molecular
layer (m-l) by stippling apart for the dotted border with the m. **Abbr**.: a, alveus; as, astrocyte;
CA1, cornu ammonis area 1; CA2, cornu ammonis area 2; CA3, cornu ammonis area 3; e,
exposed blade; ec, exposed crest; f, fimbria; h, hidden blade; o, oriens layer; ; py, pyramidal
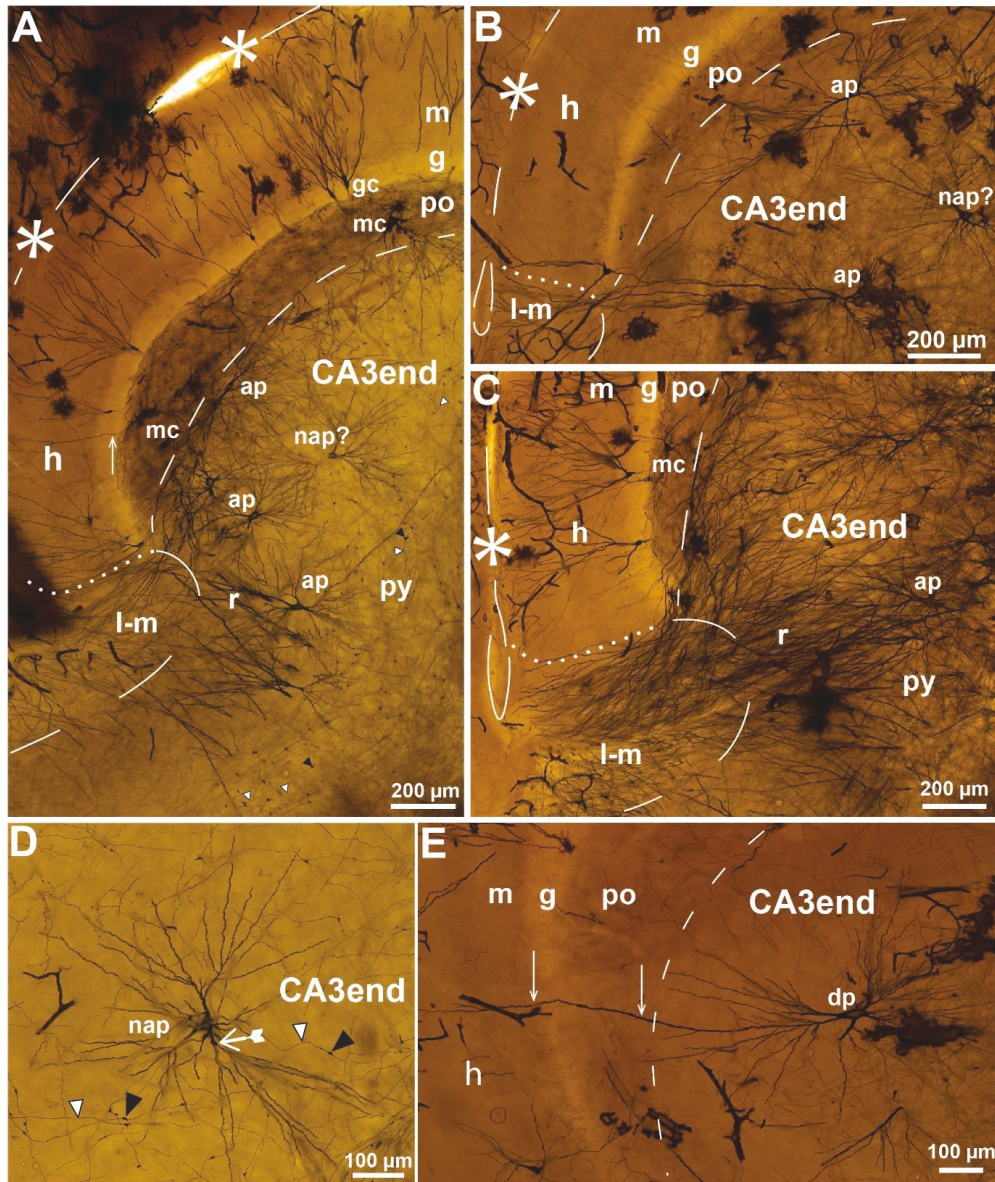layer; r, radiate layer; sg, subgranular zone; Sub, subiculum.
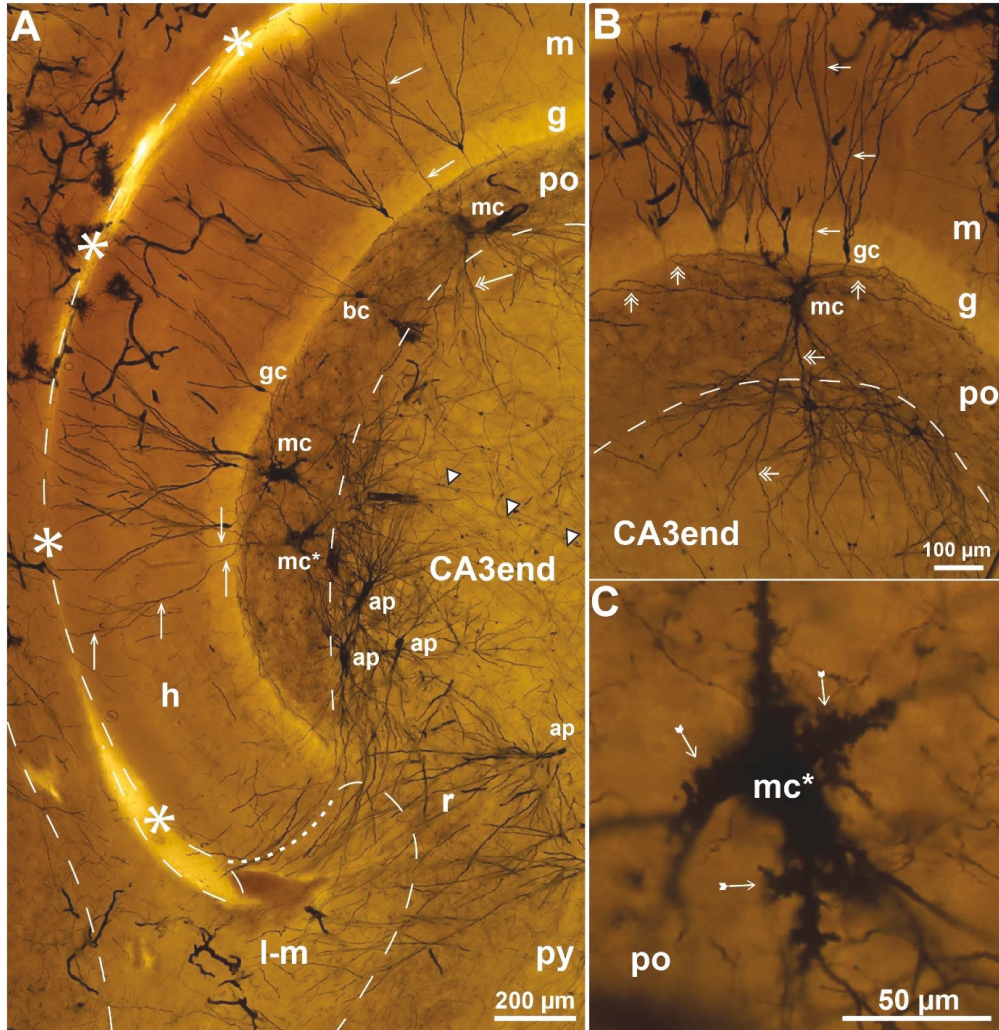
Figure 4. Mossy cells in sheep

Photomicrographs of a Golgi-stained section of the DG cut perpendicular to the long

septotemporal axis of the hippocampus at a temporal level. (A) represents the boxed area in

Fig. 3A with three impregnated mossy cells (mc) and one basket cell (bc) in the polymorphic

layer (po) and four apical pyramidal cells (ap) in the subjacent CA3 end with dendrites

entering the lacunar-molecular layer (l-m). (B) exhibits a single mc with the soma in the po, a

gm-dendrite (arrows) ascending to the granular (g) and molecular layers (m) and distal

dendrites (double arrows) coursing in the subgranular zone or entering the subjacent CA3 end

where they intertwine with the dendrites of two small CA3-interneurons respecting the border

with the po. (C) is a higher magnification of the mossy cell marked mc* in (A). Excrescences

are marked by tailed arrows, the main mossy fibres by white arrowheads, the hippocampal

fissure by stipples and asterisks and a loop in the end, the po/CA3 border and the l-m by

stippling apart from the l-m/m border which is dotted. Abbr.: gc, granule cell; h, hidden

blade; py, pyramidal layer; r, radiate layer.

Figure 5. Pyramidal cells in sheep

Photomicrographs of Golgi-stained sections of the DG cut perpendicular to the long

septotemporal axis of the hippocampus at temporal (A,C, E), middle (B), and septal (D)

levels. The section in (A) is adjacent to that of Fig. 4A and features the hidden blade (h) of the

DG with part of the CA3 end. A gm-dendrite of a mossy cell is marked by a white arrow. In

A, B and C (the latter representing a heavily impregnated section from the surface of a tissue block) apical dendrites of apical pyramidal cells (ap) reach the lacunar-molecular layer (l-m), while a cell without such dendrites may be a non-apical pyramidal cell (nap?). (D) a single nap from the middle of the CA3 end with proximal dendrites exhibiting small excrescences (tailed arrow). Mossy fibers (white arrowheads) are equipped with giant terminals (black arrowheads). (E) a dentate pyramidal cell (dp) extends a gm-dendrite (white arrows) through the polymorphic layer (po), granular layer (g) and molecular layer (m) of the h. The hippocampal fissure is marked by stipples and asterisks and a loop in the end, the po/CA3 border and the l-m by stippling apart from the dotted l-m/m border. **Abbr.**: gc, granule cell; mc, mossy cell; py, pyramidal layer; r, radiate layer.
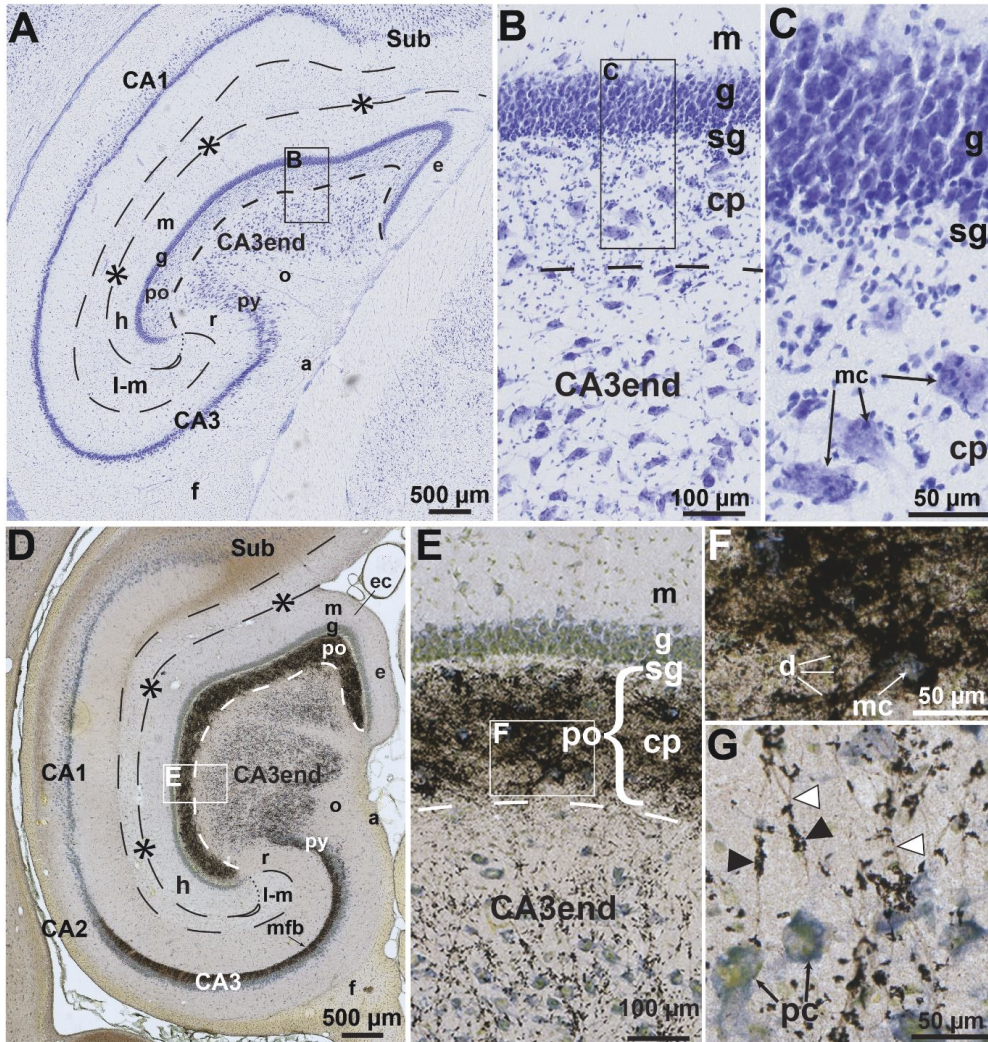
Figure 6. The pig dentate gyrus in thionin- and Timm-thionin-staining

Photomicrographs of thionin-(A-C) and Timm-thionin-(D-G) stained sections probably cut in the horizontal plane at non-specified levels. Boxed area in (A), (B), (D), and (E) are reproduced at higher magnification in (B), (C), (E), and (F), respectively. A Timm-negative subgranular zone (sg) of the polymorphic layer (po) is present in all blades. The hippocampal fissure is marked by stipples and asterisks and a loop in the end, the po/CA3 border and the lacunar-molecular layer (l-m) by stippling apart from the dotted l-m/molecular layer (m) border, mossy fibers by white arrowheads, and giant terminals by black arrowheads. **Abbr.:**

alveus; CA1, cornu ammonis area 1; CA2, cornu ammonis area 2; CA3, cornu ammonis area 3; cp, collateral plexus; e, exposed blade; ec, exposed crest; f, fimbria; g, granular layer; h, hidden blade; mfb, mossy fiber bundle; mc, mossy cell; o, oriens layer; pc, pyramidal cell; py, pyramidal layer; r, radiate layer; Sub, subiculum.
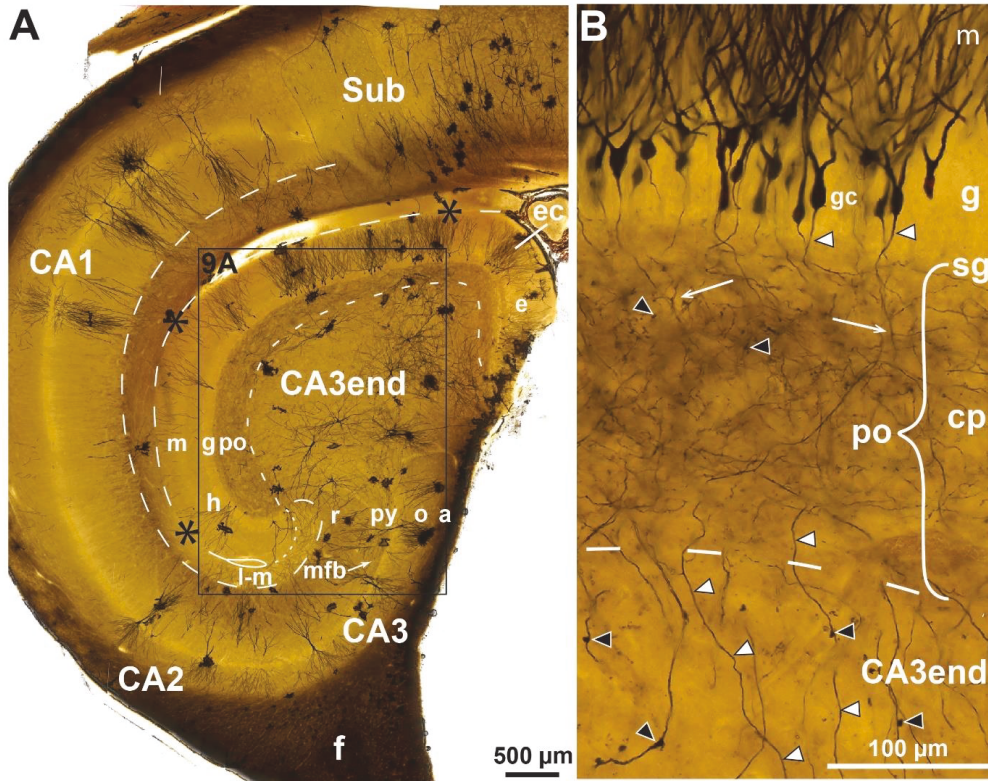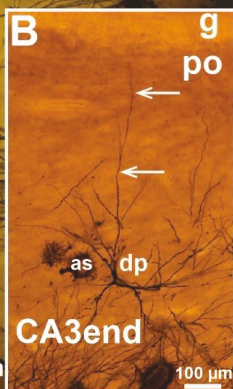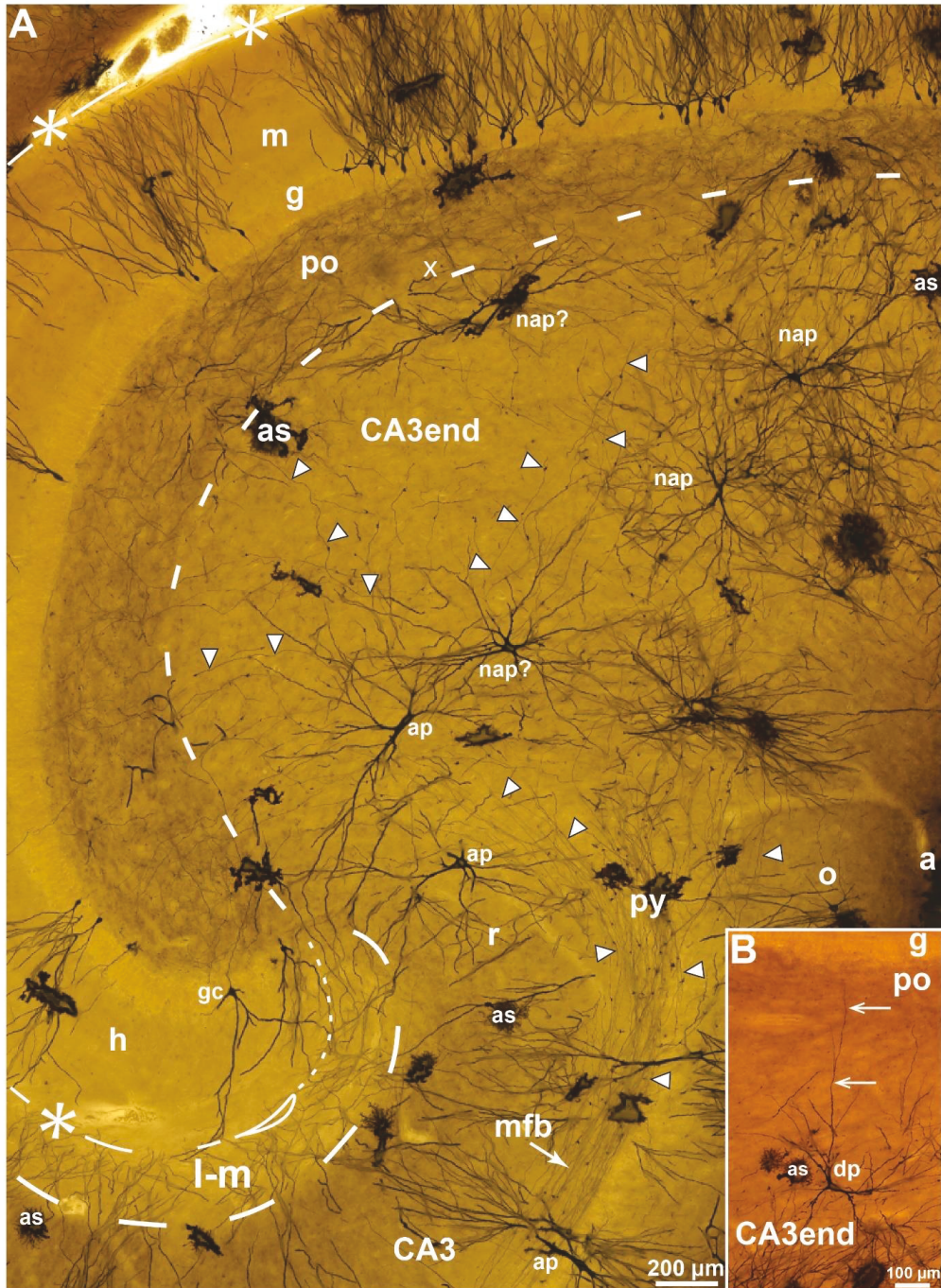
Figure 7. Collateral plexus in Golgi sections of pig

Photomicrographs of Golgi-stained sections of the DG cut perpendicular to the long septotemporal axis of the hippocampus at midlevel. Boxed area in (A) is reproduced in Fig. 9. (B) Detail with impregnated granule cells (gc), mossy fibers (white arrowheads) which give off collaterals (branching points indicated by white arrows) within the collateral plexus (cp) but not within the CA3 end. Giant terminals (black arrowheads) are smaller in the cp than in the CA3 end. The hippocampal fissure is marked by stipples and asterisks and a loop in the end, the cp/CA3 border and the lacunar-molecular layer (l-m) by stippling apart from the dotted l-m/molecular layer (m) border. **Abbr**.: a, alveus; CA1, cornu ammonis area 1; CA2, cornu ammonis area 2, CA3, cornu ammonis area 3; e, exposed blade; ec, exposed crest; f, fimbria; g, granular layer; h, hidden blade; o, oriens layer; po, polymorphic layer; py, pyramidal layer; r, radiate layer; sg, subgranular zone; Sub, subiculum.
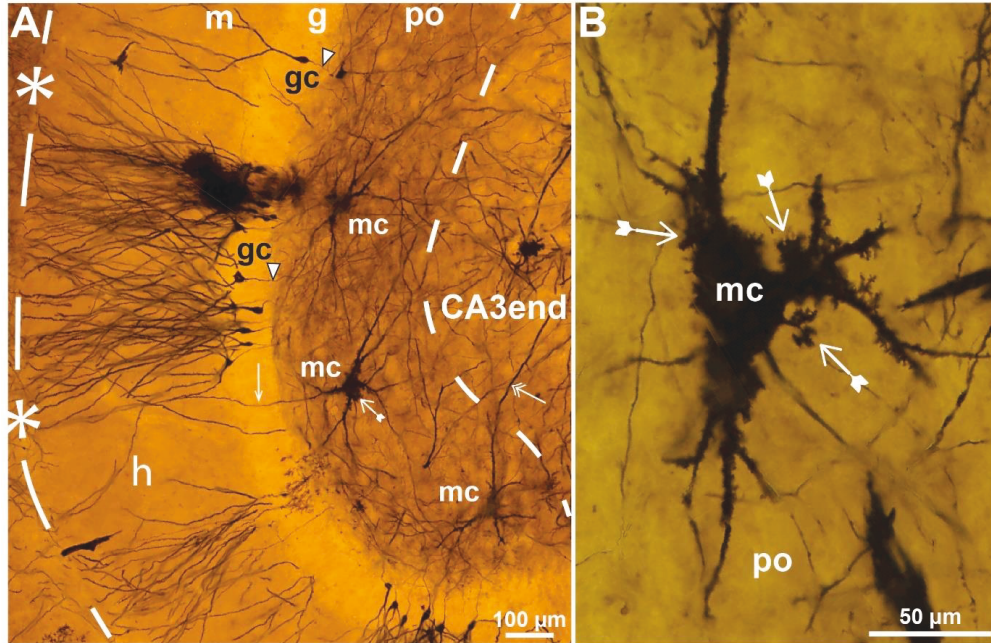
Figure 8. Mossy cells in pig

Photomicrographs of Golgi-stained sections cut perpendicular to the long septotemporal axis of the hippocampus at midlevel. (A) features three mossy cells (mc) in the polymorphic layer (po), one of which with a gm-dendrite (arrow) ascending to the granular (g) and molecular (m) layers, another with a distal dendrite (double arrow) descending to the CA3 end. (B) A single mc at higher magnification with large excrescences (tailed arrows) on primary and secondary dendrites and soma. The hippocampal fissure is marked by stipples and asterisks, the po/CA3 border by stippling, and mossy fibers by white arrowheads. **Abbr**.: gc, granule cell; h, hidden blade.

A

m
g
po
x

nap?

as

CA3end

nap

as

nap

as

nap?

ap

ap

ap

nap?

py

r

o

a

gc

as

h

B

g

po

l-m

as

mfb

as

dp

CA3end

CA3

ap

200 μm

100 μm

Figure 9. Pyramidal cells in pig

Photomicrographs of Golgi-stained sections cut perpendicular to the long septotemporal axis of the hippocampus at middle (A) and septal (B) level. (A) Higher magnification image of the boxed area in Fig. 7A with apical (ap) and non-apical (nap) pyramidal cells in the CA3 end. The hippocampal fissure is marked by stipples and asterisks and a loop in the end, the po/CA3 border and the lacunar-molecular layer (l-m) by stippling apart from the dotted l-m/molecular layer (m) border, mossy fibres by white arrowheads. (B) Dentate pyramidal cell (dp) with a single dendrite (arrows) penetrating the polymorphic layer (po) of the middle blade. **Abbr.:** a, alveus; as, astrocyte; CA3, cornu ammonis area 3; g, granular layer; gc, granule cell; h, hidden blade; mfb, mossy fiber bundle; o, oriens layer; py, pyramidal layer; r, radiate layer; x, excavation.
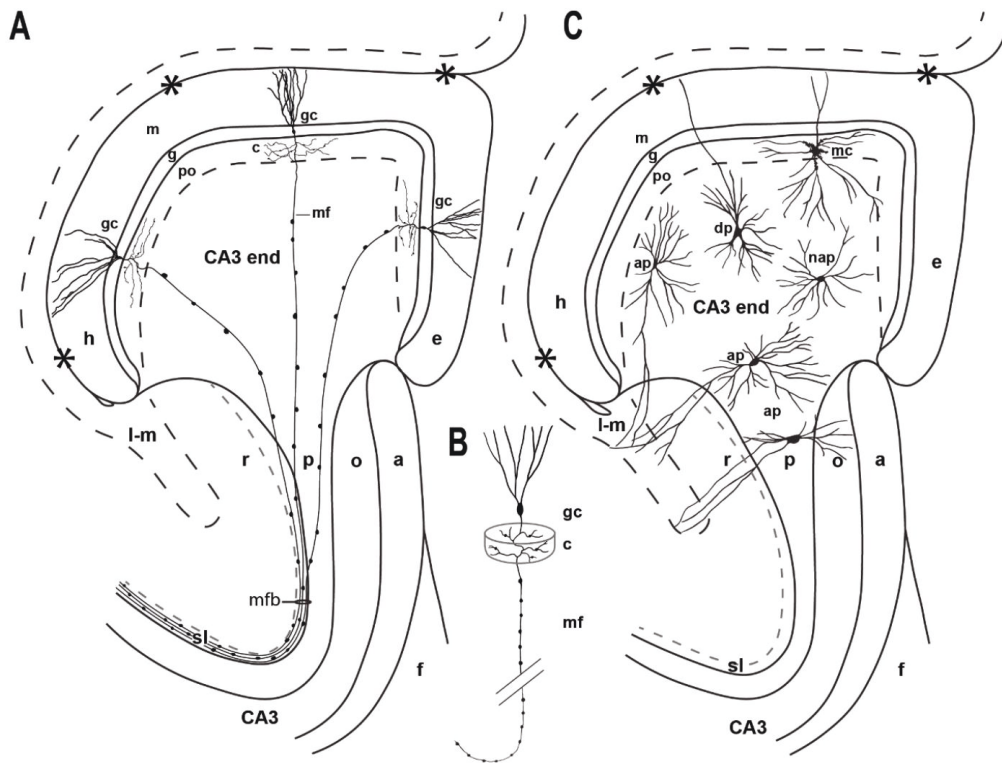
Figure 10. Summary diagram

Summary diagram of the dentate gyrus and the subjacent CA3-end in sheep and pig in

sections cut perpendicular to the long, septotemporal axis of the hippocampus, with focus on:

(A) The mossy fiber system with its origin in the granule cells (gc), the collaterals (c) in the

polymorphic layer (po), and the main mossy fibers featuring regularly spaced giant terminals

and converging through the CA3-end towards the mossy fibre bundle (mfb) in the main CA3;

(B) A single gc with mossy fibre (mf) and c seen in a slightly different view in order to

emphasize the 3-D dimensions and orientation of the collateral tree. (C) The position of the

mossy cells (mc) with soma in the po and examples of the three pyramidal cell subtypes, i.e.,

the apical pyramidal cells (ap), dentate pyramidal cells (dp), and non-apical pyramidal cells

(nap) with soma in the CA3 end; Abbr.: a, alveus; e, exposed blade; f, fimbria; g, granular

layer; h, hidden blade; l-m, lacunar-molecular layer; m, molecular layer; o, oriens layer; p,

pyramidal layer; po, polymorphic layer; r, radiate layer; sl, stratum lucidum.

TABLES

Table 1

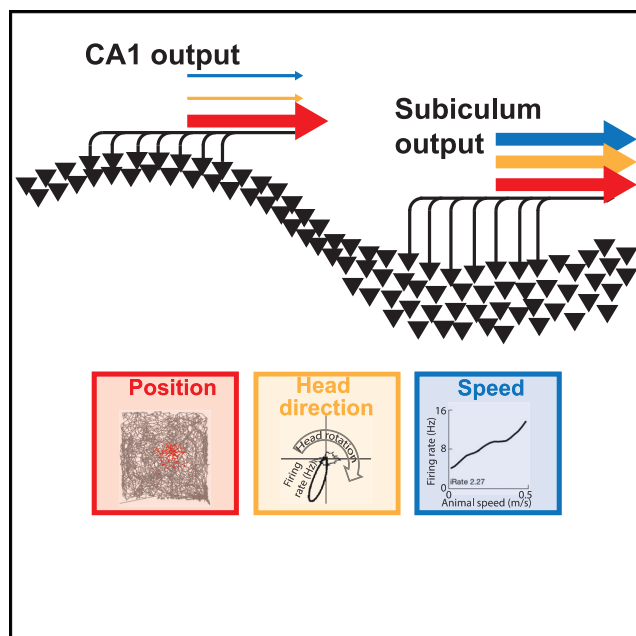| Animal ID	TBL 75	TBL 76	TBL 80	FIJ-2	FIJ-3
Species	Sheep	Sheep	Domestic pig	Domestic pig	Domestic pig
Age	8 weeks	8 weeks	NA	NA	NA
Sections	2 x 5 blocks A-E	2 x 5 blocks A-E	5 blocks 1-5	3 sections	3 sections
Golgi	A,C,E	A,C,E	1-5		
Timm/thionin.	B,D	B,D			

PAPER 3

Task-dependent mixed selectivity in the subiculum

Graphical abstract

Authors

Debora Ledergerber, Claudia Battistin,
Jan Sigurd Blackstad, ...,
May-Britt Moser, Yasser Roudi,
Edvard I. Moser

Correspondence

debora.lederberber@kliniklengg.ch
(D.L.),
yasser.roudi@ntnu.no (Y.R.),
edvard.moser@ntnu.no (E.I.M.)

In brief

Ledergerber et al. show that pyramidal cells in the subiculum combine navigational variables—position, head direction, and speed—more extensively than their counterparts in hippocampal CA1 so that such mixed selectivity is stronger during goal-directed navigation than free foraging and that navigational information is decoded more efficiently from a mixed-selective code.

Highlights

- CA1 and subiculum neurons respond conjunctively to position, head direction, and speed

- The degree of conjunctive coding ("mixed selectivity") is stronger in the subiculum

- Mixed selectivity is stronger during goal-directed navigation than in free foraging

- Decoding of each navigational covariate is more accurate with mixed selectivity

Cell Reports

Article

Task-dependent mixed selectivity in the subiculum

Debora Ledergerber,[1,2,*] Claudia Battistin,[1] Jan Sigurd Blackstad,[1] Richard J. Gardner,[1] Menno P. Witter,[1] May-Britt Moser,[1] Yasser Roudi,[1,*] and Edvard I. Moser[1,3,*]

[1]Kavli Institute for Systems Neuroscience and Centre for Neural Computation, Norwegian University of Science and Technology, Olav Kyrre s gate 9, MTFS, 7489 Trondheim, Norway
[2]Present address: Swiss Epilepsy Center, Klinik Lengg AG, Bleulerstrasse 60, 8008 Zurich, Switzerland
[3]Lead contact
*Correspondence: debora.lederberber@kliniklengg.ch (D.L.), yasser.roudi@ntnu.no (Y.R.), edvard.moser@ntnu.no (E.I.M.)
https://doi.org/10.1016/j.celrep.2021.109175

SUMMARY

CA1 and subiculum (SUB) connect the hippocampus to numerous output regions. Cells in both areas have place-specific firing fields, although they are more dispersed in SUB. Weak responses to head direction and running speed have been reported in both regions. However, how such information is encoded in CA1 and SUB and the resulting impact on downstream targets are poorly understood. Here, we estimate the tuning of simultaneously recorded CA1 and SUB cells to position, head direction, and speed. Individual neurons respond conjunctively to these covariates in both regions, but the degree of mixed representation is stronger in SUB, and more so during goal-directed spatial navigation than free foraging. Each navigational variable could be decoded with higher precision, from a similar number of neurons, in SUB than CA1. The findings point to a possible contribution of mixed-selective coding in SUB to efficient transmission of hippocampal representations to widespread brain regions.

INTRODUCTION

The hippocampus has a well-established role in mnemonic and navigational functions of the brain (Hasselmo, 2012; Morris, 2007; O'Keefe and Nadel, 1978; Scoville and Milner, 1957; Squire, 1992). Its interplay with other cortical regions is thought to be indispensable for the formation and retrieval of episodic and positional memories (Buzsáki, 1989; McClelland et al., 1995; Squire, 1992; Squire et al., 2015; Winocur and Moscovitch, 2011). The subiculum (SUB) has an important anatomical position as an interface between the hippocampus and other brain areas (Cappaert et al., 2015; O'Mara, 2006). It is the major long-range projection area of the hippocampus, the origin of a substantial part of the fornix, and the source of large parts of non-fornical output reaching a range of cortical and subcortical downstream areas. Along with the CA1 area, it sends outputs to infralimbic, prefrontal, orbitofrontal, and medial and lateral entorhinal cortices (MECs and LECs) and to subcortical structures, including the septal complex, the mammillary nucleus, the hypothalamus, the thalamus, and the amygdala (Cappaert et al., 2015; Cembrowski et al., 2018a; Ishizuka, 2001; O'Mara et al., 2001). However, even though CA1 and SUB have many overlapping target areas, their patterns of connectivity are very different; the majority of CA1 neurons each send collateral projections to at least two targets elsewhere in the brain, whereas in the case of the SUB, such branching is observed only in a minority of neurons (Bienkowski et al., 2018; Cembrowski et al., 2018b; Naber and Witter, 1998; Wit-

ter, 2006). This difference raises the possibility that the hippocampus uses CA1 and SUB outputs differentially to distribute information to downstream brain regions.

Although neuronal representations in CA1 have been known for half a century to show strong spatial selectivity, as expressed in place cells (O'Keefe and Dostrovsky, 1971; O'Keefe and Nadel, 1978), data from SUB are scarce and it has remained elusive what SUB adds to the hippocampal computation. Subpopulations of SUB neurons have broad spatial firing fields (Sharp, 1997, 2006; Sharp and Green, 1994), of which some, known as boundary-vector cells, are oriented in parallel to elongated geometric boundaries (Lever et al., 2009; Stewart et al., 2013). Vector trace cells fire at given distances and directions from discrete objects or boundaries, with firing fields that may outlast the presence of the object or boundary (Poulter et al., 2020). Yet, other SUB cells encode the animal's axis of movement (heading direction) when animals navigate on elevated multidirectional tracks (Olson et al., 2017). In all tasks in which SUB neurons have been recorded, they appear to be more broadly tuned to features of behavior or environment than neurons in other regions of the hippocampal formation. SUB is likely to receive navigational input from narrowly tuned place cells in CA1 (O'Keefe, 1976; O'Keefe and Dostrovsky, 1971); from grid cells in the MEC and pre- and parasubiculum (Boccara et al., 2010; Fyhn et al., 2004; Hafting et al., 2005); from head direction cells (Taube and Burton, 1995; Taube et al., 1990), border cells, and object vector cells (Høydal et al., 2019; Solstad et al., 2008) in the same regions; and from speed

cells in the hippocampus and MEC (Kropff et al., 2015). The specificity of these putative inputs brings up the question of what the broader representations in SUB add to the output of the hippocampal formation.

Navigation-tuned cells in the hippocampal formation express similar types of information in multiple environments. This is in contrast to neuronal representations in many other brain areas, where spatial selectivity is apparent only under task conditions relevant to the brain region, such as in prefrontal cortex (Jung et al., 1998; Padilla-Coreano et al., 2019; Pratt and Mizumori, 2001), posterior parietal cortex (Nitz, 2006; Whitlock et al., 2012), primary visual cortex (Goltstein et al., 2018; Saleem et al., 2018), amygdala (Peck et al., 2014), and nucleus accumbens (Lansink et al., 2012; Mulder et al., 2005). Navigational information in these regions may be derived from representations in the hippocampus (Remondes and Wilson, 2013; Spellman et al., 2015), but it remains unclear whether, and how, outputs from hippocampus would be modified in a task-specific manner before reaching these diverse regions. Given the potential role of SUB in distributing hippocampal output to widespread regions of the brain (Cappaert et al., 2015; Gigg, 2006; O'Mara, 2006), we hypothesized that, rather than generating *de novo* representations, SUB modifies representations from upstream neural populations in CA1, presubiculum, and entorhinal cortex to facilitate decoding by downstream regions during hippocampal-dependent behaviors.

It has been suggested that networks consisting of neurons that encode multiple stimulus features simultaneously or conjunctively, using a "mixed selectivity" (MS) code, have several computational advantages over networks in which neurons respond predominantly to single features (Miller et al., 1996; Rigotti et al., 2013). Besides a high representational capacity, networks with high-dimensional coding in individual neurons have the advantage that a wide span of task-relevant aspects is accessible to linear classifiers, as the number of classifications that can be performed by a linear readout grows exponentially with the dimensionality of the information carried by the neurons (Fusi et al., 2016). Increasing the level of MS in SUB might therefore be a mechanism by which the hippocampal formation makes relevant output more accessible to downstream target regions.

With these advantages of MS in mind, we asked if SUB modifies output from the hippocampus by combining, in individual neurons, multiple features of the navigation experience in ways that depend on current task goals. Considering that much of the output from CA1 is also passed on to SUB, we performed simultaneous *in vivo* electrophysiological recordings in these regions in rats performing either random foraging or a spatial navigation task. We compared representations in SUB and CA1 for three navigational covariates, namely, position (P), head direction (H), and speed (S). We report that individual neurons in SUB combine these behavioral covariates more extensively than their counterparts in CA1 and more strongly during goal-directed spatial navigation than during free foraging. This coding scheme was paralleled by more accurate decoding of the navigational covariates from SUB than from CA1, providing regions downstream of SUB with broad spectra of information even from limited numbers of SUB output cells.
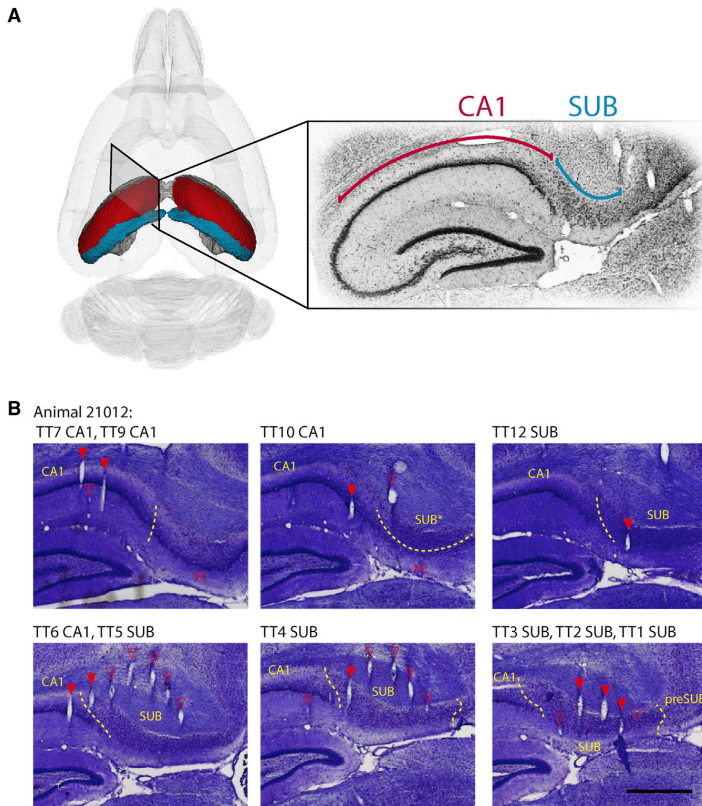
RESULTS

Anatomical location of recording electrodes

In order to understand what the SUB adds to the navigational output of the hippocampus, we performed extracellular recordings in CA1 and SUB (Figure 1A). All tetrodes were placed in the dorsal one-third of each region (see sectioning plane in Figure 1A). In Nissl-stained coronal sections, CA1 was identified as the narrow, densely packed layer of small pyramidal cells that extends from CA2 (with a less compact cell layer and larger neurons) to SUB (defined as the thicker, more diffuse layer of medium-sized neurons located dorsomedially to CA1). Moving away from the septal pole, SUB gradually widens, extending all the way medially until an additional granule layer is added ventrally, almost at the midsagittal side of the hemisphere. This additional layer belongs to the retrosplenial cortex (RSC; area 29) in the septal part of the hippocampal formation (RSC in Figure S1) and to the dorsal presubiculum in more temporal parts of the structure (preSUB in Figures 1B and S1A). At the septal pole, CA1 continues medially into the fasciola cinereum (FC in Figures 1B and S1; Boccara et al., 2015). Recordings from FC were not included in our study. Recordings from nearby SUB were included if the tetrodes were more than 50 um away from FC (SUB* in Figure 1B and Figure S1; see "Histology and reconstruction of tetrode placement" in STAR Methods).

We isolated 760 putative principal neurons from recordings in 8 rats (see STAR Methods; Table S1). Only cells with clear cluster separation from other background and other neurons were accepted (Figures S2A–S2C). Among the accepted neurons, 421 were located in SUB and 325 in CA1 (346 neurons in 3 rats, of which 96 in CA1 and 249 in SUB, were recorded in sessions in which CA1 and SUB were recorded in parallel). In SUB, the recording electrodes were distributed quite evenly along the proximo-distal axis (from CA1 to FC, RSC, or preSUB), whereas in CA1, there was a bias for the electrodes to be positioned in mid to distal parts of the subfield, i.e., nearer the SUB boundary (only 2 out of 18 tetrodes were located near the proximal end of CA1, near CA2) (tetrodes 1 and 11 in animal 24101 in Figure S1). However, the number of neurons recorded was distributed more evenly along the proximo-distal axis (approximate neuron numbers in the respective regions: 35 in proximal CA1, 223 in mid CA1, 49 in distal CA1, 292 in proximal , and 136 in distal SUB; arbitrary boundaries dividing subfields in three equal bands; Table S1).

Position coding in CA1 and SUB

With the aim of investigating the neurophysiological properties of SUB during active foraging and navigation, rats were trained in 2 tasks. First, 5 of the 8 rats were trained in an open field (OF) foraging task in which rats searched for randomly scattered cookie crumbs in a dimly-lit 1.5-m-wide square enclosure on a floor consisting of a black even mat without incisions. A cue card was attached on one of the walls. Second, all 8 rats were trained in a spatial task (ST) adapted from Pfeiffer and Foster (2013) in which the rats alternated between free search and goal-directed memory-based navigation. The same enclosure was used as for the OF but the floor mat was removed,

A

CA1   SUB

B Animal 21012:
TT7 CA1, TT9 CA1   TT10 CA1   TT12 SUB

TT6 CA1, TT5 SUB   TT4 SUB   TT3 SUB, TT2 SUB, TT1 SUB

Figure 1. Recording locations in CA1 and SUB

(A) Left side: Schematic of the hippocampal formation, with the CA1 in red and the SUB in blue. Right side: Nissl-stained section showing the arrangement of CA1, with its dense layer of cell bodies (underneath the dark red line following the curvature of CA1), and the SUB, where neurons are more loosely packed (underneath the blue curved line).

(B) Reconstruction of the tetrode (TT) locations in a representative animal (no. 21012). A micro-drive with two parallel rows each of seven TTs (six recording TTs and one reference TT) was implanted along the transverse axis of the hippocampus. For unambiguous reconstruction of TT locations, the brain was sectioned at a 45-degree angle between the sagittal and coronal planes, parallel to the rows of TTs. Filled red arrows indicate TT traces near the estimated recording location (usually at the end of the TT track), and empty red arrowheads indicate traces of TT tracks that are visible in this section but are above (or below) the recording locations. Dashed yellow lines indicate borders between SUB and neighboring regions (preSUB, presubiculum; FC, faciola cinerata). For recording locations in SUB that were dorsal to the FC (labeled with SUB*) or the border between CA1 and SUB, we included data only from neurons that could confidently be assigned to be 50 μm or more away from the border. Scale bar, 1 mm.

uncovering a square grid of 1-cm-diameter holes in the floor. The walls of the arena and their location in the room with respect to all distal landmarks remained constant between OF and ST (Figures S2D and S2E). During the ST, chocolate oat milk was provided alternately at a fixed "home well" and in a randomly selected well ("random well") of the arena (Pfeiffer and Foster, 2013). The animals memorized the home well location and learned to navigate back to it straight after consuming the randomly placed reward (Figure S2D), as reflected in their behavioral latencies (Figure S2F). Training in OF and SF was conducted on alternating sessions.

We first compared the spatial tuning properties of CA1 and SUB neurons. These analyses were performed on combined data from ST and OF because no major differences in spatial tuning were detected in separate analyses (Figures S3A–S3D). In agreement with previous studies (Kim et al., 2012; Sharp and Green, 1994), the average firing rate of principal neurons was significantly higher in SUB (4.44 ± 0.14 Hz) than in CA1 (1.7 ± 0.12 Hz, $p = 4.6e$-53, Welch's test; Figures 2A and S3A). Similarly, as in previous studies (Sharp, 1997, 2006; Sharp and Green, 1994), CA1 cells had sharply defined firing fields (Figure 2A; 95% of spikes in CA1 neurons fell into $25.7\% \pm 1.1\%$

of the spatial bins), whereas SUB neurons tended to fire continuously across the environment (Figure 2A; 95% of the neuron spikes fell into $56.3\% \pm 0.7\%$ of the spatial bins), often expressing some degree of boundary vector-like bias in activity, which is in line with earlier findings (Lever et al., 2009; Stewart et al., 2013) (Figures 2A, S3A, and S5B). The information rate of the neurons, or their amount of position information per time interval (Skaggs et al., 1993), was similar in CA1 and SUB (Figures 2B and S5C; medians and median absolute deviation [MAD] are 0.47 ± 0.27 bits/s in CA1 and 0.42 ± 0.26 bits/s in SUB; $p = 0.02$, Mann-Whitney U-test), whereas information content, or the information a neuron's spikes provide about P (Skaggs et al., 1993), was markedly smaller in SUB (Figure 2C and S5D; median and MAD for CA1: 0.84 ± 0.57 bits/spike, for SUB: 0.11 ± 0.16 bits/spike; $p = 1.1e$-70, Mann-Whitney U-test).

The difference in information content but not rate between CA1 and SUB raises the question of what benefits are conferred by increasing the mean firing rate and therewith sacrificing information per spike during the processing step from CA1 to SUB. One possibility is that SUB, by integrating positional information over longer timescales, might combine input from CA1 with information from other sources (including inputs encoding variables besides P). With this possibility in mind, we investigated whether information about other behavioral variables is expressed in spike trains of SUB neurons.
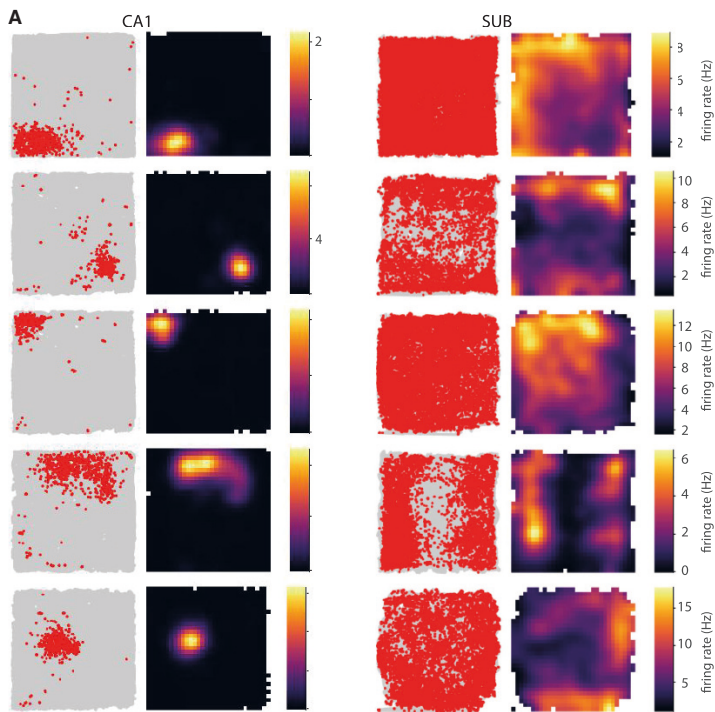
Figure 2. Difference in position coding in CA1 and SUB

(A) Example path plots (left) and rate maps (right) from neurons in CA1 (left column) and SUB. Path of the animal during the entire session is shown in gray with emitted spikes overlaid in red. Color bars to the right indicate firing rate.

(B and C) Frequency distributions showing P information rate (B) and information content (C) for all neurons recorded in CA1 (red) and SUB (blue) in all animals. Dashed line, median of each distribution.
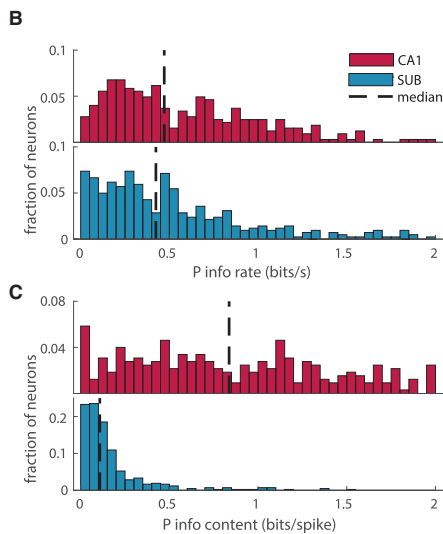
Representation of multiple covariates including H and S in SUB and CA1

Previous studies found that subsets of CA1 and SUB neurons show some degree of modulation by navigational variables like head direction (H) modulation and running speed (S). In CA1, place cells may be tuned to H inside their place fields (Acharya et al., 2016; Langston et al., 2010; Leutgeb et al., 2000). Weak H tuning has also been reported for spatially modulated neurons in SUB (Sharp and Green, 1994). Similarly, place cells in CA1 respond to some degree to running speed, whereas speed tuning has not been reported in SUB to our knowledge (Czurkó et al., 1999; Kropff et al., 2015; McNaughton et al., 1983).

Based on these observations, we set out to compare quantitatively, in the same recordings, the extent to which cells in CA1 and SUB represent navigational covariates besides P, like H and S. The H tuning curves of the recorded neurons revealed various degrees of modulation by H, in both CA1 (Figure 3A, 2nd column) and SUB (Figure 3B, 2nd column). Consistent with previous reports in CA1 (McNaughton et al., 1983; Skaggs et al., 1993), the information rate in CA1 neurons was lower for H than for P (Figures 3C and 3D; median and MAD of the CA1 population was 0.47 ± 0.27 bits for P and 0.04 ± 0.04 bits for H; p = 6.87e−67 Mann-Whitney U-test). In contrast, we found that in SUB neurons, information rates for H and P were in the same order of magnitude, albeit they were significantly different (median and MAD for H: 0.22 ± 0.15 bits/s and for P: 0.42 ± 0.26 bits/s; p = 4.4e−13 Mann-Whitney U-test). CA1 and SUB neurons showed similar levels of H information content (medians and MAD 0.07 ± 0.06 bits/spike for CA1 and 0.06 ± 0.04 bits/spike for SUB; p = 0.98 Mann-Whitney U-test).

A similar pattern could be seen for speed information rates and contents (Figure 3E and 3F). CA1 and SUB neurons had similar information content for speed (0.07 ± 0.07 bits/spike in CA1 versus 0.04 ± 0.04 bits/spike in SUB), whereas information rates for speed were higher in SUB than CA1 neurons (0.04 ± 0.04 bits/s in CA1 and 0.10 ± 0.10 bits/s in SUB; p = 6.8e−9 Mann-Whitney U-test).

## Modeling spike rate with a GLM reveals MS in SUB

Measuring information rate separately for each different covariate (P, H, and S) entails some important limitations. These three behavioral covariates are strongly interdependent, meaning that an effect that is selectively tuned to one covariate might manifest spuriously when measured in relation to a different covariate (Acharya et al., 2016). This undesirable effect may result in both false-positive and false-negative tuning outcomes. One solution to this challenge is to use multiple-variable statistical methods, such as the generalized linear model (GLM). The GLM considers multiple covariates simultaneously and thus allows the influences on a cell's activity to be ascribed in a principled manner to the covariates that provide the strongest prediction.

Therefore, we extended the analysis by using a Poisson GLM framework (Hardcastle et al., 2017; McCullagh and Nelder, 1989) to investigate tuning of the neurons to P, H, and S, while accounting for any deceptive correlations between the covariates induced by sampling (ST and OF still combined; Figures S3E–S3G). Alongside the behavioral covariates (P, H, and S), we

also included two covariates representing basic influences on neural activity, namely, ensemble activity (E), defined as the Z-scored spike count summed over all other neurons on the same tetrode as the cell in question; and the theta phase (T) of the filtered local field potential (see STAR Methods). These two covariates were treated as "internal covariates," as their influence is exerted only in the local neuronal network and they are themselves modulated by the animal's behavior. They were important, however, for accurately fitting the model to the spike counts, as they remove a possible bias due to correlation between P, H, and S and the internal covariates. For analyzing the functional properties of the two brain regions, we focused our attention on the behavioral covariates P, H, and S (see STAR Methods). All the covariates (P, H, S, E, and T) were binned along their respective dimension (30 × 30 bins for P; and 10 bins for each H, S, E, and T), and continuity in the predicted tuning curves was enforced by a smoothness prior (STAR Methods). All models resulting from specific subsets of the covariates (ranging from single-covariate models, e.g., only P, to the most complex model containing all five covariates [PHSET]) were trained and tested by 10-fold cross-validation for every cell. Bin size and smoothness were treated as hyperparameters and selected by optimizing the cross-validated log-likelihood (LLH) for each single covariate model (Figure S4). For each neuron, the full-model GLM (PHSET) yielded tuning curves for P, H, and S (Figures 4A–4C), which qualitatively reproduced the tuning curve for the data (Figures 4A–4C).

Model selection was performed in a forward stepwise fashion, starting from single-covariate models and adding one covariate at a time by using a non-parametric test and a 5% significance level (see STAR Methods). Except in Figure S3G, models containing internal covariates E and/or T were pooled with corresponding models without this covariate (e.g., neurons best modeled by the PHT, PHE, and PHTE were counted to the group of the PH model). For every neuron, we determined which model provided the best fit to the neuron's firing properties in the data (Figure 4D), which in turn allowed us to assess model performance at the population level (Figure 4E). The proportion of neurons for which the most complex model (PHS) performed significantly better than any simpler model was higher for SUB than CA1 (53.7% in SUB versus 46.5% in CA1, percentages of each region; Figure 4E; difference, >99.9 percentile of a distribution of shuffled data in which cells were randomly assigned to anatomical region). Conversely, the proportion of neurons from one region best fitted by the PS model was significantly lower in SUB than in CA1 (25.9% in CA1 and 8.8% in SUB; difference, >99.9 percentile of a shuffled distribution; Figure 4E). These findings may suggest that both CA1 and SUB cells express high levels of MS, but the degree of mixing is stronger in SUB. To confirm that our GLM framework correctly picked up neurons with combined tuning properties, we simulated synthetic neurons by using inhomogeneous Poisson spike trains that were either purely tuned to P, H, or S or expressed known mixed combinations of the three. Classifying these synthetic cells with our GLM showed that the model selection procedure is not prone to overfitting by including spurious covariates (Figure S4F).

One caveat of the model selection analysis is that it only allows us to conclude that a number of CA1 and SUB neurons were
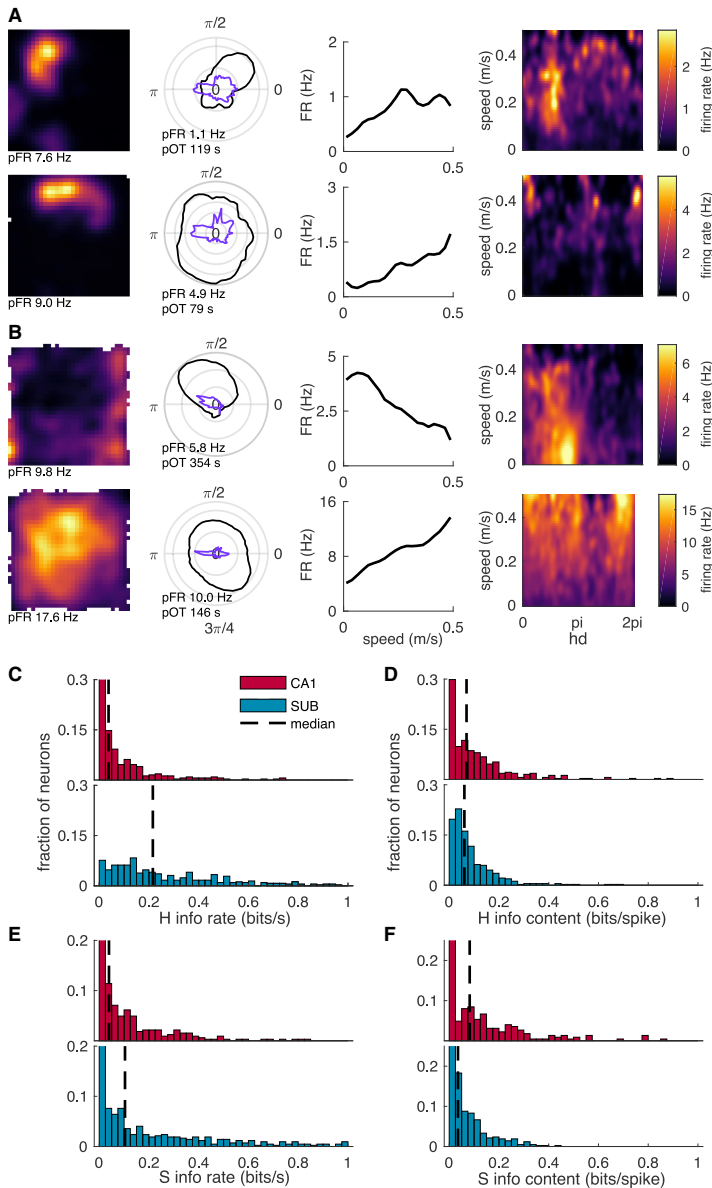
Figure 3. Information rate for H and S is higher in SUB than CA1

(A and B) Example neurons from CA1 (A) and SUB (B). Representative firing rate maps (first column; as in Figure 2), H tuning curves (second column; polar plots showing firing rate FR as a function of H), S tuning curves (third column; linear plots showing firing rate as a function of S), and H versus S rate maps (fourth column; firing rate color coded as a function of H and S). Peak firing rates (pFRs) are indicated for rate maps and H tuning curves. In the second column, the black curve shows firing rate, and purple shows occupancy time. Peak occupancy time (pOT) is indicated.

(C and D) Frequency distribution showing scores for H information content (in C) and information rate (in D) across all neurons recorded in CA1 (red) and SUB (blue). Dashed lines, median of each distribution.
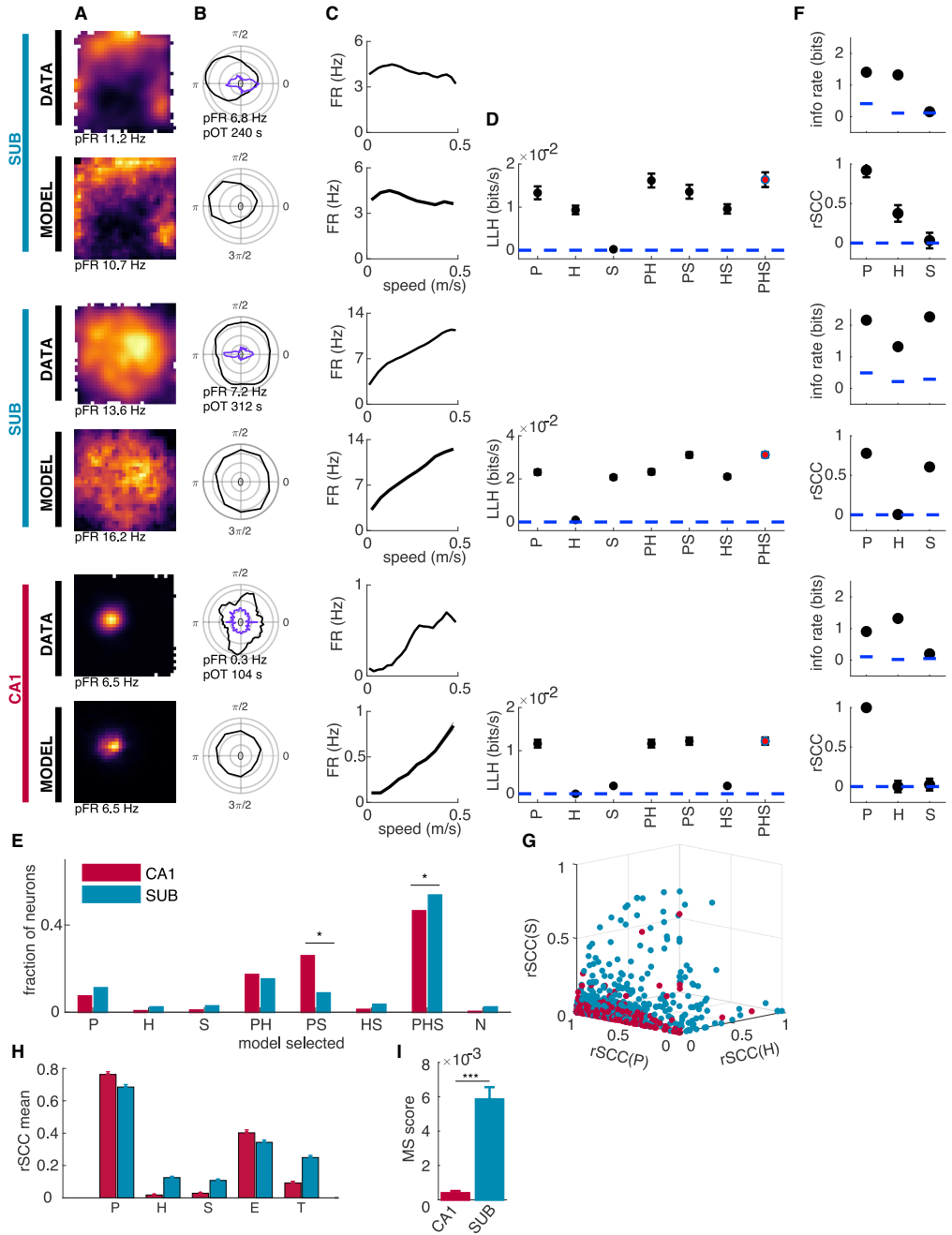
(E and F) Distribution of S information content (in E) and information rate (in F) across all neurons recorded in CA1 (red) and SUB (blue). Dashed lines indicate medians.

(rSCC) by taking the difference between the LLH of the selected model and the LLH of the model with the respective covariate removed. This term was then divided by the square root of the sum of the squares of all differences. The contributions of covariates not used in the selected model were set to zero (see equation in STAR Methods section "Relative single covariate contributions"). rSCC was in many cases correlated with information rate for the respective covariate (Figure 4F), although occasionally there were large differences. Although the measure of information rate is biased due to correlations between covariates, rSCC is derived from the GLM framework, allowing us to simultaneously quantify the contribution of multiple covariates. This leads to a more differentiated estimate of the contribution of individual covariates to the cell's firing rate (Figure 4F, see rSCC versus information rate in the two SUB neurons).

At the population level, plotting the rSCC for CA1 and SUB neurons separately (Figure 4G) revealed that CA1 neurons were largely distributed along the axis for P, showing very little contribution of H and S to their firing pattern, despite the fairly large number of cells that selected the PHS model in the above analyses. In contrast, SUB neurons were scattered throughout the entire space, indicating the differential combinations of the three covariates determining the firing of the neurons.

modulated by P, H, and S in a statistically significant manner. It did not inform us about how strong this modulation was. As a next step, we therefore investigated how strongly each neuron's firing rate was determined by either an individual covariate (P, H, or S) or a combination of them. Using the GLM framework, we quantified the relative contribution of every single covariate

Similarly, wide scatter was seen in both proximal and distal SUB (Figure S5G). These observations suggest that, despite showing a high level of MS in terms of model selection, CA1 neurons singled out one covariate—P—that dominated their tuning properties, whereas SUB neurons more strongly combined multiple covariates, expressing a conjunctive code. The internal covariates E and T were an important factor for determining the firing rates of neurons in both regions. E was represented similarly in both populations, whereas T was the more important covariate in spike trains of the SUB than of the CA1 population (Figure 4H). In order to quantify this coding difference between CA1 and SUB, we introduced a MS score. The MS score is the product of all rSCCs in each neuron (see STAR Methods section "Mixed selectivity score (MS-score)"). This results in a maximal score for neurons that have equal contributions of P, H, and S to their firing rate. The average MS score for SUB neurons was $5.8e-3 \pm 7.1e-4$, which is one order of magnitude larger than that for the CA1 neurons, which had an MS score of $3.8e-4 \pm 1.2e-4$ (Figure 4I; Wilcoxon rank-sum test, $p = 6.86e-9$). MS scores were comparable between proximal and distal parts of SUB (Figure S5H). Thus, in contrast to CA1 cells, SUB neurons integrate information regarding P, H, and S through a highly mixed-selective code in which every neuron expresses differential contributions of the three covariates.

MS in SUB is task modulated

To better understand the function of MS during navigation, we next compared the neural representations of behavioral covariates between the two tasks (ST and OF). Although tuning to P, H, and S (Figures S3A and S3B), as well as information rate and information content (Figures S3C and S3D), Figures S3 failed to show much difference between OF and ST, we hypothesized that the level of MS in the network is more strongly dependent on task factors. Using the previously introduced GLM, we found that, for CA1, the distribution of selected models was similar between OF and ST (Figure 5A; no changes in model selection were higher than the 99.9th percentile of a shuffled distribution). However, the proportion of SUB neurons for which the most complex model (PHS) performed significantly better than the others increased from OF to ST (Figure 5A). Other changes in model selection between OF and ST were not significant; however, the in-

crease from 39.4% to 55.9% of neurons best fitted with the PHS model was significantly beyond the 99.9th percentile of a distribution of shuffled data (Figure 5A). A total of 2.3% and 1.4% of the neurons in SUB and CA1, respectively, were tuned to P only during ST and not in OF. In SUB, 6.9% and 15.4% more principal neurons were tuned to H and S, respectively, in ST but not in OF. In CA1, 5.8% of the neurons lost their tuning for S after transitions from OF to ST (Figure 5B). When considering tuning to E and T (which were always fitted in parallel to the other three covariates), it was apparent that the activity in the largest proportion of SUB neurons (35.6% in OF and 51.6% in ST) was best fitted by all five covariates (Figure S3E), whereas in CA1, the largest proportions of neurons (42.5% in OF and 41.5% in ST) were best fitted by a four-covariate model (Figure S3E), in most cases PHET or PSET (see Figure S3G). The task change did not affect the overall likelihood of the best-performing model (Figure S3F), indicating that the fitting procedure performed similarly in both behavioral situations.

The increase in MS in SUB was reflected in the relative contribution of each single covariate to the firing rate of the neurons. When we plotted the rSCC separately for OF and ST, it appeared that during the ST condition the SUB datapoints are more dispersed in the 3D plot, indicating a more equal contribution of the three covariates to the firing pattern of the cells (Figure 5C). To quantify this phenomenon, we calculated the MS score introduced before. Taking the product between all rSCC s of the three covariates showed that, after transitions from OF to ST, there was a significant increase in MS in the SUB (from $1.3e-3 \pm 0.58e-3$ in OF to $2.8e-3 \pm 0.42e-3$ in ST, $p = 0.00018$, Wilcoxon rank-sum test). In CA1, the MS score was low under both task conditions ($0.02e-3 \pm 0.02e-3$ in OF to $0.07e-3 \pm 0.01e-3$ in ST, $p = 0.47$, Wilcoxon rank-sum test, Figure 5D). In summary, even if there is no obvious remapping between OF and ST (neither in CA1 nor in SUB), the population decoding improved in the ST condition.

High decoding accuracy for P, H, and S in SUB

The previous analyses established that a statistical model requires the mix of P, H, and S covariates to best explain the data and more so in SUB than CA1 and in ST than OF. However, it is not straightforward to directly translate these results into

Figure 4. Modeling the data with a generalized linear model (GLM) shows contribution of P, H, and S to firing rates of individual neurons

(A–C) Spatial rate maps and tuning curves for H and S for three example neurons generated from data (top panels labeled with DATA) or from spike trains reproduced with the GLM (bottom panels labeled with MODEL). Symbols as in Figure 3. Note minimal tuning to H in the CA1 neuron (pFR, ~0.3 Hz).

(D) Log-likelihoods (black circles) resulting from fitting the spike train of each neuron in (A)–(C) with models encoding one covariate—P, H, or S—or with combined models containing two or more covariates. Models that performed significantly better than all less-complex models are indicated in red. Error bars indicate SEM across 10 cross-validation folds. Log-likelihoods from models containing ensemble activity (E) or theta (T) as additional covariates (Figure S3) were collapsed with simpler models containing P, H, and/or S (for example PE is collapsed with P).

(E) Bar graphs showing fractions of neurons from CA1 (red bars) and SUB (blue bars) selecting the different models. With the exception of the PHS and PS models, models were not selected at significantly different frequencies by the two populations. PS, however, was selected by 25.9% CA1 compared to 8.8% of SUB neurons and PHS was selected by 46.5% of the neurons in CA1 as compared to 53.7% in SUB (difference, >99.9 percentile of a model-selection shuffled distribution).

(F) Information rate (info rate; top panels) and relative single-covariate contribution (rSCC; bottom panels) for the neurons shown to the left in (A)–(D). Note that even if all three neurons in (D) select the most complex model (PHS), the rSCCs indicate that the firing of the CA1 neuron is predominantly determined by the animal's position, whereas the firing of the two SUB neurons is determined by P and H or P and S, respectively.

(G) 3D plot of the rSCCs of P, H, and S. Each neuron is represented by one datapoint in red for CA1 and in blue for SUB. Note abundance of SUB neurons with high values for more than one rSCC.

(H) rSCC mean and SEM across the populations of neurons in CA1 (red) and SUB (blue) for all covariates, namely, P, H, S, E, and T.

(I) Mixed selectivity score (MS score) defined as the product between rSCC(P), rSCC(H), and rSCC(S). Error bars indicate SEM.
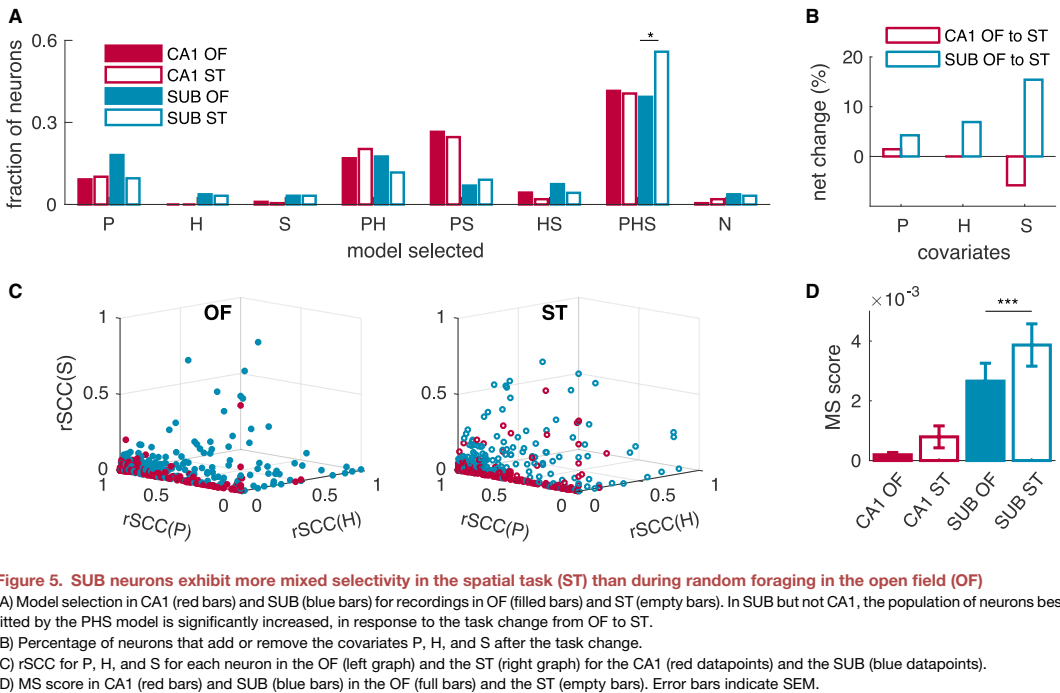
Figure 5. SUB neurons exhibit more mixed selectivity in the spatial task (ST) than during random foraging in the open field (OF)
(A) Model selection in CA1 (red bars) and SUB (blue bars) for recordings in OF (filled bars) and ST (empty bars). In SUB but not CA1, the population of neurons best fitted by the PHS model is significantly increased, in response to the task change from OF to ST.
(B) Percentage of neurons that add or remove the covariates P, H, and S after the task change.
(C) rSCC for P, H, and S for each neuron in the OF (left graph) and the ST (right graph) for the CA1 (red datapoints) and the SUB (blue datapoints).
(D) MS score in CA1 (red bars) and SUB (blue bars) in the OF (full bars) and the ST (empty bars). Error bars indicate SEM.

what can actually be read out from these codes in upstream cell populations. In order to understand what the large amount of MS in SUB might add to the hippocampal output, we therefore tried to decode P, H, and S simultaneously from cell populations in either CA1 or SUB.

Methodological constrains limited the number of simultaneously recorded neurons in SUB (the recording range was three to five neurons per SUB tetrode). In order to study decoding performance as a function of population size and extrapolate the decoding power of the two regions across tasks for a large number of neurons, we exploited the GLM framework to resample all the recorded neurons over two concatenated sessions for ST and OF, respectively (see STAR Methods section "Resampling of neurons"). To attain population sizes large enough for decoding, we randomly assembled populations of neurons that had not been simultaneously recorded in the first place. This allowed decoding of P, H, and S at the same time. Decoding of all three covariates was more accurate when using data from SUB than CA1 (Figures 6A and 6B). To assess the significance of this difference, we shuffled the neural populations with respect to their anatomical origin and computed the differences between two sets of randomized selections of neurons (ensuring equal probability to select neurons from the CA1 or the SUB cell population; Figure S6). This shuffling analysis showed that the difference in decoding accuracy deviated significantly from a distribution of shuffled differences ($p < 10e-3$) for decoding P, H, and S in the OF and the ST. Although smaller decoding errors for SUB than for CA1 were found across all population sizes, these differ-

ences were only significantly different from the differences in a shuffled distribution for population sizes larger than 100 neurons for P, larger than 20 neurons for H, and larger than 50 neurons for S (for population sizes of 5, 20, 50, 100, and 150, respectively, significance values were, for P: $p = 0.66, 0.61, 0.32, 0.005$, and 0; for H: $p = 0.02, 0, 0, 0$, and 0 and for S: $p = 0.595, 0.240, 0.042, 0.033$, and 0.009).

To better understand the difference in coding in SUB versus CA1, we also estimated the relative amount of perfectly decoded bins (PDBs). The PDB is the number of time bins in the time series for which the decoder settled on the exact bin of P, H, or S where the animal was in during that time bin. For all three covariates, namely, P, H, and S, the amount of PDB was higher when using SUB as opposed to CA1 neurons (Figure 6C; these differences were significantly different from randomized distributions; Figure S6A). Figure S7A shows furthermore that in same-length time windows, the decoder reaches bin size decoding of P, H, and S in SUB whereas in CA1 it does not. This finding indicates that, for all three covariates, the neural code in SUB allowed more accurate decoding than the one from CA1, suggesting that the code of the SUB is an effective way of transmitting signals to downstream target regions.

Comparing decoding accuracies across the two tasks showed that the decoding error for P, H, and S was significantly reduced in the ST versus OF (Figures 6A and 6B; $p < 10e-3$ compared to a shuffled distribution; Figure S6B). Decoding accuracy was higher in the ST than the OF also when counting the number of PDBs (Figure 6C). Although this was true for both CA1 and
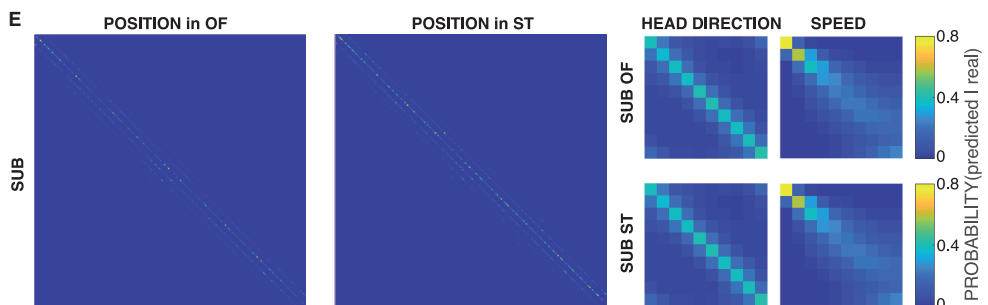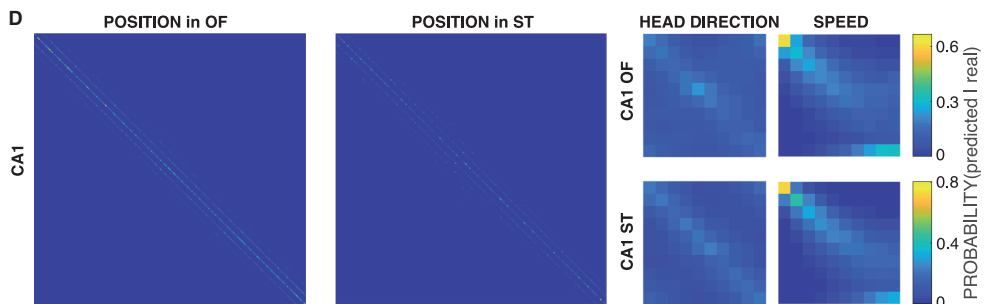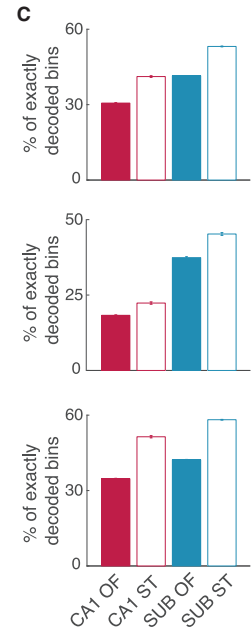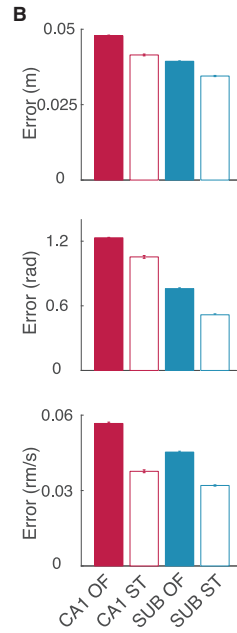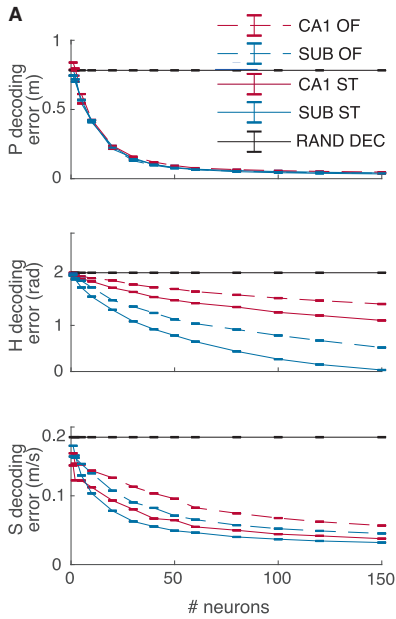
(legend on next page)

SUB, overall, the SUB reached a significantly lower number of decoding errors as well as higher proportions of PDB for P, H, and S (Figures 6A and 6B; p < 10e−3 in shuffling test of significance; Figure S6B). In order to ensure that the improved decoding in the ST did not result from a behavioral bias, we plotted confusion matrices displaying decoding accuracies for the different bin identities (Figures 6D and 6E). For H and P, the confusion matrices did not show any bias toward disproportionally better decoding in certain bin clusters of the data than others. For speed decoding, however, we observed a bias toward better decoding in the lowest speed bins (0–0.1 m/s). This bias was present for decoding from CA1 and SUB and for the OF and ST and might be a result of the disproportionally high sampling in these bins. Furthermore, even though the average speed was similar between OF and ST, the distribution was skewed toward lower and higher values (meaning that in the ST, the animal would be more often entirely immobile in order to consume the reward and then run faster to the next well). We therefore tested if decoding was affected by these differential speed distributions. By sampling the speed equally for decoding from OF and ST, we could show that decoding of all three covariates—P, H, and S—was still improved in the ST over the OF (Figures S7B–S7D).

Decoding was more accurate in the ST for both SUB and the CA1 data (see Figure 6A). Even if decoding accuracy from SUB outperforms the one from CA1 data for every behavioral covariate and session type, the improved decoding cannot be solely attributed to higher levels of MS of SUB neurons. As correlations between behavioral covariates (independent of the neural spiking) might affect decoding results, we estimated the mutual information (MI) between P, H, and S. This analysis shows that MI between behavioral covariates tends to be higher in ST than in OF (MI in ST versus OF between P and H: 1.25 bit versus 0.58 bit; between P and S: 0.76 bit versus 0.51 bit; between H and S: 0.01 bit versus 0.02 bit). Because our decoder maximizes its likelihoods for all three behavioral covariates simultaneously, the higher MI between behavioral covariates likely affects decoding accuracy independently of MS coding in SUB (even if the conjoint covariate activity is nowhere part of the model). Higher decoding accuracies will therefore be a combination of higher levels of MS in SUB neurons and a better readout due to stronger correlated behavioral covariates in the ST.

One might argue that the superiority of decoding in the SUB data might be affected by our choice of GLM as a modeling framework, as the goodness-of-fit of a model always depends on the choice of the measure used. However, in our data, neural activity in CA1 and SUB is equally well modeled by the GLM when the goodness-of-fit is measured by the difference in the likelihood of the best model and the average firing rate model (Figure S7E). Furthermore, when the goodness-of-fit is measured with explained deviance, the model fit is even better in CA1 than in SUB neurons (Figure S7F). Additionally, the task choice does not appear to affect the model performance. We therefore consider it unlikely that the decoding results should be merely a consequence of our choice of the GLM as a modeling framework.

The higher decoding accuracy in SUB is somewhat surprising given that the tuning curves of SUB neurons are broader and have a more slowly changing visual appearance than tuning curves from CA1 neurons (see tuning curves for P, H, and S in Figures 2 and S5). A possible explanation for this would be that at the population level, neural activity in SUB is fluctuating at a shorter spatial scale than in CA1. The visual appearance of the spatial autocorrelations for all neurons recorded in SUB and CA1 (Figure S7G) seems to suggest that the two population vectors change at different scales. Plotting the average population vector autocorrelation as a function of distance between spatial bins (Figure S7H) shows that the peak in SUB is narrower than that in CA1. The more accurate P decoding from SUB data might therefore reflect a faster change of the population code between nearby spatial locations in SUB than that in CA1. This therefore points to an important role of SUB at integrating multiple information streams from the hippocampal formation and providing an accurate navigational code to downstream regions.

DISCUSSION

Downstream regions of the hippocampal formation rely on output from the CA1 and SUB subfields during behaviors when navigational and mnemonic information is relevant. Although spatial coding in CA1 has been investigated extensively in place cells, it has remained elusive how SUB transforms the positional code. Here, we record neural activity during two different spatial behaviors and show that SUB provides a mixed selective code, from which three correlates of navigation—P, H, and S—can each be decoded at higher accuracies, from a similar number of neurons, than from the CA1 output. The presence of MS is consistent with an early report of place and H tuning in the same SUB cells (Sharp and Green, 1994) but takes the finding further by quantifying the mixing of three navigational variables and by showing that decodability is enhanced compared to that in CA1. Our experiments further demonstrate that MS in SUB increases with navigational task demands, suggesting a

Figure 6. More accurate decoding of P, H, and S from a fixed number of cells in SUB compared to CA1
(A) Decoding of P (top panel), H (middle panel), and S (bottom panel) for different numbers of resampled neurons. For all three covariates, decoding errors are smaller in SUB (blue) than CA1 (red) and smaller in the ST (full lines) than in the OF (dashed lines).
(B and C) Decoding error (B) and percentage of perfectly decoded bins (the number of time bins in which the decoded was the exact same as where the animal roamed at this instance; C) in a population of 150 neurons, shown separately for P (top panels), H (middle panels), and S (bottom panels). Note smaller decoding error for position in SUB than CA1. Error bars correspond to 1 SEM over 20 samples of the identities of the resampled cells.
(D and E) Confusion matrices for decoding in CA1 (D) and SUB (E). Columns show decoded covariates, namely, P (left), S (middle), and H (right); rows show tasks, namely, OF (top) and ST (bottom). Within each confusion matrix C, rows identify decoded covariate bins, wehreas columns identify bins for the covariate in the data, such that position confusion matrices are 900 × 900 and H or S matrices are 10 × 10. The color-coded element C_{ij} of the confusion matrix represents the fraction of time bins for which the decoded covariate bin is i given that the actual covariate bin was j. Bright-yellow colors indicate a maximum overlap, whereas dark-blue colors indicate no overlap between decoded and actual covariate.

behaviorally dependent information transfer to downstream regions. The activity of individual SUB neurons, which are informative on a broader spatial scale (and consequently, a longer temporal scale) than CA1 cells, may represent an integration of inputs from CA1 with information from other areas. In the present work, the combination of covariates into a mixed representation is demonstrated for three navigational parameters, namely, P, H, and S. However, it has been shown that hippocampal neurons respond also to other covariates like odors (Dusek and Eichenbaum, 1997), texture (Wood et al., 2000), and time (Eichenbaum, 2017; Fortin et al., 2002; Hampson and Deadwyler, 2003; Kesner et al., 2002). This raises the possibility that SUB neurons combine a wide range of covariates, resulting potentially in a behavior-dependent mixed code for retrieval of a broad spectrum of experiences in downstream regions.

In an information theoretical analysis, Kim et al. (2012) showed that SUB is well suited to transmit information about the animal's position by using fewer neurons than the CA1 region. We show here, with experimental data, that we can indeed decode P at a higher accuracy from SUB data than from CA1 data, when the number of cells is the same. A similar enhancement was seen in SUB for decoding H and S. For P, decoding can also be extremely accurate in CA1 when a high number of neurons is available (Pfeiffer and Foster, 2013; Wilson and McNaughton, 1993), but it is unclear if the density of connectivity to distant downstream regions is high enough to integrate over such large arrays of inputs. As SUB is the major recipient of CA1 output (Cappaert et al., 2015), projection density to this region might allow SUB to integrate over a large array of neurons in order to translate the sparse code from CA1 into a code that can be decoded accurately from a lower number of neurons at the next stage. Neurons in CA1 have been shown to combine different behavioral covariates in tasks for which multiple factors, such as olfactory, tactile, and positional cues, are salient to the animal (Komorowski et al., 2009). This type of MS has high similarities with later defined non-linear MS in other systems (Fusi et al., 2016; Rigotti et al., 2013). In contrast, the SUB neurons we show in the present study are highly mixed-selective even in situations in which the cognitive map is primarily concerned with representing spatial parameters. The GLM seems to be picking up both non-linear and linear MS. Although the model selection process appears to be sensitive to even small contributions of different covariates to the firing rate of the neurons (non-linear mixing), the MS score is sensitive to the degree at which a given covariate modulates the firing rate (linear mixing). SUB neurons appear to combine the different covariates by extensive linear mixing, allowing it to broadcast the hippocampal output in a manner that is complementary to CA1 and may facilitate efficient readout in distant brain areas.

Although P, H, and S are represented in both CA1 and SUB neurons, the combinatorial expression of those variables was a lot more common in SUB neurons. MS neurons have previously been found in a number of cortical and subcortical brain areas (Asaad et al., 1998; Freedman and Assad, 2009; Hardcastle et al., 2017; Meister et al., 2013; Rigotti et al., 2013; Rishel et al., 2013), including the hippocampal areas CA1 and CA3 (Acharya et al., 2016; McKenzie et al., 2014; Wood et al., 2000). Here, we provide additional evidence that CA1 neurons

encode multiple variables simultaneously, but we show further that representations in this subfield are dominated by P, whereas other navigational covariates have a less predominant influence on the firing rates. So even if from the perspective of the model selection process, MS exists in both CA1 and SUB, SUB displays a more evenly mixed code, as expressed in the MS score.

Our recordings in the ST further show that neurons in SUB change their level of MS depending on the task in which the animal is involved. Although it has been observed that SUB neurons change their strength of tuning to movement direction depending on the animal's behavior (Olson et al., 2017), we show here that task-dependent changes in tuning strength, in environments with high visual similarity, are not limited to direction (H in our case) but also encompass S and P. Higher cortical areas like the prefrontal and the posterior parietal cortex have previously been shown to adapt their mixed selective neural response to different task demands (Mante et al., 2013; Parthasarathy et al., 2017; Raposo et al., 2014; Stokes et al., 2013). The present findings suggest that, in the hippocampal formation, navigational output is modified by increasing the level of MS through a processing step in SUB. This is accompanied with improved decoding accuracies in both the OF and the ST. As the decoding accuracies in the ST also increase when compared to OF for CA1 data, these improvements cannot be explained solely at the level of neuronal representation but likely result from a combination of increased MS and a higher correlation between behavioral covariates. In concrete terms, this means that in SUB, in which H and S are highly expressed in the firing patterns of the cells, these covariates might help improve decoding accuracy for P and vice versa. This likely serves a mechanism for downstream regions to obtain access to a broad spectrum of hippocampal information when it is behaviorally relevant. However, although mixed-selective coding of P, H, and S proved to be effective at predicting variation on these variables, we cannot claim that these variables constitute the only neural code of SUB. The models compare only the covariates that are put into them. As SUB has been shown to be important for learning and memory (Cembrowski et al., 2018a; Morris et al., 1990; Roy et al., 2017), it is likely that its activity relates also to behavioral or cognitive variables that were absent from our analysis of navigational behavior.

Previous theoretical work has shown that mixed-selectivity coding schemes offer certain computational advantages over single-variable selectivity. When multiple covariates are combined in various quantities in the population of neurons projecting to a downstream target region, a downstream neuron can linearly combine an arbitrary subset of the inputs in order to reconstruct the value of a single covariate (Fusi et al., 2016; Ganguli and Sompolinsky, 2012). This means that, with no need for precise prepatterned connections, all the information can be transmitted, allowing downstream regions to integrate different covariates without having to repattern connections. Keeping in mind that neurons from SUB may consist of genetically compartmentalized subpopulations with each projecting to only a few selected target areas (Bienkowski et al., 2018; Cembrowski et al., 2018b; Naber and Witter, 1998; Witter, 2006), the mixed code from SUB may be specifically tailored to ensure that a wide range of covariates computed in the

hippocampal formation is accessible to distant projection areas, despite the limited number of SUB cells that may project there. Although the widespread projections from CA1 provide position information to a large array of downstream areas, the SUB output ensures the inclusion of a broader spectrum of task-relevant information in the hippocampal output, which is encoded in ways that can be integrated efficiently by downstream target regions.

STAR★METHODS

Detailed methods are provided in the online version of this paper and include the following:

- KEY RESOURCES TABLE
- RESOURCE AVAILABILITY
  - Lead contact
  - Materials availability
  - Data and code availability
- EXPERIMENTAL MODEL AND SUBJECT DETAILS
- METHOD DETAILS
  - Electrode implantation and surgery
  - Recording procedures
  - Behavioral procedures
  - Histology and reconstruction of tetrode placement
- QUANTIFICATION AND STATISTICAL ANALYSIS
  - Spike sorting and single-unit selection
  - Tracking, rate maps and tuning curves
  - Spatial correlation across session type
  - Calculating information rate and information content
  - Preparation of the data for the Poisson GLM
  - Poisson GLM
  - Poisson spiking
  - Testing performance of GLM framework with synthetic cells
  - Learning
  - Hyperparameters optimization
  - Model selection
  - Splitting between external and brain internal variables
  - Relative single covariate contributions (rSCC)
  - Mixed selectivity score (MS-score)
  - Tuning curves predicted by the model
  - Goodness of fit
  - Testing for significance in model selection between CA1 or SUB and between OF or ST
  - Decoding
  - Resampling of neurons
  - Randomization of decoding
  - Statistical testing

REFERENCES

Acharya, L., Aghajan, Z.M., Vuong, C., Moore, J.J., and Mehta, M.R. (2016). Causal Influence of Visual Cues on Hippocampal Directional Selectivity. Cell 164, 197–207.

Asaad, W.F., Rainer, G., and Miller, E.K. (1998). Neural activity in the primate prefrontal cortex during associative learning. Neuron 21, 1399–1407.

Bienkowski, M.S., Bowman, I., Song, M.Y., Gou, L., Ard, T., Cotter, K., Zhu, M., Benavidez, N.L., Yamashita, S., Abu-Jaber, J., et al. (2018). Integration of gene expression and brain-wide connectivity reveals the multiscale organization of mouse hippocampal networks. Nat. Neurosci. 21, 1628–1643.

Boccara, C.N., Sargolini, F., Thoresen, V.H., Solstad, T., Witter, M.P., Moser, E.I., and Moser, M.-B. (2010). Grid cells in pre- and parasubiculum. Nat. Neurosci. 13, 987–994.

Boccara, C.N., Kjonigsen, L.J., Hammer, I.M., Bjaalie, J.G., Leergaard, T.B., and Witter, M.P. (2015). A three-plane architectonic atlas of the rat hippocampal region. Hippocampus 25, 838–857.

Brown, E.N., Barbieri, R., Ventura, V., Kass, R.E., and Frank, L.M. (2002). The time-rescaling theorem and its application to neural spike train data analysis. Neural Comput. 14, 325–346.

Buzsáki, G. (1989). Two-stage model of memory trace formation: a role for "noisy" brain states. Neuroscience 31, 551–570.

Cappaert, N., Strien, N.M., and Witter, M.P. (2015). Hippocampal Formation. In The Rat Nervous System (Academic Press).

Cembrowski, M.S., Phillips, M.G., DiLisio, S.F., Shields, B.C., Winnubst, J., Chandrashekar, J., Bas, E., and Spruston, N. (2018a). Dissociable Structural and Functional Hippocampal Outputs via Distinct Subiculum Cell Classes. Cell 173, 1280–1292.e18.

Cembrowski, M.S., Wang, L., Lemire, A.L., Copeland, M., DiLisio, S.F., Clements, J., and Spruston, N. (2018b). The subiculum is a patchwork of discrete subregions. eLife 7, e37701.

Czurkó, A., Hirase, H., Csicsvari, J., and Buzsáki, G. (1999). Sustained activation of hippocampal pyramidal cells by 'space clamping' in a running wheel. Eur. J. Neurosci. 11, 344–352.

Dusek, J.A., and Eichenbaum, H. (1997). The hippocampus and memory for orderly stimulus relations. Proc. Natl. Acad. Sci. USA 94, 7109–7114.

Eden, U.T., and Kramer, M.A. (2010). Drawing inferences from Fano factor calculations. J. Neurosci. Methods 190, 149–152.

Eichenbaum, H. (2017). On the Integration of Space, Time, and Memory. Neuron 95, 1007–1018.

Fortin, N.J., Agster, K.L., and Eichenbaum, H.B. (2002). Critical role of the hippocampus in memory for sequences of events. Nat. Neurosci. *5*, 458–462.

Freedman, D.J., and Assad, J.A. (2009). Distinct encoding of spatial and nonspatial visual information in parietal cortex. J. Neurosci. *29*, 5671–5680.

Fusi, S., Miller, E.K., and Rigotti, M. (2016). Why neurons mix: high dimensionality for higher cognition. Curr. Opin. Neurobiol. *37*, 66–74.

Fyhn, M., Molden, S., Witter, M.P., Moser, E.I., and Moser, M.-B. (2004). Spatial representation in the entorhinal cortex. Science *305*, 1258–1264.

Ganguli, S., and Sompolinsky, H. (2012). Compressed sensing, sparsity, and dimensionality in neuronal information processing and data analysis. Annu. Rev. Neurosci. *35*, 485–508.

Gigg, J. (2006). Constraints on hippocampal processing imposed by the connectivity between CA1, subiculum and subicular targets. Behav. Brain Res. *174*, 265–271.

Goltstein, P.M., Meijer, G.T., and Pennartz, C.M. (2018). Conditioning sharpens the spatial representation of rewarded stimuli in mouse primary visual cortex. eLife *7*, e37683.

Guisan, A., and Zimmermann, N.E. (2000). Predictive habitat distribution models in ecology. Ecol. Modell. *135*, 147–186.

Hafting, T., Fyhn, M., Molden, S., Moser, M.-B., and Moser, E.I. (2005). Microstructure of a spatial map in the entorhinal cortex. Nature *436*, 801–806.

Hampson, R.E., and Deadwyler, S.A. (2003). Temporal firing characteristics and the strategic role of subicular neurons in short-term memory. Hippocampus *13*, 529–541.

Hardcastle, K., Maheswaranathan, N., Ganguli, S., and Giocomo, L.M. (2017). A Multiplexed, Heterogeneous, and Adaptive Code for Navigation in Medial Entorhinal Cortex. Neuron *94*, 375–387.e7.

Hasselmo, M.E. (2012). How We Remember: Brain Mechanisms of Episodic Memory (MIT Press).

Høydal, Ø.A., Skytøen, E.R., Andersson, S.O., Moser, M.-B., and Moser, E.I. (2019). Object-vector coding in the medial entorhinal cortex. Nature *568*, 400–404.

Ishizuka, N. (2001). Laminar organization of the pyramidal cell layer of the subiculum in the rat. J. Comp. Neurol. *435*, 89–110.

Jung, M.W., Qin, Y., McNaughton, B.L., and Barnes, C.A. (1998). Firing characteristics of deep layer neurons in prefrontal cortex in rats performing spatial working memory tasks. Cereb. Cortex *8*, 437–450.

Kesner, R.P., Gilbert, P.E., and Barua, L.A. (2002). The role of the hippocampus in memory for the temporal order of a sequence of odors. Behav. Neurosci. *116*, 286–290.

Kim, S.M., Ganguli, S., and Frank, L.M. (2012). Spatial information outflow from the hippocampal circuit: distributed spatial coding and phase precession in the subiculum. J. Neurosci. *32*, 11539–11558.

Komorowski, R.W., Manns, J.R., and Eichenbaum, H. (2009). Robust conjunctive item-place coding by hippocampal neurons parallels learning what happens where. J. Neurosci. *29*, 9918–9929.

Kraus, B.J., Brandon, M.P., Robinson, R.J., 2nd, Connerney, M.A., Hasselmo, M.E., and Eichenbaum, H. (2015). During Running in Place, Grid Cells Integrate Elapsed Time and Distance Run. Neuron *88*, 578–589.

Kropff, E., Carmichael, J.E., Moser, M.-B., and Moser, E.I. (2015). Speed cells in the medial entorhinal cortex. Nature *523*, 419–424.

Langston, R.F., Ainge, J.A., Couey, J.J., Canto, C.B., Bjerknes, T.L., Witter, M.P., Moser, E.I., and Moser, M.-B. (2010). Development of the spatial representation system in the rat. Science *328*, 1576–1580.

Lansink, C.S., Jackson, J.C., Lankelma, J.V., Ito, R., Robbins, T.W., Everitt, B.J., and Pennartz, C.M.A. (2012). Reward cues in space: commonalities and differences in neural coding by hippocampal and ventral striatal ensembles. J. Neurosci. *32*, 12444–12459.

Leutgeb, S., Ragozzino, K.E., and Mizumori, S.J.Y. (2000). Convergence of head direction and place information in the CA1 region of hippocampus. Neuroscience *100*, 11–19.

Lever, C., Burton, S., Jeewajee, A., O'Keefe, J., and Burgess, N. (2009). Boundary vector cells in the subiculum of the hippocampal formation. J. Neurosci. *29*, 9771–9777.

Mante, V., Sussillo, D., Shenoy, K.V., and Newsome, W.T. (2013). Context-dependent computation by recurrent dynamics in prefrontal cortex. Nature *503*, 78–84.

McClelland, J.L., McNaughton, B.L., and O'Reilly, R.C. (1995). Why there are complementary learning systems in the hippocampus and neocortex: insights from the successes and failures of connectionist models of learning and memory. Psychol. Rev. *102*, 419–457.

McCullagh, P., and Nelder, J.A. (1989). Generalized Linear Models (Chapman and Hall/CRC).

McKenzie, S., Frank, A.J., Kinsky, N.R., Porter, B., Rivière, P.D., and Eichenbaum, H. (2014). Hippocampal representation of related and opposing memories develop within distinct, hierarchically organized neural schemas. Neuron *83*, 202–215.

McNaughton, B.L., Barnes, C.A., and O'Keefe, J. (1983). The contributions of position, direction, and velocity to single unit activity in the hippocampus of freely-moving rats. Exp. Brain Res. *52*, 41–49.

Meister, M.L.R., Hennig, J.A., and Huk, A.C. (2013). Signal multiplexing and single-neuron computations in lateral intraparietal area during decision-making. J. Neurosci. *33*, 2254–2267.

Miller, E.K., Erickson, C.A., and Desimone, R. (1996). Neural mechanisms of visual working memory in prefrontal cortex of the macaque. J. Neurosci. *16*, 5154–5167.

Morris, R. (2007). Theories of Hippocampal Function. In The Hippocampus Book (Oxford University Press), pp. 581–714.

Morris, R.G., Schenk, F., Tweedie, F., and Jarrard, L.E. (1990). Ibotenate Lesions of Hippocampus and/or Subiculum: Dissociating Components of Allocentric Spatial Learning. Eur. J. Neurosci. *2*, 1016–1028.

Mulder, A.B., Shibata, R., Trullier, O., and Wiener, S.I. (2005). Spatially selective reward site responses in tonically active neurons of the nucleus accumbens in behaving rats. Exp. Brain Res. *163*, 32–43.

Naber, P.A., and Witter, M.P. (1998). Subicular efferents are organized mostly as parallel projections: a double-labeling, retrograde-tracing study in the rat. J. Comp. Neurol. *393*, 284–297.

Nitz, D.A. (2006). Tracking route progression in the posterior parietal cortex. Neuron *49*, 747–756.

O'Keefe, J. (1976). Place units in the hippocampus of the freely moving rat. Exp. Neurol. *51*, 78–109.

O'Keefe, J., and Dostrovsky, J. (1971). The hippocampus as a spatial map. Preliminary evidence from unit activity in the freely-moving rat. Brain Res. *34*, 171–175.

O'Keefe, J., and Nadel, L. (1978). The hippocampus as a cognitive map (Oxford University Press).

O'Mara, S. (2006). Controlling hippocampal output: the central role of subiculum in hippocampal information processing. Behav. Brain Res. *174*, 304–312.

O'Mara, S.M., Commins, S., Anderson, M., and Gigg, J. (2001). The subiculum: a review of form, physiology and function. Prog. Neurobiol. *64*, 129–155.

Olson, J.M., Tongprasearth, K., and Nitz, D.A. (2017). Subiculum neurons map the current axis of travel. Nat. Neurosci. *20*, 170–172.

Padilla-Coreano, N., Canetta, S., Mikofsky, R.M., Alway, E., Passecker, J., Myroshnychenko, M.V., Garcia-Garcia, A.L., Warren, R., Teboul, E., Blackman, D.R., et al. (2019). Hippocampal-Prefrontal Theta Transmission Regulates Avoidance Behavior. Neuron *104*, 601–610.e4.

Parthasarathy, A., Herikstad, R., Bong, J.H., Medina, F.S., Libedinsky, C., and Yen, S.-C. (2017). Mixed selectivity morphs population codes in prefrontal cortex. Nat. Neurosci. *20*, 1770–1779.

Peck, E.L., Peck, C.J., and Salzman, C.D. (2014). Task-dependent spatial selectivity in the primate amygdala. J. Neurosci. *34*, 16220–16233.

Pfeiffer, B.E., and Foster, D.J. (2013). Hippocampal place-cell sequences depict future paths to remembered goals. Nature *497*, 74–79.

Pillow, J.W. (2009). Time-rescaling methods for the estimation and assessment of non-Poisson neural encoding models. In Advances in Neural Information Processing Systems 22, Y. Bengio, D. Schuurmans, J.D. Lafferty, C.K.I. Williams, and A. Culotta, eds. (Curran Associates, Inc.), pp. 1473–1481.

Poulter, S., Lee, S.A., Dachtler, J., Wills, T.J., and Lever, C. (2020). Vector trace cells in the subiculum of the hippocampal formation. Nat. Neurosci. 24, 266–275.

Pratt, W.E., and Mizumori, S.J.Y. (2001). Neurons in rat medial prefrontal cortex show anticipatory rate changes to predictable differential rewards in a spatial memory task. Behav. Brain Res. 123, 165–183.

Raposo, D., Kaufman, M.T., and Churchland, A.K. (2014). A category-free neural population supports evolving demands during decision-making. Nat. Neurosci. 17, 1784–1792.

Remondes, M., and Wilson, M.A. (2013). Cingulate-hippocampus coherence and trajectory coding in a sequential choice task. Neuron 80, 1277–1289.

Rigotti, M., Barak, O., Warden, M.R., Wang, X.-J., Daw, N.D., Miller, E.K., and Fusi, S. (2013). The importance of mixed selectivity in complex cognitive tasks. Nature 497, 585–590.

Rishel, C.A., Huang, G., and Freedman, D.J. (2013). Independent category and spatial encoding in parietal cortex. Neuron 77, 969–979.

Roy, D.S., Kitamura, T., Okuyama, T., Ogawa, S.K., Sun, C., Obata, Y., Yoshiki, A., and Tonegawa, S. (2017). Distinct Neural Circuits for the Formation and Retrieval of Episodic Memories. Cell 170, 1000–1012.e19.

Saleem, A.B., Diamanti, E.M., Fournier, J., Harris, K.D., and Carandini, M. (2018). Coherent encoding of subjective spatial position in visual cortex and hippocampus. Nature 562, 124–127.

Scoville, W.B., and Milner, B. (1957). Loss of recent memory after bilateral hippocampal lesions. J. Neurol. Neurosurg. Psychiatry 20, 11–21.

Sharp, P.E. (1997). Subicular cells generate similar spatial firing patterns in two geometrically and visually distinctive environments: comparison with hippocampal place cells. Behav. Brain Res. 85, 71–92.

Sharp, P.E. (2006). Subicular place cells generate the same "map" for different environments: comparison with hippocampal cells. Behav. Brain Res. 174, 206–214.

Sharp, P.E., and Green, C. (1994). Spatial correlates of firing patterns of single cells in the subiculum of the freely moving rat. J. Neurosci. 14, 2339–2356.

Skaggs, W.E., McNaughton, B.L., and Gothard, K.M. (1993). An Information-Theoretic Approach to Deciphering the Hippocampal Code. In Advances in

Neural Information Processing Systems 5, [NIPS Conference] (Morgan Kaufmann Publishers Inc.), pp. 1030–1037.

Solstad, T., Boccara, C.N., Kropff, E., Moser, M.-B., and Moser, E.I. (2008). Representation of geometric borders in the entorhinal cortex. Science 322, 1865–1868.

Spellman, T., Rigotti, M., Ahmari, S.E., Fusi, S., Gogos, J.A., and Gordon, J.A. (2015). Hippocampal-prefrontal input supports spatial encoding in working memory. Nature 522, 309–314.

Squire, L.R. (1992). Memory and the hippocampus: a synthesis from findings with rats, monkeys, and humans. Psychol. Rev. 99, 195–231.

Squire, L.R., Genzel, L., Wixted, J.T., and Morris, R.G. (2015). Memory consolidation. Cold Spring Harb. Perspect. Biol. 7, a021766.

Stewart, S., Jeewajee, A., Wills, T.J., Burgess, N., and Lever, C. (2013). Boundary coding in the rat subiculum. Philos. Trans. R. Soc. Lond. B Biol. Sci. 369, 20120514.

Stokes, M.G., Kusunoki, M., Sigala, N., Nili, H., Gaffan, D., and Duncan, J. (2013). Dynamic coding for cognitive control in prefrontal cortex. Neuron 78, 364–375.

Taube, J.S., and Burton, H.L. (1995). Head direction cell activity monitored in a novel environment and during a cue conflict situation. J. Neurophysiol. 74, 1953–1971.

Taube, J.S., Muller, R.U., and Ranck, J.B., Jr. (1990). Head-direction cells recorded from the postsubiculum in freely moving rats. I. Description and quantitative analysis. J. Neurosci. 10, 420–435.

Whitlock, J.R., Pfuhl, G., Dagslott, N., Moser, M.-B., and Moser, E.I. (2012). Functional split between parietal and entorhinal cortices in the rat. Neuron 73, 789–802.

Wilson, M.A., and McNaughton, B.L. (1993). Dynamics of the hippocampal ensemble code for space. Science 261, 1055–1058.

Winocur, G., and Moscovitch, M. (2011). Memory transformation and systems consolidation. J. Int. Neuropsychol. Soc. 17, 766–780.

Witter, M.P. (2006). Connections of the subiculum of the rat: topography in relation to columnar and laminar organization. Behav. Brain Res. 174, 251–264.

Wood, E.R., Dudchenko, P.A., Robitsek, R.J., and Eichenbaum, H. (2000). Hippocampal neurons encode information about different types of memory episodes occurring in the same location. Neuron 27, 623–633.

STAR★METHODS

KEY RESOURCES TABLE

REAGENT or RESOURCE	SOURCE	IDENTIFIER
Chemicals, peptides, and recombinant proteins		
Cresyl Violet for Nissl stain	Sigma Alderich	1.05235
Deposited data		
Spike-time, position, head direction and theta phase data; histology data	This paper	Provided upon request
Experimental models: Organisms/strains		
Rat: Long-Evans	Charles River, in-house	https://www.criver.com/products-services/find-model/long-evans-rat?region=3616
Software and algorithms		
MATLAB R2019b	Mathworks	https://se.mathworks.com/
MClust 4.4	A.D. Redish	http://redishlab.neuroscience.umn.edu/MClust/MClust.html
Custom-made analysis code	This paper	Provided upon request
Other		
Polyimide-coated platinum-iridium (90-10%) wires	California Fine wire	N/A
Hyperdrive	Custom made	N/A
Microdrive	Axona LTD	N/A
Axio Scan.Z1	Zeiss	N/A

RESOURCE AVAILABILITY

Lead contact
Further information and requests for resources and reagents should be directed to and will be fulfilled by the Lead Contact, Edvard I. Moser (edvard.moser@ntnu.no).

Materials availability
This study did not generate new unique materials.

Data and code availability
Datasets and code supporting the current study will be provided upon request.

EXPERIMENTAL MODEL AND SUBJECT DETAILS

Data were collected from eight male Long Evans rats, which were experimentally naive and 3–5 months old (350–600 g) at the time of implantation. The rats were group housed with 3–8 of their male littermates prior to surgery and were singly housed in large Plexiglas cages (45 × 44 × 30 cm) thereafter. The rats were kept on a 12 h light/12 h dark schedule, and humidity and temperature were strictly controlled. The experiments were performed in accordance with the Norwegian Animal Welfare Act and the European Convention for the Protection of Vertebrate Animals used for Experimental and Other Scientific Purposes. All experiments were approved by the Norwegian Food Safety Authority.

METHOD DETAILS

Electrode implantation and surgery
Tetrodes were constructed from four twisted 17-μm polyimide-coated platinum-iridium (90%/10%) wires (California Fine Wire). The electrode tips were plated with platinum to reduce electrode impedances to between 120–300 kΩ at 1 kHz.

Anesthesia was induced by placing the animal in a closed Plexiglas box filled with 5% isoflurane vapor. Subsequently, the animal received a subcutaneous injection of buprenorphine (0.03 mg kg^{-1}), atropine (0.05 mg kg^{-1}) and meloxicam (1.0 mg kg^{-1}) and was mounted on a stereotactic frame. The animal's body rested on a heat blanket to maintain its core body temperature during the surgical procedure. Anesthesia was maintained with isoflurane, with air flow at 1.0 liters/min and isoflurane concentration 0.75%–3%, as determined according to breathing patterns and reflex responses.

The scalp midline was subcutaneously injected with the local anesthetic lidocaine (0.5%) prior to incision. After removal of the periost, holes were drilled vertically in the skull, into which screws (M1.4) were inserted. Two screws positioned over the cerebellum were used as the electrical ground. Craniotomies were drilled anterior to the transverse sinus. Subsequently, the animal was implanted with either a hyperdrive containing 14 independently moveable tetrodes (seven animals), or a microdrive, containing a single bundle of eight tetrodes. Hyperdrive implants were always on the left side. Hyperdrive tetrodes were implanted perpendicular to the long axis of the HPC (at a 45 deg angle) between −5.5 to −5.7 mm AP and 1.2 to 1.8 ML. Each tetrode was immediately advanced by 940 μm. Microdrive tetrodes were inserted in the right HPC at −6.9 AP (from right sinus) and 2.0 ML. The tetrodes were immediately inserted to a depth of 1.5 mm. Implants were secured with dental cement (Meliodent). 8–12 h after the beginning of the surgery, the animal was treated with an additional dose of buprenorphine (0.03 mg kg^{-1}).

Recording procedures

Over the course of 1–3 weeks, tetrodes were lowered in steps of 320 μm or less, until high-amplitude theta-modulated activity appeared in the local field potential at a depth of approximately 2.0 mm. In hyperdrive experiments, at least one of the tetrodes was used to record a reference signal from white matter areas. The drive was connected to a multichannel, impedance matching, unity gain headstage. The output of the headstage was conducted via a lightweight multiwire tether cable and through a slip-ring commutator to a Neuralynx data acquisition system (Neuralynx, Tucson, AZ; Neuralynx Digital Lynx SX, for all hyperdrive-implanted animals) or via a counterbalanced lightweight multiwire cable to an Axona acquisition system (Axona Ltd., Herts, UK, for the one microdrive-implanted animal). Both cables allowed the animal to move freely within the available space. Unit activity was amplified by a factor of 3,000–5,000 and bandpass filtered 600–6,000 Hz (Neuralynx) or 800–6,700 Hz (Axona). Spike waveforms above a threshold set by the experimenter (50–80 μV) were timestamped and digitized at 32 kHz (Neuralynx) or 48 kHz (Axona) for 1 ms. In some Neuralynx recordings, the raw signals were also recorded (32 kHz). Local field potential (LFP) signals were recorded from one per tetrode for the hyperdrives and one in total per Axona microdrive. LFP signals were amplified by a factor of 250–1,000, low-pass filtered at 300–475 Hz and sampled at 1,800–2,500 Hz. The LFP channels were recorded referenced to the ground screw positioned above the animal's cerebellum (Neuralynx and Neuropixels) or against an electrode from one microdrive tetrode (Axona). For Neuralynx and Axona recordings, LEDs on the headstage were used to track the animal's movements at a sampling rate of 25 Hz (Neuralynx) or 50 Hz (Axona).

Behavioral procedures

The rats were food restricted, maintaining their weight at a minimum of 90% of their free-feeding body weight, and were food deprived 12–16 h before each training or recording session. During the 3–6 weeks prior to surgery and testing, the animals were trained to find the wells filled with chocolate oat milk and alternate between targeted search and direct run toward the home well (ST). When animals achieved a success rate higher than 90% in the ST they were also introduced to random foraging in the open field (OF) (approximately 1 to 1.5 weeks prior to implantation). The arena was a 150 × 150 cm square box with a black floor mat during the OF and a rubber-spray covered plastic plate with 37 small hemisphere incisions of 1 cm diameter arranged in a regular lattice. A cue card (a white A4 paper) on one of the walls indicated orientation. The two environments were located in the exact same place with all distal cues constant and surrounded by the same 50-cm-high black walls. As a reward, vanilla or chocolate biscuit crumbs were randomly scattered in the OF condition and in the ST, chocolate oat milk was provided via the wells in the floor. Curtains were not used, and abundant visual cues were available to the foraging rat. Between sessions in the OF and ST, the rat was placed next to the arena on an elevated flowerpot lined with towels.

Each recording day consisted of two OF and two ST sessions of each roughly 30 min. The ST was run such that all 36 random wells had to be visited at least once, resulting in 36 to 38 home run trials. Care was given that all the arena floors and walls were clean prior to beginning each recording. Data from multiple sessions of the same type was concatenated for analysis purposes. Recordings were generally performed during the dark phase of the 12 h/12 h light cycle.

Histology and reconstruction of tetrode placement

Rats were anesthetized with isoflurane (5%) and then received an overdose of sodium pentobarbital. They were subsequently perfused intracardially with saline followed by 4% formaldehyde. The brains were extracted, stored in 4% formaldehyde to be later frozen and cut in coronal sections (animals 20360, 22295, 23783, 24101 and 24116) and para-coronal sections (animal 20382, 21012 and 22098; sections were 45 degrees offset of coronal and sagittal sections in order to align with the angle of drive implantation). Sections of 30 μm were subsequently stained with cresyl violet (Nissl) and the relevant parts of CA1 and SUB were collected for analysis. For hyperdrive implants, all tetrodes from the 14-tetrode bundle were individually identified from digital photomicrographs by comparing tetrode traces from successive sections.

The depth of the recording sites was determined post hoc by comparing the deepest visible electrode trace in the tissue with the distance the electrodes were moved between the recording day and the day the animal was perfused. E.g. in Figure 1B tetrode 5 is visible in two images: the leftmost and the middle image in the second row. The track in the middle image, indicated with an empty red triangle (second triangle from the left), is the lowest point in the brain sections where the electrode track could be observed. Between the day the animal was perfused and the last day a neuron had been recorded on tetrode no. 5 the electrode had been moved 270 μm. We therefore assume that the recording sites for this electrode had been approximately 270 μm above this point. This is located in the proximal SUB which at this proximo-distal level extends above the CA1 cell layer. For tetrode no. 12 in animal 20382 the electrode was 100 μm above the recording end point and in animal 20360 the last recordings of tetrodes 8, 9 and 11 have been 100, 210 and 300 μm above the location of the electrode-tip on the day of perfusion. For four-tetrode microdrives, the tetrode bundle as a whole was localized with a similar method.

In order to approximate the anatomical distribution of the recorded cells along the proximo-distal axis, the respective regions were subdivided into proximal, middle and distal CA1 and proximal or distal SUB, respectively. The boundary between the respective subregions was approximated by dividing the region in every section into three or two (for CA1 or SUB, respectively) equally large subregions (see black dashed lines in sections of Figure S1).

QUANTIFICATION AND STATISTICAL ANALYSIS

Spike sorting and single-unit selection
Spike sorting was performed offline using manual cluster cutting methods with MClust (A. D. Redish, http://redishlab.neuroscience.umn.edu/MClust/MClust.html). Spike rate autocorrelation and cross-correlation were used as additional tools for separating or merging spike clusters. Single units were discarded if more than 0.5% of their inter-spike interval distribution was comprised of intervals less than 2 ms or if they had a mean spike rate less than 0.5 Hz. Additionally, interneurons were separated and excluded from the dataset by removing clusters with narrow waveforms and high firing rates during manual spike sorting.

Tracking, rate maps and tuning curves
Animal position was estimated by tracking the LEDs or reflective markers mounted on the implant. Only time epochs in which the animal was moving at a speed above 2 m s^{-1} were used for spatial analyses.

To generate 2D rate maps for the open-field arena, position estimates were binned into a 5 × 5 cm square grid. The spike rate in each position bin was calculated as the number of spikes recorded in the bin, divided by the time the animal spent in the bin. The resultant 2D rate map was smoothed with a Gaussian kernel with σ = 1.5 bins.

The animal's head direction was determined from the relative positions of LEDs or reflective markers on the implant. Head direction tuning curves were calculated by binning the head direction estimates into 6° bins. The spike rate in each angular bin was calculated as the number of spikes recorded in the bin divided by the time the animal spent in the bin. The resultant tuning curve was smoothed with a Gaussian kernel with σ = 1 bin, with the ends of the tuning curve wrapped together.

Spatial correlation across session type
For the spatial correlations across session types (i.e., spatial memory task (ST) versus open field (OF) the data from open field and foster maze were concatenated, respectively. Half of the session was chosen by taking 5 minutes intervals of the data which then were shifted forward n times with 30 s intervals. For each shifted sub-portion of the data, the rate map was calculated and correlated with the other half of the data. The number of shifts needed to get a stable value was determined in a saturation process where for every cell increasing number of shifts were used until three consecutive values of the correlation were below 0.5 standard deviations.

Calculating information rate and information content
Information rate (I_{rate}) and information content ($I_{content}$) were calculated as described in Skaggs et al. (1993). Briefly, every covariate space was binned (900 bins of 5 X 5 cm for position, 10 bins for head direction and 10 bins for speed) and the neurons spikes were allocated to the respective bin the animal was occupying while they were emitted. The total number of spikes in every bin was then divided by the total session time to receive $\lambda(x)$, the average firing rate in bin x. Using λ, the mean firing rate of the neuron across the entire session and $P(x)$, the probability of the animal to occupy bin x, information rate for each neuron across the entire session was calculated by:

$$I_{rate} = \int_x \lambda(x) log_2 \frac{\lambda(x)}{\lambda} P(x) dx$$

To calculate information content per spike, I_{rate} was divided by the average firing rate of the neuron across the entire session λ.

$$I_{content} = \frac{I_{rate}}{\lambda}$$

In order to ensure that the information values are minimally affected by any biases, we subtracted from all information measures the mean of the value obtained for the same measure for 100 shuffled spike distributions. The values reported in the text are with these biases removed, although our results do not qualitatively change if we do not remove the bias.

Preparation of the data for the Poisson GLM

Spike time stamps obtained from the spike sorting procedure were binned using bins of length $dt = 20$ ms to get a spike count train vector $\mathbf{n} = \{n(t)\}_{t=1}^{T}$ per each cell, where $n(t)$ is the spike count in time bin t, while T is the total number of time bins. The behavioral covariates taken into account are:

P xy-position of the rat on the horizontal plane;

H head direction of the rat on the horizontal plane;

S running speed of the rat;

while the internal covariates consist of:

T theta phase, i.e., the phase of the band-pass filtered (5 to 12 Hz) and Hilbert-transformed local field potential.

E ensemble spike signal, defined as the z-scored sum of the spike counts of all neurons simultaneously recorded at the same tetrodes.

All covariates were interpolated at the centers of the time bins to achieve the same temporal resolution of the spike counts. By means of an optimization procedure over the entire population of neurons (see section Hyperparameters optimization) we chose to bin each covariate C in to N_C bins. Finally for each covariate C in each time bin t we built a binary state vector $\mathbf{X}^C(t)$ of length N_C, with entries $X_i^C(t) = 1$ if the animal behavioral state at time t fell in the i-th bin for the covariate C, while $X_i^C(t) = 0$ otherwise. Unless explicitly stated the OF and ST sessions were concatenated.

Poisson GLM

We adopted a Poisson GLM to explicitly model the stochastic response of each neuron to the covariates C. The choice of a Poisson random component as used in Hardcastle et al. (2017) is further motivated in subsection '*Poissonian spiking*'. The models $\mathcal{M}$ we consider, are combinations of behavioral and internal covariates $C = P, H, S, T, E$. For a given model $\mathcal{M}$ the probability of recording k spikes in time bin t of length dt is Poissonian:

$$Prob\left(k \big| \{\mathbf{X}^C(t)\}_{C \in \mathcal{M}} \{\beta^C\}_{C \in \mathcal{M}}\right) = exp\left(-FR(\{\mathbf{X}^C(t)\}_{C \in \mathcal{M}})dt\right) \frac{(FR(\{\mathbf{X}^C(t)\}_{C \in \mathcal{M}})dt)^k}{k!} \tag{Equation 1}$$

where $FR(\{\mathbf{X}^C(t)\}_{C \in \mathcal{M}})$ is the expected firing rate in time bin t, and

$$FR(\{\mathbf{X}^C(t)\}_{C \in \mathcal{M}}) = exp\left(\sum_{C \in \mathcal{M}} \sum_i \beta_i^C X^C(t)_i\right) \Big/ dt \tag{Equation 2}$$

depends on the behavioral/internal state vectors $\mathbf{X}^C$ in time bin t and the vector of predictors β^C for all covariates $C \in \mathcal{M}$. The predictors are estimated by the learning procedure explained in section "Learning."

Poisson spiking

We selected the Poisson distribution to fit the stochasticity of the firing process after explorative analysis of our data and rigorous testing. First, we observed that the spiking data are not binary for time bin lengths $dt \geq 1$ ms. This indicated that the Bernoulli distribution may not be a suitable choice. Second, we verified that the inter-spike-interval (ISI) distribution is well fitted by an exponential up to 60 ms (the deviations at 1-2 ms can be attributed to the refractory period). The ISI distribution expected for Poisson firing is indeed exponential.

In addition, we looked at the Fano Factors of the spike count N for each cell, defined as:

$$PFano\ Factor(N) = \frac{variance(N)}{mean(N)} \tag{Equation 3}$$

This analysis indicated that the *variance(N)* versus *mean(N)* plots are well fitted by the line that bisects the first quadrant of the coordinate system for time bin lengths $dt \geq 40$ ms. The coefficient of determination of the fit $R - square$ is an indication of how much the spiking process deviates from a homogeneous Poisson process, for which a Fano Factor of 1 is expected in the long run.

Notice that the Poisson GLM in Equation 1 is not a homogeneous Poisson process (the firing rate of Equation 1 depends on the covariates which vary in time), it becomes homogeneous Poisson once the covariates in Equation 1 are fixed. We used the asymptotic distribution of the Fano Factor for the homogeneous Poisson (Eden and Kramer, 2010) to test how poissonian the spike counts are at fixed covariates. We run the test after conditioning the spike counts on the covariate position in a 30 times 30 grid superimposed to the recording box. The number of position bins was optimized for this test and bins with occupancy shorter than 250 ms were excluded by this analysis. The test with 5% significance level resulted in an average fraction of position bins rejected by cell of 0.0589 ± 0.0009. Finally, instead of conditioning on position, we conditioned on time, by testing the Fano Factor of the spike count in 500 ms time windows. The conditioning in time is motivated by slow varying covariates which enforce to the firing rate a different

timescale from the spiking timescale. This approach resulted into an even smaller average rejection rate, suggesting that position may not be the only covariate modulating the activity of this cells. The average fraction of 500 ms time windows in which the Poisson hypothesis has to be rejected with a 5% confidence is 0.0152 ± 0.0002.

Testing performance of GLM framework with synthetic cells
We simulated pure position, head-direction and speed tuned inhomogeneous Poisson spike trains and mixed combinations of the three to validate the performance our GLM framework.

Learning
In order to determine the selectivity of a neuron to the covariates $C = P, H, S, T, E$, given the recorded spike count train vector $\mathbf{k}$ and the vectors of covariates $\mathbf{X}^C(t)$ in each time bin t, we optimized the predictors β_i^C of the Poisson GLM in Equation 1 for each model $\mathcal{M}$ to minimize the cost function:

$$L\left[\{\beta^C\}_{C\in\mathcal{M}}\big|\{\mathbf{X}^C(t)\}_{C\in\mathcal{M}}, \gamma, \mathbf{k}\right] = -\sum_t \ln \text{Prob}\left(k(t)\big|\{\mathbf{X}^C(t)\}_{C\in\mathcal{M}}, \{\beta^C\}_{C\in\mathcal{M}}\right) + \frac{1}{2}\sum_{C\in\mathcal{M}}\gamma^C\sum_i\left(\beta_i^C - \beta_{i-1}^C\right)^2 \qquad \text{(Equation 4)}$$

such that the learned parameters are $\{\beta^C\}_{C\in\mathcal{M}} = \text{argmin}_{\{\infty\}_{C\in\mathcal{M}}} L[\{\beta\}_{C\in\mathcal{M}}\big|\{\mathbf{X}^C(t)\}_{C\in\mathcal{M}}, \gamma, \mathbf{k}]$. The first term in the loss function of Equation 4 is the negative log-likelihood of the spike count train vector $\mathbf{k}$, while the second term is a penalty on large differences in parameters between nearest neighboring covariate bins and therefore enforces smoothness in the model predicted tuning curves. The smoothness hyperparameter γ^C controls the strength of the smoothness penalty for the covariate C and was optimized *a priori* on the entire population of neurons, as explained in section Hyperparameters optimization. The minimization of the function $L[\{\beta\}_{C\in\mathcal{M}}\big|\{\mathbf{X}^C(t)\}_{C\in\mathcal{M}}, \gamma, \mathbf{k}]$ in the parameter space was performed using the MATLAB *minunc* function. The learned parameters β were used for estimating model performance, constructing model predicted tuning curves (see section Tuning curves predicted by the model) and decoding.

In addition to the models containing the behavioral/internal covariates we also fitted a model with only the bias term ($\text{FR}(\beta_0) = \exp(\beta_0)/dt$), which we term the average firing rate model. Model performance for each cell was assessed in a 10-fold cross-validation setup: of the whole spike count train one tenth was held out as test set, while the rest constituted the training dataset, on which parameters were learned. The difference in log-likelihood of the test spike count train between the model $\mathcal{M}$ and the average firing rate Poisson model (also learned on the training data) was taken and then divided by the number of time bins in the test set. The cross-validation procedure was repeated for 10 non-overlapping test sets, resulting in 10 values of the log-likelihood increase over the average firing rate model per time bin $\{\text{LLH}_i(\mathcal{M})\}_{i=1}^{10}$. Their average across cross-validation folds $\text{LLH}(\mathcal{M}) = \frac{1}{10}\sum_i \text{LLH}_i(\mathcal{M})$ was regarded as the main indicator of model $\mathcal{M}$ performance.

Hyperparameters optimization
For optimizing the hyperparameters (Figure S4), number of bins N_C and smoothness hyperparameter γ^C for each covariate $C = P, H, S, T, E$, we computed the model performance LLH(C) on a grid in the hyperparameters space ($N_C = \{2,5,10,20,30,40,50,60,70\}$, $\gamma^C = \{0.08, 0.8, 0, 80, 800\}$), for each of the single covariate model $\mathcal{M} = C$ separately and for each cell independently. The values of LLH(C) at fixed hyperparameters were then averaged over all cells in the population, and the values of the hyperparameters at its maximum on the grid were taken as candidate optimal hyperparameters. To compare model performance at the maximum to its neighboring vertices on the grid in the hyperparameters space, we employed the one tailed Wilcoxon signed-rank test between the population vector of LLH(C) at the maximum and the same vector in its nearest neighbors on the grid. The values of the hyperparameters including the smallest number of covariate bins N_C, whose corresponding vector of average normalized log-likelihoods was not significantly different from the maximum (p > 0.05 in the Wilcoxon signed-rank test), were chosen as new candidate optimal hyperparameters. This procedure was then iterated until all neighboring models with smaller numbers of covariate bins were significantly different in model performance according to our test. The hyperparameters were then held fixed during learning on the entire population of neurons and for all models.

The optimal number of bins and smoothness hyperparameters are respectively $N_P = 30$ (along each edge of the squared enclosure, 900 in total) and $\gamma^P = 8$ for position, $N_H = 10$ and $\gamma^H = 800$ for head direction, $N_S = 10$ and $\gamma^S = 800$ for speed, $N_T = 10$ and $\gamma^T = 800$ for theta, $N_E = 20$ and $\gamma^E = 80$ for ensemble activity.

Model selection
Learning was performed for all 31 models $\mathcal{M}$, i.e., the single covariate models P, H, S, E, T, the two covariate models $PH, PS, HS, PE, PT...$, all the three, the four covariate models up to the five covariates model $PHSET$. The learning method is described in section "Learning." We adopted a forward model selection procedure (Hardcastle et al., 2017) aiming at selecting the model with the highest performance and the smallest number of covariates. As a starting point we used the average firing rate model (only bias). So, we considered the model with the largest performance LLH($\mathcal{M}$) among the single covariate models, e.g., $\mathcal{M}^1 = S$. The vector of log-likelihood increases over the average firing rate model $\{\text{LLH}\}_{i=1}^{10}$ across cross-validation folds for the selected single covariate model $\mathcal{M}^1$ was compared to the same vector for the average firing rate model (a vector of zeros), by means of the one-tailed Wilcoxon

signed rank test. If significantly different ($p < \alpha$ in the one tailed Wilcoxon signed rank test), then the single covariate model became the new candidate selected model, otherwise the average firing rate model was selected and the search in the model space interrupted. In the former case, the model with the largest LLH($\mathcal{M}$) among the two covariate models, including the covariate selected in the former step, e.g., $\mathcal{M} = PS,HS,TS,SE$, was considered, e.g., $\mathcal{M}^2 = PS$. In full analogy with the previous selection step, the vector of log-likelihood increases over the average firing rate model $\{\text{LLH}\}_{i=1}^{10}$, across cross-validation folds for the single covariate model $\mathcal{M}^1$ was compared to the same vector for the two covariate model $\mathcal{M}^2$, by means of the Wilcoxon signed-rank test. If the mean of the vector for $\mathcal{M}^2$, LLH($\mathcal{M}^2$), was significantly larger than the mean of the vector for $\mathcal{M}^1$, LLH($\mathcal{M}^1$),($p < \alpha$ in the one tailed Wilcoxon signed-rank test) the model $\mathcal{M}^2$ was identified as candidate model. If not significant the search in the model space was interrupted and the single covariate model $\mathcal{M}^1$ became the selected model. The forward search was carried on in this fashion by including one covariate at each step to the candidate selected model, up to the selected model resulting in a not significantly different outcome in the Wilcoxon signed-rank test. We checked the sensitivity of the model selection procedure to the significance level α.

Splitting between external and brain internal variables

In the current study we were interested in how CA1 and SUB neurons compare in their mapping of navigational covariates P, H and S. The covariates E and T (ensemble firing and theta) were treated as brain internal states which helped fitting the model but did not directly explain the behavior of the animal. We therefore used them as auxiliary variables which helped to get the best possible fit, by on the one hand 'explaining away' spikes that otherwise would have been attributed to position, head direction or speed and on the other reducing the level of noise in the spike trains such that other spikes could be better attributed to the correct navigational covariate. For example, it might be conceivable that a neuron has a higher firing rate always when the the other neurons at the tetrodes (E) have a high firing rate because the neuron is not well enough isolated from the ensemble. In a scenario in which the ensemble responds to speed, including E in our model will attribute some spikes of that neuron to ensemble firing and less to the speed response. For an extended graph with all models displayed separately, see Figure S3G.

Relative single covariate contributions (rSCC)

The model selection procedure is highly sensitive to individual covariates. Even very small influences of covariates on the firing rates of the neurons are classified as significant. In subsequent analyses we therefore investigated how strongly each neuron's firing rate is determined by either an individual covariate. We measured the contribution of a single covariate C included in the selected model $\mathcal{M}^{\hat{a}}$ in explaining the firing rate of a neuron in terms of the difference in model performance between the selected model and the model resulting from removing the covariate C from the selected model, $\mathcal{M}^{\hat{a}}, C$. We therefore defined the rSCC (C) for covariate $C \in \mathcal{M}^{\hat{a}}$ as LLH($\mathcal{M}^{\hat{a}}$) $-$ LLH($\mathcal{M}^{\hat{a}}, C$) normalized by

$$\sqrt{\sum_{C \in \mathcal{M}^{\star}} \text{LLH}(\mathcal{M}^{\hat{a}}) - \text{LLH}(\mathcal{M}^{\hat{a}}, C)^2}$$

where LLH($\mathcal{M}$) is the normalized log-likelihood of the model $\mathcal{M}$ on the held-out data averaged across cross-validation folds of PHS, C refers to the two-covariate model that does not include the covariate C. Single covariate contributions of covariates not included in the selected model were set to zero.

Mixed selectivity score (MS-score)

The MS-score was defined as the product of rSCC of position, head direction and speed:

$$\text{MS} = \prod_{C \in \{P,H,S\}} \text{rSCC}(C)$$

The product of rSCC is a measure that maximizes at the point where different covariates contribute equally to the firing rate of the cell. As a measure of mixed selectivity, it was therefore preferred over the sum of rSCC or the maximal Euclidean distance from zero as both of these options would be similar for two neurons with either a large contribution of an individual covariate and small contributions the two other, or similarly large contributions of the three covariates.

Tuning curves predicted by the model

Model predicted tuning curves were constructed on the basis of the model including all covariates, $\mathcal{M} = PHSTE$, whose parameters β were learned as explained in section "Learning." A tuning curve is the average firing rate of a neuron as a function of relevant stimulus parameters, in our case covariate bins; for the model predicted tuning curves the average is taken over the distribution of the other covariates. In case of uniform sampling and assuming independence between covariates, the expected value of the firing rate in the i-th bin of covariate C^* for Poisson neurons as defined in Equation 4 is:

$$\mathbb{E}\left[\text{FR}\left(\{\mathbf{X}^C\}_{C \neq C^*}, X_i^{C^*} = 1\right)\right]_{\{\mathbf{x}^c\}_{C \neq C^*}|X_i^{C^*}=1} = \frac{\exp(\beta_i^{C^*})}{dt} \prod_{C \neq C^*} \frac{1}{N_C} \sum_j \exp(\beta_j^C). \tag{Equation 5}$$

Goodness of fit

In order to assess the goodness of fit of the GLM, in addition to LLH($\mathcal{M}$), the average of the explained deviance across cross validation folds exD($\mathcal{M}$) was estimated (Brown et al., 2002; Guisan and Zimmermann, 2000; Kraus et al., 2015; Pillow, 2009). The explained deviance of model $\mathcal{M}$ in cross-validation fold i is defined as $exD_i(\mathcal{M}) = \frac{LLH_i(\mathcal{M})}{LLH_i(S)}$ where S is the so-called saturated model, a maximum-likelihood Poisson GLM optimized on the test data (in practice the firing rate FR in Equation 2 is set equal to the spike count k(t) in each time bin t). Then $ex\,D(\mathcal{M}) = \frac{1}{10} \sum_{i=1}^{10} exD_i(\mathcal{M})$ quantifies the fraction ascribable to model $\mathcal{M}$ of log-likelihood increase with respect to the average firing rate model of the best Poisson model.

Testing for significance in model selection between CA1 or SUB and between OF or ST

For Figures 4E and 5B we used a shuffling procedure to test whether the type of model selected for a proportion of neurons was significantly affected by the anatomical location of the neurons or the task in which the neurons were recorded. For the pair of conditions being compared (either CA1 versus SUB, or OF versus ST), each neuron was randomly assigned to one of the two conditions with equal probability, and for each model (e.g., PH or PHS) the absolute difference was calculated between the proportion of neurons selecting it in the two conditions. This process was repeated 10000 times, yielding a distribution of shuffled differences for each model. If the actual difference between the two groups was outside the 99.9[th] percentile of 10000 such shuffled differences, we considered the difference for a given model (e.g., PH or PHS) to be significant.

Decoding

We exploited the Poisson GLM framework defined in section Poisson GLM for decoding simultaneously position P, head direction H and speed S. We employed the model including all behavioral covariates P, H, S and the internal covariate theta T. Given the learned parameters $\beta^{\mathbf{C}}$ with $C = P,H,S \cup I$, the vectors of spike counts $\mathbf{k}_n$, for cells $n = 1,\dots N$ and the internal observed covariates $\mathbf{X}^I(t)$, the decoded covariates at time t, $\{\mathbf{X}^C(t)\}_{C \in PHS}$, were chosen as those maximizing the objective function:

$$\Gamma(\{\mathbf{X}^C(t)\}_{C \in PHS}|\mathbf{k}_{n\,n=1}^N, \mathbf{X}^I(t)) = \sum_{s=-3\sigma}^{3\sigma} K(s) \sum_{n=1}^N \log \text{Prob}(k_n(t+s)|\{\mathbf{X}^C(t)\}_{C \in PHS}, \mathbf{X}^I(t), \{\beta^C\}_{C \in P,H,S \cup I}). \qquad \text{(Equation 6)}$$

In Equation 6 $K(s)$ is a Gaussian kernel of zero mean and standard deviation σ, while $\text{Prob}(k_n(t+s)|\{\mathbf{X}^C(t)\}_{C \in PHS}, \mathbf{X}^I(t), \{\beta^C\}_{C \in P,H,S \cup I})$ is the probability of observing the spike count k_n at time $t+s$, given the covariates $\{\mathbf{X}^C(t)\}_{C \in PHS}, \mathbf{X}^I(t)$ according to the Poisson model in Equation 2 with parameters. $\{\beta^C\}_{C \in P,H,S \cup I}$

Decoding is then maximizing the weighted log-likelihood of the spike counts of all cells in a time window of size $6\sigma + 1$ centered at the time point t. The parameter σ has been optimized for the entire dataset (both regions and both tasks).

Maximization of the objective function Γ was performed by grid search on the covariates lattice defined by the binning adopted for learning, where the number of bins has been optimized as explained in Section "Hyperparameters optimization."

Resampling of neurons

For decoding we sampled differently sized subpopulations (from 5 to 150 neurons) and maximized the likelihood of the spike counts in the space of all three behavioral covariates. Within the selected population, resampled neurons were randomly assembled from different sessions without consideration of whether they had been recorded in parallel or not in the first place. From each neuron we used the parameters Learned using the GLM model with covariates PSTH (sec. "Encoding") and generated Poisson spikes using the model predicted firing rates for Poisson spikes. All the combinations of position, head direction, speed and theta were realized during a recorded session of one of the animals in this study. To differentiate between OF and ST we resampled neurons recorded in the OF and in the ST separately and only employed ST recorded neurons for decoding the ST session and OF recorded neurons for decoding the OF session. This allowed us to decode the three covariates P, H and S simultaneously at every time bin t (while theta was given) by optimizing the likelihood of the weighted spike counts from Gaussian filtered time window $t - \Delta t$ to $t + \Delta t$ (where $2\Delta t$ is the size of the decoding window: 400 ms). The GLM used for encoding provides an estimate of the tuning curves in the 6-dimensional covariate space (2 dimensions for P and 1 for each H, S, E and T), assuming that each covariate contributes multiplicatively to the instantaneous firing rate. In absence of this (or alternative) assumptions on how covariates combine to contribute to the firing rate of a cell, a reliable estimate of the tuning curves in this 6 dimensional behavioral space would require much higher coverage.

Randomization of decoding

The randomized decoding distributions for Figure S6, are built by taking the difference between two means from decoding 20 times from a randomly selected subpopulation of neurons, while ensuring equal probability to select CA1 or SUB neurons. The randomization runs over 1000 iterations and it is assessed whether the difference between decoding error of CA1 and SUB population is larger than the 99th percentile of the randomized differences.

Statistical testing

The experimenters were not blind to subject treatments and no statistical methods were employed to predetermine sample size. Details regarding data distributions, statistical tests and sample size are presented in the main text, figures, and figure legends. Data presented as mean ± standard error of the mean (SEM), unless otherwise specified. All data was analyzed with custom-written MATLAB scripts (https://se.mathworks.com/). Nonparametric tests were used to analyze data violating normal distribution assumptions (Mann–Whitney U test), and all statistical tests performed were two-tailed with significance level set at $p < 0.05$ while P-values where always provided as numerical values.

PAPER 4

This article is awaiting publicaton and is not included in NTNU Open

"It's for us that the University exists, for the dispossessed of the world; not for the students, not for the selfless pursuit of knowledge, not for any of the reasons that you hear. We give out the reasons, and we let a few of the ordinary ones in, those that would do in the world; but that's just protective coloration. Like the church in the Middle Ages, which didn't give a damn about the laity or even about God, we have our pretenses in order to survive. And we shall survive—because we have to."

— John Williams, Stoner

NTNU

Norwegian University of
Science and Technology